THE HENRYK NIEWODNICZAŃSKI INSTITUTE OF
NUCLEAR PHYSICS POLISH ACADEMY OF SCIENCES

DOCTORAL THESIS

Beyond the Standard Model searches in the sector of heavy quarks and exotic long-lived particles

---

Author:	*Supervisor:*
Mateusz GONCERZ	Prof. Marcin KUCHARCZYK
	Auxiliary supervisor:
	Dr. Bartłomiej RACHWAŁ

A thesis submitted in fulfilment of the requirements
for the degree of Doctor of Philosophy

in the

LHCb Experiment Department
Division of Particle and Astroparticle Physics

2024

THE HENRYK NIEWODNICZAŃSKI INSTITUTE OF NUCLEAR PHYSICS
POLISH ACADEMY OF SCIENCES

Abstract

LHCb Experiment Department
Division of Particle and Astroparticle Physics

Beyond the Standard Model searches in the sector of heavy quarks and exotic long-lived particles

by Mateusz GONCERZ

The thesis considers three aspects of Beyond the Standard Model searches, focusing on experimental signatures with heavy particle jets and exotic particles decaying in displaced secondary vertices. The $Z^0\left(\rightarrow \mu^+\mu^-\right) b\bar{b}$ production cross-section is measured in the forward kinematic region, using proton-proton collisions collected by the LHCb experiment at the centre-of-mass energy of 13 TeV. The value is preliminarily evaluated as 70.70 ± 26.56 (syst.) $\pm$ 0.74 (stat.) pb, which is compatible with the Next-to-Leading Order prediction. Next, the sensitivity of the CLIC detector to exotic long-lived particle signatures is studied for the first stage of its planned operation. A Hidden Valley scenario with a QCD-like hidden sector and a $H \rightarrow \pi_v^0\pi_v^0 \rightarrow b\bar{b}b\bar{b}$ process are analysed. The hypotheses of $m_{\pi_v^0} \in (25, 35, 50)$ GeV and $\tau_{\pi_v^0} \in (1, 10, 100, 300)$ ps are considered and the upper limits on $\sigma\left(H\right) \cdot BR\left(H \rightarrow \pi_v^0\pi_v^0\right)$ are calculated at 95% confidence level. They are found to be at the order of 10^{-4} pb and are several orders of magnitude better than for currently operating detectors. Finally, the central software has been developed for the planned MUonE experiment, aiming to perform a precise measurement of the hadronic contribution to the anomalous muon magnetic moment. It includes algorithms for all the crucial stages of experimental data analysis, i.e. event reconstruction, detector simulation, alignment and offline selection. It is successfully used to perform an analysis of the data collected during 2018 test beam. The algorithm and detector performance are also evaluated for the ultimate apparatus, using Monte Carlo simulation. The extended physics program of MUonE experiment, including searches for exotic long-lived particles with leptonic final states, is considered and discussed.

INSTYTUT FIZYKI JĄDROWEJ IM. HENRYKA NIEWODNICZAŃSKIEGO
POLSKIEJ AKADEMII NAUK

Streszczenie

Zakład Eksperymentu LHCb
Oddział Fizyki i Astrofizyki Cząstek

Poszukiwanie zjawisk wykraczających poza Model Standardowy w sektorze ciężkich kwarków i egzotycznych długożyciowych cząstek

Mateusz GONCERZ

Praca doktorska rozważa trzy aspekty poszukiwań zjawisk wykraczających poza Model Standardowy, skupiając się na eksperymentalnych sygnaturach z ciężkimi dżetami oraz egzotycznymi cząstkami rozpadającymi się w przesuniętych wierzchołkach wtórnych. Przekrój czynny na produkcję $Z^0\,(\to \mu^+\mu^-)\,b\bar{b}$ został zmierzony w części "do przodu" przestrzeni fazowej, wykorzystując dane ze zderzeń proton-proton, zebrane przez eksperyment LHCb przy energii 13 TeV w układzie środka masy. Wartość została wstępnie oszacowana na $70.70 \pm 26.56\,(\text{syst.}) \pm 0.74\,(\text{stat.})$ pb i jest zgodna z przewidywaniami Next-to-Leading Order. Następnie zbadana została czułość detektora CLIC, w pierwszej z jego planowanych faz działania, na sygnatury egzotycznych cząstek długożyciowych. Przeanalizowano scenariusz Ukrytej Doliny (Hidden Valley), z dodatkowym sektorem cząstek o strukturze podobnej do QCD, oraz proces $H \to \pi_v^0\pi_v^0 \to b\bar{b}b\bar{b}$. Zbadane zostały hipotezy $m_{\pi_v^0} \in (25, 35, 50)$ GeV oraz $\tau_{\pi_v^0} \in (1, 10, 100, 300)$ ps, a górne limity zostały obliczone na poziomie ufności 95%. Są one rzędu 10^{-4} pb i są kilka rzędów wielkości lepsze niż dla obecnie działających detektorów. Na koniec, opracowane zostało centralne oprogramowanie dla planowanego eksperymentu MUonE, który ma wykonać precyzyjny pomiar hadronowego przyczynku do anomalnego momentu magnetycznego mionu. Zawiera ono algorytmy dla wszystkich niezbędnych stadiów analizy danych eksperymentalnych, tj. rekonstrukcji przypadków, symulacji detektora, jego pozycjonowania oraz selekcji przypadków w trybie offline. Oprogramowanie zostało z powodzeniem użyte do analizy danych zebranych podczas wiązki testowej w 2018 roku. Wydajność algorytmów oraz detektora zostały również oszacowane dla jego ostatecznej konfiguracji, przy użyciu symulacji Monte Carlo. Wzięty pod uwagę został rozszerzony program fizyczny eksperymentu MUonE, zawierający poszukiwanie egzotycznych cząstek długożyciowych z leptonowymi sygnaturami rozpadu.

Acknowledgements

The thesis was supported by the PRELUDIUM grant, under the contract 2023/49/N/ST2/02173, and OPUS grant, under the contract 2022/45/B/ST2/00318, from the National Science Centre NCN (Poland) as well as by computing grants from the Academic Computer Centre Cyfronet AGH.

Contents

Chapter 1

Introduction

The Standard Model (SM) combines contemporary knowledge about fundamental particles, their composite systems and three fundamental interactions, which can be formulated within the framework of quantum mechanics (electromagnetic, weak and strong). Due to missing description of other known phenomena (in particular, gravity and dark matter), it is considered to be only a low energy limit of an underlying theory. The search for discrepancies between the SM predictions and experimental measurements, as well as signatures of Beyond the Standard Model (BSM) processes, plays thus an important role in validating and guiding further theoretical development. The thesis covers three topics, corresponding to their different aspects. Namely, the search for BSM phenomena in the currently operating LHCb experiment, evaluation of the sensitivity of future CLIC detector to exotic dark matter signatures and, finally, the development of software and event reconstruction algorithms for the upcoming MUonE experiment, including the context of searches for exotic long-lived particles with leptonic final states.

The thesis is structured as follows. The necessary theoretical and experimental introduction is provided in chapter 2. Chapters 3 and 4 are dedicated to the measurement of a $Z^0b\bar{b}$ production cross-section in the Large Hadron Collider beauty (LHCb) experiment, performed by the author of this thesis. The process plays an important role both in the Standard Model (primarily as a benchmark for different approaches to theoretical calculations) and as a probe for BSM phenomena, due to the sensitivity to higher order corrections induced by exotic particles. The analysis is currently in the LHCb publication procedure [1] and is supported by a PRELUDIUM grant (2023/49/N/ST2/02173) from the National Science Centre, with the author being the principal investigator. The first of the two chapters gives an overview of the LHC accelerator and LHCb detector, while the second discusses the analysis and results.

The second study focuses on a class of dark matter candidates, which decay producing displaced secondary vertices (with respect to the beam axis and the primary interaction point). Such experimental signatures are a result of their interactions with the Standard Model sector being strongly suppressed and allow for efficient searches with modern particle detectors and dedicated event reconstruction algorithms. While there has not been any evidence for their existence so far, the candidates for LHC successors (and in particular the Compact Linear Collider, CLIC, which the study considers) are expected to provide a sensitivity which is orders of magnitude better than currently operating detectors. The sensitivity is evaluated by the author for the first of the envisioned stages of CLIC operation (at the centre-of-mass energy of 350 GeV), extending the already existing result for the last stage (3 TeV). The displaced vertex signatures are modelled assuming exotic pions decaying exclusively into pairs of heavy b quarks within the Hidden Valley framework. Both studies have been published together in the Journal of High Energy Physics [2]. The overview of CLIC collider and detector are given in chapter 5, while the analysis and results are described in chapter 6.

Chapters 7 and 8 are dedicated to the MUonE experiment, which has been recently proposed to strengthen the discrepancy of measurement and the Standard Model prediction, observed for the anomalous magnetic moment of a muon. The experiment aims to reduce the uncertainty of the prediction by measuring its contributions, which cannot be calculated from first principles. The construction of the detector, however, makes it also sensitive to a relatively wide variety of dark matter candidates with displaced vertex signatures. The author is the main developer of the FairMUonE software for an off-line data processing, including algorithms for detector simulation and alignment as well as event reconstruction and analysis. It has been successfully used during the MUonE test beams in 2018, 2022 and 2023. Furthermore, the analysis of data collected in 2018 (performed with a major contribution from the author) has been published in the Journal of Instrumentation [3].

A summary of results presented in the thesis is given in chapter 9. Chosen aspects of the aforementioned analyses were also presented at international conferences, with some of them being featured in published proceedings [4, 5].

Chapter 2

Theoretical and experimental overview

2.1 Introduction

As mentioned in the introduction, the Standard Model of particle physics encompasses all of contemporary knowledge about particles and their three fundamental interactions – electromagnetic, weak and strong. Despite its incredible predictive power, it has significant limitations which motivate searches for new physics phenomena. In particular, it does not include any description of gravity or incorporate particles that could fulfil the role of dark matter, which is necessary to explain cosmological observations [6, 7]. A number of extensions have thus been proposed to address this issue (e.g. the supersymmetry model discussed in section 2.3.1). Usually, the dark matter candidates they propose are assumed to be rather massive and have non-zero lifetimes, hence they are often referred to as the long-lived particles (LLPs). As a consequence, they can also travel a significant distance before decaying, resulting in an experimental signature with a secondary vertex, displaced from the primary interaction point they originated in. This, in turn, offers an effective way of searching for them with dedicated detectors and event reconstruction algorithms.

On the other hand, the absence of exotic particle discoveries in direct searches calls for the parallel exploration of alternative experimental approaches. In particular, the associated production of a Z^0 boson and a pair of b quarks ($Z^0b\bar{b}$), studied in this thesis, is one of the primary examples of sensitivity to higher order corrections. Such corrections may be caused by exotic particles appearing in the intermediate interactions and thus yield an indirect evidence for their existence. A different alternative is offered by colliders and detectors with a much cleaner experimental environment or unique design. Aside from the study of $Z^0b\bar{b}$ production, the thesis investigates the ability of detecting Hidden Valley particles using the CLIC detector [8] and to search for exotic particles in the MUonE experiment [9].

A discussion of the physics motivation for the MUonE experiment is excluded from this chapter and can be found in section 7.2. Similarly, because its sensitivity to long-lived particles is a direct consequence of a unique detector design, the relevant discussion is included in section 7.4. The following section 2.2 gives a concise summary of the Standard Model. Section 2.3 provides an overview of its chosen limitations, which motivate the search for Beyond the Standard Model theories, and gives a brief description of chosen representatives. Section 2.4 discusses the importance of studying $Z^0b\bar{b}$ production and section 2.5 summarises the relevant existing results for the $Z^0b\bar{b}$ production cross-section and sensitivity of current detectors to Hidden Valley particles.

2.2 The Standard Model of particle physics

The Standard Model [10–12] is a Quantum Field Theory (QFT), which combines the Electroweak Theory (EWT, [13–19]) and Quantum Chromodynamics (QCD, [20–22]) into a mathematically self-consistent framework. It describes the properties and interactions (electromagnetic, weak and strong) of elementary particles with spin 0 (scalar bosons), 1/2 (fermions) and 1 (vector bosons). The fermions, which are subdivided further into quarks and leptons, are the building blocks of ordinary matter. In particular, quarks can form composite states called hadrons (e.g. proton, neutron). The simplest ones are mesons (quark and anti-quark) and baryons (three quarks or three anti-quarks), however, exotic states with more than three quarks have also been observed (e.g. pentaquarks [23]).

The interactions are mediated by vector bosons. Each one corresponds to a particular charge, which is a fundamental property of an elementary particle. Photons γ are carriers of the electromagnetic force and couple to the electric charge. Weak interactions are mediated by Z^0 (neutral current) and $W^\pm$ (charged current) bosons, which couple to weak charge and weak isospin, respectively. The quarks carry a colour charge and interact strongly by exchanging gluons, which themselves are also charged and can interact with each other. The colour charge is never observed, because the creation of new quark-antiquark pairs is more energetically favourable than breaking the bond between two quarks. This behaviour is known as colour confinement and leads to bare quarks immediately combining with such pairs to form hadrons. The phenomenological description included in many Monte Carlo generators is based on the Lund model [24], which introduces a one dimensional flux string representing the potential energy stored in the colour field between two quarks. The potential energy grows linearly with their relative distance ($E = \kappa \cdot d$), with the typical value of the tension coefficient at the order of $\kappa = 1\,\mathrm{GeV/fm}$. When it gets sufficiently high, the string breaks and the stored energy is converted into a new quark-antiquark pair (a process known as fragmentation). A cascade of creation and recombination (hadronization) results in a collimated stream of, mostly light, composite particles called *particle jet*. The only exception is the heaviest known quark (t), which decays via weak interaction.

By construction, all particles in the Standard Model are massless, which does not agree with measurements. The masses are thus introduced by extending the model with an additional scalar field, called the Higgs field. The weak vector bosons (Z^0, $W^\pm$) acquire mass via the Higgs mechanism [19, 25–27], while fermions by interacting with the Higgs field (Yukawa interactions [19]). The gluons and photon remain massless. The quantum of a Higgs field, a scalar Higgs boson, was observed by the CMS and ATLAS experiments at the Large Hadron Collider (LHC) [28, 29].

Elementary particles and their interactions

The development of the SM and its precursors was driven largely by experimental discoveries of new particles and their observed properties. Although the list is not necessarily closed, seventeen fundamental ones are currently known – six quarks (u, d, c, s, b, t), three charged leptons (e^-, μ^-, τ^-), three neutrinos (ν_e, ν_μ, ν_τ), four vector bosons (γ, Z^0, $W^\pm$ and gluon) and the scalar Higgs boson H. Each fermion has an anti-particle, which is its identical copy with an opposite electric charge. The quarks and leptons are organised into three generations, each containing two quarks, a charged lepton and its corresponding neutrino.

Each particle is associated with multiple quantum numbers. The most important, aside from spin, are the lepton number L, baryon number B, electric charge Q, colour charge C and the third component of weak isospin T_3. The first four (L, B, Q, C) are conserved in interactions. T_3 is not, but its linear combination with charge Q, called weak hypercharge, $Y = 2\left(Q - T_3\right)$ is. The lepton and baryon numbers play a role of particle counters, i.e. $L = n_l - n_{\bar{l}}$, the difference in the number of leptons and anti-leptons, and $B = \frac{1}{3}\left(n_q - n_{\bar{q}}\right)$ – the difference in the number of quarks and anti-quarks. The fraction $\frac{1}{3}$ is included by convention to make the baryon number of the simplest composite particles an integer – 0 for mesons, 1 for baryons and -1 for anti-barions. A non-zero value of the charges indicates that a particle can interact via the electromagnetic (Q), weak (Q, I_3) and strong (C) interaction. All four are dimensionless, although Q represents the multiplicity of an elementary charge e. The colour charge is expressed, analogous to primary colours, as red, green and blue (or r, g, b for short). Because of colour confinement, all composite particles must be colour neutral. All mesons are thus states of opposite colour charges ($r\bar{r}$, $g\bar{g}$, $b\bar{b}$) and baryons universally contain all three (rgb, $\bar{r}\bar{g}\bar{b}$). Table 2.1 lists the basic properties of fermions. The masses of particles are listed in table 2.2 and are free parameters of the SM, which have to be measured experimentally. Upper limits are given for neutrinos – they are known to have non-zero masses due to oscillations, but the values are not well established. Within the SM, they are considered to be massless, although a detailed discussion is beyond the scope of this introduction.

family	generation			L	B	Q	T_3	C
leptons	e^- ν_e	μ^- ν_μ	τ^- ν_τ	1	0	-1 0	$-\frac{1}{2}$ $+\frac{1}{2}$	0
quarks	u d	c s	t b	0	$\frac{1}{3}$	$+\frac{2}{3}$ $-\frac{1}{3}$	$+\frac{1}{2}$ $-\frac{1}{2}$	r, g, b

TABLE 2.1: Division of fermions into generations and their corresponding quantum numbers. The numerical values are negated for anti-particles.

family	flavour	mass
quarks	u	$2.16^{+0.49}_{-0.26}$ MeV
	d	$4.67^{+0.48}_{-0.17}$ MeV
	s	$93.4^{+8.6}_{-3.4}$ MeV
	c	1.27(2) GeV
	b	$4.18^{+0.03}_{-0.02}$ GeV
	t	172.69(30) GeV
leptons	e^-	0.51099895000(15) MeV
	μ^-	105.6583755(23) MeV
	τ^-	1776.86(12) MeV
	ν_e	massless in SM / less than 1.1 eV at 90% CL
	ν_μ	massless in SM / less than 1.1 eV at 90% CL
	ν_τ	massless in SM / less than 1.1 eV at 90% CL
bosons	Z^0	91.1876(21) GeV
	$W^\pm$	80.377(12) GeV
	gluon	massless
	photon	massless

TABLE 2.2: Masses of elementary particles [30].

The strong interaction is mediated by gluons, which carry a pair of C charges – colour and anti-colour (e.g. $r\bar{b}$). The interaction is represented by a change of quark colour charge due to emission/absorption of a matching gluon. The gluons interact also with each other, which makes the strength of the interaction between two quarks smaller as they get closer together (a phenomenon known as asymptotic freedom). On the other hand, the strength quickly grows with the relative distance, which keeps quarks in stable bound states and causes colour confinement. Strong interaction is short ranged, with typical distances at the order of one femtometre (close to the size of a proton).

The electromagnetic and weak interaction are unified within the Electroweak Theory. The former has infinite range and is mediated by photons between electrically charged particles ($Q \neq 0$). The weak interaction has an effective range of about three orders of magnitude higher than the strong one and is mediated by the three massive vector bosons ($W^\pm$ and Z^0). The interactions where W^- and W^+ are exchanged are special, because they can change quark flavour (only between states of different T_3 value). Consequently, they are responsible for nuclear decays, e.g. β^- which involves a change of a neutron (udd) into a proton (uud), $n \to p^+ + W^- (\to e^- + \bar{\nu}_e)$. They also violate all fundamental symmetries – charge (C), parity (P) and time (T) – as well as a combined charge-parity (CP) symmetry and are thus one of the elements (although not sufficient) explaining the difference between the amount of matter and anti-matter in the universe. An important feature of the weak interaction is the sensitivity to particle's chirality (relative orientation of the spin and momentum), which makes a division of fermions into left and right-handed necessary. Only left-handed (spin antiparallel to momentum) particles and right-handed (parallel) anti-particles couple to $W^\pm$. Z^0 couples with all four configurations, but the interactions with "non-matching" types are strongly suppressed.

The approximate relative strengths of the three interactions in the SM and gravity are 1 (strong) - 10^{-2} (electromagnetic) - 10^{-13} (weak) - 10^{-38} (gravity). Within the QFT, they are expressed as coupling constants, which – despite the name – can vary with certain parameters (e.g. energy scale of a process). This is usually referred to as running of the coupling constant. A notable example is the strong interaction, where it increases significantly at low energy scale, making the perturbative approach to calculations unfeasible.

The dynamics of SM are encoded in a Lagrangian with a gauge symmetry group $SU(3)_C \times SU(2)_T \times U(1)_Y$, where the subscripts stand for colour, weak isospin and hypercharge. The gauge invariance is ensured by defining the general form of the covariant derivative, acting on a fermion field ψ, as:

$$D_\mu \psi = \left(\partial_\mu - i\,\frac{g_s}{2}\,\lambda_\alpha\, G^\alpha_\mu - i\,\frac{g}{2}\,\sigma_j\, W^j_\mu - i\,\frac{g'}{2}\,Y\, B_\mu \right) \psi, \tag{2.1}$$

where appropriate terms are chosen, depending on the fermion type, and λ (Gell-Mann matrices), σ (Pauli matrices) and Y (weak hypercharge) are the generators of $SU(3)_C$, $SU(2)_T$ and $U(1)_Y$, respectively. The tensors – G, W and B – define the fields of strong and electroweak bosons, with g quantifying the strength of their coupling to fermions. The $SU(3)_C$ group has eight generators, which give rise to eight gluons. The remaining four introduce the massless electroweak bosons – W_1, W_2, W_3 and B, which mix to produce massive $W^\pm$ and Z^0 observable states, and a massless photon γ (see section below).

The general form of the SM Lagrangian density (called Lagrangian from this point on) is:

$$\mathcal{L}_{SM} = \mathcal{L}_{\text{gauge}} + \mathcal{L}_{\text{fermion}} + \mathcal{L}_{\text{Higgs}} + \mathcal{L}_{\text{Yukawa}}, \tag{2.2}$$

where the last two terms incorporate the Higgs field and its interactions with the fermion fields, which generate their masses. $\mathcal{L}_{\text{gauge}}$ is the kinetic term, describing propagation of vector bosons, with terms bilinear in the corresponding field strength tensors (derived from fields in eq. (2.1)):

$$\mathcal{L}_{\text{gauge}} = -\frac{1}{2}\,tr\left(G_{\mu\nu}G^{\mu\nu}\right) - \frac{1}{2}\,tr\left(W_{\mu\nu}W^{\mu\nu}\right) - \frac{1}{4}\,B_{\mu\nu}B^{\mu\nu}. \tag{2.3}$$

Finally, $\mathcal{L}_{\text{fermion}}$ describes the matter content of the SM and its interactions. The general form is:

$$\mathcal{L}_{\text{fermion}} = \bar{\psi}\, i\, \gamma^\mu\, D_\mu\, \psi, \tag{2.4}$$

where γ^μ are the Dirac matrices, D_μ is defined in eq. (2.1) and the sum over all fermions is implied. Expanding the expression for covariant derivative yields the kinetic part (from the ∂_μ term) and the interaction part. The calculations within the SM usually involve a perturbative expansion of relevant interaction terms. The terms of resulting series can then be expressed as Feynman diagrams and evaluated independently [31].

Higgs mechanism and Yukawa interactions

The symmetries of SM Lagrangian prevent direct inclusion of terms, which could generate the masses of fermions and weak bosons (for example, the simplest candidate – $m\bar{\psi}\psi$ – transforms differently than W and B fields). To address this issue, a scalar Higgs field with Mexican hat potential (fig. 2.1) is introduced. It is chosen to be invariant under the electroweak gauge group, $SU(2)_T \times U(1)_Y$, and hence preserves the Lagrangian symmetry and renormalizability. Below a critical temperature, usually assumed to be approximately 160 GeV or 10^{-12} seconds after the Big Bang, the field moves from the metastable centre of the potential to a minimum and acquires a non-zero vacuum expectation value. The resulting Nambu-Goldstone modes get absorbed as longitudinal components of the gauge fields and enable weak bosons to become massive, while the remaining radial degree of freedom (up and down the hill) gives rise to the Higgs boson.

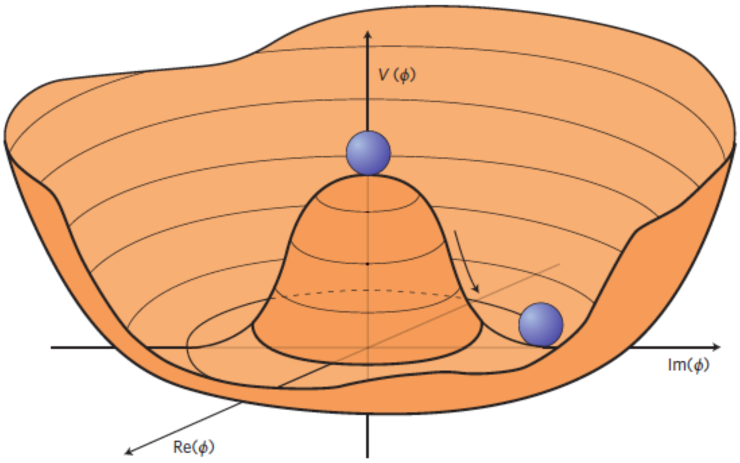

FIGURE 2.1: Shape of the Higgs potential. Figure taken from [32].

The complex scalar Higgs field is an isospin doublet, consisting of a charged and neutral component:

$$\phi = \begin{pmatrix} \phi^+ \\ \phi^0 \end{pmatrix}, \tag{2.5}$$

while the potential is defined as:

$$V(\phi) = \mu^2 \phi^\dagger \phi + \lambda \left(\phi^\dagger \phi\right)^2 . \tag{2.6}$$

The μ^2 has units of mass squared and is chosen as strictly negative to produce a non-zero vacuum expectation value. The dimensionless parameter λ is positive and controls the steepness of the potential in the radial direction, and hence the mass of the Higgs boson. Ground state satisfies:

$$v^2 = |\phi|^2 = -\frac{\mu^2}{2\lambda} > 0 \tag{2.7}$$

and fixes the mass to $m_H = \sqrt{2\lambda} v$. Evolution of the Higgs field is introduced into the SM Lagrangian as:

$$\mathcal{L}_{\text{Higgs}} = \left(D_\mu \phi\right)^\dagger \left(D^\mu \phi\right) - V(\phi), \tag{2.8}$$

where the covariant derivative D_μ contains only electroweak terms, i.e.

$$D_\mu \phi = \left(\partial_\mu - i\frac{g}{2}\sigma_j W_\mu^j - i\frac{g'}{2} Y B_\mu\right)\phi. \tag{2.9}$$

The observable weak boson states are linear combinations of massless electroweak bosons:

$$W^\pm = \frac{1}{\sqrt{2}}\left(W_1 \mp i W_2\right), \tag{2.10}$$

with masses generated by the $\frac{1}{2}m_{W^\pm}^2 W_\mu^\dagger W^\mu = \frac{1}{2}\left(\frac{gv}{2}\right)^2 W_\mu^\dagger W^\mu$ term in eq. (2.8). The remaining W_3 and B bosons mix to form the photon γ and Z^0:

$$\begin{pmatrix} \gamma \\ Z^0 \end{pmatrix} = \begin{pmatrix} \cos\theta_w & \sin\theta_w \\ -\sin\theta_w & \cos\theta_w \end{pmatrix} \begin{pmatrix} B \\ W_3 \end{pmatrix}, \tag{2.11}$$

with θ_w being the so-called Weinberg angle. The mass of the Z^0 boson is then expressed as

$$m_{Z^0} = \frac{m_{W^\pm}}{\cos\theta_w} = \frac{v\sqrt{g^2 + g'^2}}{2}, \tag{2.12}$$

while γ remains massless.

To explain the fermion masses, the SM Lagrangian has to be extended further with Yukawa interactions of the fermion and Higgs fields. They have a general form of

$$\mathcal{L}_{\text{Yukawa}} = G_\psi\, \bar{\psi}\, \phi\, \psi, \tag{2.13}$$

with sum over all fermions implied and corresponding mass coefficients dependent on the coupling of individual fermions to the Higgs field (y_f):

$$m_f = \frac{y_f\, v}{\sqrt{2}}. \tag{2.14}$$

2.3 Limitations of the Standard Model and its selected extensions

The predictions of the SM are almost universally consistent with measurements – an important benchmark is the value of fine structure constant, which currently stands in agreement at the level of one part per billion. While the counterexamples are very few (including primarily the anomalous magnetic moment of a muon, discussed in chapter 7), it can only be considered as a low energy limit of a more fundamental theory due to the way it is constructed. The main issues being the absence of any notion of gravity and the incompatibility with the Standard Model of Cosmology [33], i.e. the lack of particles that could play the role of cold dark matter (other than possibly a small contribution of right-handed, or sterile, neutrinos). The need arises from various cosmological anomalies, which suggest the existence of a large amount of mass in the universe that does not interact electromagnetically (and thus causes gravitational effects without being directly observable, e.g. in galaxy dynamics, gravitational lensing or cosmic microwave background [6]). Alternative solutions – like the MOdified Newtonian Gravity (MOND) [34] – have been proposed, but are either not mathematically consistent or explain the phenomena only partially. The contemporary predictions estimate that dark matter constitutes about 27% [7] of the total mass and energy in the universe (with approximately 5% being the ordinary baryonic matter and the rest attributed to Dark Energy, which is also not accounted for in the SM).

Furthermore, the introduction of masses via the Higgs mechanism gives rise to an unexplained large difference in the strength of gravitational and weak interactions (known as the hierarchy problem). The measured mass of the Higgs boson (approximately 126 GeV) is also much smaller than expected, i.e. it should approach the Planck scale (10^{19} GeV) due to significant quantum corrections, originating in interactions with virtual particles. The fact that these corrections cancel out almost exactly is commonly viewed as an unnatural level of fine-tuning. Finally, the SM does not derive many of the important quantities from first principles and instead relies on experimental data to determine them. Specifically, it has 19 free parameters which correspond to the coupling strengths (3), Higgs potential (2), masses of the particles (9), the mechanism of flavour changing in weak interactions (4) and the level of CP violation in strong interactions (1).

Different SM extensions and alternatives have been developed to address the above-mentioned issues to a varying degree. The so-called Theories of Everything (TOE) aim to combine the description of all known phenomena into a coherent framework, usually by introducing a new mathematical approach (e.g. superstring theory [35] and loop quantum gravity [36]). Similarly, the Grand Unified Theories (GUTs) postulate unification of the three fundamental interactions with quantum mechanical description (electromagnetic, weak and strong) above certain energy scale. This idea is motivated by the loose convergence of the corresponding coupling constants, which happens close to 10^{16} GeV. The unification is achieved by embedding the SM within a gauge group with higher symmetry (e.g. $SO(10)$ [37]), which is then broken down in a manner similar to the Higgs mechanism. In addition, models much smaller in scale and aiming to solve only a subset of issues also exist. By extending the SM, the alternative frameworks introduce new particles which can be searched for both directly and indirectly (through their influence on known phenomena). Most also predict good candidates for dark matter, either explicitly or by assuming the existence of a hidden particle sector. Their important feature are significant lifetimes, which are caused by the suppression of decays into the Standard Model final states, and – consequently – experimental signatures with displaced secondary vertices.

A class of models that addresses the hierarchy problem by design is called supersymmetry (discussed further in section 2.3.1). They are considered as "near-GUTs" for achieving an approximate convergence of coupling constants by modifying their running rather than the underlying gauge group. They also predict particles consistent with dark matter characteristics and, in most cases, incorporate a hidden particle sector. Section 2.3.2 introduces the Hidden Valley framework, which is commonly used to formalise the concept of such sectors. Finally, section 2.3.3 describes the axion model, proposed to address the issue of unnatural suppression of CP violation in strong interactions within the SM. All three classes of models predict the existence of long-lived particles, each possessing different characteristics.

2.3.1 Supersymmetry

The supersymmetry [38, 39] postulates existence of a fundamental symmetry between fermions and bosons. It is based on the same gauge group as the Standard Model, but extends its particle content by assigning each a supersymmetric partner, which is of the opposite type (i.e. its spin is shifted by 1/2). Because the number of fermions and bosons is doubled, and they contribute quantum corrections to the Higgs mass with opposite sign, its value is stabilised without fine-tuning required. By convention, the superparticles are named by adding "s" in front of the fermion name (e.g. selectron) or "ino" at the end of the boson name (e.g. gluino). They share most of their characteristics with the corresponding SM particles (i.e. charges and quantum numbers). However, since candidates are not observed experimentally (up to approximately 1 TeV [40]), they have to be significantly heavier and hence in any realistic scenario the symmetry has to be broken at some energy scale.

The supersymmetric models reproduce approximate convergence of coupling constants at 10^{16} GeV by modifying their energy-dependent behaviour (as illustrated in fig. 2.2) and can include gravity, although by directly incorporating General Relativity rather than providing a unified framework [41]. They are also used to address the hierarchy problem as part of other models (e.g. supersymmetric GUTs).

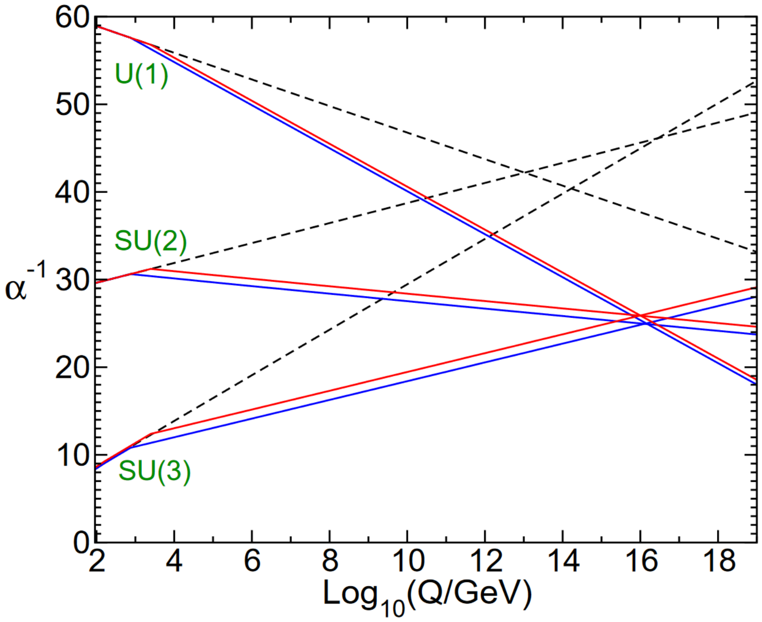

FIGURE 2.2: The inverse of coupling constants, corresponding to the three interactions in the Standard Model, as a function of the energy scale. Dashed lines show the Standard Model values, coloured in one of the supersymmetry variants. Figure taken from [38].

The most widely adopted realisation of supersymmetry is the minimally supersymmetric Standard Model (MSSM, [38, 42]), which is minimal in a sense of adding the least new fields while producing a model that is phenomenologically consistent with experimental observations. It introduces exactly one superpartner for each fermion and vector boson, however, the Higgs sector has to be more complex to ensure cancellation of gauge anomalies and mass generation for all particles. It comprises two doublets, which couple to the up-type quarks (H_u) as well as down-type quarks and charged leptons (H_d). Both have a neutral and charged component, i.e.

$$H_u = \begin{pmatrix} H_u^+ \\ H_u^0 \end{pmatrix} \tag{2.15}$$

$$H_d = \begin{pmatrix} H_d^0 \\ H_d^- \end{pmatrix}, \tag{2.16}$$

and a corresponding superpartner ($\tilde{H}_u$, $\tilde{H}_d$). The vacuum expectation values (v_u and v_d) are fixed by the electroweak energy scale, $v_u^2 + v_d^2 \approx (246\text{ GeV})^2$.

The Higgs mechanism generates five massive Higgs bosons. The lightest one (h^0) is neutral and CP-even. It is also the most compatible with the Standard Model Higgs boson and, in certain scenarios, can have a similar mass. Remaining ones are predicted to be relatively heavy (potentially exceeding 1 TeV) and are the neutral and CP-even H^0, neutral and CP-odd A^0, and a charged pair $H^\pm$. Furthermore, the mixing of gauginos and Higgsinos produces additional states – four neutralinos ($\tilde{\chi}_1^0$, $\tilde{\chi}_2^0$, $\tilde{\chi}_3^0$, $\tilde{\chi}_4^0$), which are mixtures of neutral electroweak gauginos ($\tilde{B}^0$, $\tilde{W}^0$) and neutral Higgsinos ($\tilde{H}_u^0$ and $\tilde{H}_d^0$), and two charginos ($\tilde{\chi}_1^\pm$, $\tilde{\chi}_2^\pm$), formed by charged winos ($\tilde{W}^\pm$)

and Higgsinos ($\tilde{H}_u^{\pm}$ and $\tilde{H}_d^{\pm}$). The neutralinos, in particular, could play a role of dark matter candidates due to their lowest mass.

Supersymmetric theories introduce a new quantum number (R-parity), defined by the baryon and lepton numbers (see section 2.2), and spin:

$$P_R = (-1)^{3(B-L)+2S}, \tag{2.17}$$

with all Standard Model states taking a value of +1 and all supersymmetric ones -1. While the exact conservation of R-parity is commonly assumed, in order to prevent protons from decaying rapidly, it also makes the lightest supersymmetric particle (LSP, usually lightest neutralino) stable. However, as the proton decay channels involve a change of both lepton and baryon number at the same time (e.g. $p^+ \to e^+\pi^0$), the R-parity can be safely broken if only one of them is violated. The resulting decays of LSPs would be necessarily suppressed and produce displaced vertices. Furthermore, to avoid issues arising from phenomenological considerations, in most scenarios the symmetry breaking mechanism is delegated to a hidden sector. Its existence implies additional candidates for dark matter, as well as possible decays with long-lived particle signatures. For example, the Higgs boson decaying into six quarks with a displaced vertex is expected [43]. Other promising signatures come from gluinos [44] or neutralinos [45–47], which can undergo detectable cascading decays to the lightest state even without R-parity violation (e.g. $\tilde{\chi}_2^0 \to \tilde{\chi}_1^{\pm} q\bar{q}'$).

An overall increase in complexity with respect to the SM requires at least 124 free parameters. This number can be significantly reduced by requiring consistency with experimental data (e.g. in the degree of flavour and CP violation). The minimal number of additional parameters, which have to be added to the 19 of the Standard Model, is five:

- a common mass for scalar superpartners at the unification scale,
- a common mass for gauginos at the unification scale,
- coupling strength of the Higgs fields and sfermions at the unification scale,
- the ratio of both vaccuum expectation values,
- and the sign of the Higgsino mass parameter μ (appearing in the $\mu H_u H_d$ term of the Lagrangian), whose magnitude can be expressed by other quantities.

This scenario is realised by a so-called Constrained MSSM/minimal Supergravity [38] (CMSSM/mSUGRA) model, where the symmetry breaking is transmitted from the hidden to visible sector through gravitational interactions. These interactions are suppressed at the Planck scale, which keeps the predicted particle masses constrained and within experimental reach.

Analogous to fermionic and bosonic fields in the Standard Model, the superpartners are combined into superfields – chiral superfields have a fermionic and scalar component (e.g. quark and squark) and gauge superfields a gauge boson and the corresponding gaugino (e.g. Z and Zino). Furthermore, the ordinary Minkowski space is promoted to a superspace, by extending it with two fermionic coordinates (conventionally labelled θ^{α} and $\bar{\theta}^{\dot{\alpha}}$) and the Poincaré algebra is extended with new generators to form the supersymmetric algebra (in the simplest variant, there are two supercharges Q and $\bar{Q}$). The supercharges play the role of operators transforming bosonic fields into fermionic and vice versa. The supercovariant derivative, acting on the superfield Φ, is then expressed as:

$$D_\alpha \Phi = \left(\frac{\partial}{\partial \theta_\alpha} - i \left(\sigma^\mu \bar{\theta} \right)_\alpha \partial_\mu \right) \Phi, \tag{2.18}$$

where σ are Pauli matrices. Requiring $\bar{D}^{\dot{\alpha}} \Phi$ to vanish gives a general form of the chiral superfield:

$$\Phi \left(x^\mu, \theta, \bar{\theta} \right) = \left[\phi + \sqrt{2}\, \theta\, \psi + \theta^2 F \right] \left(x^\mu, \theta, \bar{\theta} \right), \tag{2.19}$$

which contains a scalar field ϕ, a fermionic field ψ and an auxiliary field F. The last one is introduced to preserve symmetry between the number of fermionic and bosonic off-shell components. The gauge superfield can be written in a similar manner, in terms of spin 1, spin 1/2 and auxiliary scalar fields, which are added to preserve the supersymmetry.

The Lagrangian is similar in nature to that of the SM, but expressed in terms of the chiral and gauge superfields. Its general form can be written as:

$$\mathcal{L} = \mathcal{L}_{\text{supersymmetry}} + \mathcal{L}_{\text{breaking term}}, \tag{2.20}$$

where the first term is an analogue of the full SM Lagrangian and incorporates the dynamics of the superfields, their interactions and terms which play a role similar to the Higgs and Yukawa ones, giving rise to the masses. The second term is responsible for supersymmetry breaking, which within the MSSM framework is realised by soft breaking terms (i.e. generating masses without introducing ultraviolet divergences and thus spoiling the renormalizability).

2.3.2 Hidden valley model

Both the Standard Model and Beyond the Standard Model theories can be extended with an additional particle sector, described by an independent gauge group. Often, they arise naturally – for example, as part of the extra dimensions introduced by String Theories [48, 49]. Due to lack of experimental evidence, however, the interactions between both sectors have to be strongly suppressed at low energy scales. One of the possible realisations is provided by the Hidden Valley [50] model, where such sectors (conventionally called v-sectors) are hidden behind a large energy barrier. The particles of each sector are neutral under the gauge group of the other and interactions are restricted primarily to – so-called – communicators, which couple to both. The commonly considered candidates are the Higgs boson, exotic heavy neutral vector boson (Z' [51]) and the LSPs (see section 2.3.1), which could decay into the Standard Model particles through the v-sector (this scenario is illustrated in fig. 2.3). At high energy scales (above the LHC reach), the interactions could also be mediated by higher dimensional operators, induced by heavy exotic particles and fields. In such a case, a direct production of v-particles would be possible at future colliders.

The existence of a hidden sector with stable or meta-stable particles is a potential solution to the problem of cold dark matter. Furthermore, because the produced v-particles decay preferably into other hidden states and decays back into the Standard Model are suppressed, the resulting experimental signatures include displaced secondary vertices. The decay lengths, predicted by the model, allow for their detection with currently operating and future particle detectors.

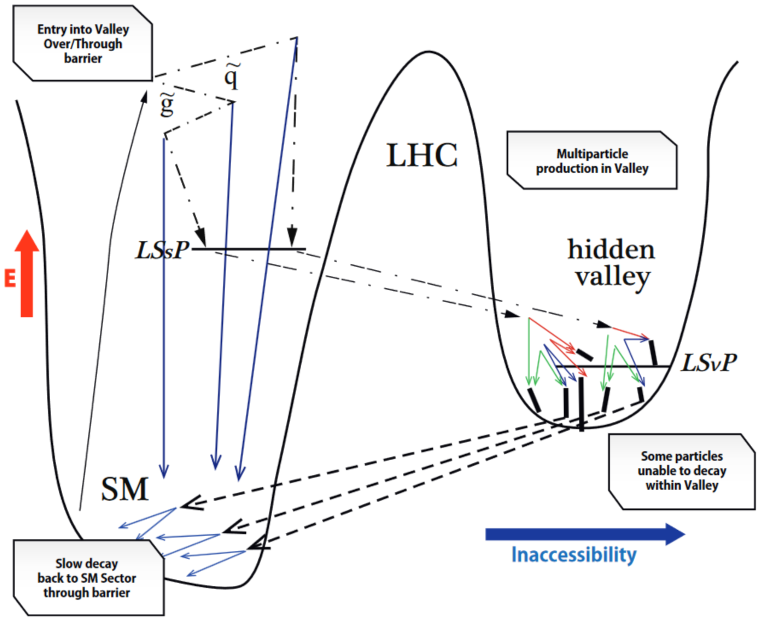

FIGURE 2.3: Example of Hidden Valley scenario, with lightest superparticle decaying into the hidden sector. Figure taken from [52].

The model is encoded in a Lagrangian, which combines independent description of both sectors and a mixing term (in the context of Hidden Valley models, it is usually referred to as the "portal" between both sectors), i.e.:

$$\mathcal{L} = \mathcal{L}_{\text{Standard Model}} + \mathcal{L}_{\text{Hidden Valley}} + \mathcal{L}_{\text{portal}}. \tag{2.21}$$

There are no major restrictions imposed on $\mathcal{L}_{\text{Hidden Valley}}$. In particular, the hidden sector may be based on a different gauge group and thus have a completely different particle content than the SM or its extending theory. Similarly, there are many ways in which the interaction between sectors can be realised. In general, $\mathcal{L}_{\text{portal}}$ will be a weighted sum of terms which mix fields and operators from both sectors, with corresponding coefficients determining the interaction strength. The commonly considered types are, for example:

- Gauge portal, which mixes the gauge boson fields from both sectors. The simplest one usually involves a hypercharge field B, i.e.:

  $$\mathcal{L}_{\text{gauge}} = \frac{\epsilon}{2} B_{\mu\nu} X^{\mu\nu}, \tag{2.22}$$

  where X is a given gauge field from the hidden sector and ϵ is often referred to as the kinetic mixing parameter.

- Higgs portal, which mixes the scalar Higgs fields:

  $$\mathcal{L}_{\text{Higgs}} = \lambda \left|H\right|^2 \left|\phi\right|^2, \tag{2.23}$$

- or fermion portal, mixing fermion fields:

  $$\mathcal{L}_{\text{fermion}} = y\, \bar{\psi}_{SM} \phi \psi_{HV}, \tag{2.24}$$

  with ϕ being some arbitrary mediator field.

Similar terms can be defined for neutrinos, new scalar fields and so on, and can get arbitrarily complex (e.g. involve field derivatives), depending on the structure of the hidden sector and chosen fields and operators. They also determine the expected phenomenology. For example, the coupling of Higgs fields from both sectors can influence the Higgs mechanism and allow Higgs boson decays into the v-sector. Similarly, a gauge portal involving electromagnetic fields could impact the properties of a photon and higher dimensional operators could alter the SM cross-sections of various processes.

The following subsections give an overview of two Hidden Valley scenarios in particular – the production of neutral v-pions through the Higgs portal, which is used to evaluate the sensitivity of CLIC detector model to displaced secondary vertices (discussed in chapter 6), and the dark photons model, which introduces light long-lived particles that can be effectively searched for in the MUonE experiment (discussed in chapter 7).

Production of v-pions through the Higgs portal

One scenario, which can be viewed as a minimal model with a non-abelian hidden gauge group (i.e. QCD-like), was proposed by Strassler and Zurek [50, 53]. It assumes a v-sector with two flavours of heavy (but close in mass) v-quarks, which combine to form three v-pions. Two of them are charged under the v-sector gauge group ($\pi_v^{\pm}$) and one remains neutral (π_v^0), while all three are neutral under the Standard Model gauge group. The remaining v-hadrons decay quickly to v-pions and v-nucleons, which are all stable except for π_v^0. In addition, the model includes a Z' boson as a communicator, with mass in a 1-6 TeV range.

The communication between sectors is realised through the Higgs portal and higher dimensional operators. While this makes a direct production of v-hadrons through a virtual Z' possible, the resulting phenomenology would be experimentally challenging (allowing for potentially large masses of the v-pions). The Higgs boson is particularly interesting as a communicator, because of its abundance at the LHC and planned future colliders. Furthermore, its available decay channels (within the Standard Model) are restricted by a relatively low mass and suppressed by small Yukawa couplings, resulting in a rather small decay width. It is, therefore, possible that a substantial fraction of its interactions proceeds through the hidden channels and could manifest as displaced secondary vertices. The interactions of the Higgs boson with a hidden scalar field ϕ would dominantly produce pairs of π_v^0, which could then decay back into the Standard Model through a virtual Z'. Moreover, because π_v^0 is spinless, its decays into light fermions are suppressed by helicity conservation and, provided it is produced in a decay of an on-shell Higgs boson, its mass is below the Z^0Z^0 threshold. Consequently, the primary decay channel is $\pi_v^0 \to b\bar{b}$ and the most experimentally interesting interaction $H \to \pi_v^0\pi_v^0 \to b\bar{b}b\bar{b}$, with both π_v^0 decaying with a displaced secondary vertex signature (as illustrated in fig. 2.4).

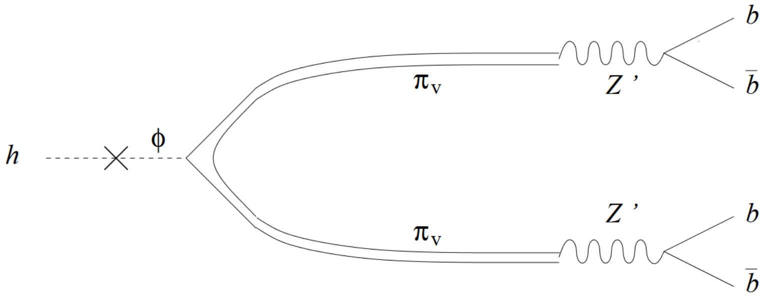

FIGURE 2.4: Production of a π_v^0 pair through the Higgs portal and their subsequent decays into $b\bar{b}$ pairs. Figure taken from [53].

Dark photon model

The dark photons model [54] is a Hidden Valley scenario, which introduces a hidden vector boson (an analogue of the Standard Model photon) and a gauge portal. It aims primarily to solve the dark matter problem, although, while the dark photon is allowed to acquire mass, it is usually considered only as a communicator and dark matter candidates are provided by other v-particles. By convention, the dark photon is labelled A' and couples directly to the Standard Model photon or the hypercharge field B, i.e.:

$$\mathcal{L}_{\text{portal}} = -\frac{\epsilon}{2} F_{\mu\nu} F'^{\mu\nu} \tag{2.25}$$

$$\mathcal{L}'_{\text{portal}} = -\frac{\epsilon'}{2} B_{\mu\nu} F'^{\mu\nu}, \tag{2.26}$$

where F and F' are their corresponding electromagnetic field strength tensors and ϵ is the kinetic mixing parameter, which determines the strength of the coupling. Other portals can be considered, but only these two generate new interactions (and thus dark photon decay channels).

The phenomenology strongly depends on whether A' is allowed to have mass, hence both scenarios are considered independently. The massless dark photon can participate in interactions only via higher dimensional operators, and they are necessarily strongly suppressed. Searches at particle colliders are thus very challenging and often rely only on detecting the missing energy. The most promising signatures are expected in the flavour sector, where they could play a role of new Flavour Changing Neutral Current and lead to rare decays of B [55, 56] and K [57–60] mesons. Other important channels include decays of the Higgs [61–63] and Z bosons [64, 65] into pairs of visible and dark photons.

Assuming a massive dark photon results in a much wider spectrum of possible interactions. For instance, what is especially important for searches at the MUonE experiment (see chapter 7), it can substitute a Standard Model photon in the electromagnetic interactions. Consequently, it can be produced in scattering of leptons on the nuclei or lepton pair annihilation, i.e.

$$l + Z \to l + Z + A' \tag{2.27}$$

$$l^- + l^+ \to \gamma + A'. \tag{2.28}$$

The characteristics of A' are usually considered in a phase space parameterised by the kinetic mixing parameter ϵ and mass $m_{A'}$. If $m_{A'} < 2m_e \approx 1$ MeV, then it is unable to decay into charged Standard Model final states and is considered "invisible", with only a missing energy signature (the decay into a photon pair is also forbidden [66]). Otherwise, it can be detected through its decays into both leptons and hadrons. A significant fraction of the phase space has already been excluded by various experiments and more are planned to extend the coverage [67]. A possible impact of MUonE experiment is discussed in section 7.4.

2.3.3 Axion model

The axion model [68] extends the Standard Model gauge group with an additional $U(1)$ symmetry, in order to introduce a mechanism which suppresses CP violation in strong interactions. While not observed experimentally, it is theoretically possible within the SM due to its Lagrangian containing a term:

$$\mathcal{L}_\theta = \theta \frac{g^2}{32\pi^2} tr \left(G^{\mu\nu} \bar{G}_{\mu\nu} \right), \tag{2.29}$$

where G is the gluon field strength tensor, $\bar{G}$ its dual, g the strong coupling constant and θ is an arbitrary dimensionless parameter (a free parameter of the SM). Both G and $\bar{G}$ transform the same under the charge conjugation, but parity transformation yields an opposite sign and thus they violate the CP symmetry. Because this is not observed experimentally, the term must be suppressed by the θ parameter. There is, in fact, a very stringent limit from the measurements of the neutron dipole moment (proportional to θ), which implies that it is effectively zero ($\theta < 10^{-10}$ [69]). Similarly to the hierarchy problem, the value seems rather arbitrary as it could be anywhere from zero to 2π, resulting in a significantly different phenomenology (e.g. kaon decay rates).

One of the proposed solutions (the Peccei–Quinn mechanism [70]) is to introduce a new complex scalar field ϕ, which is invariant under the $U(1)$ symmetry group. The potential is chosen, in a way similar to the Higgs mechanism, as:

$$V(\phi) = \mu^2 \left(|\phi^2| - \frac{f_a^2}{2} \right)^2, \tag{2.30}$$

where f_a is referred to as the decay constant and μ is an arbitrary dimensionless number. Once the field moves from the meta-stable origin to a non-zero ground state of the potential, the remaining angular degree of freedom gives rise to the axion, with axion field a. Furthermore, the $\mathcal{L}_\theta$ acquires an additional term and is now of form:

$$\mathcal{L}_\theta = \left(\theta - \frac{a}{f_a} \right) \frac{g^2}{32\pi^2} tr \left(G^{\mu\nu} \bar{G}_{\mu\nu} \right), \tag{2.31}$$

while the effective potential of the axion field is induced as:

$$V_{eff}(a) = \Lambda_{QCD}^4 \left[1 - \cos\left(\theta - \frac{a}{f_a} \right) \right], \tag{2.32}$$

with Λ_{QCD} being the QCD scale (the energy scale at which quarks become confined in hadrons, approximately 200-300 MeV). The field naturally assumes a value which minimises the effective potential and suppresses the $\mathcal{L}_\theta$ term without any fine-tuning required. The decay constant f_a plays a role of the symmetry breaking scale and is a free parameter, which has to be determined experimentally. The mass of the axion is non-zero and is approximated by the ratio:

$$m_a \approx \frac{\Lambda^2_{QCD}}{f_a}. \tag{2.33}$$

Since the models assume relatively low axion masses, and it interacts very weakly with the Standard Model sector, it can be considered as a dark matter candidate. The mass is also experimentally constrained, with the lower limit coming from the amount of dark matter observed in the universe and the upper from lack of evidence, because the coupling strength is proportional to the axion mass. Depending on the model and source of constraints, it is expected to be within the 10^{-6} eV $< m_a <$ 10^{-2} eV range [68, 71], although heavy "axion-like particles" are also explored [72, 73]. While they can decay into leptons and hadrons (e.g. pions), the only experimentally viable channel for very light axions is $a \rightarrow \gamma\gamma$, which can be searched for with the MUonE detector (see chapter 7). The main challenge is a potentially very high lifetime, resulting in a significant displacement of the decay vertex. Such vertices can still be detected and identified even if axions originate outside of detectors (e.g. in cosmic interactions), but with much lower efficiency. On the contrary, the heavier axion-like particles could be both produced and decay in the detector volume (with lifetime inversely proportional to mass) – for example in the Z and H boson decays [74] or in Primakoff scattering [75] on nuclei in a target ($\gamma + Z \rightarrow a + Z$).

2.4 Associated production of a Z^0 boson and $b\bar{b}$ pair

At the LHC, the associated production of a Z^0 boson and $b\bar{b}$ pair proceeds dominantly through gluon fusion (fig. 2.5a), constituting approximately 80% of interactions, and the quark pair annihilation (fig. 2.5b). Owing to the presence of heavy quarks, it is sensitive to a variety of BSM phenomena. In particular, the higher order corrections induced by exotic particles appearing in the quantum loops or the production enhancement due to similar experimental signatures (e.g. $b' \rightarrow Z^0 b$ or $Z^0 Z' \rightarrow Z^0 b\bar{b}$, where b' is a hypothetical 4th generation quark [76]). Both would manifest as the deviation of a measured production cross-section from its value predicted by the Standard Model. Furthermore, Z' and b' are expected to be rather massive and decay into boosted final states in the forward kinematic region, available primarily to the LHCb experiment (see chapter 3).

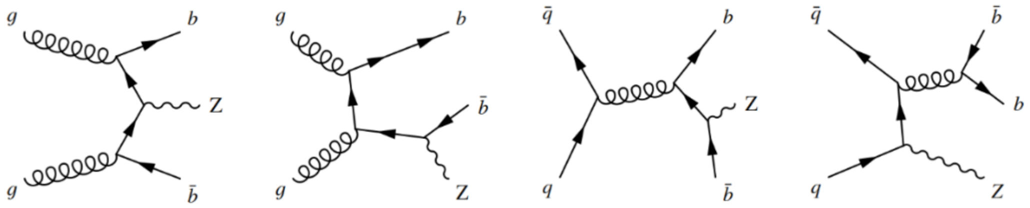

(A) gluon fusion

(B) annihilation of quark anti-quark pair

FIGURE 2.5: Leading Order Feynman diagrams of associated production of Z boson and two b quarks at the LHC.

Aside from playing a role of a communicator in Hidden Valley scenarios (see section 2.3.2), Z' is common among theories introducing new gauge groups (e.g. Little Higgs models [77]) as well as GUTs motivated by string theories (like the E_6 model [78]). Furthermore, at hadron colliders it can be produced in the s-channel and thus searched for directly through its invariant mass resonance. Recently, the $Z' \rightarrow HZ^0$ channel was explored by the CMS collaboration at the centre-of-mass energy of 13 TeV and with Z^0 decaying leptonically [79]. A Z' with mass below 3.5 (3.7) TeV has been excluded at 95% confidence level in models where it couples predominantly to fermions (bosons). The b' quark, on the other hand, is a part of an open question of the total number of existing fermion families. So far, the 4th generation has not been completely ruled out and the only strict upper bound is 9 (from the asymptotic freedom of QCD). Bearing in mind experimental considerations, coming mostly from Higgs [80, 81] and Z^0 [82] boson phenomenology, a new family could be introduced with a significant mass gap. However, no evidence has been found by either ATLAS [83] or CMS [84] experiments. Since both ATLAS and CMS are General Purpose Detectors (GPDs), whose acceptance covers only the central kinematic region (i.e. perpendicular to the beam axis, rather than in the forward/backward direction alongside), they may not be fully sensitive to boosted Z' and b'. It is therefore necessary to extend the search to the LHCb experiment.

The associated production of vector bosons and heavy jets is equally important for the Standard Model sector. In particular, the calculations involving beauty quarks can be performed using two alternative approaches. The four flavour scheme (4FS) treats them as massive point-like objects, while the four lighter quarks are described with parton distribution functions (PDFs) and only they take part in the perturbative evolution and running of the strong coupling constant. This approach remains relevant only at the energy scale close to b quark mass, because of terms containing the logarithm of their ratio appearing in the cross-section formula. With sufficiently high collision energies, these quickly become large and may spoil the convergence of perturbative series. At such scales, however, mass effects are not relevant anymore and the logarithmic terms can be re-summed through all orders in the coupling constant by means of the renormalization group equations. This gives rise to the second approach, the five flavor scheme (5FS), in which the mass of a b quark is defined to be strictly zero and a PDF is introduced instead (i.e. the b quark is considered as a proton constituent). From a theoretical standpoint, both methods become equivalent in the limit of infinite perturbative series. In fact, they can be combined at any order as long as the overlapping terms are accounted for. This can be done in a multitude of ways, with the simplest being a weighted sum of both results, known as Santander Matching [85]. A different method replaces the re-summed logarithms of 5FS with their massive counterparts of 4FS up to an order at which they were calculated. Such a result retains the logarithmic precision of 5FS, while also introducing the fixed-order precision of 4FS in massive terms [86].

An important feature of 5FS is the allowed presence of b quarks in the initial state of Feynman diagrams (due to them being treated as partons), which can significantly simplify calculations of certain processes. It is thus easier to achieve higher order precision, at the cost of reduced sensitivity to mass effects and potential loss of observables (especially differential ones due to a simpler nature of lowest order interactions). In general, 5FS offers better stability and usually better predictions at comparable orders [87, 88], but it is best suited for inclusive quantities like the total production cross-section. However, a good agreement is observed between the two most of the time. It is also suggested, that at hadron colliders the logarithmic terms are suppressed and become relevant only at large Björken-x, thus making both approaches essentially interchangeable otherwise [89]. Nonetheless, detailed studies with a variety of processes are still required for a complete understanding of both schemes and their field of application. The role of LHCb detector is particularly important, because of its ability to probe the b quark's PDF in a unique forward pseudorapidity range.

The measurement of $Z^0 b\bar{b}$ production cross-section is also important in the context of the Higgs physics program. Because the Higgs boson couples to other particles with strength proportional to their mass and its mass is smaller than that of a top quark, the $H \to b\bar{b}$ decay channel strictly dominates, with a branching fraction at the order of 56-58% [90]. The resulting experimental signature would be nearly impossible to detect in the multi-jet environment of hadron colliders, hence the properties of the Higgs boson are studied primarily through its associated production with a vector boson. With the latter decaying dominantly into leptons with high transverse momenta, the signal events can be observed much easier (see [91] for an example of analysis based on this concept). Assuming a $pp \to Z^0 H \to Z^0 b\bar{b}$ interaction chain, the $Z^0 b\bar{b}$ production becomes an irreducible background source, which has to be accounted for in the measurement. A precise knowledge of its cross-section is thus required, in order to normalise its contribution to the combined background model.

2.5 Summary of prior research

The following sections provide an overview of studies similar to those discussed in this thesis. Section 2.5.1 discusses previous searches for long-lived particles with experimental signatures similar to one studied in chapter 6 (i.e. decaying into heavy jets in a displaced vertex). Section 2.5.2 summarises previous measurements of the associated production of a Z^0 boson and heavy particle jets.

The studies related to signatures that could be investigated using the MUonE detector are not included, as the experiment and its physics program are still in the planning phase at the time of writing this thesis. Although, a discussion of a preliminary evaluation of its sensitivity to dark photons is included in chapter 7.

2.5.1 Sensitivity to exotic long-lived particles

The decays of long-lived particles with heavy jet signatures have been studied multiple times in various experiments and at different centre-of-mass energies, in particular at D0 [92], CDF [93], ATLAS [94–98], CMS [99–101] and LHCb [102–104]. The most stringent upper limits reported by each are discussed below, assuming a communicator consistent with the Standard Model Higgs boson as well as π_v^0 masses and lifetimes similar to those considered in the study included in this thesis (see chapter 6). They are at the order of $(1-10)$ pb for D0, $(10-10^2)$ pb for CDF, $(10^{-1}-1)$ for ATLAS and CMS (normalised to the Higgs boson production cross-section) and $(10^{-1}-10)$ for LHCb (also normalised). The lowest observed values are thus at the order of 1 pb (absolute) and 10^{-1} (normalised).

The earliest searches were performed by D0 [92] and CDF [93] experiments at Tevatron, using p^+p^- collisions at the centre-of-mass energy of 1.96 TeV. Both focused on the Higgs boson decaying exclusively into a pair of π_v^0, with each decaying subsequently into a pair of b quarks. The studies considered Higgs boson masses in 90-200 GeV range, π_v^0 masses between 15 and 65 GeV and a variety of decay lengths, with maximum restricted by the detectors' design. No signal excess was observed, hence the upper limits on the product of Higgs boson production cross-section and branching fraction into the $\pi_v^0 \pi_v^0$ final state were determined at 95% CL. Example results are shown in figs. 2.6 and 2.7 as function of the π_v^0 decay length and proper lifetime.

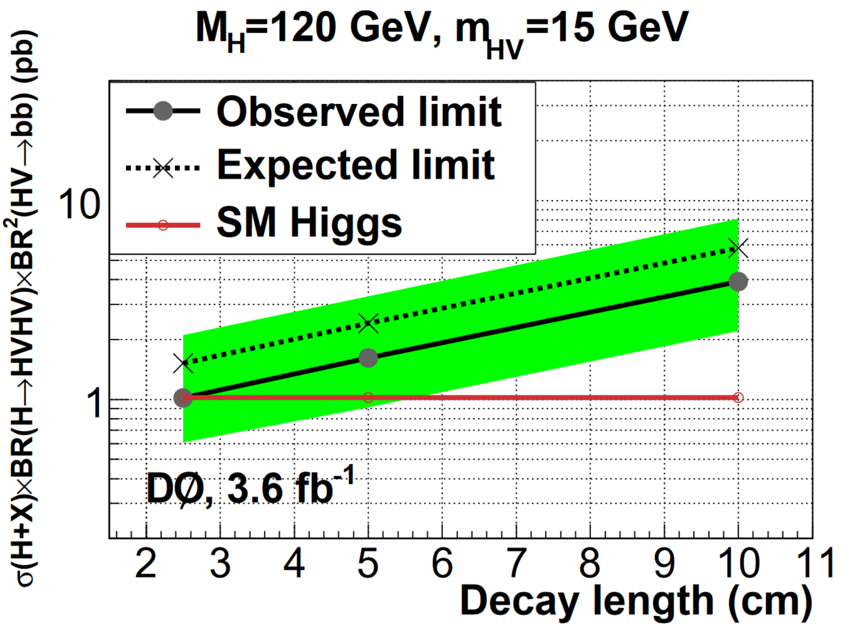

FIGURE 2.6: The upper limits on $\sigma\left(H+X\right)\cdot BR\left(H\rightarrow\pi_v^0\pi_v^0\right)\cdot BR^2\left(\pi_v^0\rightarrow b\bar{b}\right)$ at 95% CL, as a function of the π_v^0 decay length. $BR\left(H\rightarrow\pi_v^0\pi_v^0\right) = BR\left(\pi_v^0\rightarrow b\bar{b}\right) = 100\%$, Higgs boson with 120 GeV mass and π_v^0 mass of 15 GeV are assumed. The Standard Model cross-section for Higgs boson production is shown with red line and green band illustrates a one standard deviation uncertainty. Figure taken from [92].

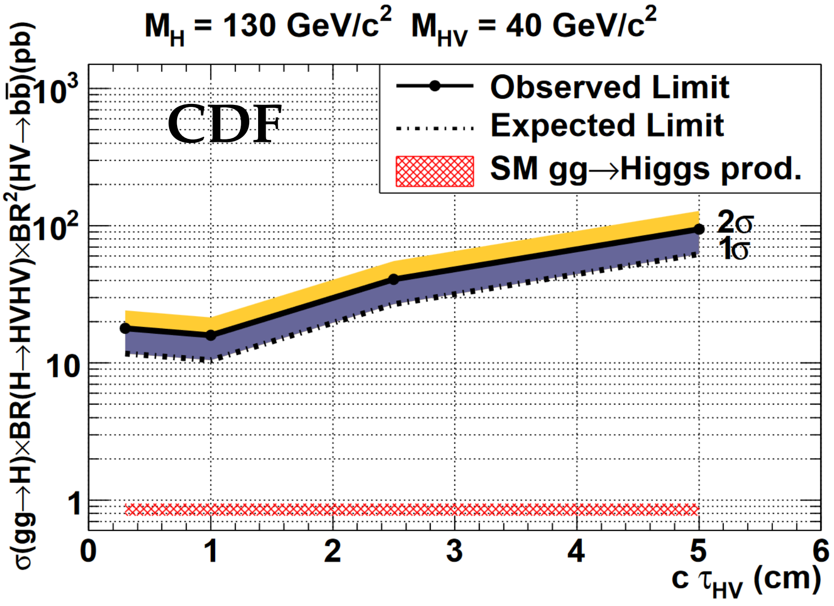

FIGURE 2.7: The upper limits on $\sigma\left(H\right)\cdot BR\left(H\rightarrow\pi_v^0\pi_v^0\right)\cdot BR^2\left(\pi_v^0\rightarrow b\bar{b}\right)$ at 95% CL, as a function of the π_v^0 proper lifetime. $BR\left(H\rightarrow\pi_v^0\pi_v^0\right) = BR\left(\pi_v^0\rightarrow b\bar{b}\right) = 100\%$, Higgs boson with 130 GeV mass and π_v^0 mass of 40 GeV are assumed. The Standard Model cross-section for Higgs boson production is shown in red, and coloured bands illustrate one and two standard deviations uncertainty. Figure taken from [93].

The ATLAS [95] experiment searched for displaced vertices in its inner detector, using pp collisions at the centre-of-mass energy of 13 TeV. An associated production of the Higgs and Z^0 bosons was considered, with the latter decaying leptonically. The Higgs was assumed to decay into a pair of neutral pseudoscalar bosons a (consistent with π_v^0), which decay exclusively into b quark pairs. The analysis used a dedicated algorithm to reconstruct secondary vertices, with loosened requirements imposed on track impact parameter, which significantly increased the reconstruction efficiency for vertices with large displacement. No statistically significant signal excess has been found and upper limits on the branching fraction of the Higgs boson were determined at 95% CL. Figure 2.8 summarises results for a masses between 16 and 55 GeV, as a function of its assumed proper lifetime.

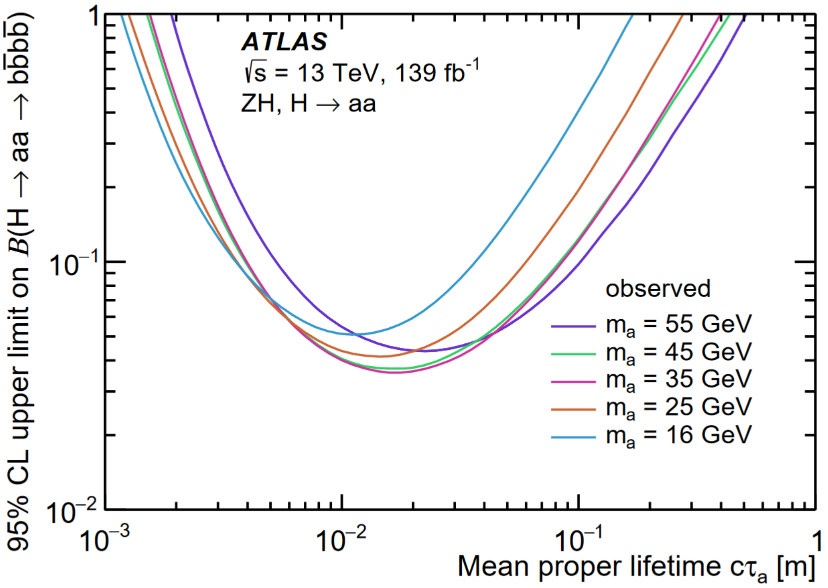

FIGURE 2.8: The 95% CL upper limits on $BR\left(H \to aa \to b\bar{b}b\bar{b}\right)$, as a function of the proper lifetime of a. $BR\left(a \to b\bar{b}\right) = 100\%$ is assumed. Figure taken from [95].

A search for similar signature ($pp \to Z^0(\to l^+l^-)H(\to SS)$, with S being a scalar long-lived particle decaying exclusively into $b\bar{b}$ pairs) was also conducted by the CMS [100] experiment. In this case, the analysis relied on detecting displaced particle jets (e.g. based on their impact parameter) and using their multiplicity to discriminate against background contributions. The determined upper limits on $H \to SS$ branching fraction are shown in fig. 2.9 for S masses between 15 and 55 GeV, as a function of S proper decay length.

The LHCb [103] experiment studied the $pp \to H \to \pi_v^0 \left(\to b\bar{b}\right) \pi_v^0 \left(\to b\bar{b}\right)$ process directly, at the centre-of-mass energy of 13 TeV. However, due to forward detector acceptance, the signal signature was assumed to contain at least one displaced vertex rather than two. Furthermore, the ability to detect vertices displaced from the primary interaction point is restricted by the dimensions of the vertex detector to approximately 200 millimetres along the beam axis and 30 millimetres transversally. The upper limits on the branching fraction of produced Higgs bosons into Hidden Valley pions, determined for different π_v^0 masses (25-50 GeV) and lifetimes (2-500 ps), are shown in fig. 2.10.

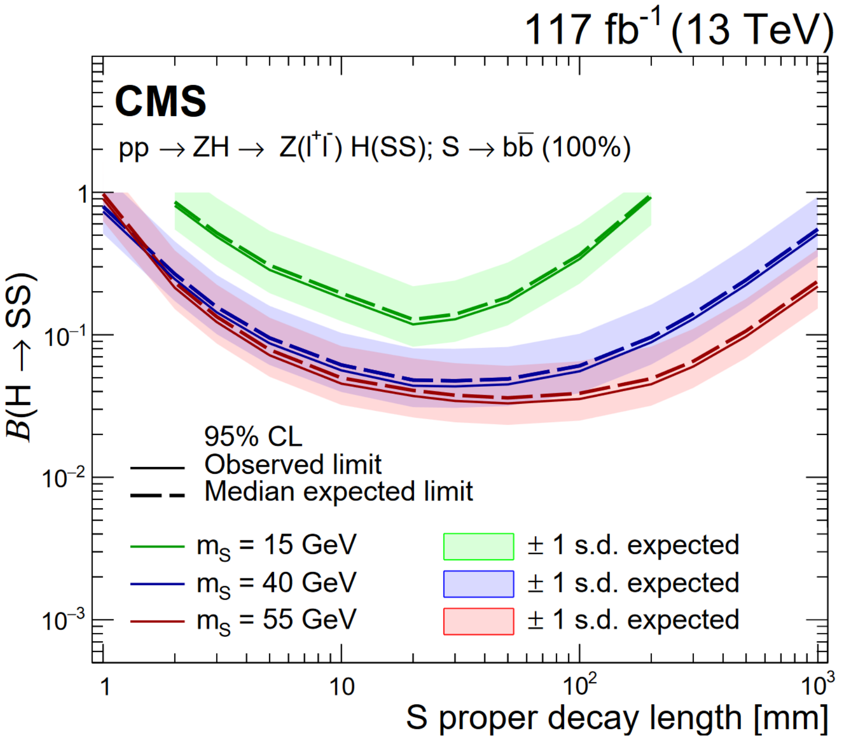

FIGURE 2.9: The 95% CL upper limits on $BR\,(H \to SS)$, as a function of the S proper decay length. $BR\left(S \to b\bar{b}\right) = 100\%$ is assumed. Coloured bands indicate one standard deviation of uncertainty. Figure taken from [100].

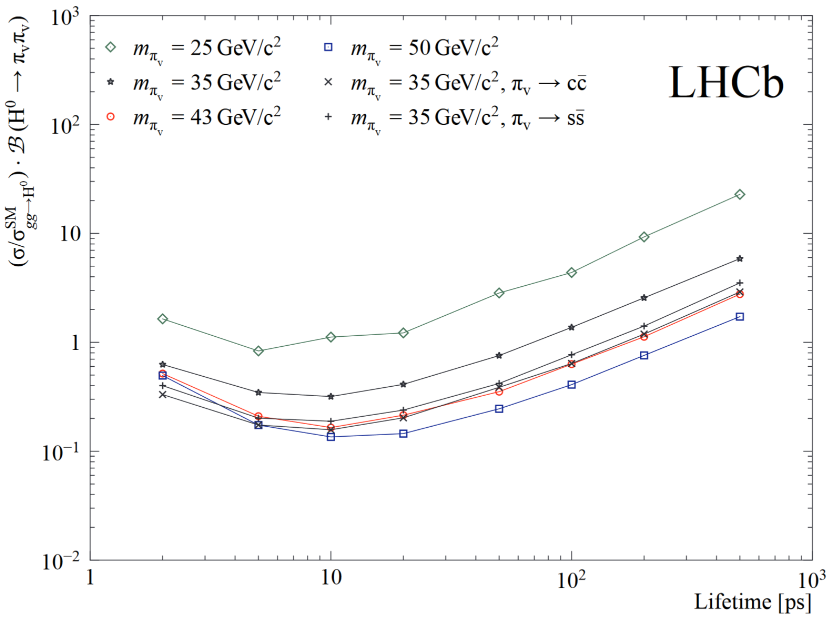

FIGURE 2.10: The 95% CL upper limits on $BR\left(H \to \pi_v^0\pi_v^0\right)$, as a function of the π_v^0 lifetime. Unless specified otherwise, π_v^0 is assumed to decay into a $b\bar{b}$ pair. In all cases, $BR\left(\pi_v^0 \to q\bar{q}\right) = 100\%$. Figure taken from [103].

2.5.2 Measurements of the $Zb\bar{b}$ production cross section

The $Z^0 b\bar{b}$ production is usually studied in the $Z^0 \rightarrow \mu^+\mu^-$ channel, as muons can be reconstructed and identified very efficiently. The earliest measurements were performed at the centre-of-mass energy of 1.96 TeV at Tevatron by CDF [105] and D0 [106] experiments. Their results show a general agreement with theoretical predictions, but at that time the full Next-to-Leading Order (NLO) calculation was not yet available. The CMS [107] and ATLAS [108] experiments have also explored the final states with Z^0 and b quarks at the centre-of-mass energy of 7 TeV. Here, the 4FS was found to give a better description of the exclusive $Z^0 + 2b$ process, while the inclusive cross-section was well modelled by the 5FS.

Recently, both ATLAS [109] and CMS [110] experiments performed measurements of the differential cross-sections for the production of Z^0 boson with at least one and at least two b quarks, using data collected at the centre-of-mass energy of 13 TeV. The CMS study finds that fiducial cross-sections (i.e. within a well-defined detector acceptance) are described better by the Leading Order (LO) simulation and overestimated at NLO, when MadGraph5 [111, 112] event generator is used. They are also overestimated by the SHERPA [113] event generator (fig. 2.11). The ATLAS experiment focused on validating the predictions of 4 and 5FS. The 5FS NLO calculations were found to better agree with the data and be consistent within the experimental uncertainty (fig. 2.12). On the other hand, the 4FS LO calculations are significantly underestimated in some variables (fig. 2.13). A 4FS+5FS NLO matching scheme was also tested, but found to be consistent with 5FS at this energy scale.

As of yet, the $Z^0 b\bar{b}$ production has not been studied in the forward rapidity region. A similar analysis has been performed in the LHCb experiment at the centre-of-mass energy of 7 TeV, but considered only a single associated b quark [114]. Therefore, it was important to extend this result to higher multiplicities and collision energies, because of the unique acceptance of the LHCb detector.

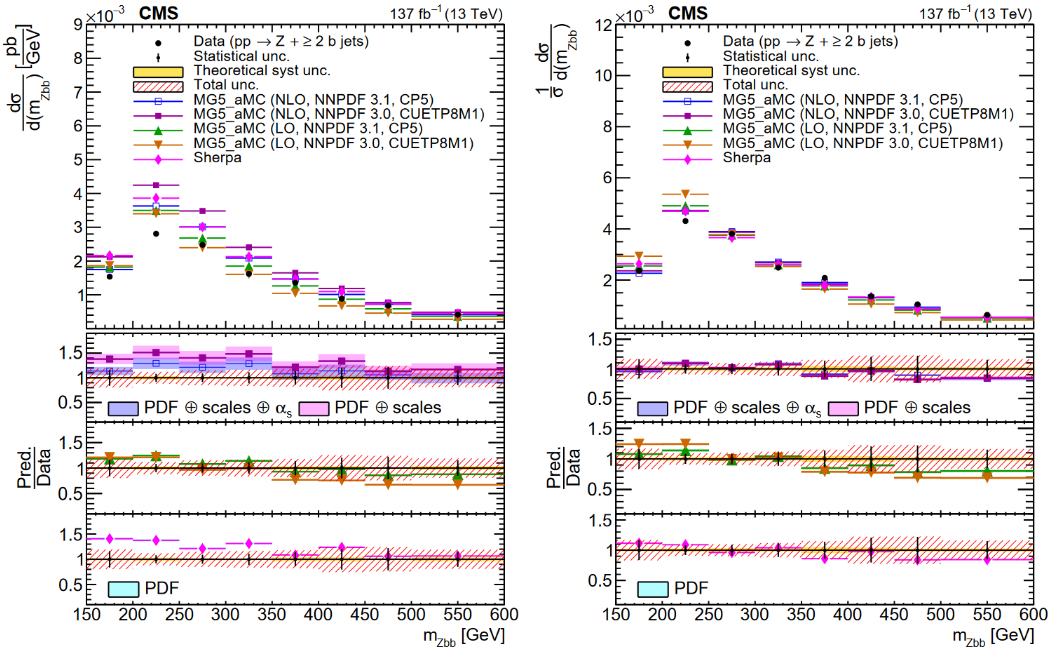

FIGURE 2.11: Differential cross-section (left) and normalized differential cross-section (right) as a function of an invariant mass of a $Z^0 b\bar{b}$ system. Figure taken from [110].

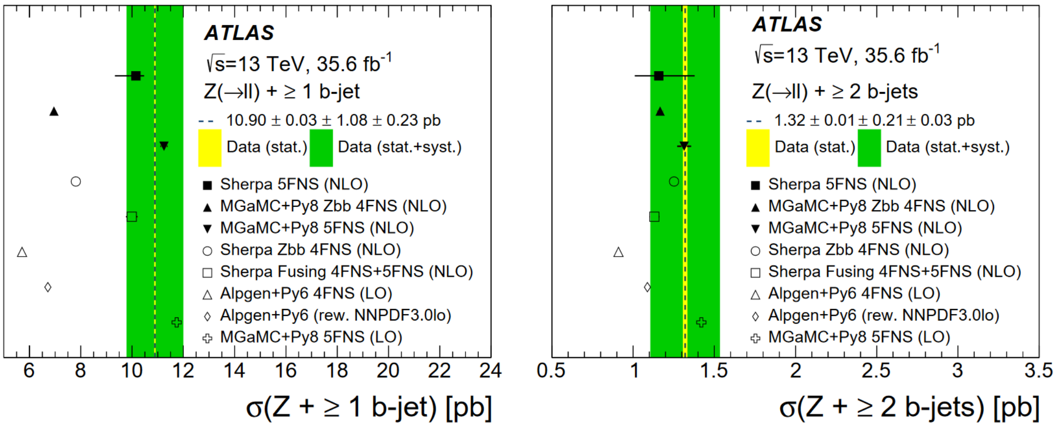

FIGURE 2.12: Measured fiducial cross-sections for final states with at least one (left) and at least two (right) b jets. Figure taken from [109].

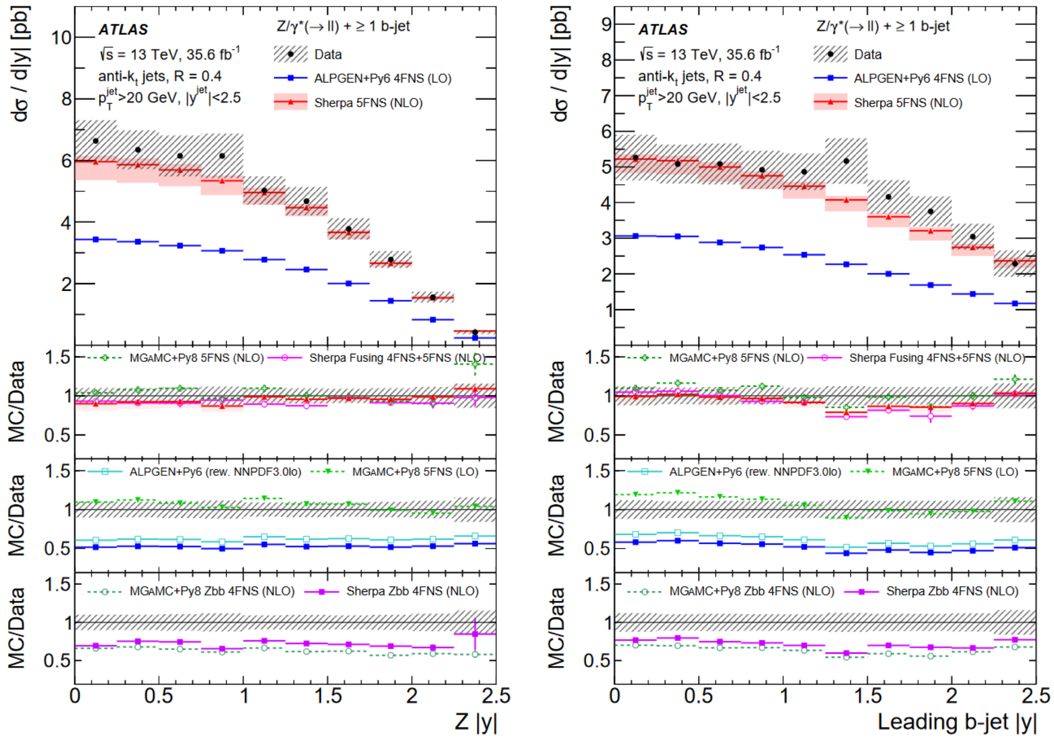

FIGURE 2.13: Differential cross-section as a function of the rapidity of the Z^0 boson and leading b jet. Figure taken from [109].

Chapter 3

LHCb experiment at the Large Hadron Collider

3.1 Introduction

The LHCb is one of the four large scale experiments located at the LHC. It was designed primarily to search for Beyond the Standard Model phenomena in the decays of rare beauty and charm hadrons as well as in the violation of CP symmetry. The scientific program includes also a wide array of studies related to exotic particles – ranging from composite quark states (e.g. pentaquarks) to long-lived dark matter candidates. Because of its forward design, the LHCb detector covers a very unique range of pseudorapidity and provides measurements complementary to those from the remaining three experiments.

The Large Hadron Collider is described in section 3.2. Section 3.3 discusses the design of LHCb spectrometer during Run 1 and 2 of the LHC. Section 3.4 provides an overview of the software framework and application stack used to process data, and section 3.5 briefly discusses the detector upgrades for Run 3 and beyond.

3.2 Large Hadron Collider

The LHC is currently the largest circular collider in operation, with the circumference close to 27 kilometres. It is located at the CERN complex near Geneva (fig. 3.1), which houses also several smaller accelerators and a variety of experiments. The LHC collides both protons and ions, including fixed target collisions with nuclei (thanks to the SMOG [115] system). Its operation has been divided into stages (referred to as Runs), which are characterised by different beam energies and layouts of the primary detectors (ATLAS [116], CMS [117], LHCb [118] and ALICE [119]). Run 1 was conducted in years 2011 (proton-proton collisions at the centre-of-mass energy of 7 TeV) and 2012 (8 TeV) with a 40 MHz bunch crossing rate and $1 \cdot 10^{-34}$ $\mathrm{cm}^{-2}\mathrm{s}^{-1}$ nominal luminosity. Run 2 covers the period from 2015 to 2018, when the proton beams were collided at the centre-of-mass energy of 13 GeV at the same rate and twice the nominal luminosity of Run 1. Run 3, for which the collision energy was increased to 13.6 TeV, is currently in progress and expected to end in 2026.

Before the beam is injected into the LHC, it passes through a series of smaller pre-accelerators. First, the hydrogen atoms are ionised in an electric field to obtain protons. They are subsequently accelerated to the energy of 50 MeV by Linac2, to 1.4 GeV by the Booster, 25 GeV by the Proton Synchrotron (PS) and 450 GeV by the Super Proton Synchrotron (SPS), after which they enter the LHC beam pipes. The beams – travelling around the LHC in both directions – are accelerated further by a series of radio-frequency cavities, operating at 400 MHz, and kept on the circular trajectory by superconducting 8.3 T magnets cooled with liquid helium. Once they require the nominal collision energy, they are bent to cross at one of the interaction points, corresponding to the four detectors.

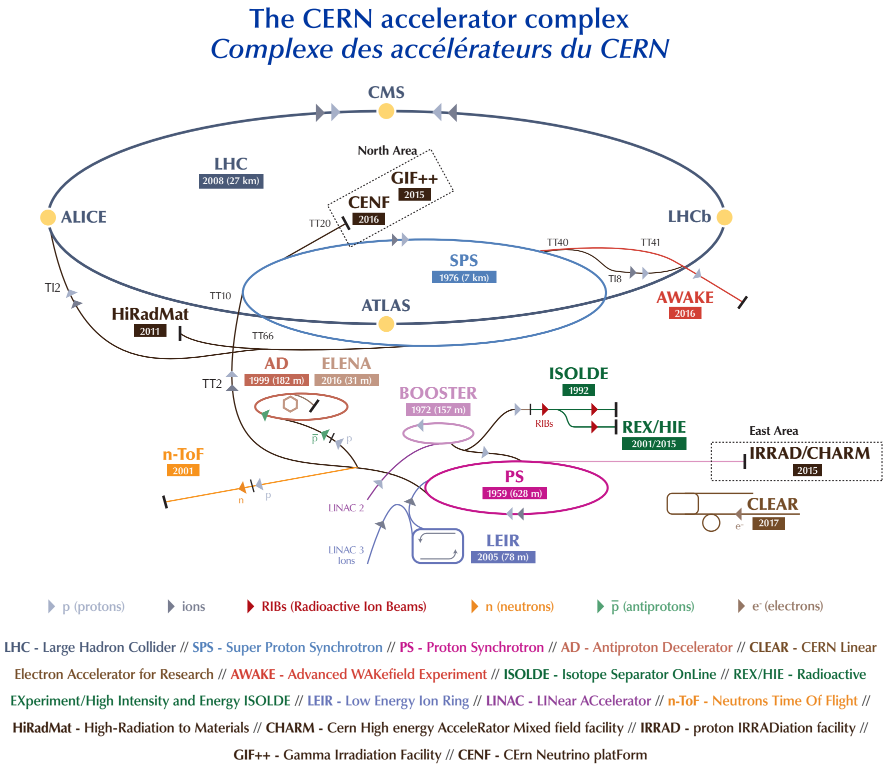

FIGURE 3.1: A schematic of the CERN accelerator complex. Figure taken from [120].

3.3 LHCb detector

The LHCb spectrometer is a special purpose detector, designed to maximise the efficiency of collecting and reconstructing decays of beauty and charm hadrons. Its geometry is motivated by the production mechanism of $b\bar{b}$ pairs, which at LHC is dominantly gluon fusion. The process is characterised by a strong asymmetry of parton momenta, causing the centre-of-mass of the entire system to be boosted along the beam axis. Consequently, the quark pairs are produced in tight forward and backward cones (fig. 3.2, left). The detector layout is thus a series of sub-systems located along the beam pipe and covering only about 4% of the solid angle (or pseudorapidity range of approximately 2 to 5). In contrast, the ATLAS and CMS experiments operate General Purpose Detectors with barrel-like design, which surround the interaction point completely. Both of them provide complementary measurements in different kinematic regions – fig. 3.2 (right) illustrates the difference in angular acceptance. Figure 3.3 shows the layout of the LHCb spectrometer, where a right-handed coordinate system with origin at the interaction point, Z axis pointing downstream and Y upwards is adopted.

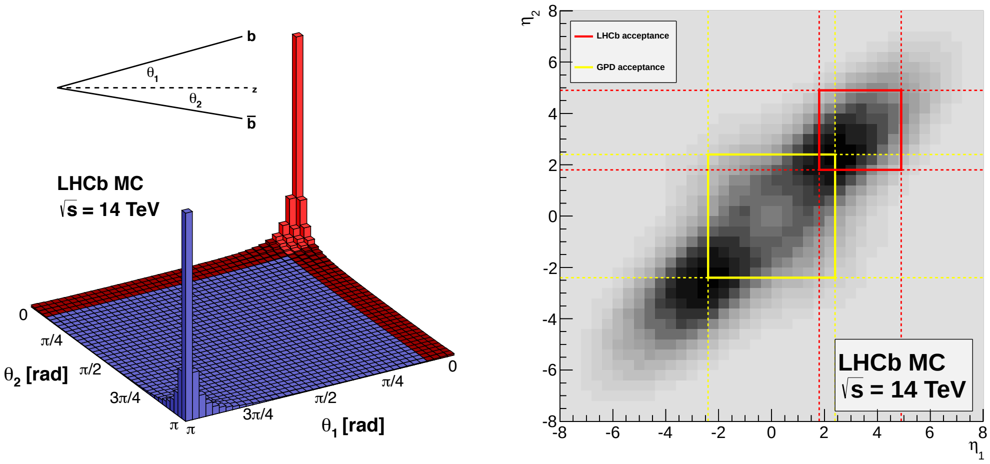

FIGURE 3.2: The angular distribution of $b\bar{b}$ pairs in a simulated sample, as a function of their polar angle with respect to the beam axis (left). The region covered by the LHCb detector is shown in red. The right figure shows the pseudorapidity distribution of $b\bar{b}$ pairs, with the acceptance of LHCb detector overlaid in red and of GPDs (like ATLAS or CMS) in yellow. Figure taken from [121].

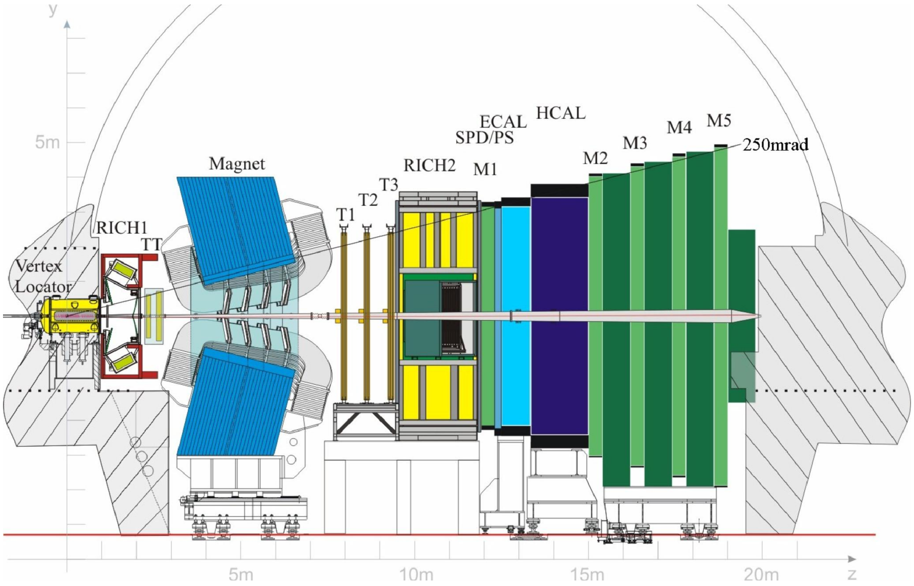

FIGURE 3.3: A cross-section of the LHCb detector layout during Run 1 and 2 of the LHC. Figure taken from [122].

Due to sensitivity of detector elements to radiation damage, the luminosity at LHCb interaction point has to be lowered by two orders of magnitude compared to the nominal LHC value. It is kept locally at a constant working point with mean value within $(2-5)\cdot 10^{23}\,\mathrm{cm}^{-2}\mathrm{s}^{-1}$, using a luminosity levelling technique (for further details, consult [123]). Consequently, the pile-up is significantly reduced and most events contain only a single interaction per bunch crossing. Throughout LHC operation, the experiment collected data from proton and ion collisions at different centre-of-mass energies. In particular, during Run 1 phase of data taking, proton-proton collisions were recorded at 7 and 8 TeV, proton-lead with 5.02 and 8.16 TeV per nucleon and lead-lead at 5.02 TeV per nucleon. During Run 2 phase, the proton-proton collisions were recorded at the centre-of-mass energy of 13 TeV. Additionally, the introduction of a SMOG [115] system allowed for fixed target collisions of protons with helium, neon and argon nuclei, which were recorded at the centre-of-mass energy of 110 GeV. Overall, Run 1 provided approximately 3 fb^{-1} integrated luminosity of proton-proton collisions and Run 2 – 6 fb^{-1} (the cumulative yield for each year of data taking is illustrated in fig. 3.4).

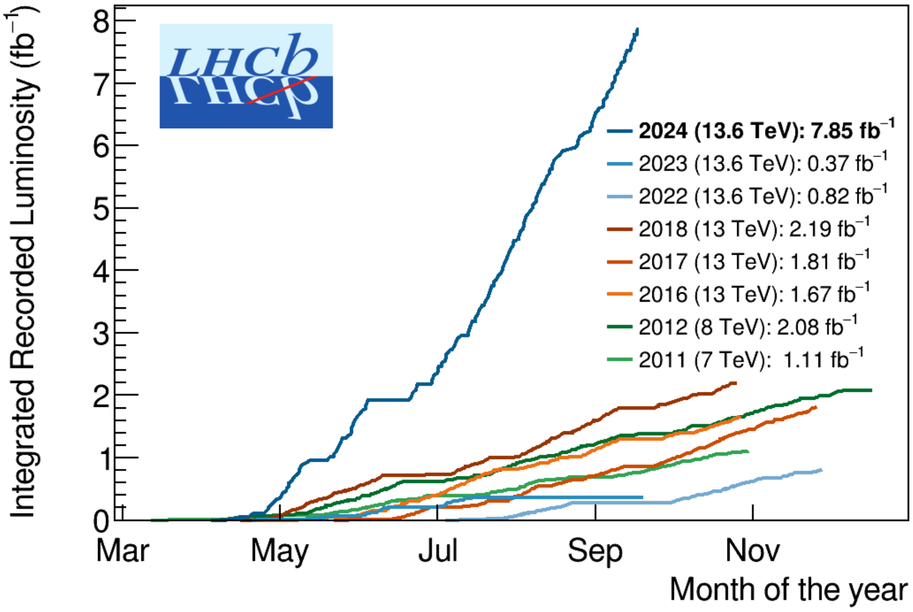

FIGURE 3.4: Integrated luminosity recorded by the LHCb experiment in each year. Figure taken from [124].

3.3.1 Tracking system

A high performance of the tracking system is fundamental to the measurements performed by LHCb. The beauty hadrons, which are produced at the interaction point (Primary Vertex – PV), have relatively high lifetimes and are significantly boosted – as a result, they can travel up to several millimetres before decaying. The Secondary Vertices (SV) of such decays are thus measurably displaced and can be reconstructed independently, providing an efficient way of identifying particle jets originating from b quarks. The tracks from such SVs are characterised by high transverse momenta and a large impact parameter (IP). The structural difference between particle jets originating in light quarks and b quarks is illustrated in fig. 3.5.

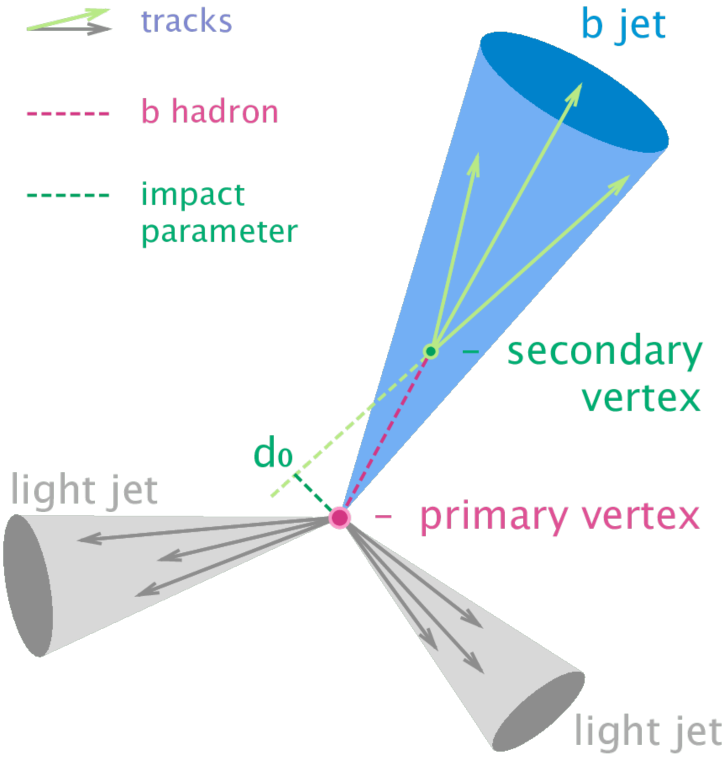

FIGURE 3.5: The structure of particle jets originating in light quarks and b quarks. Figure taken from [125].

The tracking system of LHCb in Run 1 and 2 comprised several subsystems. The VErtex LOcator (VELO) was installed close to the interaction point and used to determine the spatial coordinates of the primary and secondary vertices as well as to reconstruct segments of the passing tracks and estimate their IP. Furthermore, a series of planar detectors was located downstream – the Tracker Turicensis (TT), Inner Tracker (IT) and Outer Tracker (OT). The first was situated in front of the magnet and provided input for the reconstruction of particles decaying outside of VELO and those bent out of the detector acceptance before reaching the subsequent tracking layers. The remaining two were located downstream of the magnet. The measurement of momentum for charged particles was achieved using the magnetic field created by a dipole magnet

Magnet

The LHCb magnet is a warm dipole magnet composed of two identical, saddle-shaped coils covering the entire LHCb acceptance. Each coil is made of pure, annealed Al-99.7 hollow conductor and contains fifteen pancakes – arranged in five triplets – held together by cast aluminium clamps. It is designed to provide a bending power of about 4 Tm for tracks with 10 metre length, while keeping the field reaching the Ring Imaging CHerenkov detector RICH1 (see section 3.3.2) below 2 mT. The magnetic field is aligned with the horizontal (bending) detector plane and its polarisation can be swapped to reduce the systematic effects in measurements of asymmetries.

VELO

VELO detector is a part of the tracking system located closest to the interaction point. Its primary role is providing input for the reconstruction of PVs, SVs and the initial segments of particle tracks. During Run 1 and 2, it consisted of a series of 21 tracking stations (fig. 3.6) mounted in a vacuum, which was kept by a 200 micrometre thick aluminium foil. To prevent radiation damage, both sides were retracted until the beam was stable and then moved back to roughly 7 millimetres from the pipe.

The stations comprised two types of silicon microstrip sensors, performing an independent measurement in the radial (R) and angular (ϕ) direction. Spacing and outer radius were optimised to guarantee that a track in the acceptance (within roughly 15-300 mrad) crosses at least four modules, when originating up to 10.6 cm from the nominal interaction point. The strip pitch varied along each sensor (40-102 μm for the R and 38-97 μm for ϕ-sensors) to ensure equal contribution to the precision of an impact parameter measurement along the track. The resulting resolution scaled linearly with the pitch from approximately 10 to 25 μm for both types of sensors (figs. 3.7 and 3.8). The precision of determining the spatial position of a vertex depended on the number of constituent tracks – for 25, it was about 13 micrometres in the transverse plane and 71 micrometres along the beam axis [126]. This is enough to significantly reduce the combinatorial background from tracks being incorrectly assigned to vertices, which is usually a dominating source for most studies of rare decays. Similarly, a very good resolution of the IP (below 35 micrometres for particles with transverse momentum above 1 GeV) was achieved, providing an effective veto for prompt backgrounds.

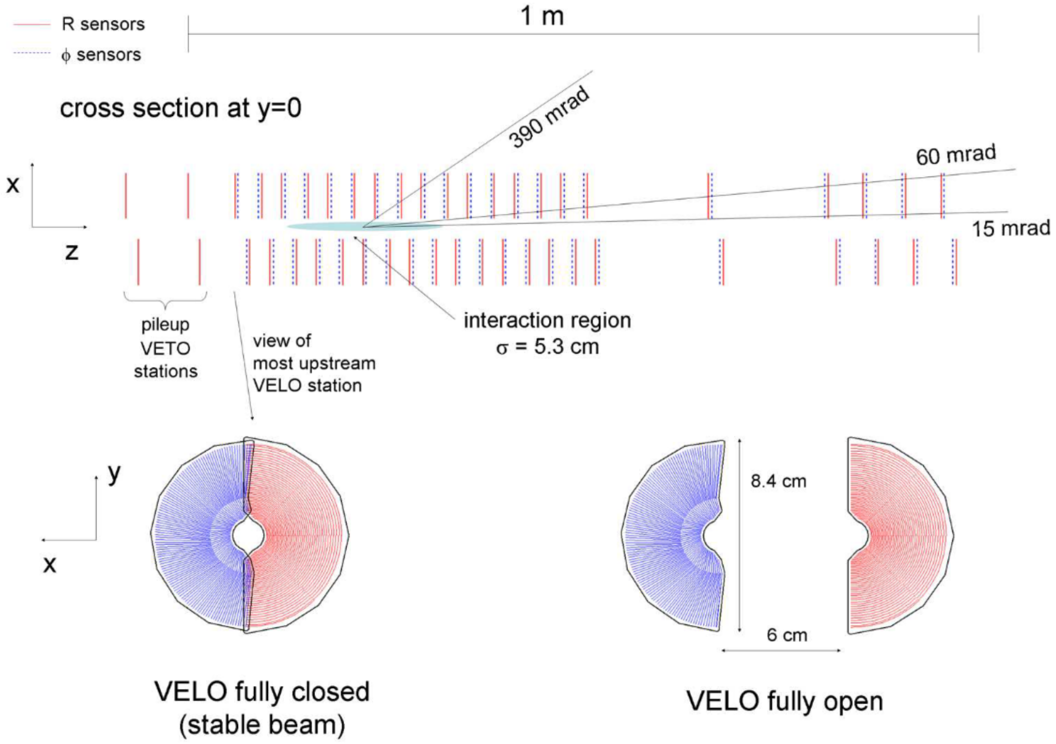

FIGURE 3.6: Cross-section of the VELO detector in the XZ plane and closed position (top), and in the XY plane in the closed (bottom left) and open (bottom right) position. Figure taken from [118].

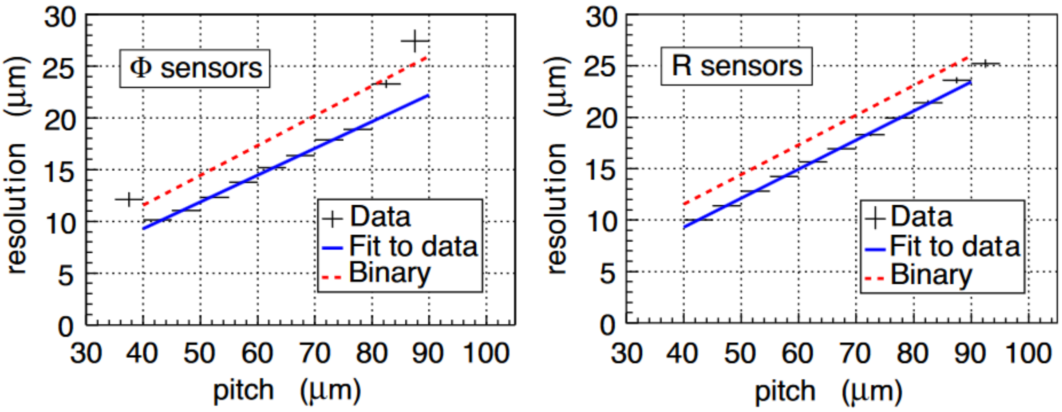

FIGURE 3.7: Hit resolution as a function of the strip pitch for both types of sensors, as measured in a test beam for particles hitting the strips at a right angle. The dashed line shows the expected resolution for digital readout. Figure taken from [118].

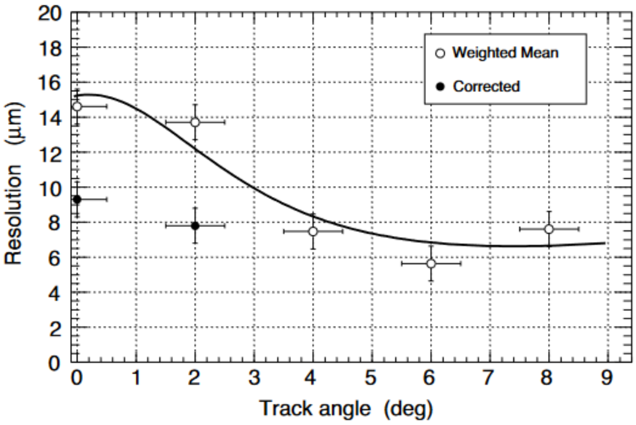

FIGURE 3.8: Dependence of the resolution of an R-type sensor with 85 micrometre strip pitch on the incident angle. Open circles show values derived from a weighted sum of charge deposited in strips, the filled circles – values corrected for the imperfections in charge distribution. Figure taken from [118].

TT, IT and OT

The planar detectors comprised two types of sensors. The Tracker Turcensis (TT), located in front of the magnet, and the innermost parts of stations T1-3 (referred to as the Inner Tracker, IT), formed the Silicon Tracker (ST) and were based on a solid-state technology. The outside parts of T1-3 (Outer Tracker, OT) used drift-time straw detectors. Figure 3.9 shows the relative scale and general layout of the ST and OT.

The elements of Silicon Tracker shared the same sensor technology (single-sided p-on-n). Each station (TT, T1-T3) comprised four tracking layers, with the two outside ones performing a measurement in the bending plane and the innermost two rotated by a stereo angle of ±5°. The TT covered an entire nominal acceptance of the LHCb detector and was composed of 500 micrometres thick, 9.64 centimetre wide and 9.44 centimetre long sensors with a strip pitch of 183 micrometres (512 readout strips in total) – fig. 3.10 (left) shows the layout of a single stereo layer. The IT stations were located in the vicinity of the beam pipe, covering approximately 1.3% of the total sensitive area – the use of solid-state detectors was necessitated by the character of $b\bar{b}$ pair production, which makes about 20% of the charged tracks pass through this region. Each IT layer comprised four parts (fig. 3.10, right), using 7.6 centimetre wide and 11 centimetre long sensors with a strip pitch of 198 micrometres (384 readout strips). The sensors below and above the beam pipe were 320 micrometre thick and ones to the sides – 410 micrometre. The TT provided a spacial hit resolution of 62 micrometres and 99.3% detection efficiency, while IT – 58 micrometres and 99.7%.

The Outer Tracker was a drift-time straw detector, covering the remaining part of the acceptance. It was arranged in the same way as its silicon counterpart, with three consecutive stations and each consisting of four tracking layers, including two stereo ones. The tubes were 4.9 millimetres in diameter and filled with a mixture of Argon (70%) and CO_2 (fig. 3.11), resulting in drift times below 50 nanoseconds and an effective resolution of 200 micrometres. In turn, it made the multiple scattering the dominating contribution to momentum uncertainty over almost the entire range of particle momenta, with the measurement resolution of $\delta p/p \approx 0.4\%$. The hit detection efficiency was close to 99%.

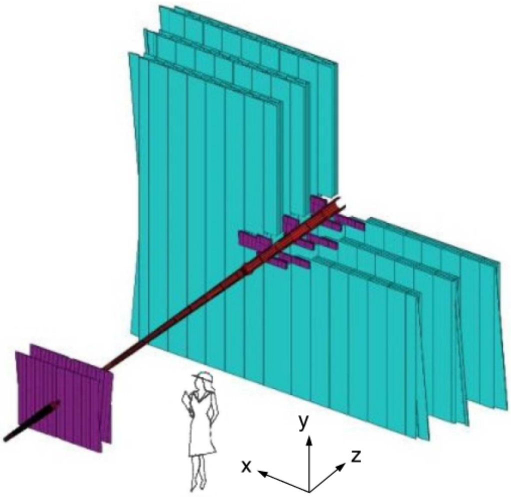

FIGURE 3.9: The relative size and layout of the Silicon Tracker (purple) and Outer Tracker (cyan). Figure taken from [118].

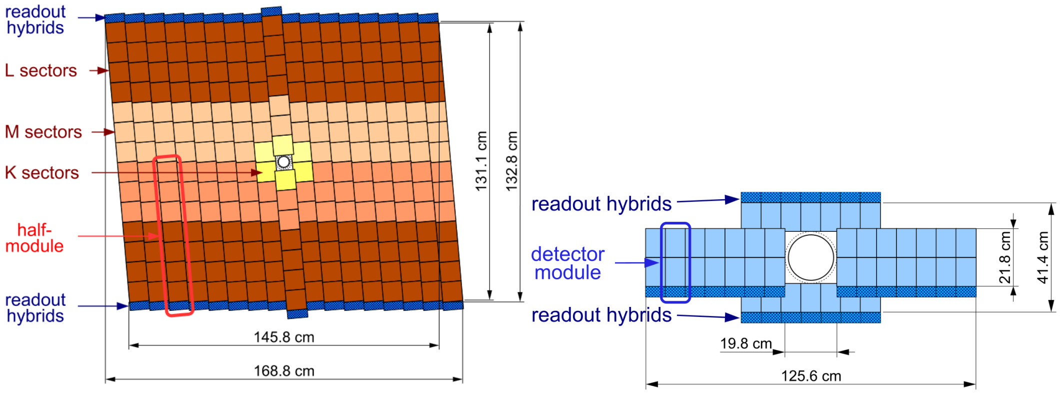

FIGURE 3.10: The layout of a single TT stereo layer (left) and an IT layer (right). Figure taken from [118].

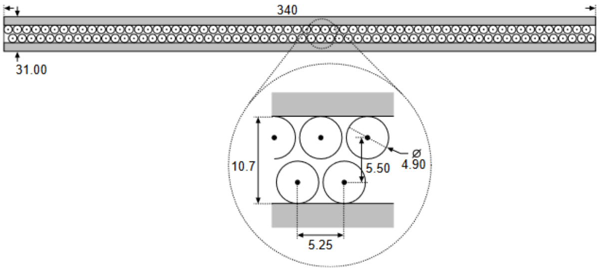

FIGURE 3.11: Cross section of a single OT layer. Figure taken from [118].

Track reconstruction

The reconstruction of particle tracks is performed within the LHCb data processing stack (described in section 3.4). During Run 1 of the LHC, the event reconstruction was performed partially in the trigger and followed with a full procedure offline. For Run 2, it takes place entirely in the High Level Trigger (section 3.3.3). The algorithm is based on reconstructing track segments using hits in selected groups of sub-detectors and combining them to form, so called, long tracks. This section gives a brief overview of the different track types, which are distinguished in the LHCb experiment (pictured in fig. 3.12), and the concept of clone and ghost tracks. Additionally, fig. 3.13 shows the track reconstruction efficiency measured with a tag-and-probe method, using $J/\psi \to \mu^- \mu^+$ decays originating in the decays of beauty hadrons. It is universally above 95%.

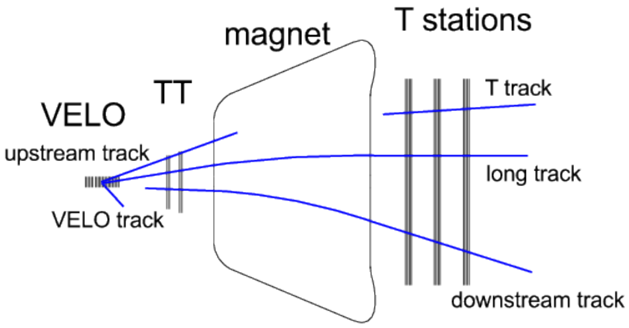

FIGURE 3.12: Different types of particle tracks distinguished in the LHCb experiment. The detector layout used in Run 1 and 2 is shown. Figure taken from [127].

The five main track categories, assuming the detector layout of Run 1 and 2, are:

- **VELO tracks**, which are straight lines (due to lack of the magnetic field) reconstructed using approximately collinear hits, registered in the VELO detector. They are used as the basis for the algorithms searching for the primary and secondary vertices.
- **Upstream tracks**, which are formed by matching VELO tracks with hits registered in the TT. Typically, these are tracks corresponding to low momentum particles, which were bent out of the acceptance before reaching the T stations.
- **T tracks**, which are reconstructed using only hits in the T stations and play a role in RICH2 pattern recognition (see section 3.3.2).

- **Downstream tracks** reconstructed by combining the segments from TT and T stations. Usually, they correspond to particles with significant lifetimes which decayed outside of VELO.
- **Long tracks**, which contain hits from all consecutive tracking detectors. They are characterised by the highest reconstruction quality and momentum resolution.

Two derivative classes of wrongly reconstructed tracks are also defined:

- **Clones**, which are tracks reconstructed using hits from the same particle.
- **Ghosts**, which form a combinatorial background of tracks reconstructed using matching hits, which do not belong to the same particle.

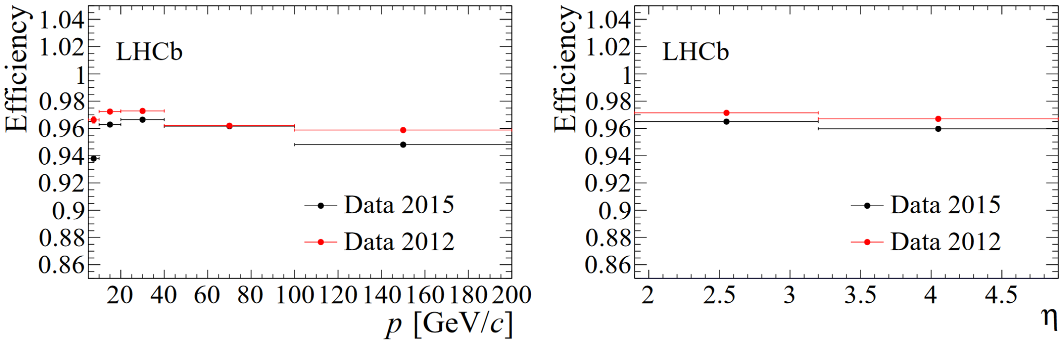

FIGURE 3.13: Track reconstruction efficiency in years 2015 (Run 2) and 2012 (Run 1) as a function of the momentum (left) and pseudorapidity (right). Figure taken from [128].

3.3.2 Particle identification

The particle candidates are reconstructed using a particle flow approach, where the information from all sub-detectors is combined to identify the particles corresponding to tracks and measure their energy. The LHCb spectrometer is equipped with a pair of Ring Imaging Cherenkov detectors (RICH), an electromagnetic and hadronic calorimeters (ECAL and HCAL, respectively) as well as a muon detection system.

RICH detectors

The primary method of particle identification uses Cherenkov radiation, emitted by charges moving faster than the speed of light in a given medium. The system is divided into two detectors (RICH 1 and 2), which contain radiators made of different materials. A simultaneous use of CF_4, C_4F_{10} and silica aerogel, provides a good separation of measured Cherenkov angles for particles with momenta between about 10 and 100 GeV (typical responses are illustrated in fig. 3.14).

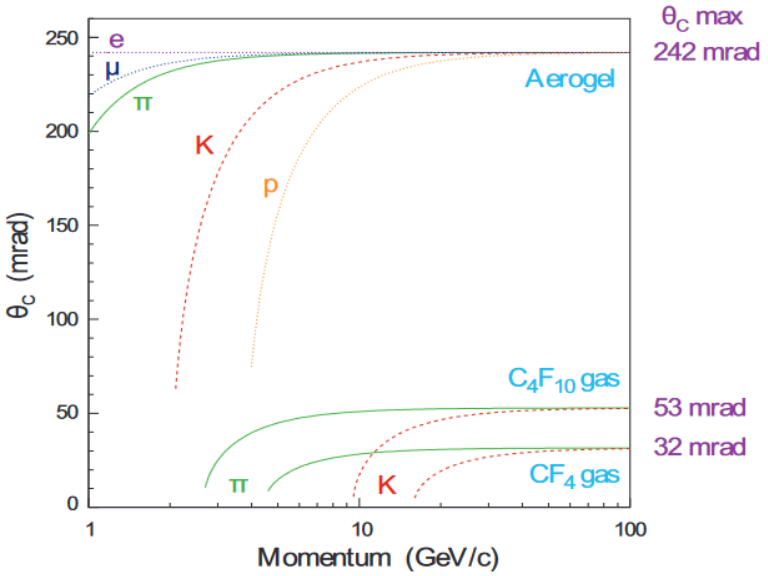

FIGURE 3.14: Typical Cherenkov angles measured in RICH for a variety of particles and momenta. Figure taken from [118].

RICH1 (fig. 3.15, left) is located in front of the magnet and covers the entire LHCb acceptance. It is designed for lower momentum tracks (10-60 GeV) and filled with a C_4F_{10} gas, with a 5 centimetre thick aerogel block installed in the middle. RICH2 (fig. 3.15, right), extends sensitivity to higher momentum particles (15-100 GeV) by employing a CF_4 gas as the radiator. It is located downstream of the magnet and covers only part of the acceptance, where the majority of energetic particles are produced (up to about 120 mrad in the bending plane and 100 mrad vertically). Both detectors contain a set of mirrors, which reflect the photons out of acceptance and focus them on two planes of Hybrid Photon Detectors. The Cherenkov angle resolution for a single photoelectron, determined in simulation, depends on the material and is 2.6 mrad for aerogel, 1.5 mrad for C_4F_{10} and 0.7 mrad for CF_4.

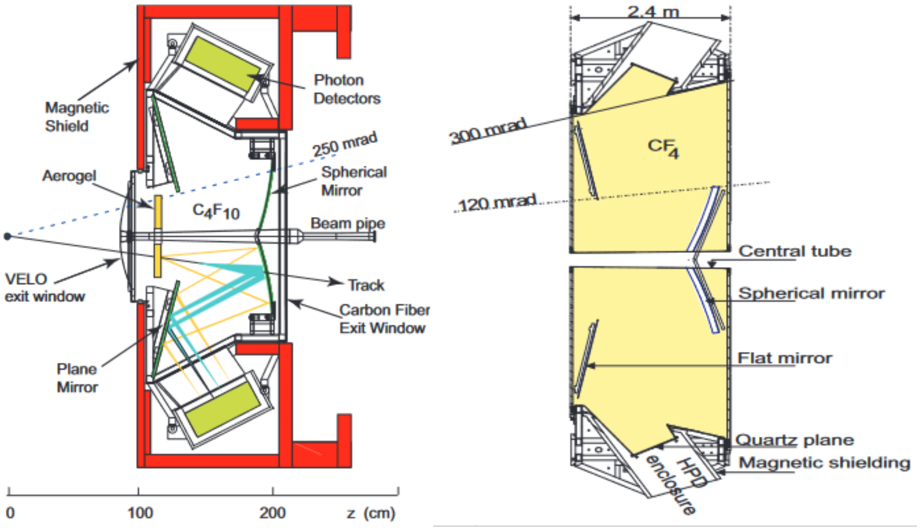

FIGURE 3.15: The cross-section of RICH1 (left) and RICH2 (right). Figure taken from [118].

Calorimeters

The energy of electrons, photons and hadrons (also neutral, e.g. π^0) is determined in the calorimeter system, by measuring the losses from electromagnetic and hadronic cascades in the absorber. The longitudinal layout is a consequence of the trigger characteristics. In particular, rejection of high background from the production of charged pions requires introduction of a preshower (PS) detector, in front of the electromagnetic calorimeter. Furthermore, to effectively select electrons with high transverse energy, the contribution from neutral pions has to be significantly reduced – a scintillator pad detector (SPD) is thus placed in the very beginning and used to detect charged particles entering the calorimeter system. Finally, the ECAL is followed with a hadronic calorimeter.

The SPD/PS detector consists of two layers of scintillators, separated by a 15 millimetre (2.5 radiation length) lead converter. Their granularity varies from 40.4-by-40.4 millimetre to 121.2-by-121.2 millimetre pads, depending on the particle flux (fig. 3.16). The layer of lead in-between makes the electrons start showering before they reach ECAL, which increases the spatial and energy resolution.

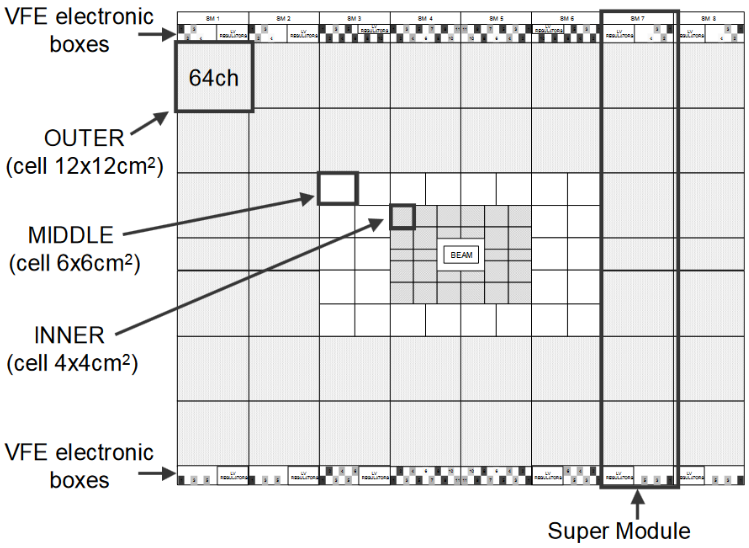

FIGURE 3.16: Layout of a single SPD/PS detector layer. Figure taken from [129].

The ECAL and HCAL follow a similar pattern, with three and two different granularities, respectively (fig. 3.17). Both detectors are of shashlik type. In the longitudinal direction, the ECAL is composed of 3300 layers of 4 millimetre thick scintillating tiles, interleaved with 2 millimetre lead sheets, which amounts to a total of 25 radiation lengths. The HCAL uses identical scintillating tiles interleaved with 16 millimetres of iron and aligned parallel to the beam axis (fig. 3.18).

Figure 3.19 shows their resolutions as a function of electron (ECAL) and pion (HCAL) energy, which are $\sigma_E/E = 10\%/\sqrt{E\text{ GeV}} \oplus 1\%$ and $\sigma_E/E = 69\%/\sqrt{E\text{ GeV}} \oplus 9\%$, respectively.

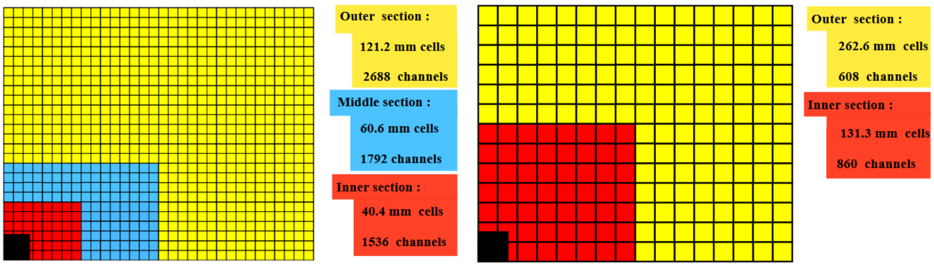

FIGURE 3.17: Granularity of one quarter of the SPD/PS and ECAL (left) and HCAL (right). Figure taken from [118].

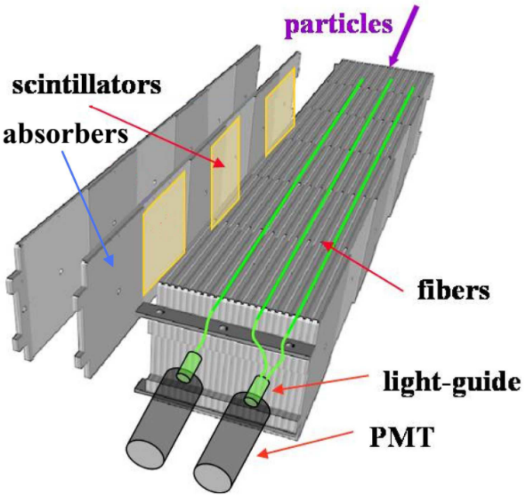

FIGURE 3.18: A schematic view of a single HCAL cell. Figure taken from [118].

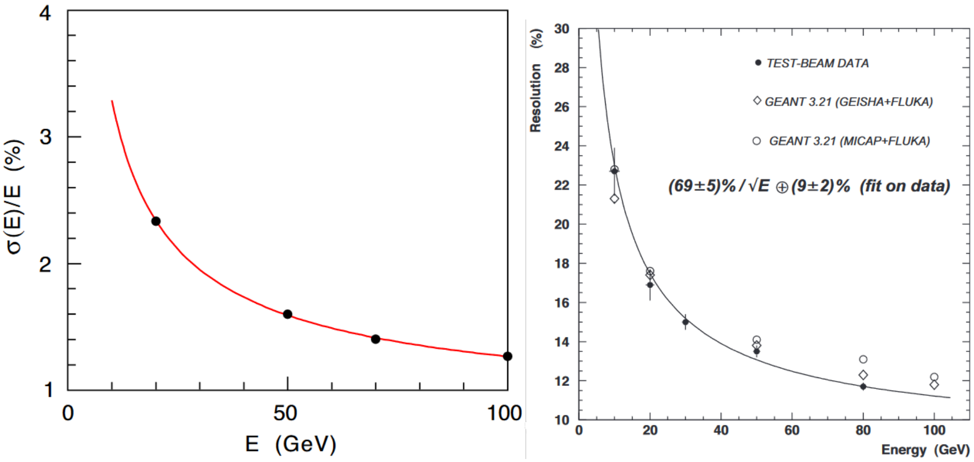

FIGURE 3.19: Resolution of the ECAL (left), measured with electrons in the outer section, and of HCAL (right), measured and simulated using pions. Figures taken from [118].

Muon detectors

Because of the excellent reconstruction and identification efficiency, muons play a very important role in many aspects of the LHCb physics program. In particular, the decays into muon final states can be used to suppress the difficult jet background from proton-proton collisions. This is used, for example, in the study described in the thesis, where the production of $b\bar{b}$ pairs is studied in association with a Z^0 boson decaying leptonically. The information from muon detectors is also required very early in the LHCb trigger, where the presence of a muon – with sufficiently high transverse momentum – is one of the selection criteria.

During Run 1 and 2, the muon system comprised five tracking stations, M1-M5. The first, removed for Run 3, was located between RICH2 and SPD/PS, serving mostly to improve the transverse momentum resolution for the muon trigger. The remaining four are installed at the very end of the detector and interleaved with 80 centimetre thick layers of iron absorber. Only stations 1-3 have a high spatial resolution in the bending (horizontal) magnet plane – stations 4 and 5 are used solely to detect particles reaching them. To keep the particle flux and channel occupancy consistent across each module, they are divided into four regions based on the distance from the beam pipe (the segmentation scales with relative ratios of 1:2:4:8, fig. 3.20). Each segment provides a boolean response to the trigger, allowing for an early measurement of muon transverse momenta with a 25% resolution, without any information from the tracking stations.

All five stations, with an exception of the innermost part of M1, utilise multi wire proportional chamber detectors, filled with a mixture of Ar, CO_2 and CF_4 (in a 40:55:5 proportion). The particle flux received by the upstream station necessitated use of gas electron multipliers in its middle, which are much more radiation resistant. They used 50 micrometre Kapton foil, cladded on both sides with 5 micrometre copper layers, and the same gasses in a 45:15:45 mixture.

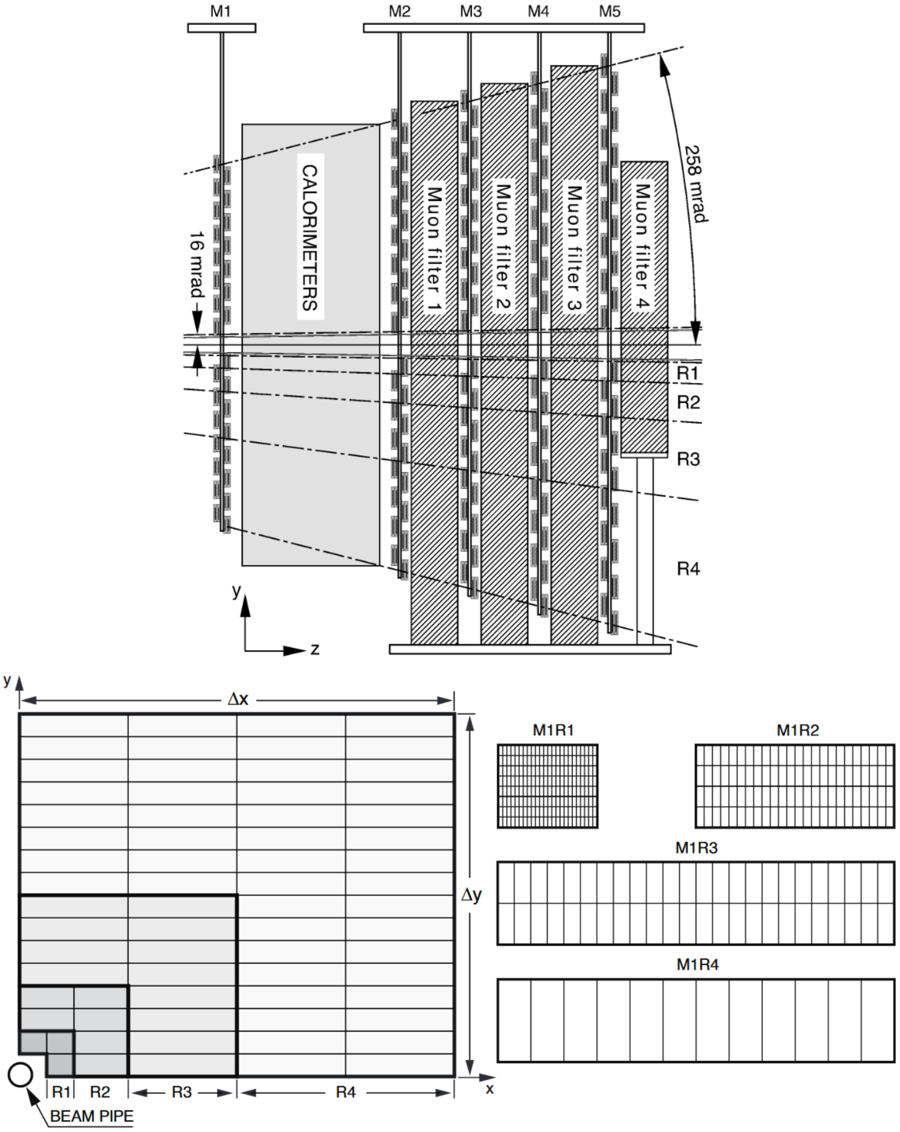

FIGURE 3.20: General layout of the muon system (top) and the cross-section of one of its quadrants (bottom left), where each rectangle represents a single chamber. Bottom right figure shows the granularity of logical pads in different regions of the M1 station – stations M2 and M3 (M4 and M5) have double (half) the number of pads in corresponding sections. Figures taken from [118].

3.3.3 Trigger system and data stripping procedure

With luminosity levelling in place, the visible interaction rate at LHCb is at the order of 40 MHz. It had to be reduced further to 12.5 kHz for Run 2 and about 2 kHz for Run 1, at which the events could be recorded on the tape for an offline analysis. This was achieved with three consecutive triggers – a hardware Level-0 (L0) and software High Level Triggers (HLT1, HLT2). At each stage, a decision was made on whether the event should be passed down the processing pipeline (illustrated in fig. 3.21 for Run 2), based on the information from detector sub-systems.

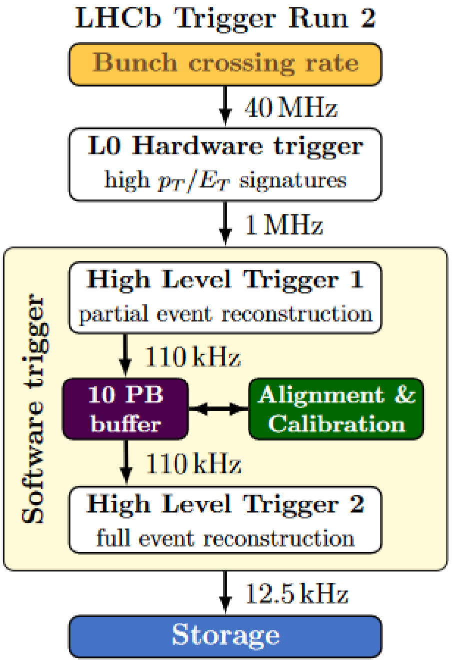

FIGURE 3.21: A schematic of the LHCb trigger pipeline. Figure taken from [128].

In Run 1 and 2, a full readout of the detector electronics was possible only with a rate below 1 MHz. The initial reduction was thus achieved by requiring a muon track with high transverse momentum and/or a deposit with high transverse energy in the calorimeter. Such events are likely to contain electrons, muons and hadrons, and interactions important to the physics program of LHCb. The selection was implemented as the L0 trigger, using Field Programmable Gate Arrays (FPGAs), and the resulting data stream was saved to a temporary memory.

The subsequent software High Level Trigger has two stages. Both are executed in real time on an online computing farm, with the output stored on local hard drives. The HLT1 detects signatures of beauty and charm hadron decays by performing partial event reconstruction and searching for tracks with high transverse momenta and impact parameter (indicating a presence of a displaced decay vertex). The selection reduces rate to about 110 kHz in Run 2 and 30 kHz in Run 1. Furthermore, the improvements introduced to algorithms after Run 1 made real time alignment and detector calibration possible. As a consequence, a full event reconstruction can be performed in the second stage of HLT (during Run 1, a partial reconstruction was performed in the HLT and was followed by an offline refinement).

In order to simplify the offline analysis, the data is organised into so-called stripping lines. Each corresponds to a set of loose selection criteria, which are used to filter recorded events. In turn, they allow users to download and process only those parts of the dataset, which may potentially contain their process of interest. Similar lines are grouped into stripping streams and managed centrally. In particular, new lines are introduced during re-stripping campaigns, when the entire dataset is reprocessed to include them.

Trigger performance for muons

As muons are important for the LHCb physics program, many trigger selections (referred to as trigger lines) focus exclusively on selecting events with high quality muon tracks. Their performance is studied using beauty hadron decays, as they can be reconstructed without imposing any trigger requirements. The L0 hardware trigger decision is based primarily on the presence of a muon candidate with sufficiently high transverse momentum and low number of associated hits in the preshower detectors (to distinguish them from charged pions). Figure 3.22 shows the efficiency of Muon and DiMuon trigger lines for muons originating in beauty hadron decays.

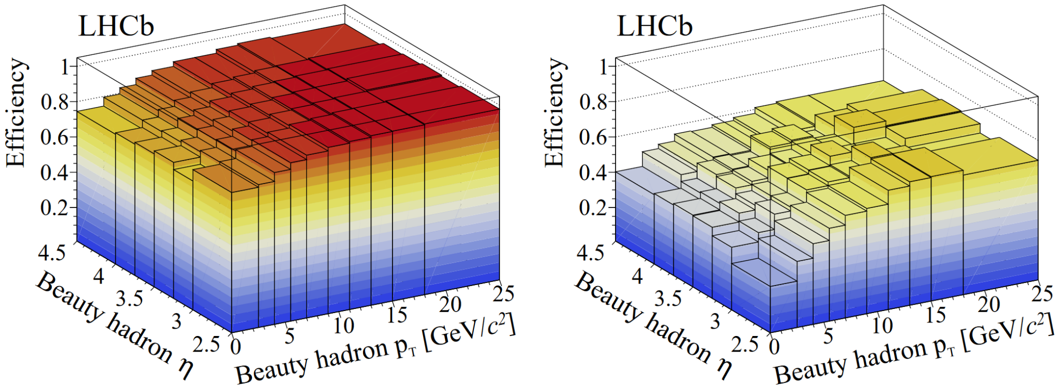

FIGURE 3.22: The efficiency of L0 Muon (left) and DiMuon (right) trigger lines as a function of the beauty hadron pseudorapidity and transverse momentum. Figure taken from [128].

The software trigger muon lines usually take as input only the muon candidates provided by the hardware trigger selection and impose additional quality requirements (e.g. higher transverse momentum, good fit quality). Figure 3.23 shows their efficiencies in the HLT1 trigger compared to an inclusive track selection based on a multivariate analysis. Importantly, the latter uses as input all events which passed the L0 trigger, not necessarily muon candidates, so the absolute efficiency of muon lines (i.e. L0 + HLT1) is lower in comparison than shown in the plots. Similarly, fig. 3.24 shows the efficiencies for HLT2 stage of the software trigger, which are normalised to candidates passing the corresponding L0 and HLT1 selection.

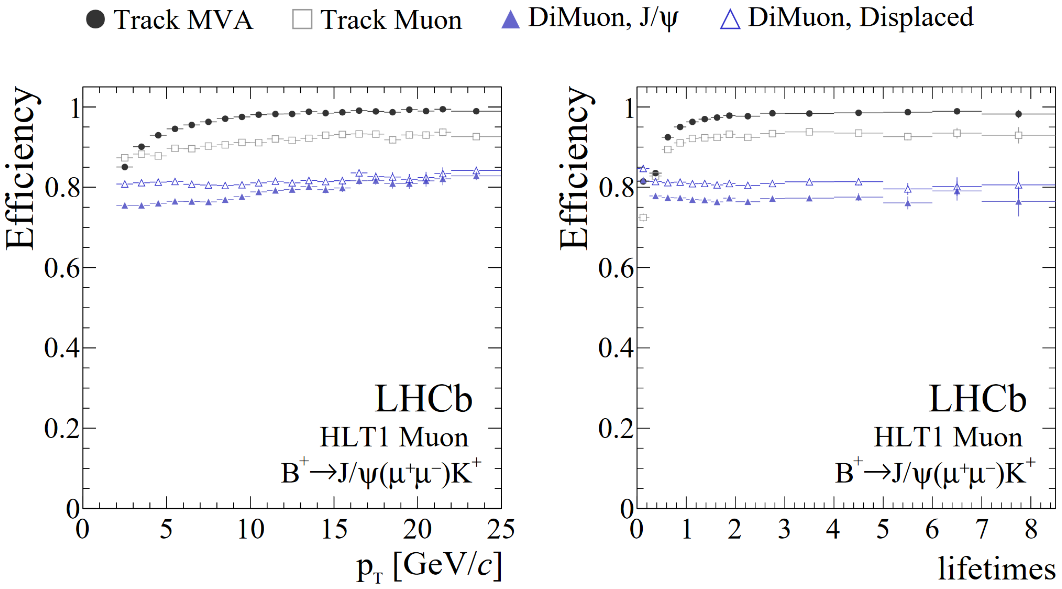

FIGURE 3.23: Efficiency of HLT1 muon lines as function of the beauty hadron transverse momentum (left) and the multiplicity of average B^+ meson lifetime (right). Track MVA represents inclusive selection based on a multivariate analysis classifier. Figure taken from [128].

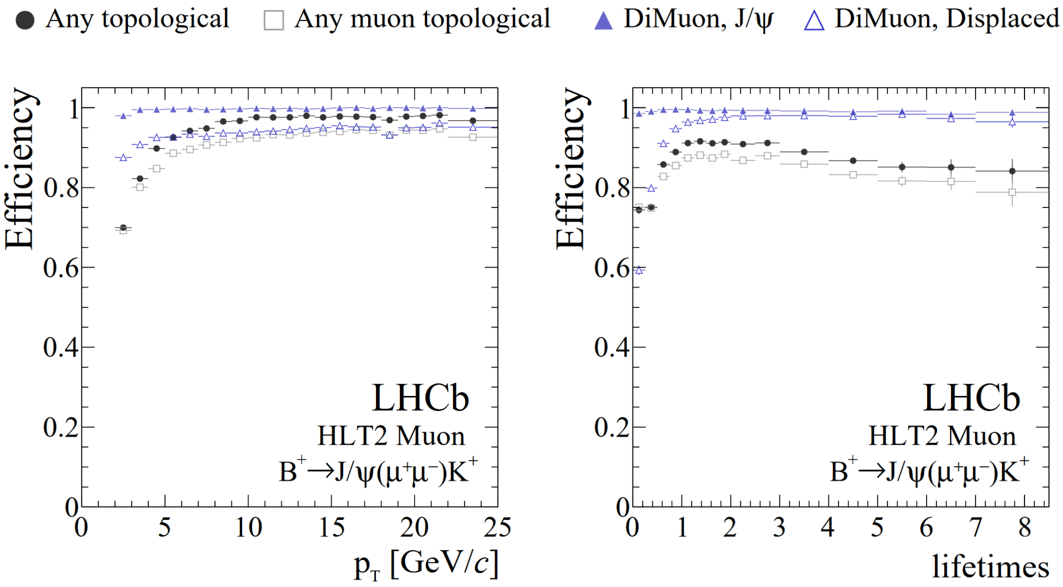

FIGURE 3.24: Efficiency of HLT2 muon lines as function of the beauty hadron transverse momentum (left) and the multiplicity of average B^+ meson lifetime (right). Figure taken from [128].

3.4 Data flow and software framework

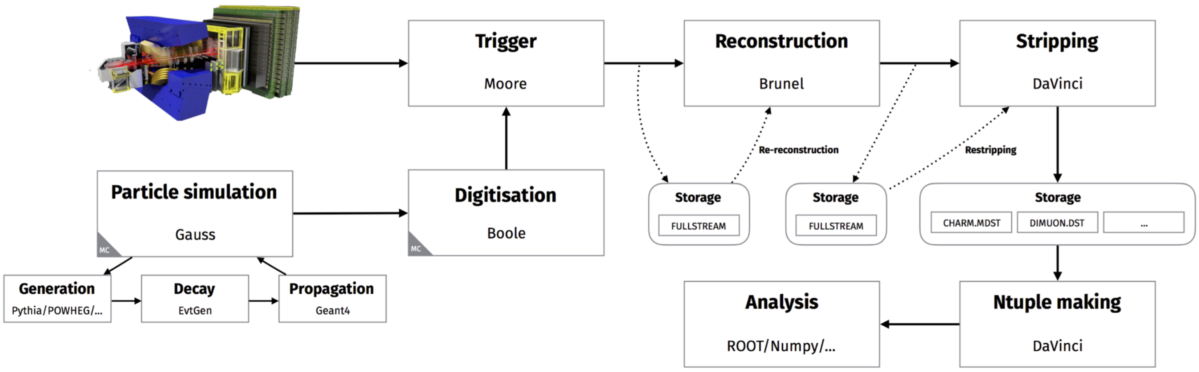

FIGURE 3.25: The offline data processing chain of LHCb. Figure taken from [130].

The offline data processing is carried out by a series of dedicated software components, organised on top of a Gaudi [131, 132] framework (fig. 3.25). The algorithms of High Level Trigger are implemented in the Moore [132] package. The resulting objects, containing information from reconstruction (e.g. tracks and calorimeter clusters), are repacked into a unified DST format by the Brunel [133] application. In case of Run 1 data, an additional offline reconstruction is also performed. The DaVinci [134] application is then used to create stripping lines and, in the analysis, to process raw DST files and produce ROOT ntuples [135].

Generation of Monte Carlo particles is performed within the Gauss [136] application, to which external event generators are interfaced (e.g. Pythia8 [137] and MadGraph5 [111, 112]). The decays are modelled with EvtGen [138] package. The simulation of particle interactions with the detector is performed using Geant4 [139], after which the response is digitised with the Boole [132] application and the Level 0 Trigger is emulated with L0App [132]. The simulated events are then passed to the Moore application and undergo the same processing as real data.

3.5 Detector upgrade

The upcoming upgrade of the LHC machine (High Luminosity LHC, [118]), necessitates significant changes in the LHCb detector, which will have to withstand an order of magnitude higher instantaneous luminosity ($\mathcal{L} = 2 \cdot 10^{34}$ cm^{-2}s^{-1}). At the same time, several new systems will be introduced to fully benefit from the change in operating conditions. The upgrade will be carried out in three stages [140, 141] – upgrade Ia has already been completed for the Run 3 of LHC, which is currently in progress, upgrade Ib is planned for Run 4 (years 2026-2030) and upgrade II for Run 5 (2031 and beyond). The main changes to the LHCb detector are briefly summarised below.

3.5.1 Upgrade I

The main goal of the first stage of the upgrade (Ia) was to completely remove the need for the L0 hardware trigger. This was achieved by replacing the readout electronics and sensors with their modern counterparts and introducing improvements to data processing software and algorithms. The general trigger structure was carried over from Run 2 with only HLT remaining (see section 3.3.3). In addition, the trigger computing farm has been moved to the surface, which enables replacement of radiation resistant elements with commercial electronics. The changes allow for a switch to a fully on-online analysis for the primary measurements in the LHCb physics program. Several upgrades to detector elements were introduced. In particular, VELO detector received improvements to allow for vertex reconstruction with higher pile-up, RICH – new photodetectors and electronics to improve particle identification and the planar trackers were replaced with new Upstream Tracker (in place of TT) and Scintillating Fibre detector (T1-3). The M1 station of the muon system was also replaced with a neutron shield to protect the tracker from particles reflected off the calorimeter.

In phase Ib, two new modules will be introduced to extend the sensitivity to low momentum particles. The particle identification system will be expanded with a time of flight detector, using reflected Cherenkov photons, which will improve the ability to identify protons and kaons with momenta below 10 GeV. Additionally, a scintillating fibre detector will be installed on the internal surface of the magnet to track low momentum particles bent out of the detector acceptance.

3.5.2 Upgrade II

The last phase of the upgrade focuses primarily on preparing the detector to operate with increased instantaneous luminosity. The main challenges are a significant increase in radiation damage over time and the multiplicity of particles (about 2500 charged particles are expected within detector acceptance). Consequently, the granularity of all detectors will be increased to improve the measurement resolution and redundancy. The VELO detector will be replaced with a 4D hybrid pixel detector, enabling use of timing information. The time of flight, combined with an overall decrease of element thickness, will allow for effective matching of reconstructed track segments even with much higher occupancy. Furthermore, RICH1 will receive additional upgrades to increase the capability of identifying low momentum particles.

Chapter 4

Measurement of the $Z^0 \left(\to \mu^-\mu^+\right) b\bar{b}$ production cross-section in the LHCb experiment

4.1 Introduction

The following study extends the measurement of the $Z^0 b\bar{b}$ production cross-section at the centre-of-mass energy of 13 TeV, performed by the ATLAS [109] and CMS [110] experiments, to the unique forward kinematic region available only to the LHCb detector. The importance of the process as a benchmark for calculations performed within the Standard Model as well as in searches for Beyond the Standard Model phenomena is outlined in section 2.4. The description of the LHCb detector is given in chapter 3. In particular, fig. 3.2 shows how its acceptance is complementary to the General Purpose Detectors of ATLAS and CMS experiments. An overview of the aforementioned measurements can be found in section 2.5.2. In the present chapter, the analysis is first outlined and then described in section 4.2 and section 4.3 gives a summary and discussion of the results. The study was conducted with the leading role of the Author of this thesis.

4.2 Analysis strategy and results

The study preliminarily determines the total $Z^0 b\bar{b}$ production cross-section at the centre-of-mass energy of 13 TeV, using data collected by the LHCb experiment throughout years 2015-2018. It focuses on the $Z^0 \to \mu^-\mu^+$ decay channel. Consequently, the signal signature consists of a muon anti-muon pair and two particle jets from b quarks hadronization. The full process is as follows:

$$pp \to Z^0 b\bar{b} \to \mu^-\mu^+ b\bar{b}. \tag{4.1}$$

Signal candidates are reconstructed in two stages. Initially, preselection requirements are applied to the full dataset, in order to extract events with a possible $Z^0 \to \mu^-\mu^+$ decay signature. Then, the events which contain only two oppositely charged muons and a pair of b jets are selected and the corresponding particles are combined into a Z^0 boson and $b\bar{b}$ di-jet. Further selection is also applied to ensure a high quality Z^0 candidate. The remaining data events still contain contributions from multiple background processes. The first category are final states with two quarks and less than two muons, which can mimic a signal signature due to muons produced in particle jets. This type is strictly dominated by the production of $b\bar{b}$ pairs and can be eliminated based on the characteristics of a Z^0 boson candidate. The second contribution consists of the production of $t\bar{t}$ pairs, which decay first into $W^+W^-b\bar{b}$ and subsequently into a $\mu^-\mu^+b\bar{b}\nu\bar{\nu}$ final state, and a production of two Z^0 bosons with one decaying into a muon and anti-muon, and the other into a $b\bar{b}$ pair. The contributions from both are significantly reduced with a multivariate analysis. Several other sources are also investigated, but found to have a negligible impact.

The resulting subset of events contains an irreducible admixture from the production of a Z^0 boson with a pair of light quarks or gluons (u, d, s, g). Because the centrally produced Monte Carlo sample for this background process is not yet available in the LHCb experiment, it is temporarily substituted with an inclusive quark pair production. The number of signal events among candidates is evaluated using a template fit of simulated distributions to the reconstructed invariant mass of a $b\bar{b}$ di-jet. The $Z^0b\bar{b}$ production cross-section is then calculated as:

$$\sigma = \frac{P \cdot N}{\epsilon \cdot \mathcal{L}}, \tag{4.2}$$

where P is the signal purity, N the number of signal events in the data sample, ϵ the total efficiency and $\mathcal{L}$ integrated luminosity. N is determined from the template fit, while P and ϵ are calculated using simulated signal sample.

The data and simulated samples used in the analysis are summarised in section 4.2.1. Section 4.2.2 describes the initial event selection and subsequent reconstruction of signal candidates. The procedure used to suppress background contributions is discussed in section 4.2.3. Section 4.2.4 describes the template fit and how the signal purity is evaluated. Finally, section 4.2.5 provides the calculation of the cross-section and discusses the measurement uncertainty.

4.2.1 Data and Monte Carlo samples

The measurement uses proton-proton collisions at the centre-of-mass energy of 13 TeV, which were recorded by the LHCb experiment in years 2015-2018 (Run 2 of LHC). An overview of the software framework used to process collected data can be found in section 3.4. The integrated luminosity for each year is given in table 4.1 and is determined using a Van der Meer method [142], providing a systematic uncertainty of 2%. The analysis is performed on a combined dataset.

year	integrated luminosity [pb^{-1}]	systematic uncertainty [%]
2015	329.7	2
2016	1665.2	2
2017	1817.4	2
2018	2185.6	2
total	5997.9	2

TABLE 4.1: Integrated luminosity corresponding to each year of data taking considered in the analysis.

The study of background contributions as well as selection and reconstruction efficiencies requires also a variety of simulated samples. They are produced centrally by the experiment and processed using the same algorithms as real data, which allows for direct comparisons. Furthermore, the number of events produced for each year of data taking (i.e. with a matching beam and detector configuration) is proportional to the integrated luminosity collected that year. They are merged and used together in the analysis, providing compatibility with collected data.

Monte Carlo samples employed in the study are summarised in table 4.2. The signal ($Z^0 b\bar{b}$ production) and $W^{\pm}(\rightarrow \mu^{\pm}\nu)b\bar{b}$ background are simulated at Next-to-Leading Order accuracy with MadGraph5 [111, 112] event generator. The remaining ones are simulated at Leading Order with Pythia8 [137], which is also used to perform quark fragmentation and hadronization in both cases. The inclusive $q\bar{q}$ di-jet sample is generated independently in four bins of the quarks' transverse momenta, because of the significant difference in the corresponding production cross-sections. Additionally, several selection criteria are applied to the particles of generated processes, in order to reject events outside LHCb detector's acceptance from the simulation. The cross-sections reported by the event generators and acceptance efficiencies, including generator level requirements listed in table 4.2, are given in table 4.3.

process	order	size [M]	comments
$Z^0(\rightarrow \mu^+\mu^-)b\bar{b}$	NLO	12.28	mass of lepton pair above 40 GeV quarks' transverse momenta above 10 GeV
$W^{\pm}(\rightarrow \mu^{\pm}\nu)b\bar{b}$	NLO	6.04	quarks' transverse momenta above 10 GeV
$b\bar{b}$	LO	32.04	at least one lepton with transverse momentum above 14 GeV required in acceptance
$c\bar{c}$	LO	6.35	at least one lepton with transverse momentum above 14 GeV required in acceptance
$Z^0(\rightarrow l^+l^-)Z^0(\rightarrow b\bar{b})$	LO	10.22	at least one lepton with transverse momentum above 5 GeV and both quarks required in acceptance
$W^{\pm}(\rightarrow l^{\pm}\nu)Z^0(\rightarrow b\bar{b})$	LO	40.25	at least one lepton with transverse momentum above 5 GeV and one quark required in acceptance
$t(\rightarrow bl\nu)\bar{t}(\rightarrow \bar{b}l\nu)$	LO	37.25	at least one lepton with transverse momentum above 15 GeV required in acceptance
$t/\bar{t}(\rightarrow b/\bar{b}\dots)$	LO	8.02	at least one lepton with transverse momentum above 17 GeV and one quark required in acceptance
$q\bar{q}$, p_T 10-15 GeV $q\bar{q}$, p_T 15-20 GeV $q\bar{q}$, p_T 20-50 GeV $q\bar{q}$, p_T above 50 GeV	LO	2.01 2.00 2.09 2.08	inclusive (q = gluons and all quarks, except t)

TABLE 4.2: A list of produced Monte Carlo samples. If not specified otherwise, all particles of the generated process are required to be in the detector's acceptance.

process	cross-section [pb]	acceptance efficiency
$Z^0(\rightarrow \mu^+\mu^-)b\bar{b}$	45.13(23)	0.041894(29)
$W^\pm(\rightarrow \mu^\pm\nu)b\bar{b}$	105.80(29)	0.045018(19)
$b\bar{b}$	3319000(1369)	0.0030263(17)
$c\bar{c}$	3523000(2429)	0.00063526(63)
$Z^0(\rightarrow l^+l^-)Z^0(\rightarrow b\bar{b})$	0.55(1)	0.092241(65)
$W^\pm(\rightarrow l^\pm\nu)Z^0(\rightarrow b\bar{b})$	0.82(1)	0.130292(80)
$t(\rightarrow bl\nu)\bar{t}(\rightarrow \bar{b}l\nu)$	31.98(42)	0.19300(14)
$t/\bar{t}(\rightarrow b/\bar{b}\dots)$	150.30(2.77)	0.044658(57)
$q\bar{q}$, p_T 10-15 GeV	59070(91.54)$\cdot 10^5$	0.1443(12)
$q\bar{q}$, p_T 15-20 GeV	12710(20.02)$\cdot 10^5$	0.1322(12)
$q\bar{q}$, p_T 20-50 GeV	6981(10.85)$\cdot 10^5$	0.1210(11)
$q\bar{q}$, p_T above 50 GeV	22610(38.37)$\cdot 10^3$	0.08825(94)

TABLE 4.3: Generator level cross-sections and acceptance efficiencies. The uncertainties given for cross-sections are systematic, for efficiencies – statistical.

4.2.2 Reconstruction of signal candidates

The amount of data collected by the experiment necessitates a gradual approach to the reconstruction of $Z^0b\bar{b}$ candidates. In particular, the initial selection has to be based purely on the information from the stripping and trigger lines, which are stored in the database for each event. The consecutive steps then further enhance the selection and reduce the number of remaining candidates.

The starting point is a selection of data events which contain a possible signature of a $Z^0 \rightarrow \mu^-\mu^+$ decay, with at least one of the reconstructed muons (there may be more than two candidates) corresponding to a high quality track. The achieved reduction in size of the dataset is enough to save the resulting sample locally. An offline selection is then applied to select only events with exactly two muons, corresponding to a high quality Z^0 candidate, and exactly two particle jets with both being identified as originating from a b quark. The remaining particles form an underlying event and provide additional variables for the multivariate analysis. The details on how the particle jets are reconstructed and identified as well as on each selection step are given, in order, in the subsections below. The results are summarised at the end of the section.

Two of the background sources require special treatment. Specifically, the $c\bar{c}$ simulated sample is too small to reconstruct at least one potential signal event. For this reason, the Z^0 boson and $b\bar{b}$ di-jet candidates are reconstructed independently, which allows to approximately estimate its contribution. Although it is overestimated by this procedure, it is found to be negligible. The second case is the inclusive $q\bar{q}$, which does not contain a Z^0 boson and hence only the $b\bar{b}$ di-jet candidate is reconstructed. The selection conditions for both are modified appropriately and explained in the subsections below. Importantly, because the latter is used to model background contributions from Z^0 boson with a pair of light quarks, the events with beauty hadrons (i.e. corresponding to $b\bar{b}$ production) are removed from the sample.

Reconstruction and identification of particle jets

The particle jets are reconstructed using an anti-k$_T$ [143] algorithm, as implemented in the FastJet [144] package, with a 0.5 jet R parameter. Their identification is based on the attributes of displaced secondary vertices from beauty and charm hadron decays, reconstructed in the VELO detector (see section 3.3.1). The procedure (details can be found in [145], an overview of the approach is given below) is performed in multiple steps. Initially, the tracks which are unlikely to come from the primary vertex are selected as input, based on their impact parameter with respect to said vertex and transverse momentum. Importantly, they are not required to be within the jet cone, as the presence of tracks outside provides additional characteristics discriminating between jets from b and c quarks. The tracks are combined into all possible pairs with invariant mass lower than that of a B^0 meson, but high enough to reject contributions from quarks lighter than c. The pairs are used as seeds for secondary vertices and those falling within the jet radius are assigned to the corresponding jet. Within the assigned collections, the vertices are merged if they share tracks. Additional criteria are then imposed to remove possible background sources (e.g. from kaon decays). After which, if any jet has more than two assigned vertices remaining, the one with the highest transverse momentum is chosen (defined as derived from a four vector sum of constituting tracks).

Two Boosted Decision Tree (BDT) classifiers are trained independently, based on the assigned secondary vertex characteristics in a simulated sample (e.g. its invariant mass and number of tracks within the jet cone). The first, BDT(b | c), is trained to distinguish between jets from b and c quarks, the second – BDT(bc | udsg) – between jets from heavy and light quarks. Figure 4.1 shows their responses for simulated samples of b, c and light quarks. Figure 4.2 illustrates the identification efficiency for heavy quark jets as a function of their transverse momentum and probability of misidentifying a light jet as coming from a heavy quark.

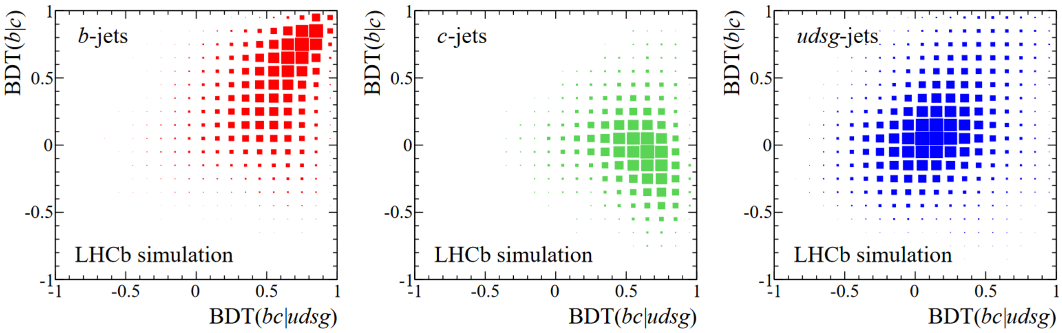

FIGURE 4.1: Response of jet tagging BDT classifiers to the simulated samples of b (left), c (middle) and light (right) jets. Figure taken from [145].

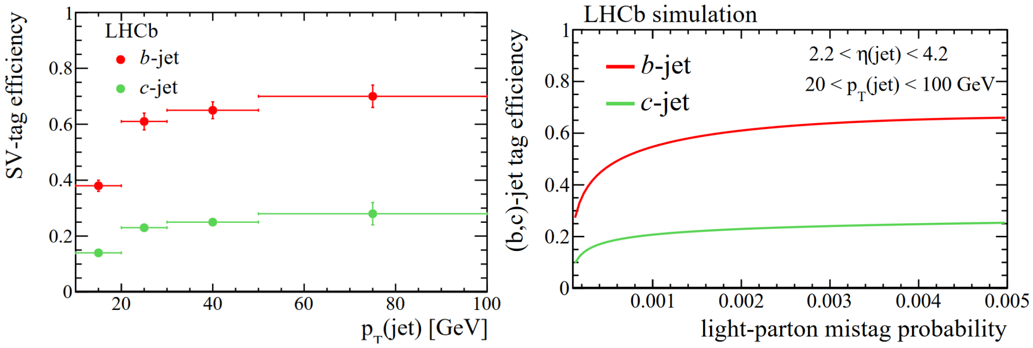

FIGURE 4.2: The efficiency of identifying b and c jets as a function of their transverse momentum (left) and the probability of misidentifying a jet from a light quark as coming from b or c quarks (right). Figure taken from [145].

Preselection of $Z^0 \rightarrow \mu^-\mu^+$ decay candidates

The initial selection aims to reduce the collected data to a subset of events which are likely to contain a $Z^0 \rightarrow \mu^-\mu^+$ decay, and is based on the information from the predefined stripping and trigger lines available directly in the database (see section 3.3.3 for explanation). Their choice follows optimized LHCb criteria for measurements involving a $Z^0 \rightarrow \mu^-\mu^+$ signature. In the first step, the events are required to be flagged as fulfilling prerequisites for the *Z02MuMu* stripping line. The line collects all reconstructed events containing muons with transverse momentum above 6 GeV, which – if combined with opposite charge – produce a Z^0 boson candidate with invariant mass ($M_{\mu^+\mu^-}$) above 40 GeV. The decision is positive if at least two such muons are found, but there may be more. At least one of them is then required to be a high quality muon, with conditions based on a combined decision from all three trigger stages. The hardware trigger line (*L0MuonEW*) selects tracks with transverse momentum above 6 GeV and imposes a requirement on the number of hits in the scintillating pads in front of the calorimeter being less than 10000 (see section 3.3.2). The HLT1 line (*Hlt1SingleMuonHighPT*) requires the track to be identified as muon and introduces selection criteria on the momentum ($p > 8$ GeV), transverse momentum ($p_T > 6$ GeV) and χ^2 of the track fit normalised to the number of degrees of freedom ($\chi^2/\mathrm{ndf} < 4$). The HLT2 trigger line (*Hlt2EWSingleMuonVHighPt*) further extends the requirement on transverse momentum to $p_T > 12.5$ GeV. Table 4.4 summarises the effective combined selection criteria for $Z^0 \rightarrow \mu^-\mu^+$ candidates (stripping) and one of the muons (trigger). A discussion of muon track reconstruction and trigger efficiencies can be found in sections 3.3.1 and 3.3.3. In case of $c\bar{c}$ production sample (where only $b\bar{b}$ di-jet candidate is reconstructed) and inclusive $q\bar{q}$ sample, the preselection requires only the presence of two reconstructed particle jets (of any flavour).

stripping	$M_{\mu^+\mu^-} > 40$ GeV $p_{T,\,\mu^\pm} > 6$ GeV
trigger	muon track $p > 8$ GeV $p_T > 12.5$ GeV track $\chi^2/\text{ndf} < 4$ nSPD < 10000

TABLE 4.4: A summary of combined requirements used in pre-selection. The details for each trigger stage and explanation of variables are given in the text.

Selection of $Z^0\,(\to \mu^-\mu^+)\,b\bar{b}$ candidates

The second selection stage is performed fully offline. Initially, the Z^0 boson candidates are reconstructed with two oppositely charged muons from the stripping selection, with one of them required to pass the trigger requirements. Events with more than one or no candidates are rejected. Additional criteria are then imposed on both muons. Specifically, they are required to:

- have transverse momenta (p_T) above 20 GeV,
- be within the pseudorapidity (η) range of 2-4.5
- and have a relative momentum uncertainty ($\sigma(p_{\mu^\pm})/p_{\mu^\pm}$) better than 10%.

Furthermore, the corresponding Z^0 candidate is required to have a reconstructed invariant mass within approximately 30 GeV of Z^0 boson invariant mass (60 GeV $<$ $\text{M}_{\mu^+\mu^-} <$ 120 GeV).

The reconstruction of a $b\bar{b}$ di-jet candidate is kept intentionally loose to maximise signal reconstruction efficiency, because the expected signal yield is very low. The background from Z^0 with light quarks is also considered further in the analysis, hence its suppression at this stage is not necessary. The requirements on jet kinematics are introduced to ensure that the characteristics of jets reconstructed in data are accurately reproduced by the Monte Carlo generators and detector simulation. The jets are first identified as coming from a b quark if the response of BDT(bc | udsg) classifier is above 0.1 and BDT(b | c) above 0.04 (see fig. 4.1 and discussion below). Only events with exactly two reconstructed jets, both identified as b, are allowed to pass. However, the presence of jets which are reconstructed but have no BDT responses assigned is allowed, as they are considered to be artefacts of the clustering algorithm and not correspond to actual particle jets. Both jets constituting the $b\bar{b}$ di-jet candidate are required to have:

- momentum (p) above 5 GeV,
- transverse momentum (p_T) above 15 GeV (the value is chosen as 5 GeV higher than the highest generator level requirement – see table 4.2 – to ensure that the requirement on the reconstructed p_T is not affected by the discrepancy between generated and reconstructed p_T distributions),
- and number of assigned particles ($N_{\text{particles}}$) greater than 4.

The selection criteria are summarised in table 4.5. The BDT classifier thresholds are optimised to saturate the efficiency of correctly identifying both jets in the simulated signal while keeping both values positive. Figure 4.3 shows the aforementioned efficiency as a function of the imposed classifier response thresholds. The fraction is normalised to the number of events with exactly two reconstructed and identified jets, which both pass the requirements in table 4.5. Efficiency for values chosen in the study is close to 70%.

In case of $c\bar{c}$ production, the reconstruction of Z^0 and $b\bar{b}$ di-jet candidates is performed independently. In the inclusive $q\bar{q}$ sample the events containing beauty hadrons are removed and only di-jet is reconstructed. Furthermore, the four momenta of remaining particles (which are neither assigned to any of the two jets nor used to reconstruct the Z^0 boson) are added together to form a pseudo-jet, which corresponds to an underlying event. Its characteristics are used as variables in the multivariate analysis, described in the following section.

$Z^0 \rightarrow \mu^-\mu^+$ candidate
60 GeV $< M_{\mu^+\mu^-} <$ 120 GeV
$p_{T,\,\mu^\pm} >$ 20 GeV
$2 < \eta_{\mu^\pm} < 4.5$
$\sigma(p_{\mu^\pm})/p_{\mu^\pm} < 10\%$

$b\bar{b}$ candidate
$p_{\text{jet}} >$ 5 GeV
$p_{T,\,\text{jet}} >$ 15 GeV
$N_{\text{particles}} > 4$
BDT(bc | udsg) > 0.1
BDT(b | c) > 0.04

TABLE 4.5: A summary of selection criteria used to reconstruct Z^0 boson and $b\bar{b}$ di-jet candidates. The variables are explained in the text.

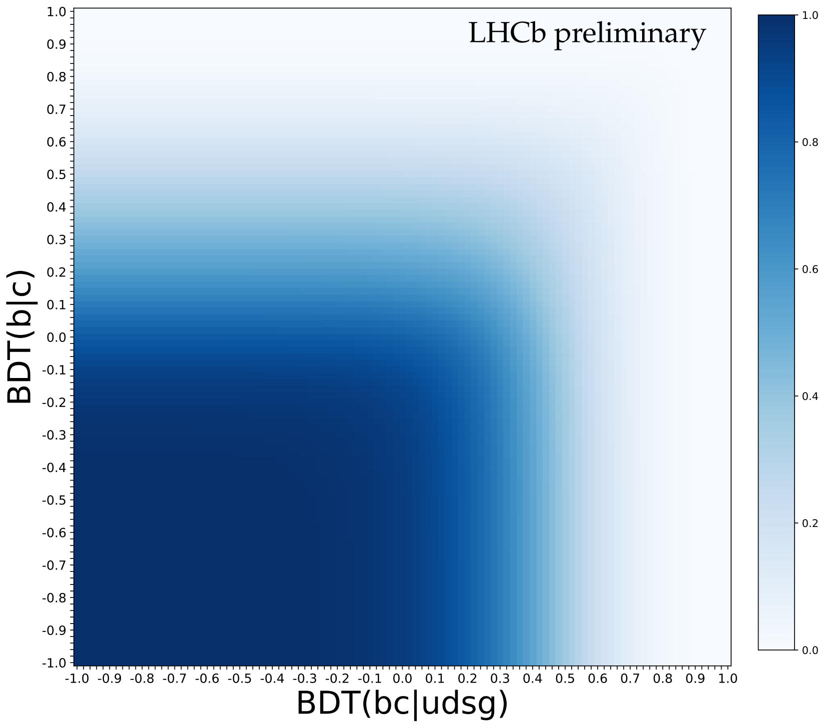

FIGURE 4.3: Fraction of simulated signal events with exactly two reconstructed and identified jets passing the selection criteria, where both were correctly identified as coming from a b quark. It is assumed that both are required to have the classifier responses above the corresponding values on the axes.

Reconstruction results

The full reconstruction finds 605 signal candidates, which still contain contributions from various background processes that also pass the selection. The yields for each year are given in table 4.6. The selection efficiencies are listed in table 4.7, where the trigger and stripping efficiencies are included in the preselection efficiency.

year	$Z(\to \mu^+\mu^-)b\bar{b}$ candidates	N/$\mathcal{L}$ [1/pb^{-1}]
2015	34	$0.103 \pm 0.018 \pm 0.002$
2016	164	$0.098 \pm 0.008 \pm 0.002$
2017	194	$0.107 \pm 0.008 \pm 0.002$
2018	213	$0.097 \pm 0.007 \pm 0.002$
total	605	$0.101 \pm 0.004 \pm 0.002$

TABLE 4.6: Number of signal event candidates reconstructed in each year of data taking considered in the analysis. The last column shows the ratio of number of candidates to the integrated luminosity. The first uncertainty is statistical, the second due to luminosity measurement.

$Z^0 b\bar{b}$ candidate reconstruction			
process	preselection eff.	reconstruction eff.	combined eff.
$Z^0(\rightarrow \mu^+\mu^-)b\bar{b}$	0.16479(12)	0.02341(11)	0.003858(18)
$W^\pm(\rightarrow \mu^\pm\nu)b\bar{b}$	0.009171(39)	0.00685(35)	0.0000628(32)
$b\bar{b}$	0.0011754(61)	0.00863(48)	0.00001014(56)
$Z^0(\rightarrow l^+l^-)Z^0(\rightarrow b\bar{b})$	0.13074(11)	0.06196(22)	0.008101(28)
$W^\pm(\rightarrow l^\pm\nu)Z^0(\rightarrow b\bar{b})$	0.006278(13)	0.01297(23)	0.0000814(14)
$t(\rightarrow bl\nu)\bar{t}(\rightarrow \bar{b}l\nu)$	0.019966(23)	0,01602(15)	0.0003199(29)
$t/\bar{t}(\rightarrow b/\bar{b}\dots)$	0.003793(32)	0.00704(71)	0.0000267(27)

Z^0 boson candidate reconstruction			
process	preselection eff.	reconstruction eff.	combined eff.
$c\bar{c}$	0.0004947(88)	0.0459(38)	0.0000227(19)

$b\bar{b}$ di-jet candidate reconstruction			
process	preselection eff.	reconstruction eff.	combined eff.
$c\bar{c}$	0.008805(37)	0.0649(11)	0.0005711(95)
$q\bar{q}$, p_T 10-15 GeV	0.000345(13)	0.071(10)	0.0000244(35)
$q\bar{q}$, p_T 15-20 GeV	0.000640(18)	0.128(10)	0.0000819(64)
$q\bar{q}$, p_T 20-50 GeV	0.001361(26)	0.2194(88)	0.000299(12)
$q\bar{q}$, p_T above 50 GeV	0.003780(43)	0.3122(63)	0.001180(24)

TABLE 4.7: A summary of preselection and reconstruction efficiencies for signal event candidates. The uncertainties are statistical. Bottom tables show the efficiencies when only a Z^0 boson or only a $b\bar{b}$ di-jet candidate is reconstructed, for reasons described in the text.

4.2.3 Rejection of reducible background contributions

Most of the 605 signal candidates, which remain after the final selection, come from various background processes matching the same criteria and have to be removed before the cross-section calculation. The first category (type I background) involves a Z^0 boson reconstructed using muon tracks originating in quark hadronization. These candidates have kinematic properties which are significantly different from a real $Z^0 \rightarrow \mu^-\mu^+$ decay and can be removed completely. The second kind (type II) involves processes with signatures similar to the signal one. The approximate contributions can be evaluated using integrated luminosity, cross-sections and reconstruction efficiencies from tables 4.1, 4.3 and 4.7. In particular, type I is expected to be dominated strictly by the $b\bar{b}$ production (a direct calculation yields about 600 events, but the number is overestimated as the cross-section does not account for the Next-to-Leading Order effects, which are significant for heavy quarks). It is followed by the $W^\pm b\bar{b}$ production, with less than 2 events expected in data. Type II background is mostly a mix of $t\bar{t}$ (about 12 events expected, but prediction also suffers from the Leading Order accuracy) and Z^0Z^0 (less than 3 events) production. The other sources can be disregarded, because either their expected contribution is below one event or they get suppressed alongside considered ones and do not require dedicated treatment.

In order to maximise the background rejection efficiency, the multivariate analysis uses classifiers trained to distinguish between signal and background events, which can exploit the correlations between training variables. Several, available in the ROOT TMVA [146] package, have been evaluated with respect to the overall stability and achievable signal retention/background rejection ratio and the Boosted Decision Tree Gradient (BDTG) was found to be the best performing. It is thus used exclusively throughout the procedure. Two of such classifiers are trained in total – the first on the $Z^0 b\bar{b}$ signal and $b\bar{b}$ background characteristics and the second with a combined $t\bar{t}$ and Z^0Z^0 background, where the expected numbers of events in the data are used as mixing weights. In both cases, the training was done in the same way. The relevant samples were first split in half, with one subset being used for training and the other to test for possible overtraining. The training was then performed with all available variables, after which their significance (as reported by TMVA algorithm) and linear correlation coefficients were investigated. The number of used variables was then minimised to ensure classifier stability. The ones with the least importance in training, but highly correlated with others, were removed and the training was repeated. The procedure was carried over iteratively, until all employed variables were at most only slightly correlated (i.e. they all provided additional information for the training algorithm). The parameters of the training (e.g. number of trees and their depth) were then tuned to minimise the overtraining by ensuring that the classifier response distributions are consistent between training and testing samples. The latter were used in the subsequent measurement.

The thresholds imposed on the responses of both classifiers are optimised to remove all expected contributions of $b\bar{b}$ production in data and to reduce those from $t\bar{t}$ and Z^0Z^0 processes to a level of approximately one event each. The details on each of the classifiers are given in the subsections below. The final subsection summarises the selection results.

Rejection of type I background

The first classifier rejects combinatorial background, with Z^0 boson candidates reconstructed using muons created during quark hadronization. It is trained exclusively on the signal and $b\bar{b}$ MC sample, using the following quantities (the generic variable names, which are used in figures shown below, are given in brackets and their distributions are shown in section 4.2.3):

- invariant mass of the Z^0 boson candidate (Z_Mass)
- transverse momentum of the Z^0 boson candidate (Z_Pt)
- smaller of transverse momenta of the two muons (muonPt_min)
- smaller of polar angles of the two muons (muonTheta_min)
- angle between the Z^0 boson and $b\bar{b}$ di-jet candidates (ZDijAngle)
- difference in transverse momenta between the Z^0 boson and $b\bar{b}$ di-jet candidates (ZDijPtBalance)
- smallest of the four angles between the muons and jets (bjetLeptonAngle_min)

- momentum of the underlying event pseudo jet (uJetP)
- polar angle of the underlying event pseudo jet (uJetTheta)

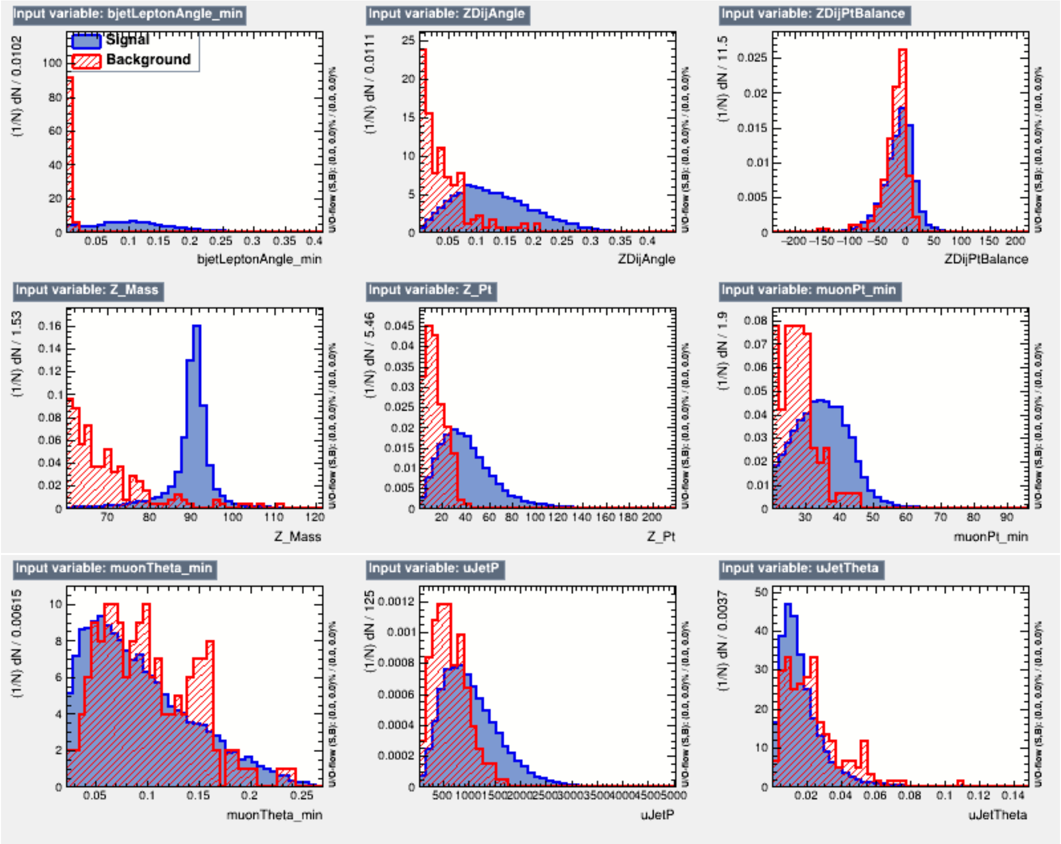

FIGURE 4.4: Variables used in training of the classifier for type I background. They are explained in the text.

Figure 4.5 shows the linear correlations of used variables. The response of the classifier and its performance are shown in fig. 4.6. The slight mismatch between training and testing background sample is caused by relatively low number of $b\bar{b}$ events used in training. The highest value of classifier response in the background testing sample is 0.32 (0.50 in training sample). Because the impact on expected signal yield is negligible around that value, the threshold is chosen as 0.5 to minimise the systematic uncertainty introduced by the classifier.

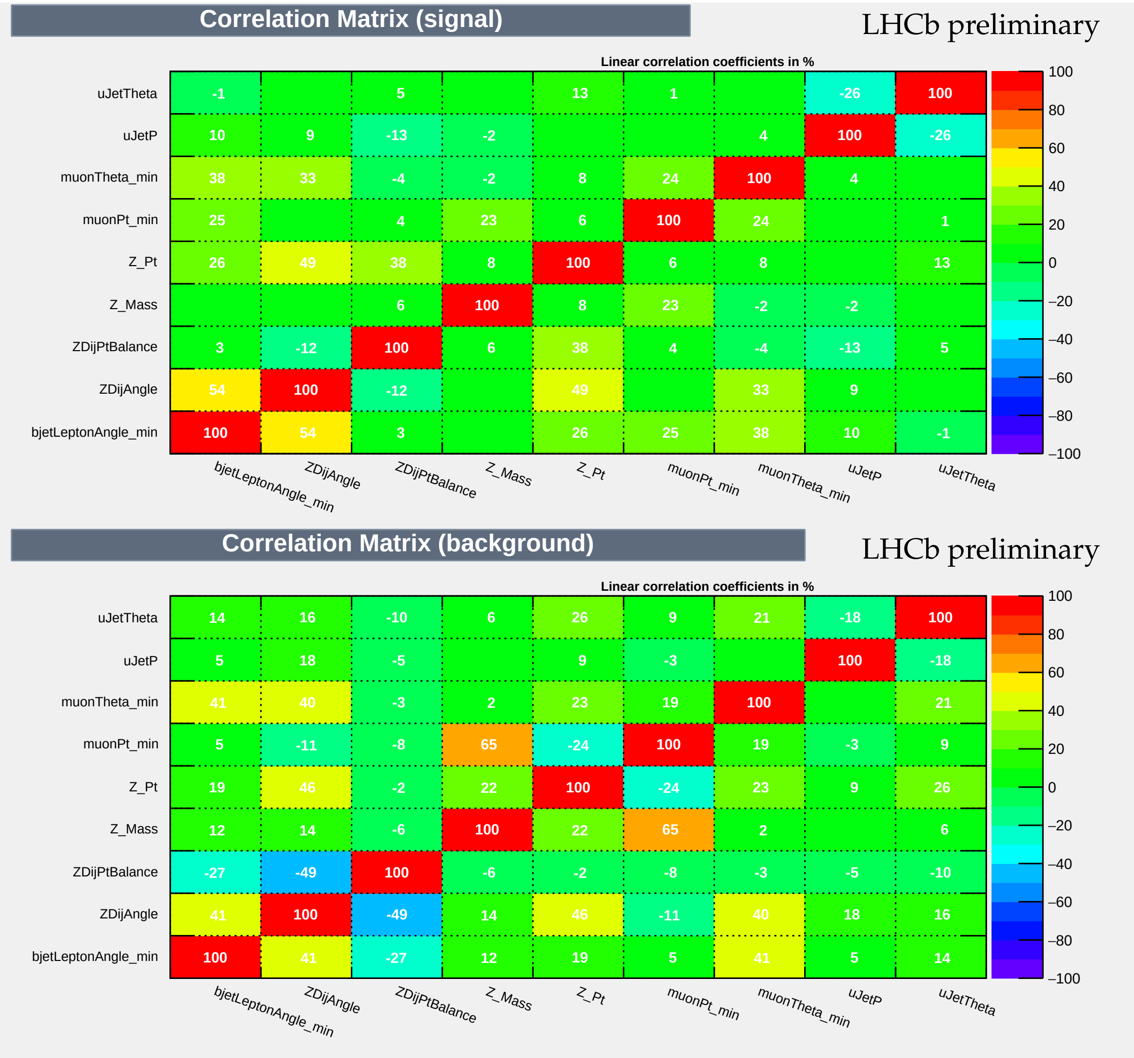

Correlation Matrix (signal)

LHCb preliminary

Linear correlation coefficients in %

	bjetLeptonAngle_min	ZDijAngle	ZDijPtBalance	Z_Mass	Z_Pt	muonPt_min	muonTheta_min	uJetP	uJetTheta
uJetTheta	-1		5		13	1		-26	100
uJetP	10	9	-13	-2			4	100	-26
muonTheta_min	38	33	-4	-2	8	24	100	4	
muonPt_min	25		4	23	6	100	24		1
Z_Pt	26	49	38	8	100	6	8		13
Z_Mass			6	100	8	23	-2	-2	
ZDijPtBalance	3	-12	100	6	38	4	-4	-13	5
ZDijAngle	54	100	-12		49		33	9	
bjetLeptonAngle_min	100	54	3		26	25	38	10	-1

Correlation Matrix (background)

LHCb preliminary

Linear correlation coefficients in %

	bjetLeptonAngle_min	ZDijAngle	ZDijPtBalance	Z_Mass	Z_Pt	muonPt_min	muonTheta_min	uJetP	uJetTheta
uJetTheta	14	16	-10	6	26	9	21	-18	100
uJetP	5	18	-5		9	-3		100	-18
muonTheta_min	41	40	-3	2	23	19	100		21
muonPt_min	5	-11	-8	65	-24	100	19	-3	9
Z_Pt	19	46	-2	22	100	-24	23	9	26
Z_Mass	12	14	-6	100	22	65	2		6
ZDijPtBalance	-27	-49	100	-6	-2	-8	-3	-5	-10
ZDijAngle	41	100	-49	14	46	-11	40	18	16
bjetLeptonAngle_min	100	41	-27	12	19	5	41	5	14

FIGURE 4.5: Linear correlation of variables used in training.

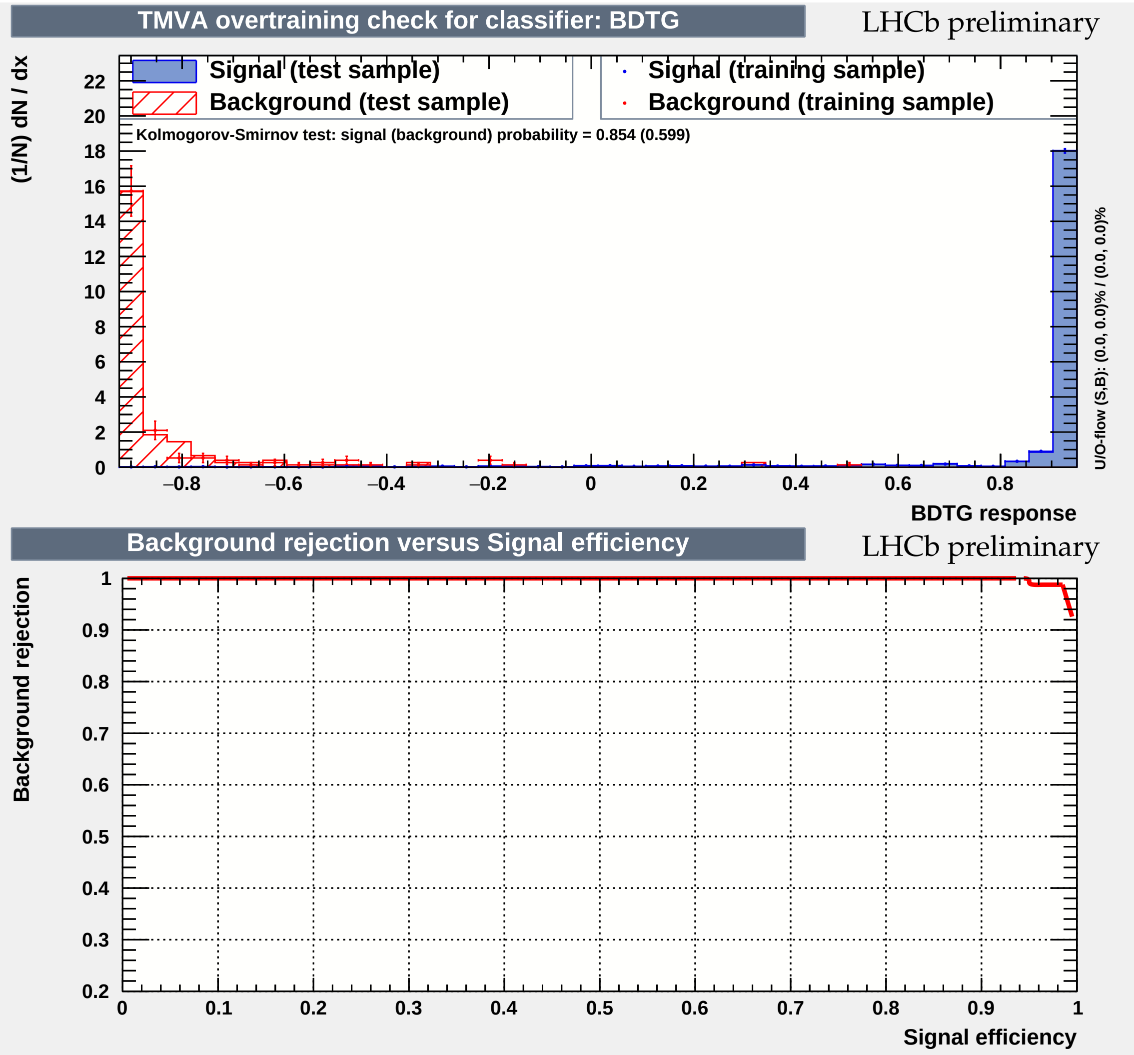

FIGURE 4.6: Response of the classifier to signal and background events in the training and testing sample (top) and the relation between background rejection and signal retention (bottom).

Rejection of type II background

The second classifier is trained to suppress the remaining contributions – the production of $t\bar{t}$ and Z^0Z^0 pairs. The distributions are formed as linear combination of both samples, with weights proportional to the expected yield after the first classifier is applied (9.2 and 2.3, respectively). The following variables are employed (generic names, which are used in figures shown below, are given in brackets and their distributions in section 4.2.3):

- invariant mass of the Z^0 boson candidate (Z_Mass)
- polar angle of the Z^0 boson candidate (Z_Theta)
- angle between the two muons (ZleptonsAngle)
- smaller of transverse momenta of the two muons (muonPt_min)
- invariant mass of the $b\bar{b}$ di-jet candidate (dijetMass)
- smaller of momenta of the two jets (bJetP_min)

- smaller of transverse momenta of the two jets (bJetPt_max)
- smallest of the four angles between the muons and jets (bjetLeptonAngle_min)
- smaller of particle multiplicity in the two jets (bJetNparticles_min)
- smaller of the BDT(b | c) classifier responses (bJetBCresponse_min)
- smaller of the BDT(bc | udsg) classifier responses (bJetHLresponse_min)
- angle between the Z^0 boson and $b\bar{b}$ di-jet candidates (ZDijAngle)
- transverse momentum of the underlying event pseudo jet (uJetPt)
- invariant mass of the underlying event pseudo jet (uJetMass)

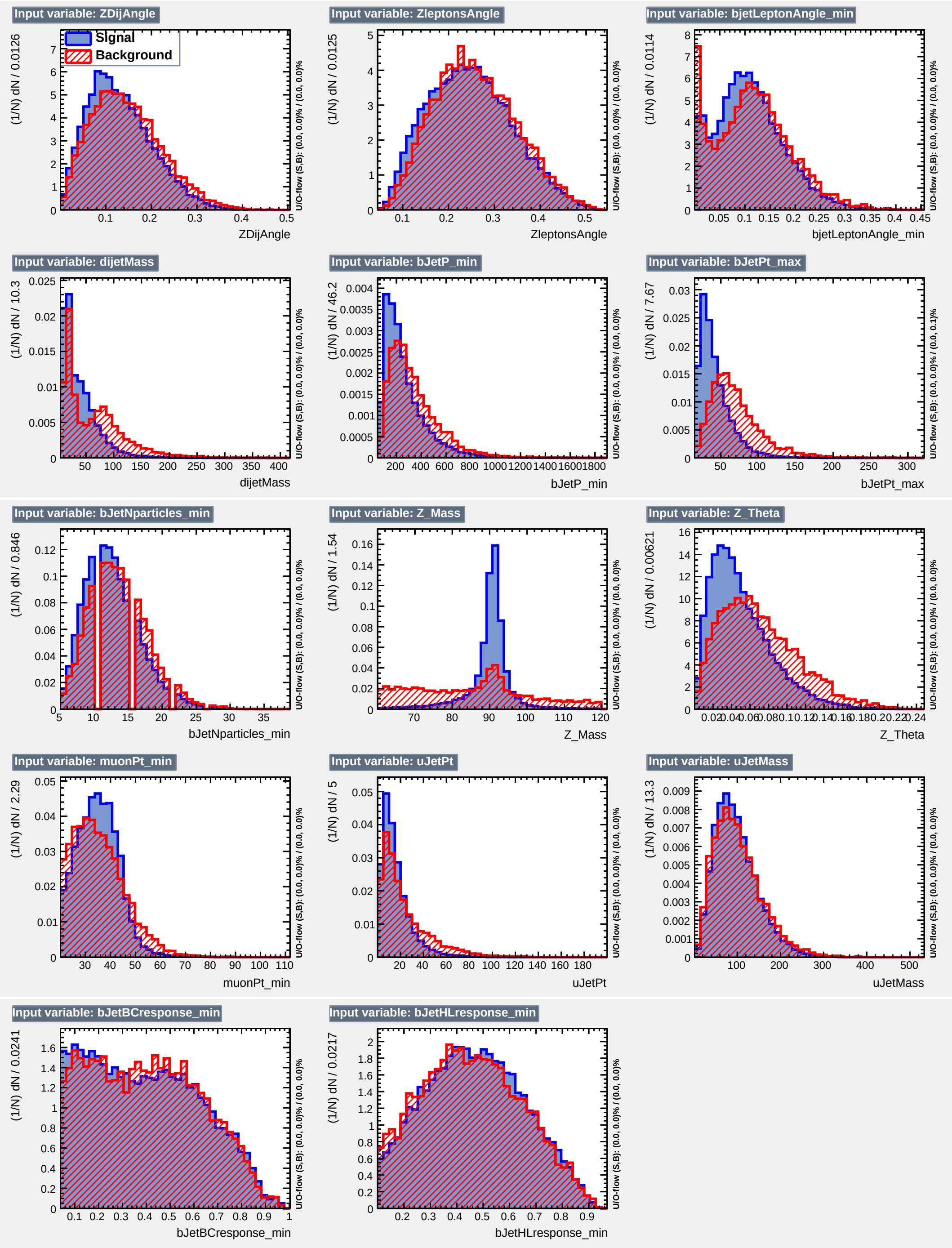

FIGURE 4.7: Variables used in training of the classifier for type II background. They are explained in the text.

Figure 4.8 shows the linear correlations of used variables. The response of the classifier and its performance are shown in fig. 4.9. The threshold is chosen as 0.2, which brings the expected yield of both background sources below one event each (fig. 4.10).

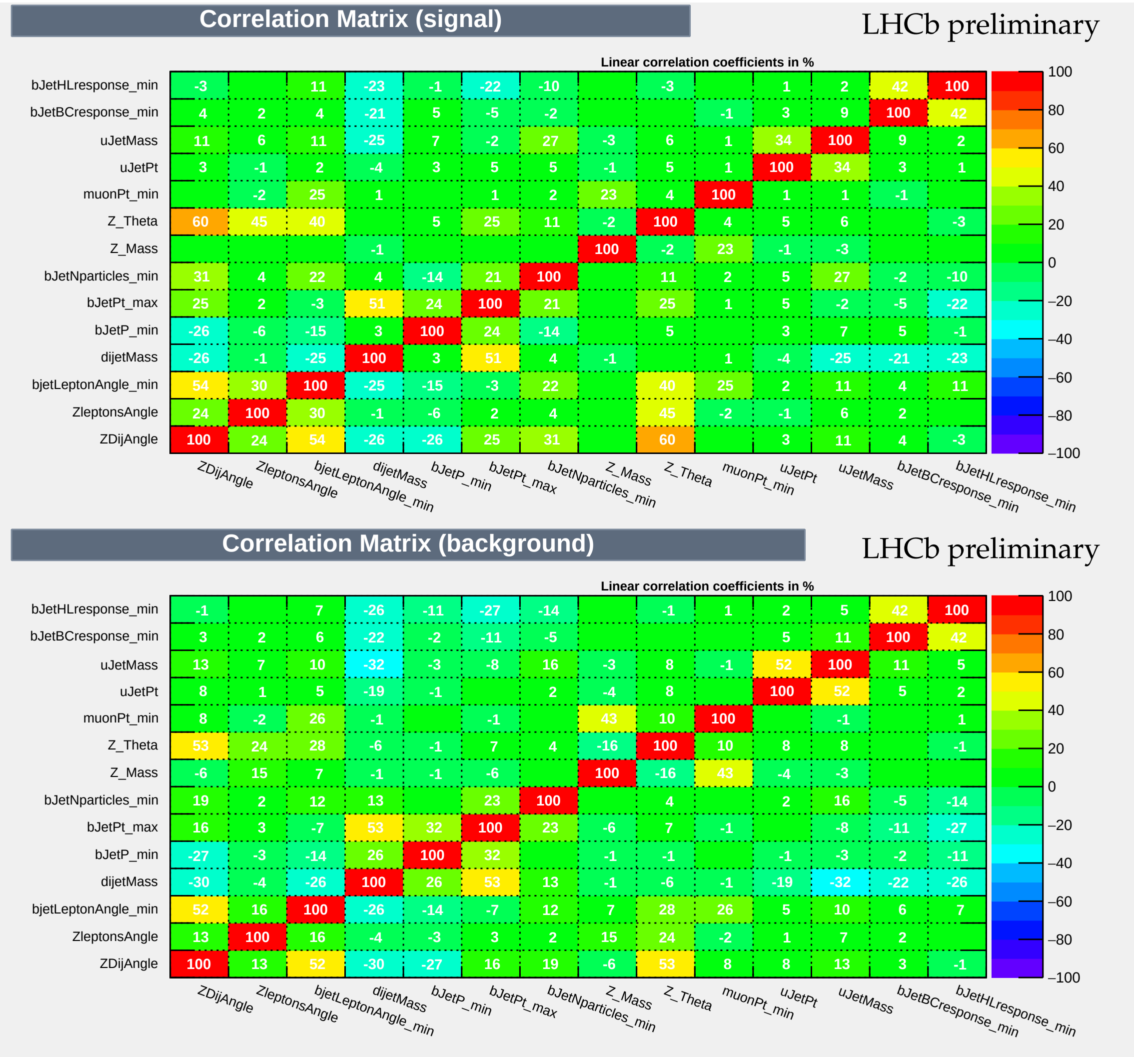

Correlation Matrix (signal)

Linear correlation coefficients in %

	ZDijAngle	ZleptonsAngle	bjetLeptonAngle_min	dijetMass	bJetP_min	bJetPt_max	bJetNparticles_min	Z_Mass	Z_Theta	muonPt_min	uJetPt	uJetMass	bJetBCresponse_min	bJetHLresponse_min
bJetHLresponse_min	-3		11	-23	-1	-22	-10		-3		1	2	42	100
bJetBCresponse_min	4	2	4	-21	5	-5	-2			-1	3	9	100	42
uJetMass	11	6	11	-25	7	-2	27	-3	6	1	34	100	9	2
uJetPt	3	-1	2	-4	3	5	5	-1	5	1	100	34	3	1
muonPt_min		-2	25	1		1	2	23	4	100	1	1	-1	
Z_Theta	60	45	40		5	25	11	-2	100	4	5	6		-3
Z_Mass				-1				100	-2	23	-1	-3		
bJetNparticles_min	31	4	22	4	-14	21	100		11	2	5	27	-2	-10
bJetPt_max	25	2	-3	51	24	100	21		25	1	5	-2	-5	-22
bJetP_min	-26	-6	-15	3	100	24	-14		5		3	7	5	-1
dijetMass	-26	-1	-25	100	3	51	4	-1		1	-4	-25	-21	-23
bjetLeptonAngle_min	54	30	100	-25	-15	-3	22		40	25	2	11	4	11
ZleptonsAngle	24	100	30	-1	-6	2	4		45	-2	-1	6	2	
ZDijAngle	100	24	54	-26	-26	25	31		60		3	11	4	-3

Correlation Matrix (background)

Linear correlation coefficients in %

	ZDijAngle	ZleptonsAngle	bjetLeptonAngle_min	dijetMass	bJetP_min	bJetPt_max	bJetNparticles_min	Z_Mass	Z_Theta	muonPt_min	uJetPt	uJetMass	bJetBCresponse_min	bJetHLresponse_min
bJetHLresponse_min	-1		7	-26	-11	-27	-14		-1	1	2	5	42	100
bJetBCresponse_min	3	2	6	-22	-2	-11	-5				5	11	100	42
uJetMass	13	7	10	-32	-3	-8	16	-3	8	-1	52	100	11	5
uJetPt	8	1	5	-19	-1		2	-4	8		100	52	5	2
muonPt_min	8	-2	26	-1		-1		43	10	100		-1		1
Z_Theta	53	24	28	-6	-1	7	4	-16	100	10	8	8		-1
Z_Mass	-6	15	7	-1	-1	-6		100	-16	43	-4	-3		
bJetNparticles_min	19	2	12	13		23	100		4		2	16	-5	-14
bJetPt_max	16	3	-7	53	32	100	23	-6	7	-1		-8	-11	-27
bJetP_min	-27	-3	-14	26	100	32		-1	-1		-1	-3	-2	-11
dijetMass	-30	-4	-26	100	26	53	13	-1	-6	-1	-19	-32	-22	-26
bjetLeptonAngle_min	52	16	100	-26	-14	-7	12	7	28	26	5	10	6	7
ZleptonsAngle	13	100	16	-4	-3	3	2	15	24	-2	1	7	2	
ZDijAngle	100	13	52	-30	-27	16	19	-6	53	8	8	13	3	-1

FIGURE 4.8: Linear correlation of variables used in training.

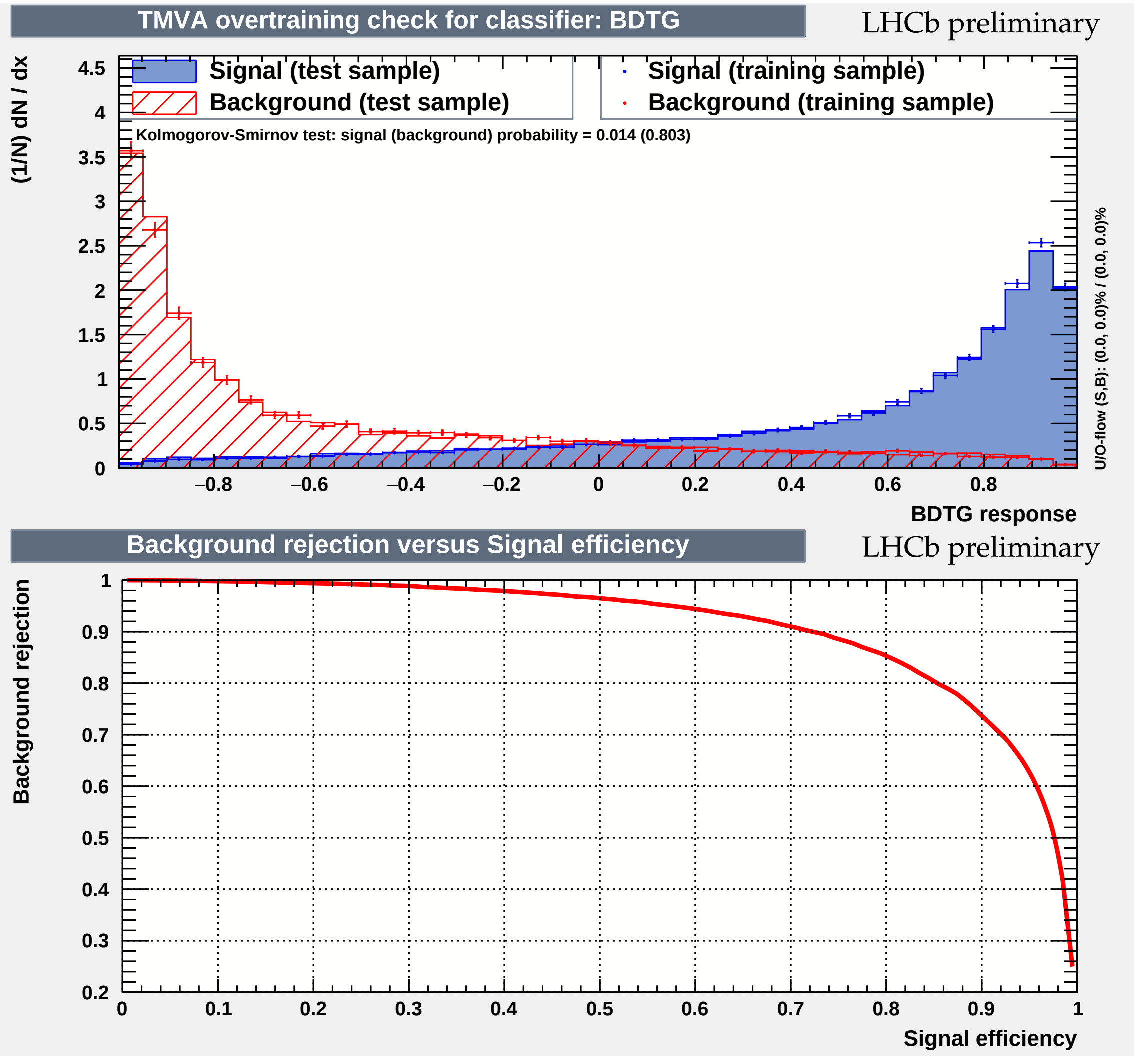

FIGURE 4.9: Response of the classifier to signal and background events in the training and testing sample (top) and the relation between background rejection and signal retention (bottom).

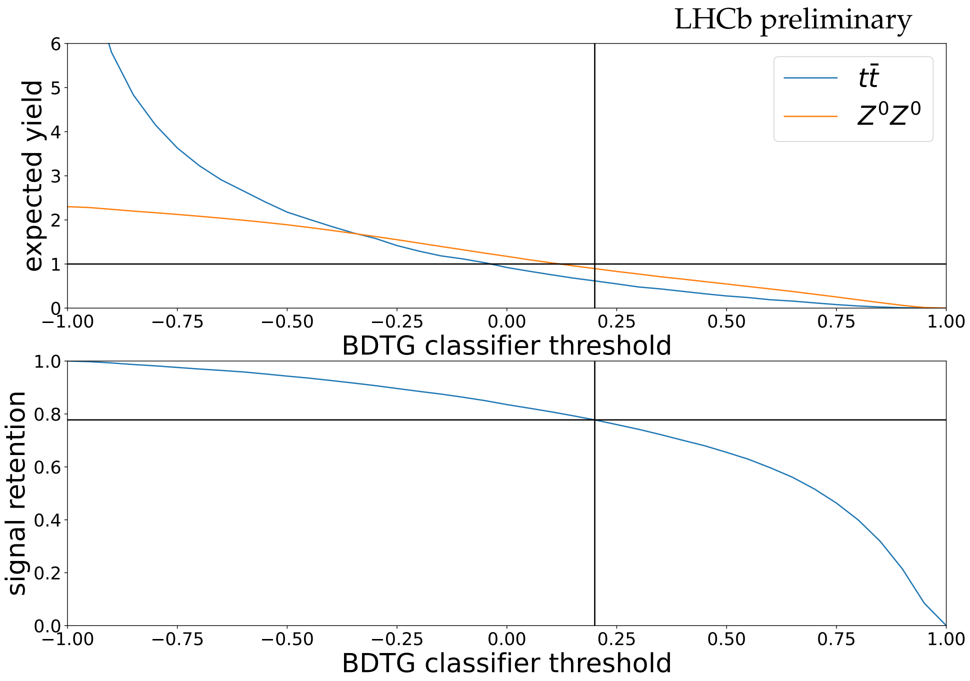

FIGURE 4.10: Expected yield of both background sources (top) and signal retention (bottom) as a function of the requirement imposed on the BDTG classifier response. Black lines show the chosen value (0.2), corresponding signal retention and a horizontal line at expected yield equal to one event.

Selection results

Applying both classifiers to the data sample yields 142 signal candidates (which still contain irreducible contribution from the production of Z^0 boson with a pair of light quarks). The signal retention, evaluated in the simulated $Z^0b\bar{b}$ sample, is 0.7246(55). The distributions of Z^0 and $b\bar{b}$ candidates' invariant masses, after the full selection and rejection of type I and II backgrounds, are shown in figs. 4.11 and 4.12. The same figures illustrate also the shapes of these distributions in a simulated $Z^0b\bar{b}$ signal sample.

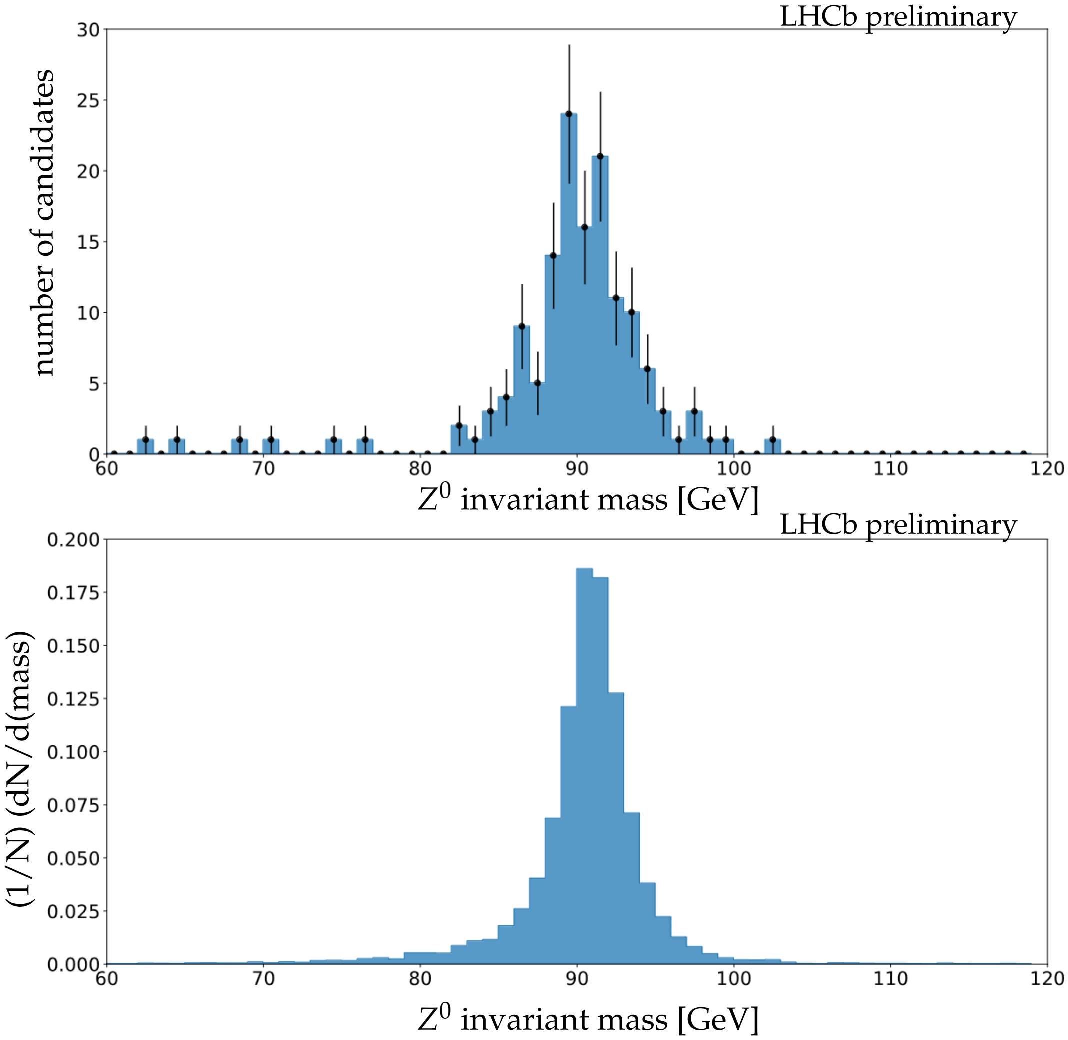

FIGURE 4.11: Invariant masses of reconstructed Z^0 boson candidates in data (top) and in simulated $Z^0 b\bar{b}$ signal sample (bottom). The uncertainties are statistical. The candidates reconstructed in data may still contain background contributions.

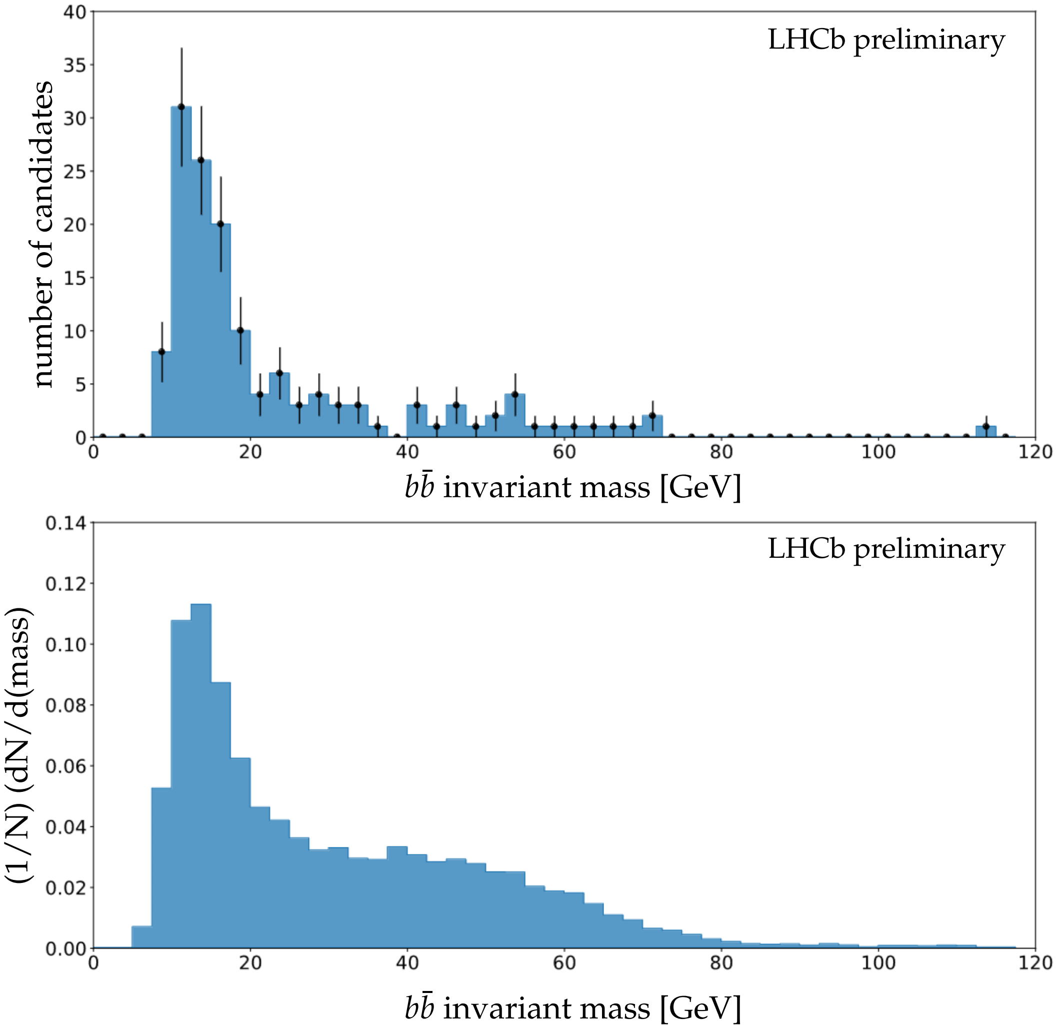

FIGURE 4.12: Invariant masses of reconstructed $b\bar{b}$ di-jet candidates in data (top) and in simulated $Z^0b\bar{b}$ signal sample (bottom). The uncertainties are statistical. The candidates reconstructed in data may still contain background contributions.

4.2.4 Signal yield and purity

The 142 signal candidates, which remain after selection and background rejection, are still dominantly events with a Z^0 boson and quarks lighter than b. This background source is irreducible without also rejecting most of the signal and, consequently, the signal yield has to be extracted using a template fitting technique. Furthermore, simulation of this process is not available in the LHCb experiment at present and local production is unfeasible, due to the large number of generated events required to overcome the low reconstruction efficiency. For this reason, the background is temporarily modelled with an inclusive production of $q\bar{q}$ pairs. Even though the fit is performed in the $b\bar{b}$ candidate invariant mass, which should not be strongly impacted by the lack of a Z^0 boson, the lack of variables related to Z^0 kinematics makes the application of background rejecting classifiers impossible. This in turn introduces bias, which is evaluated as contribution to the systematic uncertainty in the next section.

As discussed throughout the chapter, the $q\bar{q}$ sample is binned in the transverse momentum of both quarks to counteract the large difference in corresponding cross-sections. Each bin is processed independently. Initially, the preselection requires at least 2 reconstructed jets present. From the remaining events, those which contain beauty hadrons (i.e. are $b\bar{b}$ production events) are removed using Monte Carlo information. The $b\bar{b}$ di-jet candidate is then reconstructed as described in section 4.2.2. The invariant mass template is created by adding distributions from each bin with weights proportional to the corresponding production cross-section, acceptance, preselection and final selection efficiency. Table 4.8 lists the weights assigned to each bin, normalised to the highest value. Combined with background rejection classifiers (which should impact each bin differently) not applied, they introduce another source of bias and systematic uncertainty. The resulting templates of $b\bar{b}$ di-jet invariant mass are shown in fig. 4.13.

p_T 10-15 GeV	0.8258
p_T 15-20 GeV	0.5459
p_T 20-50 GeV	1
p_T above 50 GeV	0.0934

TABLE 4.8: The weights assigned to each bin of inclusive $q\bar{q}$ sample.

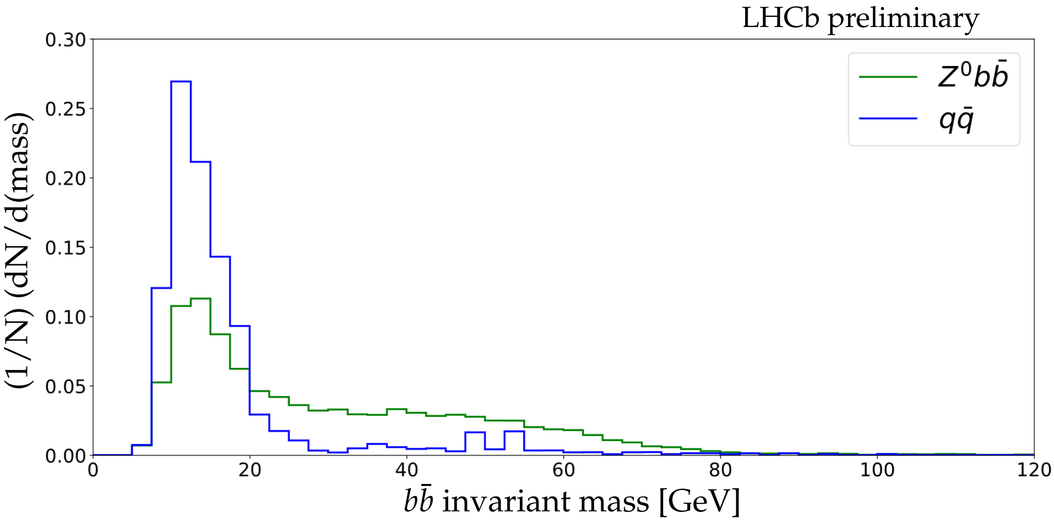

FIGURE 4.13: Templates of $b\bar{b}$ di-jet invariant mass used in the fit.

The template fit is performed by minimising the expression:

$$\chi^2 = \sum_{\text{bins}} \frac{\left[\text{data}_i - \left(S \cdot Z^0 b\bar{b} + B \cdot q\bar{q}\right)_i\right]^2}{\sigma^2_{\text{data},i}}, \tag{4.3}$$

where the first term in the numerator is the number of data candidates in the i-th bin and second – in the i-th bin of a weighted sum of signal and background templates. σ_{data} is a Poissonian error, calculated as the square root of the data bin.

Both templates are normalised to the sample size, hence S and B correspond directly to the number of signal and background events, respectively. Figure 4.14 shows fit results, where the number of $Z^0 b\bar{b}$ signal events among data candidates is evaluated as 50.8 ± 5.3.

Signal purity is determined in a simulated sample after full reconstruction and selection. Both muons are required to come from the generated Z^0 boson and both jets to contain products of beauty hadron decays among the assigned particles. The fraction of signal events fulfilling these criteria is found to be 0.9776(53).

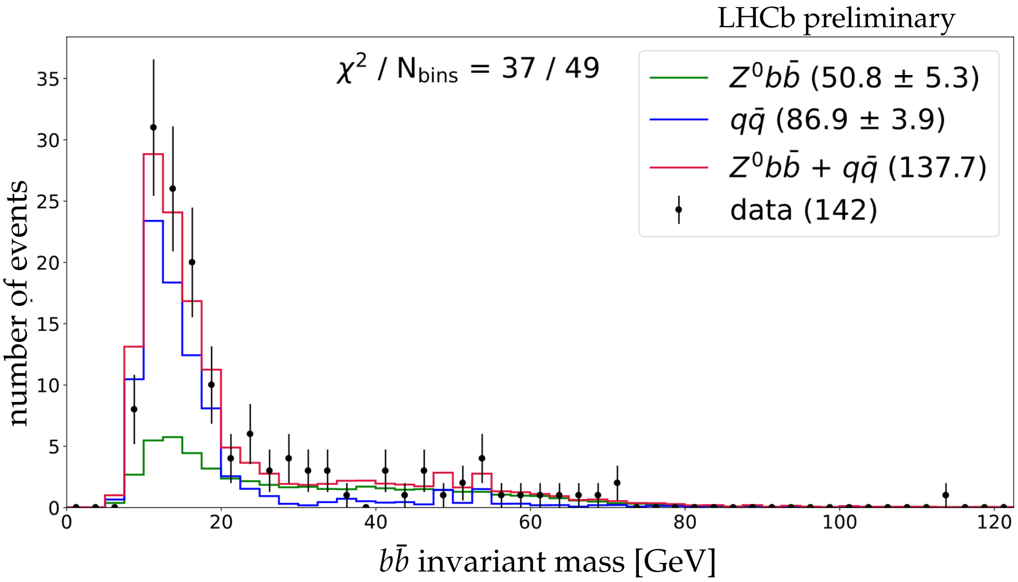

FIGURE 4.14: Fit of the $b\bar{b}$ di-jet invariant mass templates to the corresponding distribution of reconstructed candidates. Numbers in brackets indicate the resulting number of events.

4.2.5 $Z^0 b\bar{b}$ production cross section

The $Z^0 (\to \mu^- \mu^+) b\bar{b}$ production cross-section is calculated by normalising the signal yield in data to the total efficiency, determined using Monte Carlo simulation, and the collected luminosity. That is:

$$\sigma_{Z^0(\to\mu^-\mu^+)b\bar{b}} = \frac{P \cdot N}{\epsilon_{\text{acceptance}} \cdot \epsilon_{Z^0 b\bar{b}} \cdot \epsilon_{\text{BDTG}} \cdot \mathcal{L}} = 70.70 \pm 0.74 \text{ pb}, \tag{4.4}$$

where the uncertainty is statistical, P is the signal purity, N signal yield, $\mathcal{L}$ the integrated luminosity and the total efficiency is a product of the detector acceptance efficiency (including generator level requirements) $\epsilon_{\text{acceptance}}$, the final $Z^0 b\bar{b}$ signal selection efficiency, $\epsilon_{Z^0 b\bar{b}}$, and signal retention in the background rejection procedure

– ϵ_{BDTG}. The corresponding values are:

$$\begin{aligned} P &= 0.9776(53) && (4.5)\\ N &= 50.8 \pm 5.3 \text{ events} && (4.6)\\ \epsilon_{\mathrm{acceptance}} &= 0.041894(29) && (4.7)\\ \epsilon_{Z^0 b\bar{b}} &= 0.003858(18) && (4.8)\\ \epsilon_{\mathrm{BDTG}} &= 0.7246(55) && (4.9)\\ \mathcal{L} &= 5997.9 \pm 120.0\ \mathrm{pb}^{-1}, && (4.10) \end{aligned}$$

where the uncertainties on N and $\mathcal{L}$ are systematic and the rest are statistical. Both kinds are discussed in detail in the subsections below.

Statistical uncertainty

The sources of statistical uncertainty are the determination of signal purity and the three selection efficiencies (from detector acceptance, reconstruction of the $Z^0 b\bar{b}$ candidates and background rejection classifiers). Their impact on the calculated production cross-section is summarised in table 4.9, below.

source	$\Delta\sigma_{Z^0(\rightarrow\mu^-\mu^+)b\bar{b}}$ [%]
signal purity	0.54
detector acceptance	0.07
$Z^0 b\bar{b}$ selection	0.47
BDTG selection	0.76
total	1.05

TABLE 4.9: Summary of statistical uncertainties.

Systematic uncertainty

The systematic uncertainty is evaluated only partially, as some contributions require proper treatment of the light quark background to be studied in detail. Currently, the main source of systematic uncertainty is the modelling of a $Z^0 q\bar{q}$ background with $q\bar{q}$ pair production, which – apart from slightly different jet kinematics in both samples – does not allow selection for the Z^0 boson candidates and application of BDTG classifiers. The consequence is a bias in the invariant mass template and a significant overestimation of the signal yield. While the issue will be solved once the Monte Carlo simulation of a $Z^0 q\bar{q}$ process becomes available, for the purpose of the thesis a very conservative estimate of the corresponding uncertainty is given instead. It is obtained by repeating the template fitting procedure (see section 4.2.4) many times, while varying each background bin by a uniformly random amount within 30% of its size. The uncertainty of signal yield is then taken to be three standard deviations of the resulting distribution (illustrated in fig. 4.15), which is approximately Gaussian. Other sources related to the determination of signal yield (e.g. number of events used to create templates, binning and fit ranges) have the same impact as varying the bin size and are thus assumed to be included in this uncertainty.

The reconstruction of a Z^0 boson introduces three sources of systematic uncertainty. The first is a result of the initial selection for $Z^0 \rightarrow \mu^-\mu^+$ decay candidates being performed before a detector level alignment and is found to be negligible. The second is related to triggering on and selecting muons with high transverse momenta. It is studied using a tag-and-probe method, with tag being a track that was fully reconstructed and identified as muon and probes – the tracks reconstructed using only hits in the muon stations. Finally, the uncertainty of reconstructing a full Z^0 boson candidate is studied by comparing a subset of simulated events with the same events corrected for previously determined uncertainties. Both are calculated for inclusive $Z^0 \to \mu^-\mu^+$ events and then scaled by a ratio of the signal yield to the total number of reconstructed $Z^0 \to \mu^-\mu^+$ candidates (50.8/872133), to evaluate the impact on a $Z^0\,(\to \mu^-\mu^+)\,b\bar{b}$ cross-section.

Likewise, several sources of systematic uncertainties related to $b\bar{b}$ di-jet reconstruction are considered. The selection based on jet identifying classifiers changes primarily the ratio of $Z^0b\bar{b}$ and $Z^0q\bar{q}$ (with $q \neq b$) contributions among the final set of data candidates. Since both are accounted for in the template fitting procedure, it is considered to be a part of the background modelling uncertainty and not included here. The remaining uncertainty is evaluated by varying the transverse momentum requirement by ±10% and the minimum number of assigned particles by ±1. The requirement on jet momentum is found to have no impact and is omitted. This uncertainty is at present overestimated, because the looser selection extends the kinematic range of $Z^0q\bar{q}$ background to a region where the quality of modelling it with $q\bar{q}$ production significantly worsens.

The next source is the selection based on BDTG classifiers, which implicitly includes the uncertainties related to reconstruction of jet parameters (e.g. jet energy resolution) used as training variables. The contribution to systematic uncertainty is determined by varying the requirements on both responses simultaneously by ±0.1 and repeating the analysis. Finally, the luminosity measurement has a constant uncertainty of 2%. Table 4.10 summarises all systematic uncertainties.

source	$\Delta\sigma_{Z^0(\to\mu^-\mu^+)b\bar{b}}$ [%]
$Z^0q\bar{q}$ background modelling	30.25
muon selection	1.04
Z^0 candidate selection	0.31
$b\bar{b}$ candidate selection	21.85
BDTG selection	3.63
luminosity measurement	2.00
total	37.56

TABLE 4.10: Summary of systematic uncertainties.

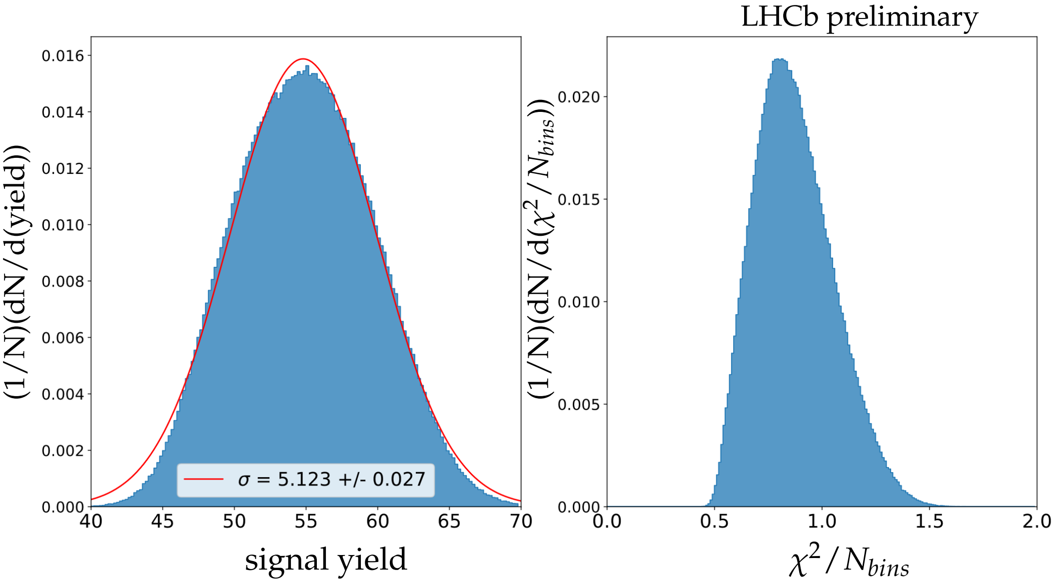

FIGURE 4.15: Distribution of signal yields obtained by repeating the template fitting procedure many times, while varying each bin randomly by up to 30% (left) and the corresponding mean fit χ^2 per bin of the di-jet invariant mass (right).

4.3 Summary and conclusions

The analysis extends measurements of the $Z^0b\bar{b}$ production cross-section, performed by ATLAS and CMS experiments (see section 2.5.2), to the complementary forward region available to the LHCb detector ($2 < \eta < 4.5$, see section 3.3). The study is performed in the $Z^0 \rightarrow \mu^-\mu^+$ decay channel, using approximately 6 fb^{-1} of proton-proton data collected at the centre of mass energy of 13 TeV. A high quality Z^0 boson candidate is reconstructed, using oppositely charged muons with high transverse momenta. Requirements imposed on the $b\bar{b}$ di-jet are kept loose to counteract the low expected signal yield, while ensuring that all considered processes are correctly represented by Monte Carlo event generators. Background contributions are suppressed with a multivariate analysis based on Boosted Decision Tree classifiers. The irreducible $Z^0q\bar{q}$ source (with $q \neq b$) is accounted for by extracting signal yield with a template fit in the $b\bar{b}$ di-jet invariant mass distribution.

Due to the unavailability of $Z^0q\bar{q}$ Monte Carlo simulation, the corresponding template is temporarily modelled with an inclusive $q\bar{q}$ production, where events containing beauty hadrons are removed. As a result, the signal yield and measured cross-section may be overestimated. Nevertheless, the value of $\sigma_{Z^0(\rightarrow\mu^-\mu^+)b\bar{b}}$ is preliminarily evaluated as 70.70 ± 26.56 (syst.) $\pm\, 0.74$ (stat.) pb, with the systematic uncertainty being strictly dominated by the $Z^0q\bar{q}$ template modelling. While it is compatible with the Next-to-Leading Order cross-section reported by MadGraph5 event generator (45.13(23) pb, see table 4.3), any further conclusions (i.e. investigation of possible BSM contributions or compatibility with 4 and 5 flavour scheme calculations, see section 2.4) require a more precise determination of the background contribution. Once the simulation of a $Z^0q\bar{q}$ process becomes available in the LHCb experiment, the signal yield will be reevaluated and cross-section recalculated.

Chapter 5

Compact Linear Collider

5.1 Introduction

Outside of very novel ideas (like a muon collider), the concepts of LHC successors fall into two main categories. Circular machines offer much higher energies of hadron collisions, as particles can be accelerated gradually while travelling around the ring. Their major disadvantage, however, is a difficult experimental environment, caused by the multi-jet background from quark interactions. Circular electron and positron colliders are also possible, but the achievable energy is significantly lower due to the enormous radiation emitted when their trajectories are bent in a magnetic field. The main candidate in this category is the Future Circular Collider (FCC, [147, 148]), which would be located close to the LHC and have a circumference of about 90 kilometres (which allows reaching energies close to 100 TeV for proton-proton collisions and about 350 GeV for electron-positron). The alternative are linear electron-positron colliders, which produce very clean interactions at energies restricted by their length. Although these energies are relatively low, compared to hadron collisions at circular colliders, the limited background could make various exotic decay signatures possible to detect, if they are available at that energy scale. Moreover, they would provide increased sensitivity to indirect searches for BSM phenomena by very precise measurements of the SM predictions (in particular in the Higgs boson sector, which remains mostly unexplored). Currently, the leading project and competitor to the FCC is the Compact Linear Collider (CLIC, [8]), which would be located at the LHC complex, crossing the collider ring (fig. 5.1). It is planned to provide e^+e^- data at the centre of mass energies of 380 GeV, 1 TeV and 3 TeV, which correspond to different Higgs boson production mechanisms and the energy frontier of e^+e^- collisions. A short run at centre-of-mass energy of 350 GeV may also be considered, with the aim to precisely measure the mass of a top quark.

The concept of the CLIC detector is a direct evolution of two previous designs, envisioned initially as candidates for the International Linear Collider – the International Linear Detector (ILD, [149]) and Silicon Detector (SiD, [150]). The ILD was planned to provide a better performance of jet reconstruction by having the calorimetry system moved radially outwards (increasing the spatial separation of particles reaching it). The SiD was designed as a much more compact and cost-effective alternative. They differ enough to warrant the existence of two corresponding models, named CLIC_ILD and CLIC_SiD [8]. Both share the cylindrical geometry and are modified with respect to the original designs, in order to account for the higher centre-of-mass energy and lower time between consecutive bunch crossings. The study presented in the thesis focuses on the CLIC_ILD detector model, as it is the primary candidate. The CLIC_ILD detector model is described in section 5.3, while the preceding section 5.2 gives an overview of the CLIC accelerator.

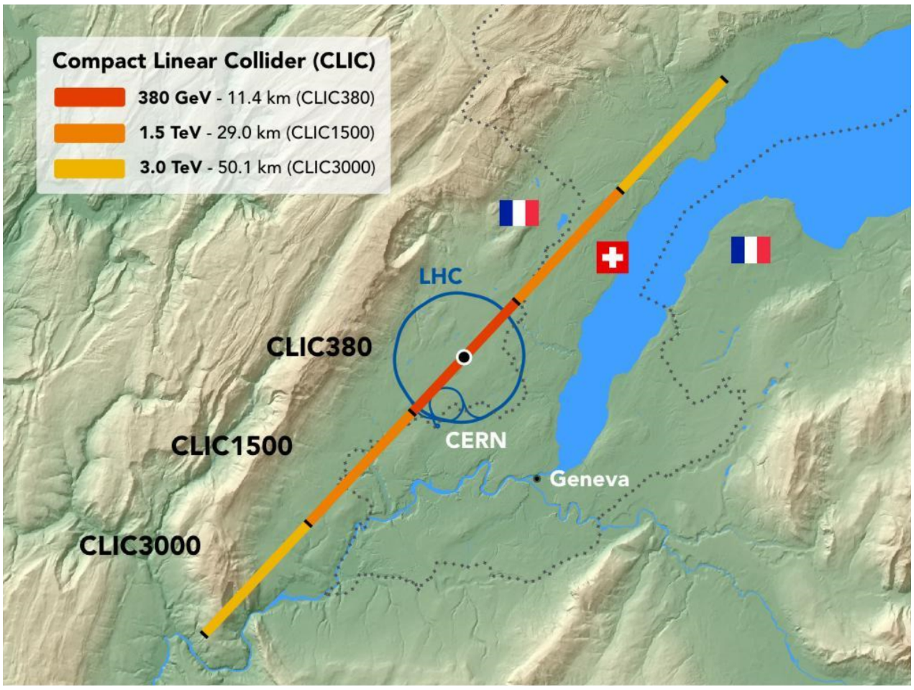

FIGURE 5.1: Outline of CLIC accelerator. Figure taken from [151].

5.2 Accelerator

In order to match the physics program, the CLIC accelerator will be built in three stages (figs. 5.1 and 5.2), spanning about 35 years. Each will be prepared and constructed during the operation of the preceding one, in order to minimise downtime. The exact operating conditions are still being optimised and are subject to change, but approximately 1 ab^{-1} of integrated luminosity is planned to be delivered at the centre-of-mass energy of 380 GeV, 2.5 ab^{-1} at 1.5 TeV and 5 ab^{-1} at 3 TeV [152].

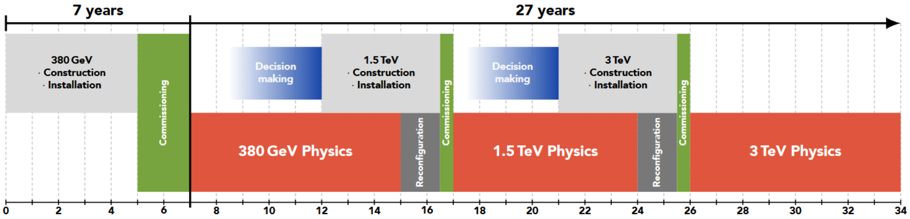

FIGURE 5.2: Timeline of CLIC development and operation. Figure taken from [151].

The first two stages use the same design of the beam complex (fig. 5.3, top), with different lengths of the main accelerator pipe. Achieving 380 GeV collision energy requires about 11.4 kilometre long tunnel, assuming the accelerating gradient of 72 MV/m. The gradient will be increased to 100 MV/m for the second stage, allowing to increase the collision energy by a factor of four, while requiring only three times larger length (about 29 kilometres). The initial electron beams will be produced using direct current (DC) electron guns, with one of them accelerated to 200 MeV. The other will be accelerated to 5 GeV and collided with a crystal to produce high energy photons, which subsequently hit a tungsten target and produce positrons. Both beams will then be brought up to 2.86 GeV by a common linear accelerator and sent into superconducting wigglers (two in case of positrons), to reduce the synchrotron radiation. They will then be accelerated to 9 GeV and injected into the main pipe.

The main accelerator pipe is symmetric with respect to the interaction point and uses a series of radio-frequency cavities. In order to generate the required gradient reliably and in a cost-effective way, the cavities are powered by a dedicated drive beam complex. It uses an independent electron beam, accelerated by klystrons, which is fed into a series of decelerators where the energy is transferred to the main accelerator through waveguides. The step-up to 3 TeV collision energy is achieved primarily by the introduction of a second complex (fig. 5.3, bottom), which significantly reduces the needed increase in length.

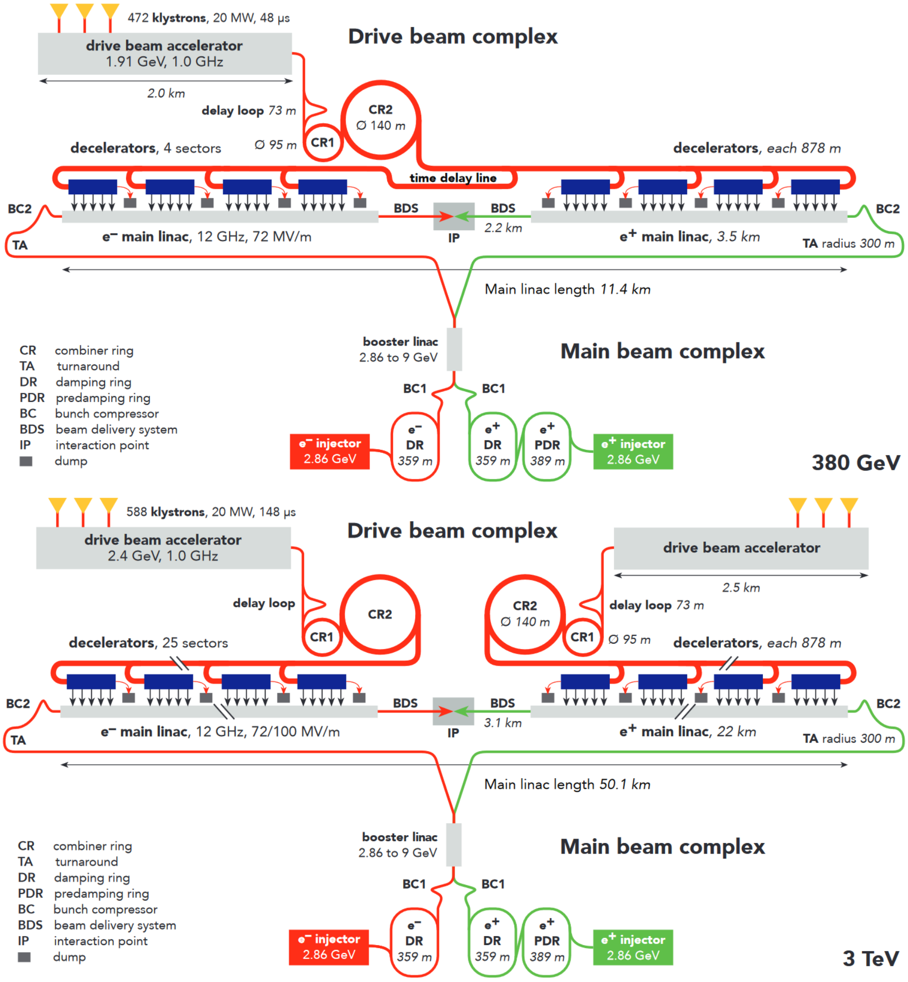

FIGURE 5.3: Accelerator configuration in the first and second (top) and the last (bottom) stage of operation. Figure taken from [151].

5.3 CLIC_ILD detector model

The CLIC_ILD detector model uses a General Purpose Detector geometry, providing a 4π coverage of the interaction point (fig. 5.4). The tracking system is a mix of silicon based vertex detector (VTX) and a time projection chamber (TPC), complemented with more silicon sensors. The calorimetry system comprises an electromagnetic calorimeter (ECAL) and two types of hadronic calorimeters (HCAL), which differ in material density due to space limitations in the barrel. The detector is surrounded by an iron yoke, interleaved with muon chambers, and has a magnet system producing a 4T field. Additionally, the forward region contains a luminosity and beam calorimeters, providing an on-the-fly measurement of the former and extending the angular acceptance down to 10 mrad. Because of the clean experimental environment and relatively low interaction rate, the detector does not require a triggering system and all events can be saved with a continuous readout.

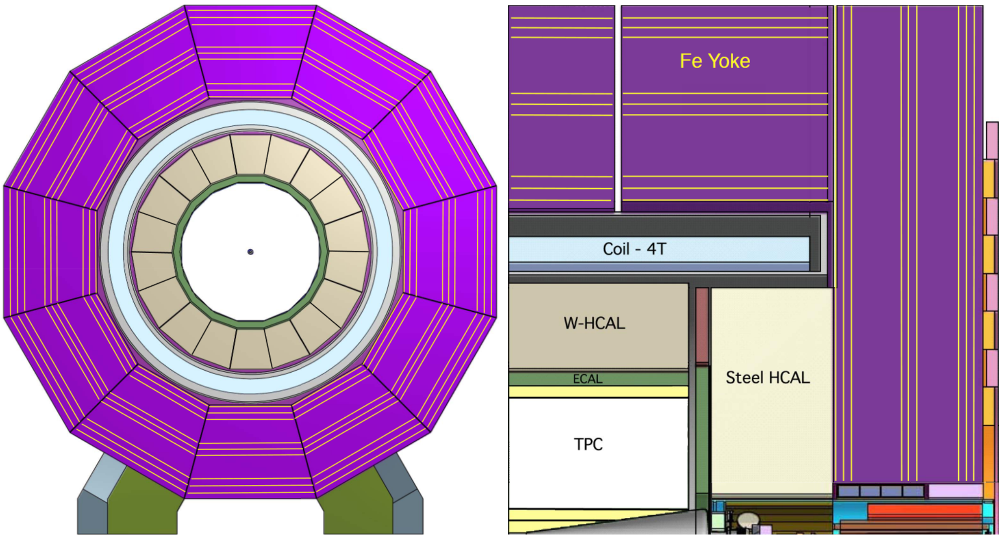

FIGURE 5.4: The transversal (left) and longitudinal (right, only one of the top quadrants is shown) cross-section of the CLIC_ILD detector model. Figure taken from [8].

5.3.1 Tracking system

The primary role of the vertex detector is the reconstruction of displaced secondary vertices from beauty and charm hadron decays, which allows for an effective identification of particle jets originating from heavy quarks. Consequently, the system provides a very precise measurement of the impact parameter and initial input for track reconstruction algorithms. It comprises six double-layer tracking planes (half of which are located around the beam pipe and the rest alongside, see fig. 5.5), which extend from approximately 30 to 60 millimetres radially and from 160 to 255 millimetres along the beam axis. All six are based on a silicon pixel technology with an active thickness of about 50 micrometres and a 20-by-20 micrometre pitch, resulting in a 2.8 micrometre spatial resolution. The resolution of the transverse impact parameter varies significantly with polar angle, being best for particles passing through layers in the barrel. Figure 5.6 illustrates this dependence for different momenta, assuming a full and simplified (fast) detector simulation. It is parameterised as $\sigma\left(d_0\right) = \sqrt{a^2 + \frac{b^2}{p^2 \sin^3\theta}}$, where p is the momentum, θ polar angle and the second term corresponds to a multiple scattering contribution. The detector model allows to achieve values of $a \leq 5$ micrometres and $b \leq 15$ micrometres $\cdot$ GeV.

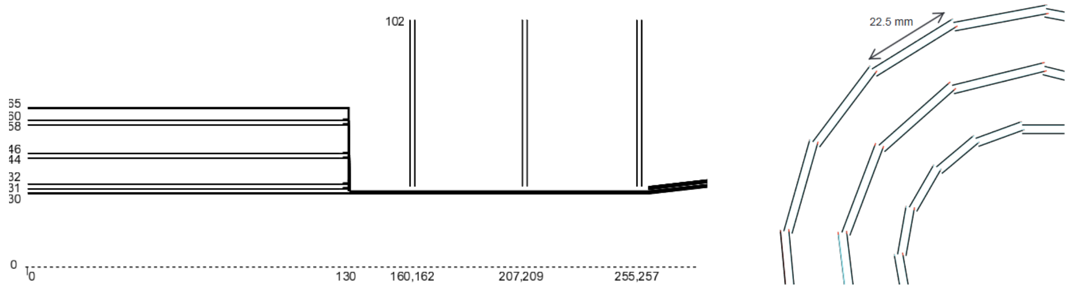

FIGURE 5.5: Vertex detector layout in the ZR (left) and XY (right) plane. Figure taken from [8].

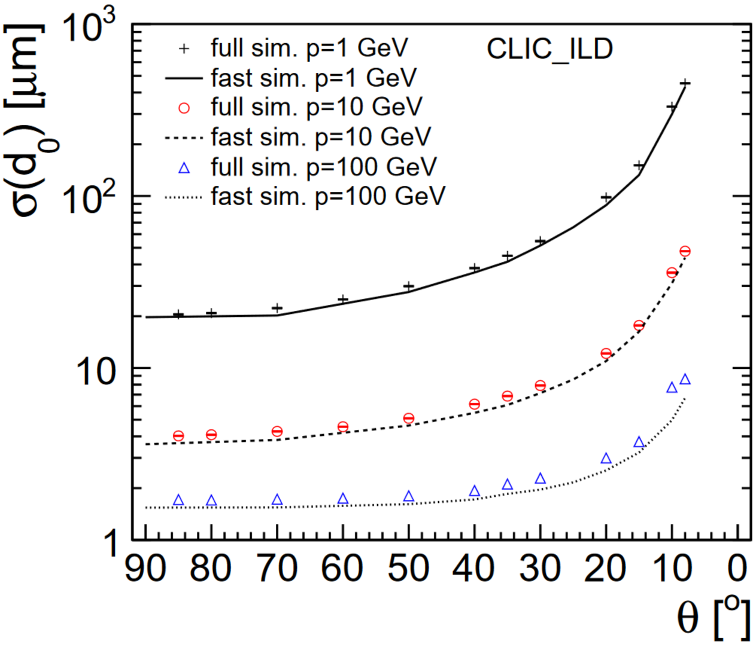

FIGURE 5.6: Simulated resolution of the transverse impact parameter, as a function of the polar angle θ, for particles with 1, 10 and 100 GeV momentum. Figure taken from [8].

Further information required for track reconstruction and identification of charged particles is provided by a gaseous Time Projection Chamber, complemented with a series of silicon detectors (fig. 5.7). The Silicon Internal Tracker (SIT1 and SIT2) is located in the barrel and supplies additional hits, which connect those from the VTX with measurements of TPC (for tracks at polar angles above approximately 26 degrees). A similar role is fulfilled by the Silicon External Tracker (SET), which improves the momentum resolution and introduces a position measurement right before the ECAL. Both use the same silicon strip layout, with the approximate measurement resolution of 7 micrometres in the RΦ plane and 50 micrometres along the beam axis. The forward side of TPC is covered with an Endcap Tracking Disk (ETD), comprising three layers rotated by a stereo angle of 60 degrees with respect to each other. Their combined spatial resolution is about 5.8 micrometres. Position measurement for tracks close to the beam pipe (down to 7 degrees) is provided by Forward Tracking Detectors (FTD), which comprise a series of 5 tracking planes (each with a resolution of 7 micrometres in the RΦ plane). The one closest to the interaction point is expected to use pixel technology, due to high background rates.

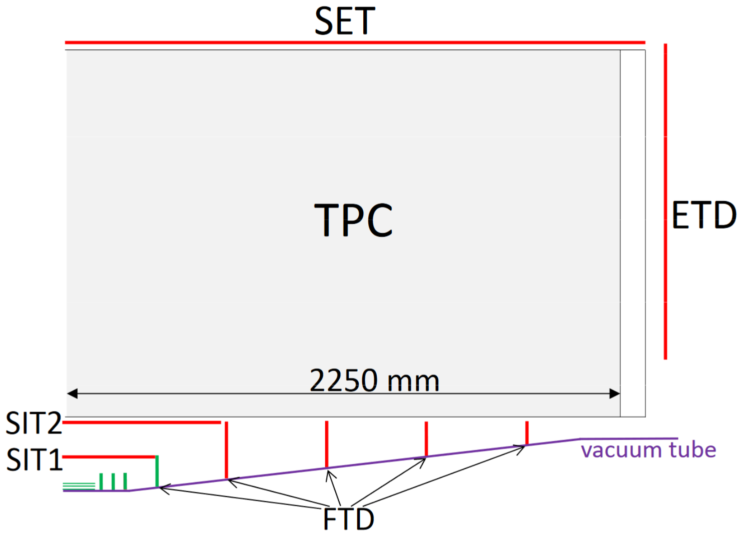

FIGURE 5.7: A schematic view of the tracking system layout with the time projection chamber (TPC) and complementary pixel (green) and strip (red) silicon sensors. Figure taken from [8].

The TPC chamber is filled with a mixture of Ar, CF_4 and iC_4H_{10} (in a 95:3:2 ratio) and covers polar angles from 12 to 168 degrees, with approximately 200 measurement points between 35 and 145 degrees and 10 outside this range. A continuous measurement allows for a very precise reconstruction of the decay vertices of long-lived particles and reliable particle identification by determining the specific energy loss (above 95% efficiency for charged leptons, when combined with information from other systems). Furthermore, combined with the strong magnetic field, the TPC provides a very good resolution of the transverse momentum measurement. It is effectively constant for particles with transverse momenta above 100 GeV, although depends on the polar angle (decreasing significantly for tracks outside the barrel region). Figure 5.8 illustrates these dependencies measured with single muons. A $\sigma\left(\Delta p_T/p_T^2\right) = a + \frac{b}{p_T}$ parameterisation is used, where the first term corresponds to the track curvature measurement and the second is due to multiple scattering. The achieved resolution below $2 \cdot 10^{-5}$ allows for a very precise determination of the Higgs boson mass in a Higgsstrahlung process ($e^+e^- \to HZ$).

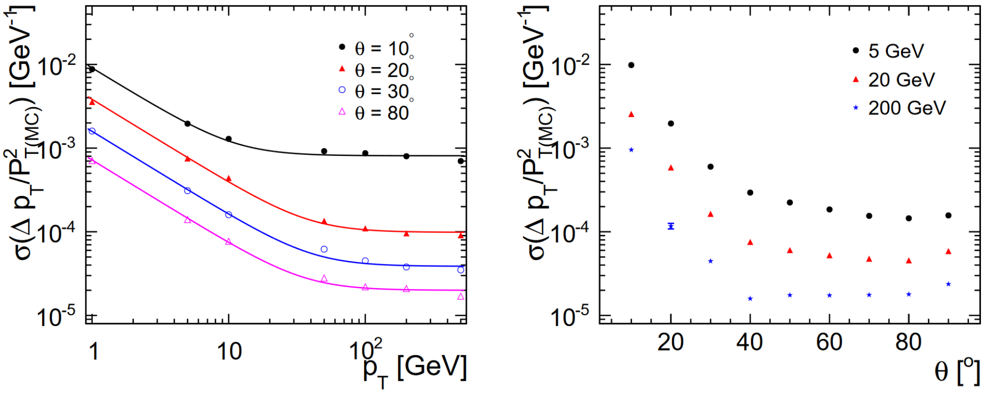

FIGURE 5.8: Transverse momentum resolution of single muons as a function of transverse momentum for different polar angles (left) and a function of polar angle for different transverse momenta (right). Figure taken from [8].

5.3.2 Calorimetry

The energy measurement for electrons and photons is performed by two electromagnetic calorimeters – one surrounding TPC in the barrel (extending from 1847 to 2020 millimetres from the beam axis) and one in the forward region (2450 to 2622 millimetres along the beam axis). Both use a tungsten absorber, arranged in 30 layers interleaved with silicon pads, and have an active thickness of 23 radiation lengths. They are followed with two hadron calorimeters, which use a different material due to spacial constraints in the barrel region. The tungsten based W-HCAL extends radially from 2058 to 3296 millimetres and has a thickness of 7.5 nuclear interaction lengths (8.5 with ECAL). The forward HCAL uses steel (also 7.5) and covers the range of 2650 to 4240 millimetres along the beam axis. Both use scintillators for the readout. Additionally, two specialised electromagnetic calorimeters are installed in the forward region. One of them provides a high precision measurement of the luminosity, while the other is located far along the beam axis (at 3281 millimetres) and extends the angular acceptance to about 10 mrad. By design, the calorimeter system should provide jet energy resolution better than 3.5% (5%) for energies between 100 and 1000 GeV (at 50 GeV). This allows to reliably discriminate between the hadronic decays of $W^{\pm}$ and Z^0 bosons, but also to effectively search for BSM signatures with heavy quarks in the final states. Figure 5.9 shows results obtained under realistic operating conditions with a calorimeter prototype. The resolution is illustrated as a function of the jet polar angle for a variety of energies and as a function of the energy for different timing requirements imposed (corresponding to different widths of the time window for tracker hits and calorimeter clusters to be considered part of the same event).

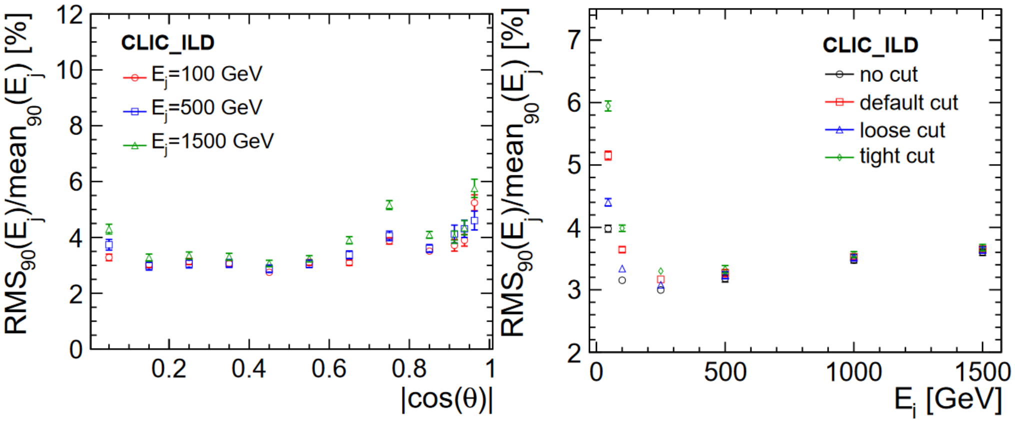

FIGURE 5.9: Reconstructed jet energy resolution as a function of the polar angle for different jet energies (left) and as a function of the jet energy for different timing requirements (right). Figure taken from [8].

5.3.3 Magnet, yoke and muon detectors

The required 4T magnetic field will be generated by a push-pull configuration, consisting of a superconducting central solenoid with ring coils on the yoke endcaps, and two anti-solenoids located in the forward region and using normal conductors. The yoke provides radiation shielding and is interleaved with nine muon detection layers in the barrel and nine in the endcaps. Figure 5.10 shows the expected muon identification efficiency and purity, as a function of the polar angle and energy, studied with isolated muons and those originating in high multiplicity heavy jet events.

Both are universally very high, with a slight decrease in efficiency visible around the polar angle of 40 degrees, where the transition between barrel and forward detectors happens.

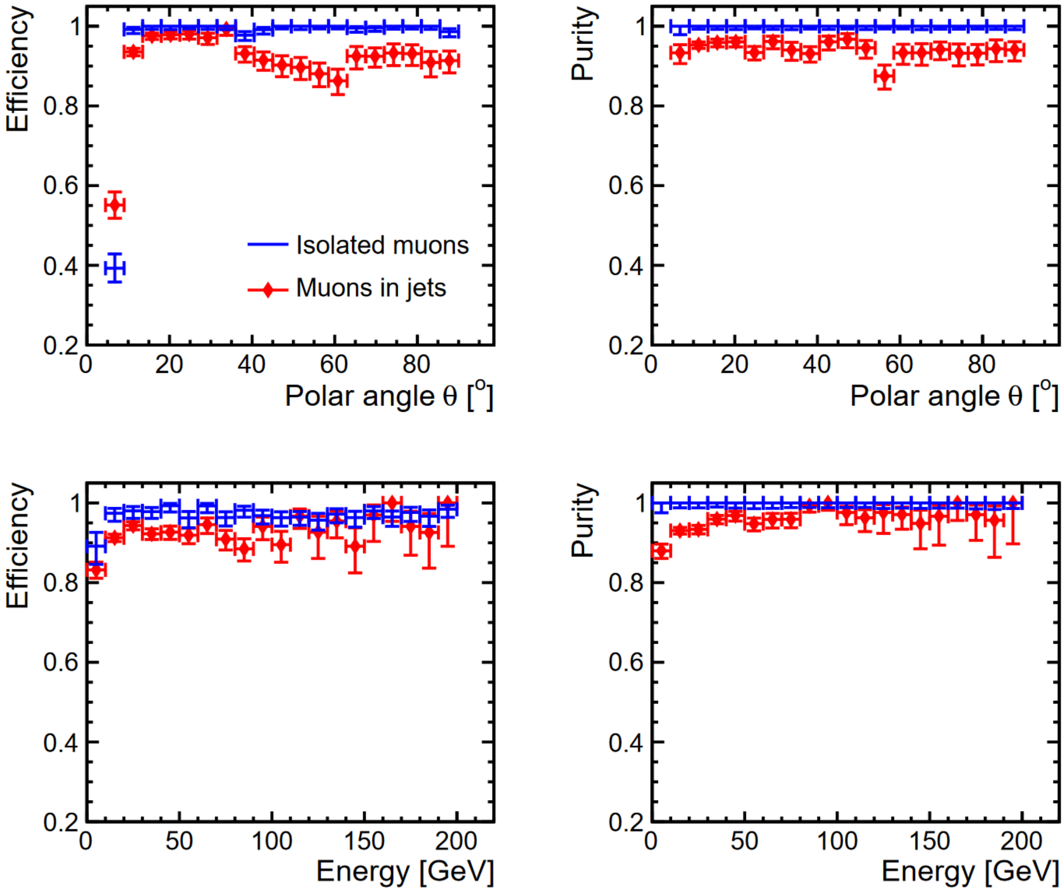

FIGURE 5.10: Expected performance of the muon identification system as a function of the polar angle and energy. Results for isolated muons are shown in blue, while red indicates muons originating in particle jets from *b* quarks. Figure taken from [8].

Chapter 6

Search for exotic long-lived particles in the CLIC experiment

6.1 Introduction

The clean experimental environment of e^+e^- collisions and a very good capability of reconstructing displaced decay vertices make CLIC experiment particularly well suited for long-lived particle searches. The following study evaluates sensitivity to the signatures representative for relatively light composite candidates in the initial stage of operation. A CLIC_ILD detector model is assumed (see chapter 5), together with a centre-of-mass collision energy of 350 GeV and 1 ab^{-1} of integrated luminosity. A Hidden Valley scenario (see section 2.3.2) is considered, with the Standard Model Higgs boson decaying into a pair of exotic pions (π_v^0). The pions are assumed to subsequently decay exclusively into pairs of Standard Model b quarks, but the results can be scaled to account for other channels. Multiple hypotheses of π_v^0 mass (25, 35 and 50 GeV) and lifetimes (1, 10, 100 and 300 ps) are explored. Furthermore, the default secondary vertex reconstruction algorithms are found to be inefficient for high multiplicity secondary vertices. A dedicated procedure is thus developed, allowing for a much higher background rejection rate. The analysis was published in the Journal of High Energy Physics [2], together with a study conducted previously for the last stage of operation (centre-of-mass energy of 3 TeV). An overview of similar searches at currently operating experiments can be found in section 2.5.1. In this chapter, the description of analysis strategy and results is given in section 6.2 and their discussion in section 6.3.

6.2 Analysis strategy and results

The study determines the upper limits on a product of production cross-section of the Higgs boson and its branching fraction into a pair of Hidden Valley pions ($\sigma(H) \cdot BR\left(H \to \pi_v^0\pi_v^0\right)$), under the assumption that both pions decay exclusively into pairs of Standard Model b quarks. At the centre-of-mass energy of 350 GeV, the Higgs boson is produced mainly in association with the Z^0 boson in a Higgsstrahlung process. The Z^0 is assumed to decay promptly into a pair of quarks, as this scenario introduces a more difficult background contribution compared to leptonic channels (due to additional particle jets present). The full interaction is:

$$e^+e^- \to HZ^0 \to \pi_v^0\pi_v^0 q\bar{q} \to b\bar{b}b\bar{b}q\bar{q}. \tag{6.1}$$

In order to provide a set of data points in a relatively wide mass and lifetime spectrum, the measurement is performed independently under different hypotheses of π_v^0 characteristics. Specifically, the masses of 25, 35 and 50 GeV, and lifetimes of 1, 10, 100 and 300 ps are considered. The analysis strategy is adopted from the study conducted for the centre-of-mass energy of 3 TeV [153] and modified to account for different Higgs boson production mechanism and background sources. Several improvements are also introduced – in particular, a more realistic approach to modelling background contributions as a linear combination of all sources rather than considering only the dominating one.

Because of their lifetimes, the π_v^0 decays produce high multiplicity secondary vertices displaced from the primary interaction point and beam axis. Therefore, the analysis focuses on maximising the efficiency of reconstructing tracks with high impact parameter and correctly associating them with π_v^0 candidates. The default Linear Collider Flavour Identification (LCFI+, [154]) algorithms are found to be inefficient in assigning tracks to significantly displaced vertices. This behaviour is expected, because they are designed primarily for reconstructing beauty and charm hadron decays, but hinders the ability to discriminate between signal and background signatures. A custom procedure is thus used to combine tracks into secondary vertices. In each event, six particle jets are reconstructed and four of them, identified as coming from b quarks, are matched with the vertices. They are used to reconstruct the π_v^0 and Higgs boson candidates, while the remaining two to form a Z^0 boson.

Several sources of background contributions are considered. The initial rejection is achieved by requiring events to have at least two secondary vertices reconstructed, which effectively suppresses processes without at least two quarks in the final state. The remaining ones are taken to be the inclusive quark production ($q\bar{q}$, $q\bar{q}\nu\bar{\nu}$, $q\bar{q}q\bar{q}$; higher multiplicities are omitted due to low cross-section), production of top quark pairs ($t\bar{t}$), which subsequently decay into $W^+W^-b\bar{b}$ and further into quarks, and $W^+W^-Z^0$ with all three bosons decaying into quark pairs. They are suppressed with a multivariate analysis, in a way which maximises the signal significance. The upper limits on $\sigma\left(H\right)\cdot BR\left(H\to\pi_v^0\pi_v^0\right)$ are then calculated for each mass and lifetime hypothesis, at 95% confidence level, using a CL(s) technique [155].

The overview of used Monte Carlo samples is provided in section 6.2.1. Section 6.2.2 describes the reconstruction of π_v^0 decay vertices. Section 6.2.3 discusses the multivariate analysis and subsequent optimisation of the requirement on the classifier response, and section 6.2.4 describes the determination of upper limits.

6.2.1 Monte Carlo samples

The signal and background processes are simulated using Whizard 1.95 [156] event generator with quark fragmentation and hadronization performed with Pythia 6.4 [157] generator. The beam induced $\gamma\gamma\to$ hadrons background is overlaid for each event and the interactions of particles with the detector are simulated using Geant4 [139] software with MOKKA [158] detector description toolkit. A separate Monte Carlo signal sample is prepared for each π_v^0 mass and lifetime hypothesis. In all cases, the mass of a Higgs boson is taken to be 126 GeV, the production cross-section – 0.93 pb – and $BR\left(\pi_v^0\to b\bar{b}\right)=BR\left(Z\to q\bar{q}\right)=100\%$. The samples are summarised in table 6.1, where the cross-sections of background processes are given as they were reported by the Monte Carlo event generator. Figure 6.1 illustrates the displacement of simulated π_v^0 decay vertices from the primary interaction point and beam axis, under different lifetime hypotheses and assuming a mass of 35 GeV. The kinematic properties of pions are shown in fig. 6.2 for different masses and assuming a 100 ps lifetime. In both cases, the distributions do not depend significantly on the hypotheses for which only one value is shown.

$m_{\pi_v^0}$[GeV]	$\tau_{\pi_v^0}$[ps]	σ[pb]	sample size
25	1	0.93	240K
25	10	0.93	240K
25	100	0.93	240K
25	300	0.93	240K
35	1	0.93	240K
35	10	0.93	240K
35	100	0.93	240K
35	300	0.93	240K
50	1	0.93	240K
50	10	0.93	240K
50	100	0.93	240K
50	300	0.93	240K
$q\bar{q}$		24.41	2M
$q\bar{q}\nu\bar{\nu}$		0.32	306K
$q\bar{q}q\bar{q}$		5.85	1.44M
$t\bar{t}$		0.45	241K
$W^+W^-Z^0$		0.01	40K

TABLE 6.1: Monte Carlo samples of signal and background processes considered in the analysis. The signal samples are catalogued based on the assumed mass and lifetime hypothesis.

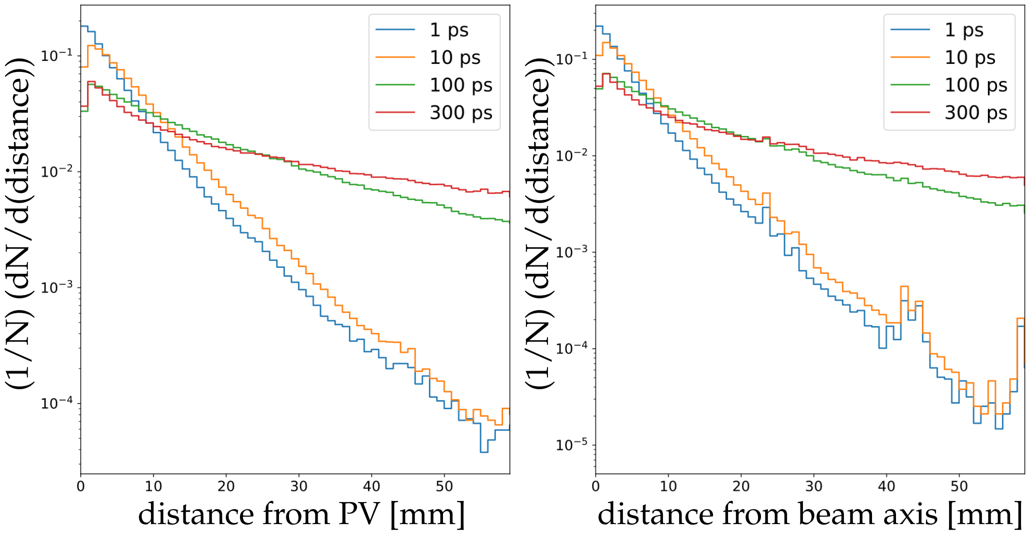

FIGURE 6.1: Displacement of simulated Hidden Valley pion decay vertices from the primary interaction point and beam axis for different lifetime hypotheses. A mass of 35 GeV is assumed.

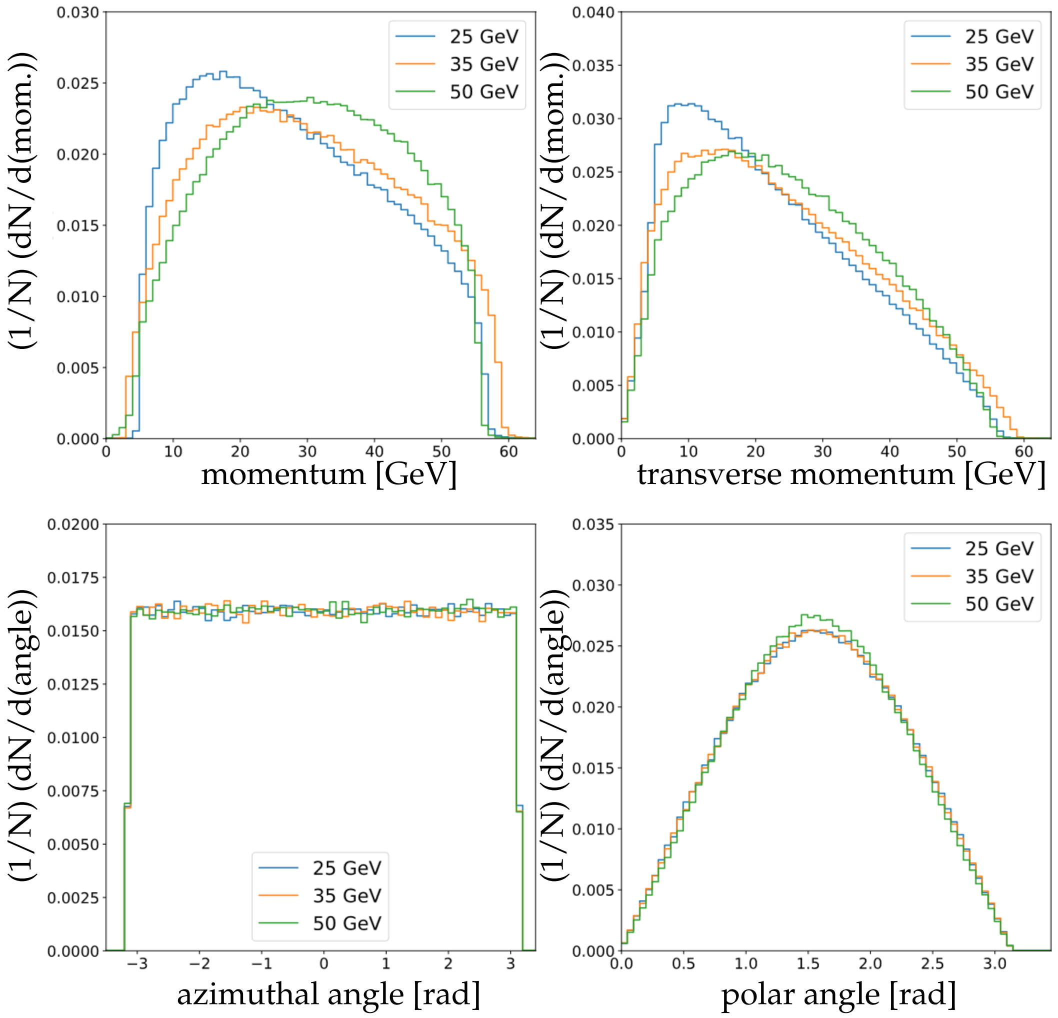

FIGURE 6.2: Kinematic properties of simulated Hidden Valley pions for different mass hypotheses. A lifetime of 100 ps is assumed.

6.2.2 Reconstruction of π_v^0 decay vertices

The reconstruction of particles and particle jets is performed within the MARLIN [159] package, using PANDORA Particle Flow Analysis [160] and FastJet [144] toolkits. The jets are identified using LCFI+ [154] package, which also provides a collection of secondary vertices reconstructed in the process. PANDORA software gives a choice of three sets of requirements (loose, default and tight), which differ in thresholds on particle transverse momenta and the width of time window used to combine hits from detectors into a single event. The analysis uses the tighter of available configurations, in order to minimise the contamination with tracks from beam induced backgrounds. In addition, the maximum values of impact parameter allowed by default are optimised for tracks from beauty and charm hadron decays (both have lifetimes of the order of 1 ps). Therefore, the thresholds on impact parameter have to be increased to not hinder the reconstruction of tracks from π_v^0 vertices. The procedure of their optimisation (resulting in a threshold of 250 mm for the longitudinal and 200 mm for the transversal component) is described in the subsection below. The next subsection provides an overview of jet reconstruction and identification algorithms. The FastJet package is used to cluster particles in each event into exactly six particle jets, to match the final state of the signal process.

Furthermore, the LCFI+ package does not allow for a sufficient loosening of thresholds used during reconstruction of secondary vertices and underestimates the multiplicity of tracks assigned to π_v^0 candidates. Because the background rejection relies on accurate reconstruction of their kinematic properties, a custom algorithm is used to correct this behaviour (details are provided in one of the following subsections). In the events where at least two vertices were formed, they are matched with particle jets in order to reconstruct the parent particles. Only jets with probability of originating from a b quark higher than 95% are considered. They are first combined into two pairs with invariant masses closest to the assumed π_v^0 mass. Each pair is then associated with a vertex, that it has the most assigned charged tracks in common with, and the remaining two jets are used to reconstruct the Z^0 boson candidate. The four jets from π_v^0 vertices are combined into a Higgs boson candidate. Reconstruction results are summarised in the final subsection.

Impact parameter requirements

The PANDORA package allows to modify the thresholds on both impact parameter components – transversal (D_0) and longitudinal (Z_0), which have to be optimised to maximise the efficiency of reconstructing tracks from highly displaced vertices of π_v^0 decays. The procedure was adopted from a previous study, where five different thresholds on D_0 and Z_0 were investigated by evaluating their impact on the multiplicity of secondary vertices reconstructed by the LCFI+ package (fig. 6.3) and distance of secondary vertices to the primary interaction point (fig. 6.4). There, the values of $Z_0 < 250$ mm and $D_0 < 200$ mm were chosen, as they saturate both distributions throughout the entire considered lifetime spectrum. The results were cross-checked at the centre-of-mass energy of 350 GeV, using a simulated signal sample with 50 GeV mass and 300 ps lifetime hypothesis which corresponds to the worst case scenario. They were found to be consistent with those obtained previously, and hence the same thresholds were used.

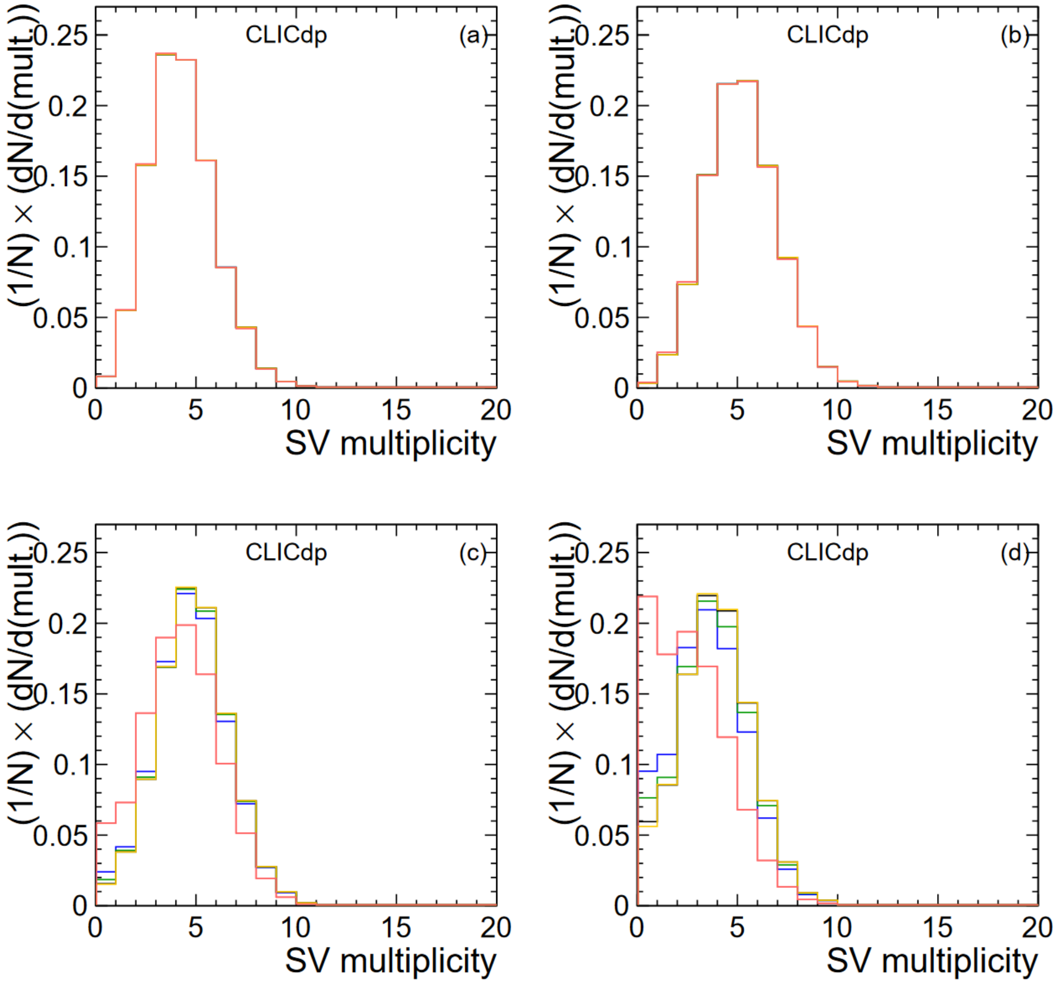

FIGURE 6.3: Multiplicity of vertices reconstructed at the centre-of-mass energy of 3 TeV for signal samples with 50 GeV mass hypothesis and lifetimes of 1 (a), 10 (b), 100 (c) and 300 (d) ps. The colours indicate different requirements on the values of the transversal and longitudinal components of the impact parameter – $Z_0 < 30$ mm and $D_0 < 20$ mm (red), $Z_0 < 80$ mm and $D_0 < 60$ mm (blue), $Z_0 < 120$ mm and $D_0 < 100$ mm (green), $Z_0 < 250$ mm and $D_0 < 200$ mm (black), $Z_0 < 400$ mm and $D_0 < 300$ mm (yellow). Figure taken from [153].

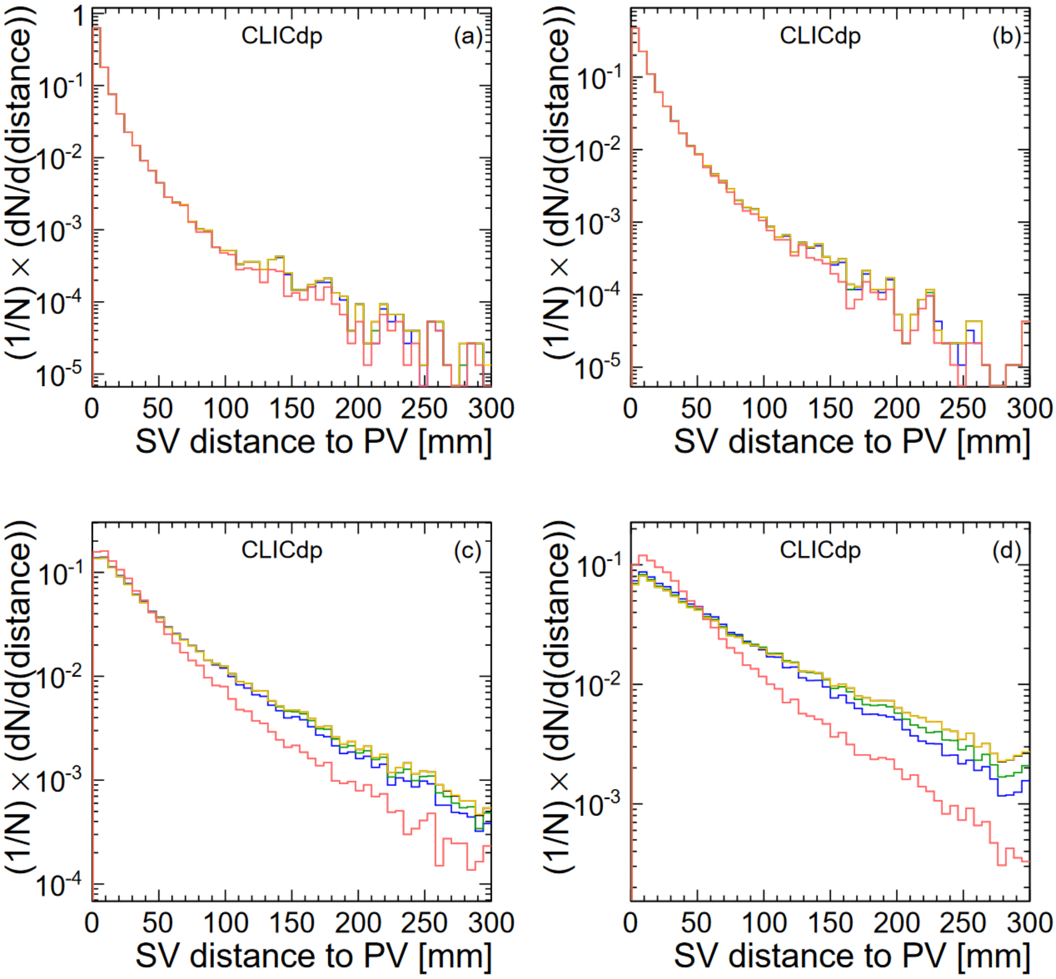

FIGURE 6.4: Distance of reconstructed vertices from the primary interaction point at the centre-of-mass energy of 3 TeV for signal samples with 50 GeV mass hypothesis and lifetimes of 1 (a), 10 (b), 100 (c) and 300 (d) ps. The colours indicate different requirements on the values of the transversal and longitudinal components of the impact parameter – $Z_0 < 30$ mm and $D_0 < 20$ mm (red), $Z_0 < 80$ mm and $D_0 < 60$ mm (blue), $Z_0 < 120$ mm and $D_0 < 100$ mm (green), $Z_0 < 250$ mm and $D_0 < 200$ mm (black), $Z_0 < 400$ mm and $D_0 < 300$ mm (yellow). Figure taken from [153].

Jet reconstruction and identification

The particle jets are initially reconstructed using a longitudinally invariant k_T [161] algorithm, as implemented in the FastJet package. The jet R parameter is chosen to be 1 and optimised to maximise the resolution of reconstructed π_v^0 and Higgs boson invariant mass. The procedure was adopted from the previous study, where the normalised root-mean-square of both masses was investigated with signal samples of varying lifetimes. Figure 6.5 shows the distributions at the centre-of-mass energy of 3 TeV, where the minima are around $R = 1$. The results were cross-checked at the energy of 350 GeV, using signal samples with 50 GeV mass hypothesis and lifetimes on both ends of the spectrum (1 and 300 ps). They were found to be consistent, and the same value of R was used in the study.

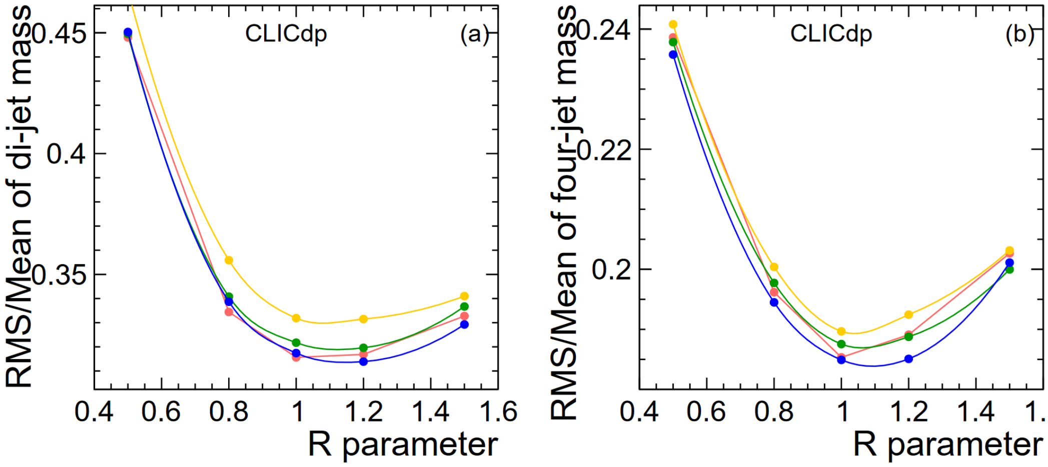

FIGURE 6.5: Normalised root mean square of π_v^0 (a) and Higgs boson (b) invariant mass at the centre-of-mass energy of 3 TeV. A sample with 50 GeV mass hypothesis and lifetimes of 1 (red), 10 (blue), 100 (green) and 300 (yellow) ps are used. Figure taken from [153].

The jets are subsequently passed through to the LCFI+ algorithms, which further refine the clustering and perform flavour identification (details can be found in [8, 154]). The identification is based primarily on the properties of secondary vertices reconstructed in the vertex detector (see section 5.3.1). The procedure starts with a collection of particle tracks that were not assigned to the primary interaction. They are paired into all possible two-track combinations, which are passed to a dedicated vertex fitter which determines their common origin coordinates. A set of selection criteria (e.g. on the invariant mass and fit χ^2) is then introduced to reduce combinatorial background. Additional tracks are assigned to the remaining candidates if they do not cause them to fail the same selection or increase the χ^2 by a value larger than a chosen threshold. Next, the best candidate with at least three tracks assigned is selected and its constituent tracks are removed from other vertices. It is then excluded and the step is repeated until there are no more candidates with three or more tracks, resulting in a collection of non-overlapping secondary vertices. The identification is performed with a Boosted Decision Tree classifier, which is trained on the properties of jets and their associated vertices with three possible labels, corresponding to the b, c and light quarks. Figure 6.6 illustrates the chance of misidentifying c and light jets as originating from a b quark as a function of the b jet identification efficiency. It is evaluated using simulated $Z^0 \to q\bar{q}$ decays, produced in collisions at the centre-of-mass energy of 91.2 GeV.

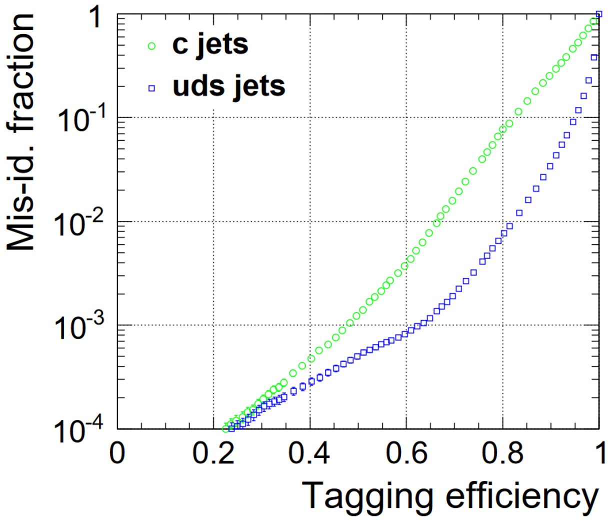

FIGURE 6.6: The fraction of c and light jets misidentified as b as a function of the b jet identification efficiency. Figure taken from [154].

Reconstruction of displaced vertices

The LCFI+ algorithm is found to underestimate the multiplicity of tracks assigned to π_v^0 vertex candidates, likely due to internal thresholds being too strict for displacements larger than those of beauty hadrons. Although several other possible causes were investigated (e.g. impact of requirements used in track reconstruction or beam induced backgrounds), none could explain the observed behaviour. The software also does not interface any settings, which could correct it. The vertices are thus reconstructed with a custom algorithm, using loose thresholds optimised specifically for significantly displaced high multiplicity vertices. The achieved improvement is illustrated in fig. 6.7, where the multiplicity of assigned tracks is consistent with predictions for Hidden Valley pions. Furthermore, an accurate reconstruction of π_v^0 vertices allows for an effective rejection of background contributions, due to their different characteristics. As an example, multiplicities of reconstructed vertices and assigned tracks in simulated signal and background samples are shown in fig. 6.8.

The procedure is performed in two stages. Initially, the points in space where tracks accumulate are searched for and corresponding tracks are combined into vertex candidates. The selection is then further refined and a weighted least square fit is used to estimate the position. A starting point is a collection of high quality charged tracks, which are unlikely to originate from the primary interaction vertex based on their impact parameter (its significance – IP/σ_{IP} – is required to be above 16). The collection is traversed until the first candidate for a base track, defined as having at least four other tracks with distance of closest approach lower than 1 millimetre, is found. These tracks, together with a base one, form a vertex candidate. For each constituting pair, a point of closest approach is determined and additional tracks are assigned if their distance of closest approach to that point is less than 1 millimetre. Once all possibilities are exhausted, used tracks are excluded and a new base one is searched for. As a result, a collection of non-overlapping secondary vertex candidates is obtained. They are then refined by dropping the associated tracks and reassigning them from the initial collection, using an iterative least square method based on the impact parameter with respect to the candidate position.

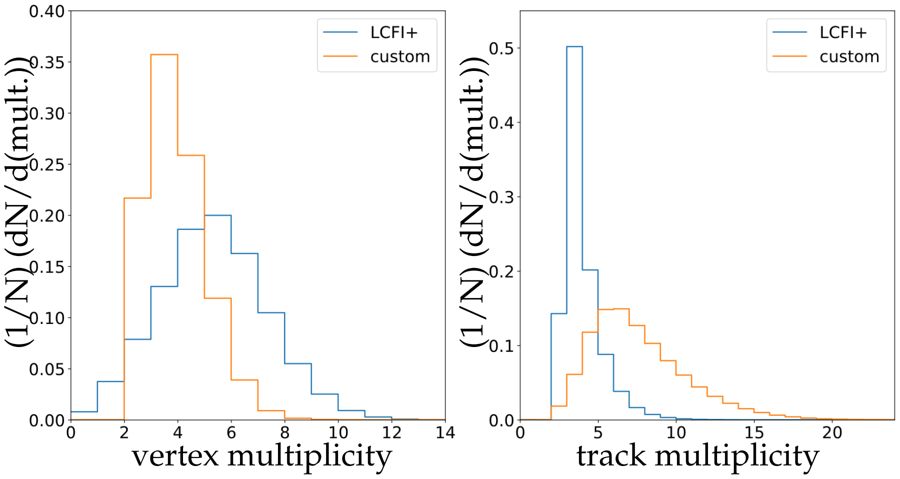

FIGURE 6.7: Multiplicity of reconstructed secondary vertices and tracks assigned to them for the default LCFI+ and custom reconstruction algorithm. A signal sample with 35 GeV mass and 100 ps lifetime hypothesis is used.

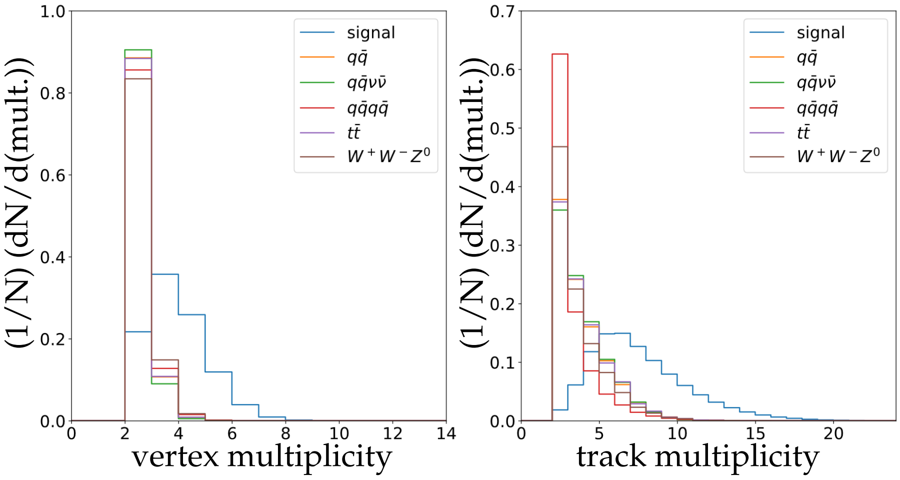

FIGURE 6.8: Multiplicity of reconstructed secondary vertices and tracks assigned to them in simulated signal (35 GeV, 100 ps) and background samples. Vertices are reconstructed using the custom algorithm and at least two are required.

Selection results

The efficiencies of selecting events with at least two reconstructed secondary vertices and four particle jets, with a probability of originating in a b quark higher than 95%, are evaluated in each simulated sample and listed in table 6.2. Reconstructed invariant masses of π_v^0, Z^0 and Higgs boson candidates are shown in fig. 6.9 for a chosen signal sample (35 GeV, 100 ps). Tails in the distributions are caused by combinatorial background from incorrectly matched jet pairs, while the shifts of peak positions primarily by the limited ability of reconstructing neutral particles.

$m_{\pi_v^0}$[GeV]	$\tau_{\pi_v^0}$[ps]	selection efficiency [%]
25	1	78
25	10	94
25	100	99
25	300	97
35	1	76
35	10	93
35	100	99
35	300	98
50	1	72
50	10	89
50	100	99
50	300	99
$q\bar{q}$		12
$q\bar{q}\nu\bar{\nu}$		12
$q\bar{q}q\bar{q}$		8
$t\bar{t}$		12
$W^+W^-Z^0$		14

TABLE 6.2: Efficiencies of selecting events with at least two secondary vertices reconstructed and four particle jets, with a probability of originating from a b quark higher than 95%. The signal samples are catalogued based on the assumed mass and lifetime hypothesis.

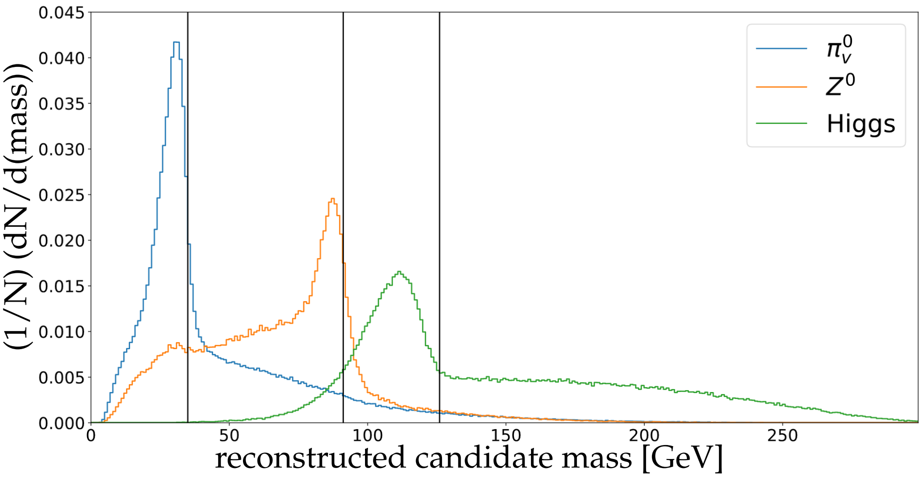

FIGURE 6.9: Masses of reconstructed candidates in a signal sample with 35 GeV mass and 100 ps lifetime hypothesis. Their generated values are shown with black lines.

6.2.3 Maximization of signal significance

In order to evaluate the detector sensitivity, a degree to which the signal is distinguishable from statistical fluctuations of the data has to be determined. The analysis uses a significance metric, defined as:

$$\frac{S}{\sqrt{S+B}}, \tag{6.2}$$

where S and B are the number of expected signal and background events, respectively, and the denominator corresponds to a Poissonian error. Moreover, the achieved significance can be maximised by suppressing background contributions.

For each π_v^0 mass and lifetime hypothesis, an independent Boosted Decision Tree classifier is trained to discriminate between signal and background signatures. Several variants, which are available in the ROOT TMVA [146] package, have been evaluated. Boosted Decision Tree Gradient (BDTG) was found to provide the best relation between background rejection and signal retention and was used exclusively. In all cases, the signal and background samples were split in half, with one subset used for training and the other to check for possible overtraining and used in the subsequent analysis. In order to represent the background realistically, the sources were combined with weights proportional to the expected number of events. The details on the classifiers and training, as well as the study of signal significance, are provided in the subsections below.

Classifiers training

A Boosted Decision Tree Gradient classifier is trained for each mass and lifetime hypothesis. Background characteristics are represented by a weighted sum of all considered sources, with weights:

$$w = \frac{\sigma \cdot \epsilon}{N}, \tag{6.3}$$

where σ is the production cross-section (table 6.1), ϵ is the selection efficiency (table 6.2) and N – a number of events in the simulated sample. Integrated luminosity is not included, because the combined distributions are normalised in training. The following variables are used (names used in figures are given in brackets and distributions are shown in fig. 6.10 for the signal sample with 35 GeV and 10 ps lifetime hypothesis):

- multiplicity of tracks assigned to the secondary vertices (assigned tracks multiplicity, seedTrackMult)
- multiplicity of reconstructed secondary vertices (number of reconstructed DVs, seedMult)
- logarithm of invariant mass of reconstructed secondary vertices (DV invariant mass, seedInvMassLog)
- logarithm of invariant mass of the π_v^0 candidates (di-jet invariant mass, seedDiJetMassLog)
- logarithm of invariant mass of the Higgs boson candidate (four-jet invariant mass, seedFourJetMassLog)
- invariant mass of the Z boson candidate (Z invariant mass, diJetZMass)
- logarithm of distance at which the transition from a three-jet to a two-jet event takes place ($y_{n-1,n}$, y1Log)
- logarithm of distance at which the transition from a four-jet to a three-jet event takes place ($y_{n+1,n}$, y2Log)

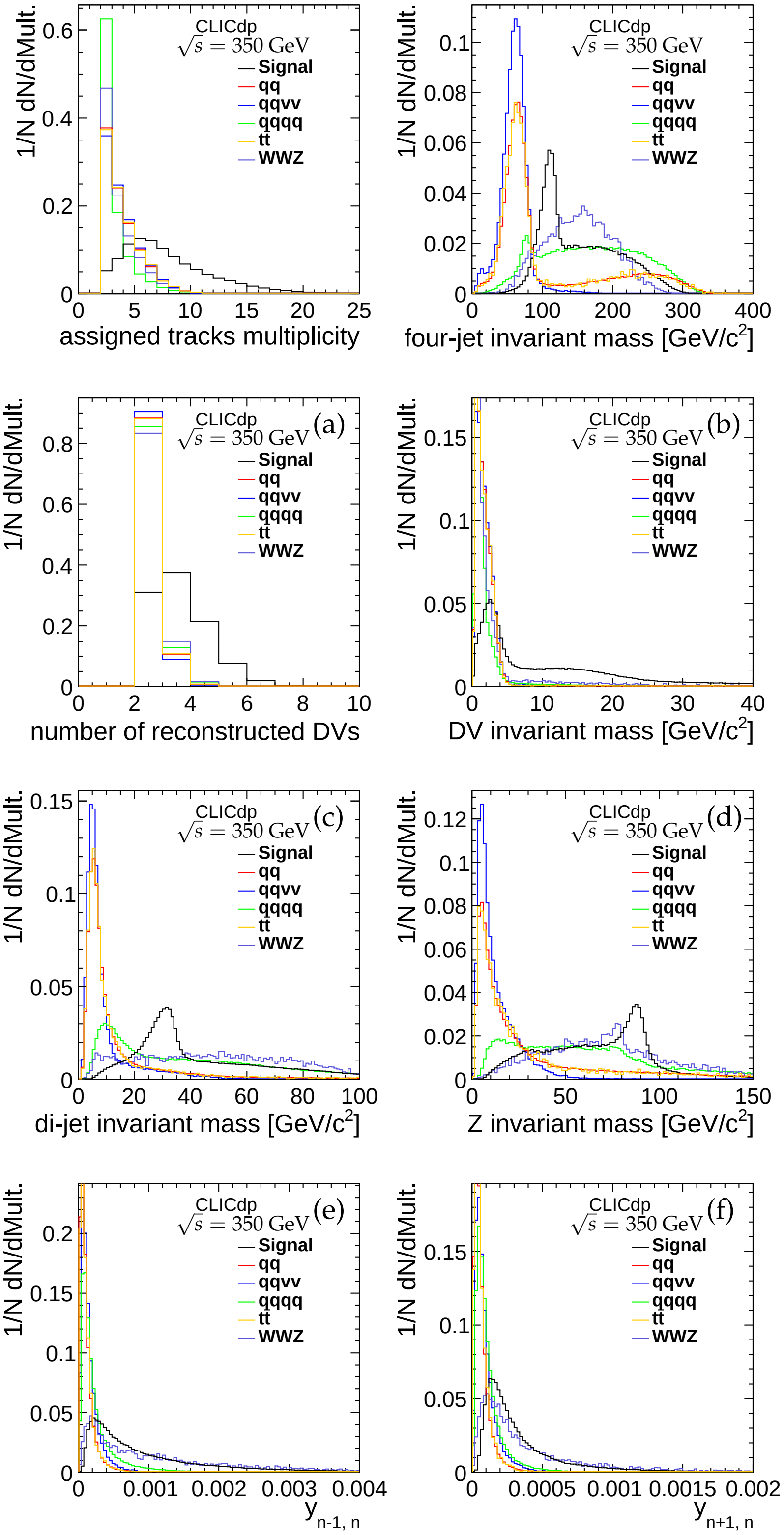

FIGURE 6.10: Distributions of variables used in classifier training in the signal with 35 GeV and 10 ps mass hypothesis and considered backgrounds. The variables are explained in the text.

Figures 6.11 and 6.12 illustrate the linear correlations between training variables in the background and signal (assuming 35 GeV mass) samples. Response of the classifier in training and testing samples are illustrated in fig. 6.13 and dependence of background rejection on the fraction of preserved signal in fig. 6.14.

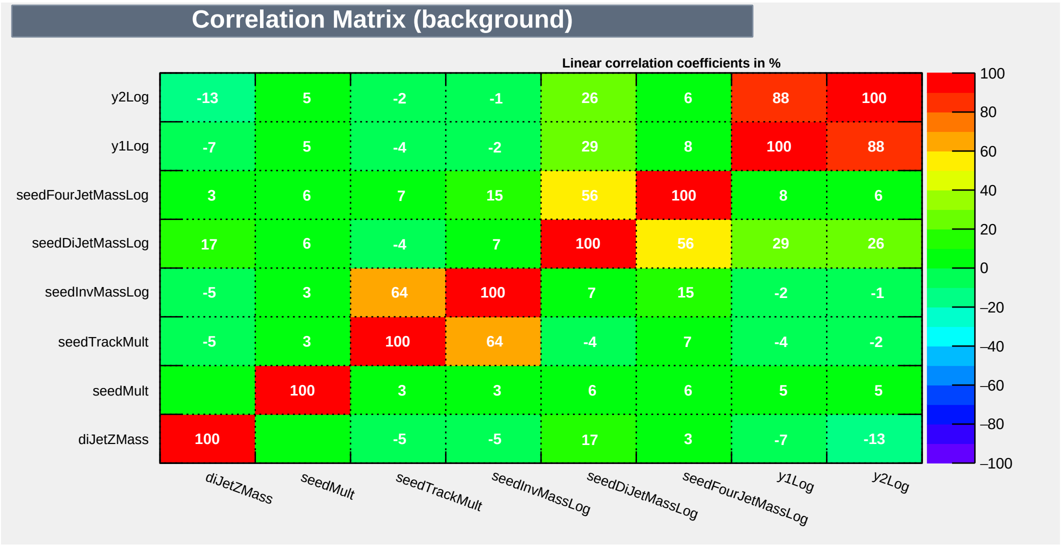

	diJetZMass	seedMult	seedTrackMult	seedInvMassLog	seedDiJetMassLog	seedFourJetMassLog	y1Log	y2Log
y2Log	-13	5	-2	-1	26	6	88	100
y1Log	-7	5	-4	-2	29	8	100	88
seedFourJetMassLog	3	6	7	15	56	100	8	6
seedDiJetMassLog	17	6	-4	7	100	56	29	26
seedInvMassLog	-5	3	64	100	7	15	-2	-1
seedTrackMult	-5	3	100	64	-4	7	-4	-2
seedMult		100	3	3	6	6	5	5
diJetZMass	100		-5	-5	17	3	-7	-13

FIGURE 6.11: Linear correlation of variables used in training.

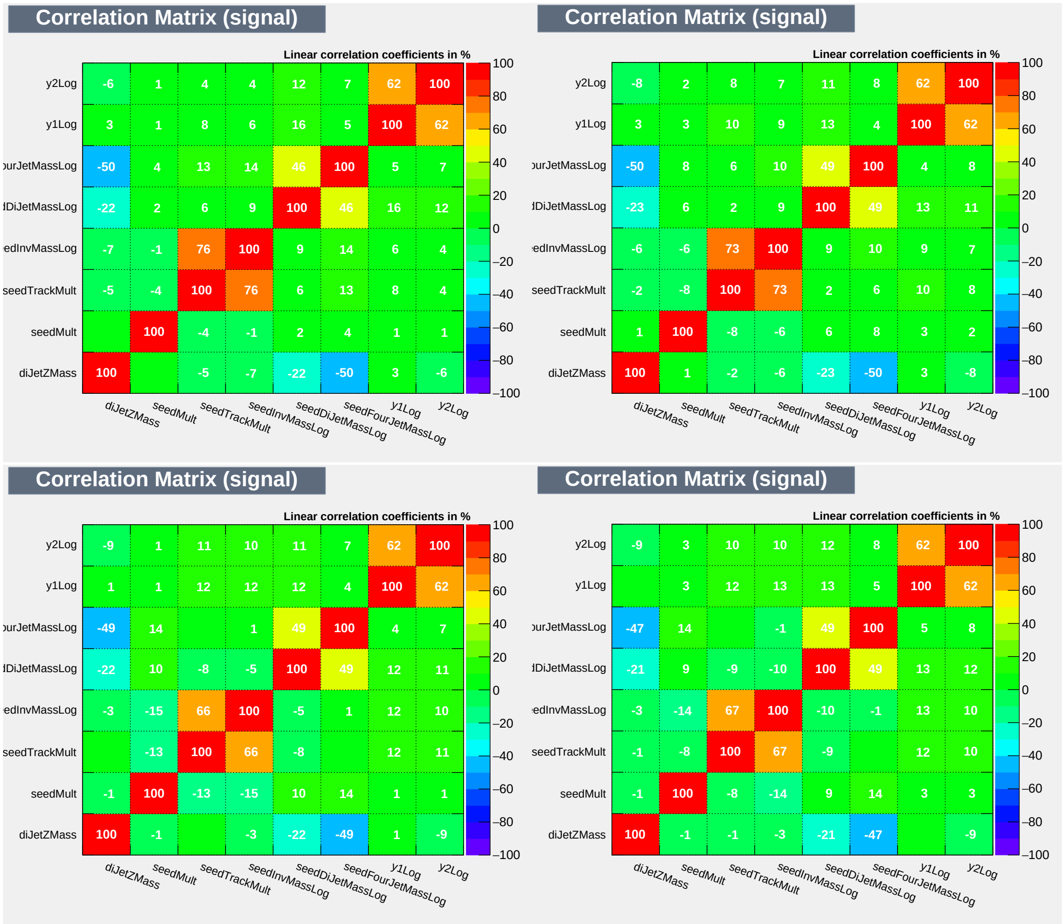

	diJetZMass	seedMult	seedTrackMult	seedInvMassLog	seedDiJetMassLog	seedFourJetMassLog	y1Log	y2Log
y2Log	-6	1	4	4	12	7	62	100
y1Log	3	1	8	6	16	5	100	62
ourJetMassLog	-50	4	13	14	46	100	5	7
lDiJetMassLog	-22	2	6	9	100	46	16	12
edInvMassLog	-7	-1	76	100	9	14	6	4
seedTrackMult	-5	-4	100	76	6	13	8	4
seedMult		100	-4	-1	2	4	1	1
diJetZMass	100		-5	-7	-22	-50	3	-6

	diJetZMass	seedMult	seedTrackMult	seedInvMassLog	seedDiJetMassLog	seedFourJetMassLog	y1Log	y2Log
y2Log	-8	2	8	7	11	8	62	100
y1Log	3	3	10	9	13	4	100	62
ourJetMassLog	-50	8	6	10	49	100	4	8
lDiJetMassLog	-23	6	2	9	100	49	13	11
edInvMassLog	-6	-6	73	100	9	10	9	7
seedTrackMult	-2	-8	100	73	2	6	10	8
seedMult	1	100	-8	-6	6	8	3	2
diJetZMass	100	1	-2	-6	-23	-50	3	-8

	diJetZMass	seedMult	seedTrackMult	seedInvMassLog	seedDiJetMassLog	seedFourJetMassLog	y1Log	y2Log
y2Log	-9	1	11	10	11	7	62	100
y1Log	1	1	12	12	12	4	100	62
ourJetMassLog	-49	14		1	49	100	4	7
lDiJetMassLog	-22	10	-8	-5	100	49	12	11
edInvMassLog	-3	-15	66	100	-5	1	12	10
seedTrackMult		-13	100	66	-8		12	11
seedMult	-1	100	-13	-15	10	14	1	1
diJetZMass	100	-1		-3	-22	-49	1	-9

	diJetZMass	seedMult	seedTrackMult	seedInvMassLog	seedDiJetMassLog	seedFourJetMassLog	y1Log	y2Log
y2Log	-9	3	10	10	12	8	62	100
y1Log		3	12	13	13	5	100	62
ourJetMassLog	-47	14		-1	49	100	5	8
lDiJetMassLog	-21	9	-9	-10	100	49	13	12
edInvMassLog	-3	-14	67	100	-10	-1	13	10
seedTrackMult	-1	-8	100	67	-9		12	10
seedMult	-1	100	-8	-14	9	14	3	3
diJetZMass	100	-1	-1	-3	-21	-47		-9

FIGURE 6.12: Linear correlation of variables used in training for a signal sample with 35 GeV mass and 1 (top left), 10 (top right), 100 (bottom left) and 300 (bottom right) ps lifetime hypothesis.

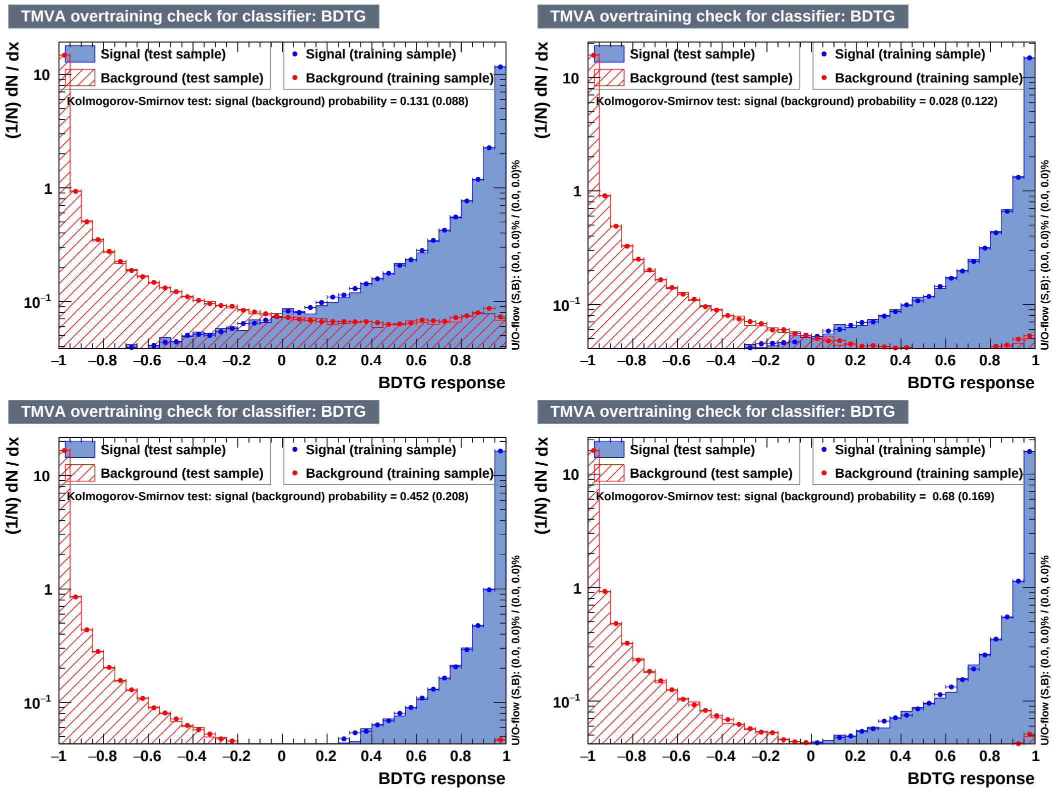

FIGURE 6.13: Classifier responses in training and testing sample for background and signal with 35 GeV mass and 1 (top left), 10 (top right), 100 (bottom left) and 300 (bottom right) ps lifetime hypothesis.

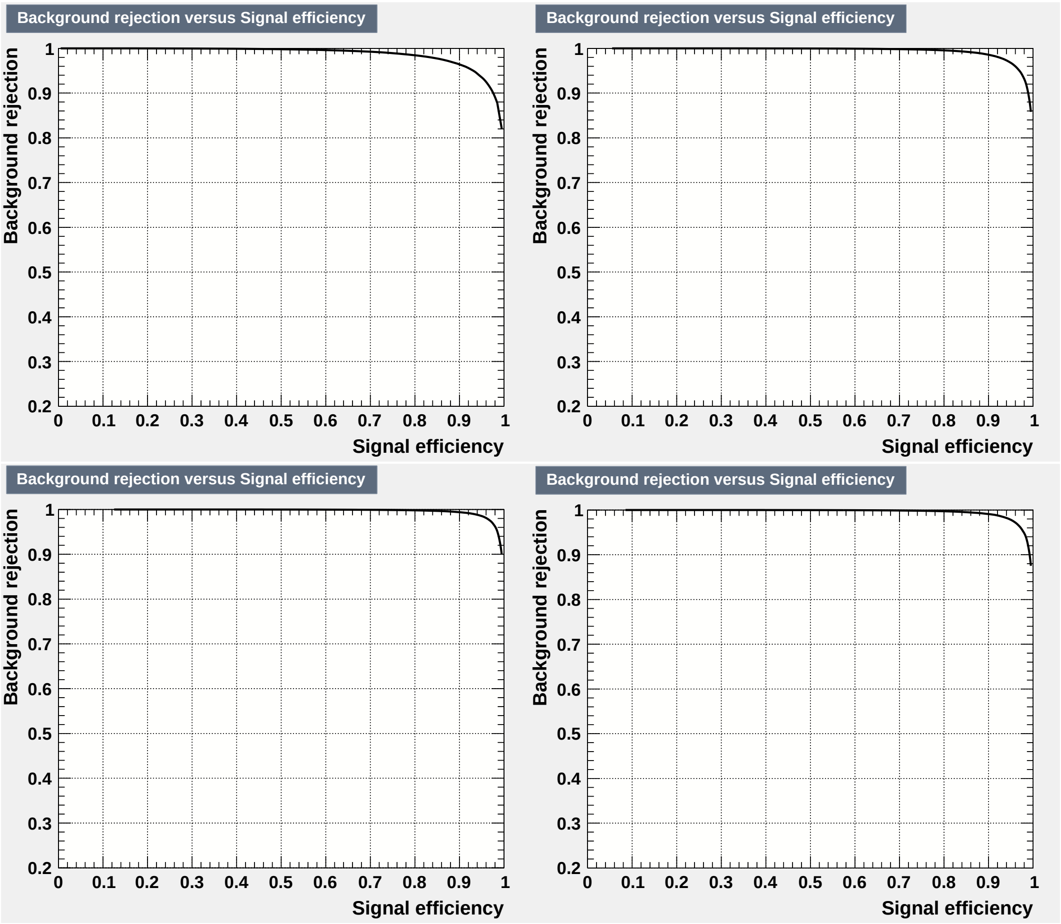

FIGURE 6.14: Relation between background rejection and signal retention for signal with 35 GeV mass and 1 (top left), 10 (top right), 100 (bottom left) and 300 (bottom right) ps lifetime hypothesis.

Signal significance

The signal significance is studied as a function of the requirement imposed on the classifier's response. Figure 6.15 illustrates the dependence for all considered masses and lifetimes. In each case, a threshold which maximises the significance is chosen. Furthermore, the resulting number of expected signal events is investigated to ensure it remains sufficiently high. It is shown in fig. 6.16, together with the expected number of background events, for a signal sample with 35 GeV mass hypothesis. The chosen classifier thresholds and corresponding signal retention and significance are listed in table 6.3. The significance increases with assumed π_v^0 mass and lifetime, which is expected as both make their decay vertices more distinct from secondary vertices from other sources. Furthermore, around the 300 ps mark, a decrease starts to be visible due to detector and acceptance effects.

$m_{\pi^0_{\mathrm{v}}}$[GeV]	$\tau_{\pi^0_{\mathrm{v}}}$[ps]	threshold	signal retention [%]	significance
25	1	0.92	62	178
25	10	0.93	74	233
25	100	0.93	81	254
25	300	0.93	77	243
35	1	0.93	64	182
35	10	0.94	76	239
35	100	0.93	85	263
35	300	0.92	83	255
50	1	0.93	69	185
50	10	0.93	81	241
50	100	0.93	89	273
50	300	0.94	86	268

TABLE 6.3: A chosen value of classifier response and the corresponding signal retention and significance. The efficiencies are rounded.

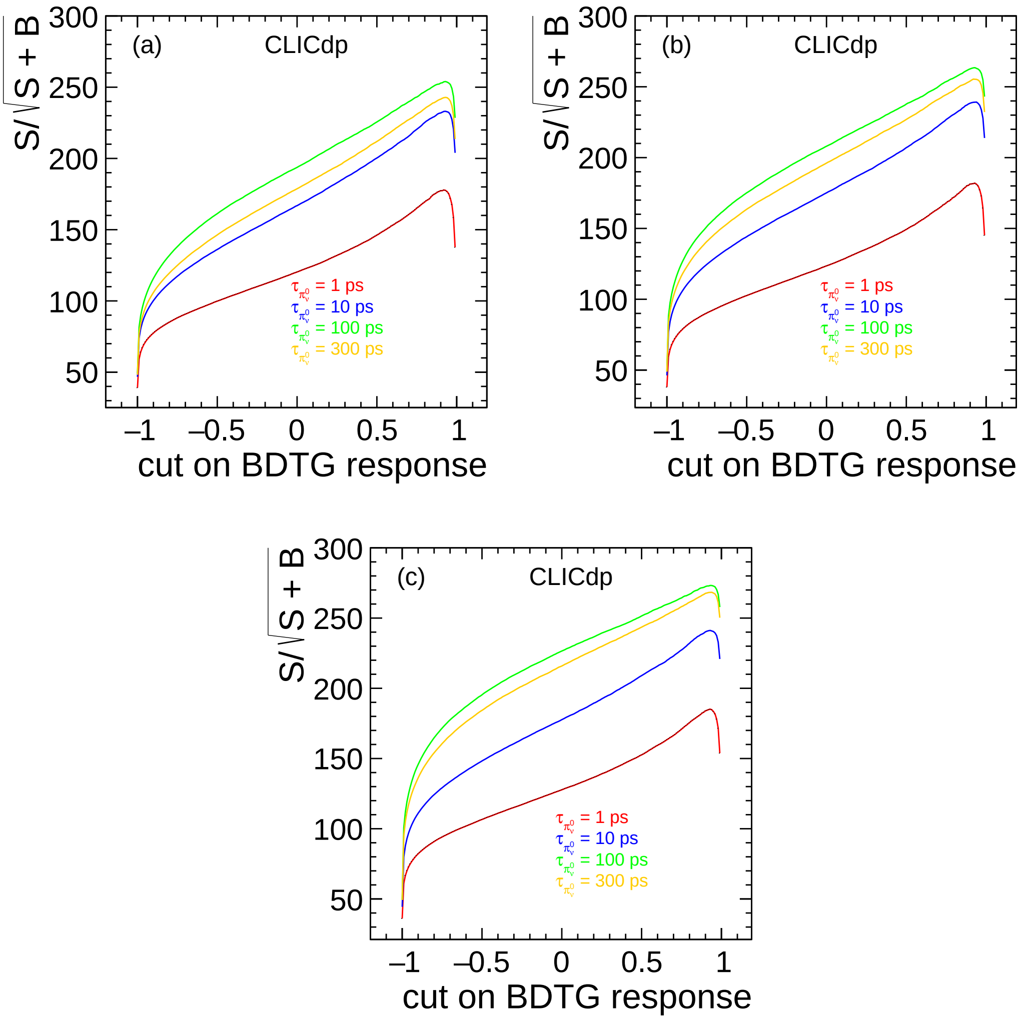

FIGURE 6.15: Signal sensitivity as a function of requirement imposed on the classifier's response for π^0_v masses of 25 (a), 35 (b) and 50 (c) GeV.

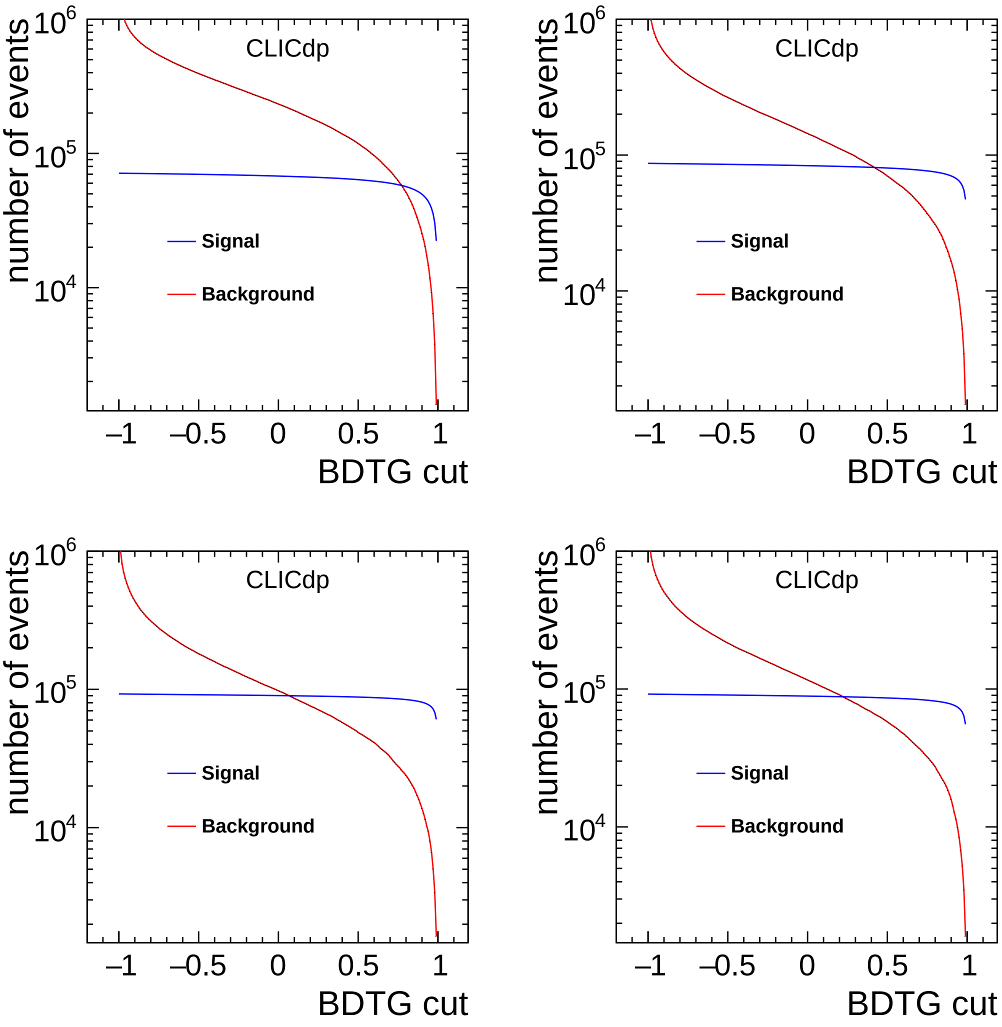

FIGURE 6.16: Number of signal and background events as a function of requirement imposed on the classifier's response for π_v^0 with mass of 35 GeV and 1 (top left), 10 (top right), 100 (bottom left) and 300 (bottom right) ps lifetime hypothesis.

6.2.4 Upper limits on $\sigma\left(H\right)\cdot BR\left(H\rightarrow\pi_v^0\pi_v^0\right)$

The upper limits on $\sigma\left(H\right)\cdot BR\left(H\rightarrow\pi_v^0\pi_v^0\right)$ are evaluated for each π_v^0 mass and lifetime hypothesis using a CL(s) technique [155]. Because the approach relies on collected data to provide reference distributions and number of events, it is assumed that the signal and background processes considered in the analysis accurately represent candidates passing the selection. The limits are calculated for signal significance (see eq. (6.2)), which corresponds to approximately 95% confidence level. The number of background events, B, is taken as the number of combined background events surviving the reconstruction and selection, and the number of signal events as

$$S=\sigma\left(H\right)\cdot BR\left(H\rightarrow\pi_v^0\pi_v^0\right)\cdot\epsilon_{\text{reconstruction}}\cdot\epsilon_{\text{BDTG}}\cdot\mathcal{L}, \tag{6.4}$$

with $\epsilon_{\text{reconstruction}}$ the efficiency of reconstructing at least two displaced vertices and four jets identified as coming from a b quark (table 6.2), ϵ_{BDTG} the fraction of signal events passing BDTG selection with optimised response threshold (table 6.3) and $\mathcal{L}$ – integrated luminosity (1 ab^{-1}). Figure 6.17 illustrates the upper limits for both the first and last stage of CLIC operation. The latter were calculated in a preceding study, while assuming 3 ab^{-1} of integrated luminosity, 3 TeV centre-of-mass energy and $e^+e^- \rightarrow H\nu_e\bar{\nu}_e \rightarrow \pi_v^0\pi_v^0\nu_e\bar{\nu}_e$ production mechanism (WW-fusion). The result uncertainty is discussed in the subsection below.

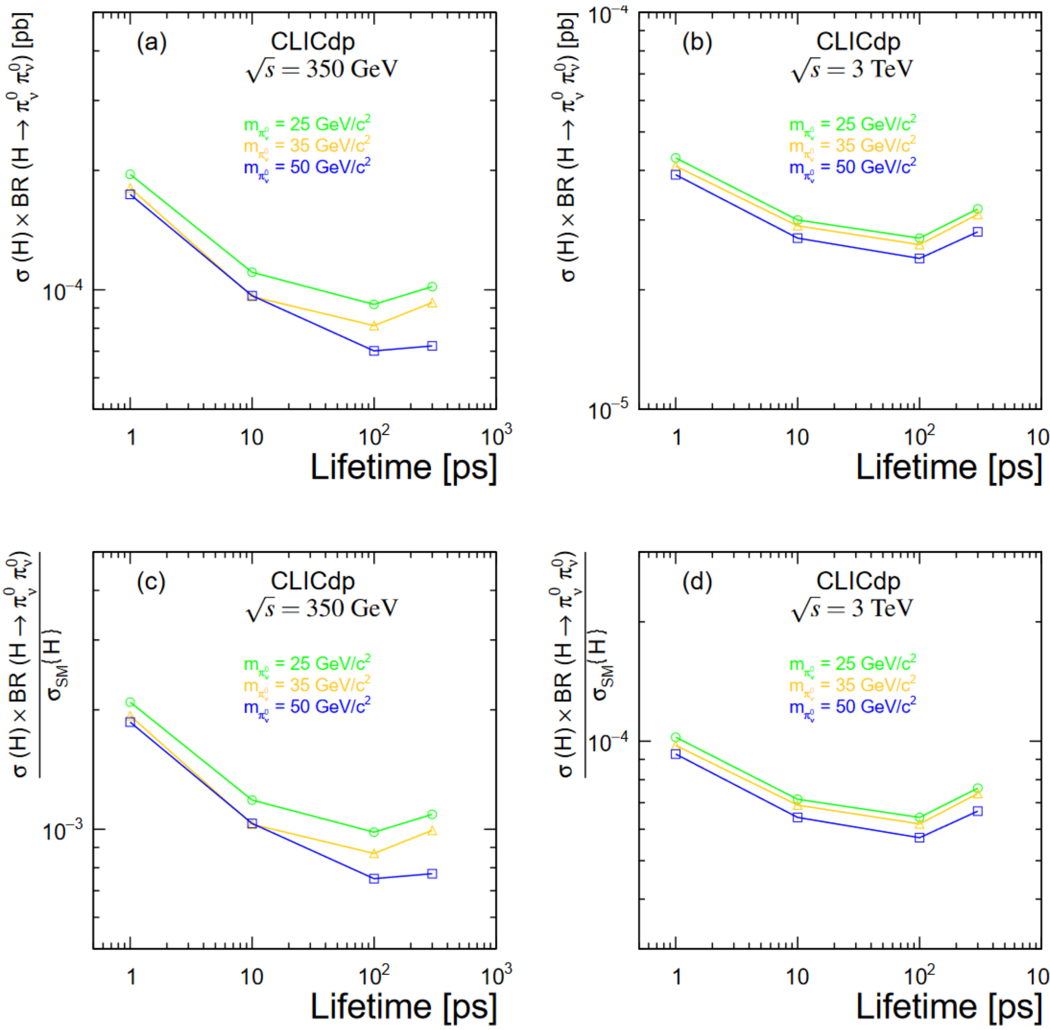

FIGURE 6.17: The upper limits on the production of Hidden Valley pions, decaying exclusively into pairs of b quarks. The left side shows results for the first stage of CLIC detector operation, while the right one – for last. The values in the bottom figures are normalised to the Standard Model cross-section of the Higgs boson production at a given energy. Figure taken from [2].

Uncertainty considerations

Since the experiment is still in a planning stage and detector details are subject to change, the study focuses primarily on establishing the order of magnitude for the upper limits on $\sigma(H) \cdot BR\left(H \rightarrow \pi_v^0\pi_v^0\right)$. Nevertheless, several possible sources of systematic uncertainty were investigated. The main contribution is expected to come from secondary vertices originating in the detector material and have a negligible impact. Likewise, the luminosity is expected to have a minor effect as it will be measured at a few permille level. The overall uncertainty is thus anticipated to be dominated by the statistics.

6.3 Summary and conclusions

The sensitivity of CLIC detector (see section 5.3) to exotic long-lived particles with displaced vertex signatures is studied for the initial stage of its operation ($\sqrt{s} = 350$ GeV, $\mathcal{L} = 1\text{ab}^{-1}$). A Hidden Valley scenario (see section 2.3.2) is assumed with a QCD-like structure in the hidden sector. The communicator is taken to be the Standard Model Higgs boson (126 GeV mass), decaying into a pair of hidden pions π_v^0. The pions are assumed to decay exclusively into pairs of b quarks, but the results can be scaled to account for other channels. The π_v^0 masses of 25, 35 and 50 GeV as well as lifetimes of 1, 10, 100 and 300 ps are considered. Furthermore, because the study concentrates mainly on the reconstruction of displaced decay vertices and the subsequent rejection of potential background sources (e.g. vertices from beauty hadrons), the results are mostly model independent and can be considered representative for relatively light composite exotic candidates.

The particles are reconstructed using default algorithms developed for future e^+e^- colliders. They are found to provide good reconstruction efficiency, even for tracks from highly displaced decay vertices. However, secondary vertices reconstructed by them do not match the predictions for π_v^0 decays well (in particular in the multiplicity of tracks associated with the vertex). As this behaviour was not possible to correct with available software options, a custom procedure is used and tuned for Hidden Valley decays. The achieved accurate representation of π_v^0 characteristics allows for a very high degree of background rejection in a multivariate analysis. The upper limits on $\sigma\left(H\right) \cdot BR\left(H \to \pi_v^0 \pi_v^0\right)$ are calculated at 95% confidence level and are at the order of 10^{-4} pb (10^{-3} when normalised to the Standard Model Higgs boson cross-section). They are found to improve as the assumed π_v^0 mass and lifetime increase (due to signal vertices becoming more distinct from other sources) and start to saturate and eventually worsen above the 100 ps mark, because of the detector acceptance. However, these effects are not strong enough to change the order of magnitude.

Overall, the CLIC experiment is expected to provide sensitivity to exotic long-lived particles, which is significantly better than for currently operating detectors (overview is provided in section 2.5.1). A comparison with upper limits determined by the LHCb experiment is particularly interesting, as the studied signatures were consistent with ones considered in this analysis. The CLIC experiment is expected to be more sensitive by 4 to 6 orders of magnitude, depending on the π_v^0 characteristics.

Chapter 7

MUonE experiment at the SPS

7.1 Introduction

The lack of observation of BSM phenomena at the LHC suggests that the required energy scale may be significantly larger. It is therefore necessary to explore alternative approaches which do not rely on a direct detection of exotic states, but may guide and validate theoretical ideas. One of the promising directions is the study of muon's anomalous magnetic moment, which – as recently measured [162] – differs from the Standard Model prediction by 5.2σ. Furthermore, because its nature is fundamentally non-perturbative, the prediction itself carries a significant uncertainty and has to be determined using data-driven or lattice QCD methods. With new measurements inevitably heading towards the limits of precision, the reduction of this uncertainty becomes crucial to strengthen the potential discovery. Among proposed solutions is the MUonE experiment [9], which aims to measure the main contribution to the aforementioned uncertainty – the Hadronic Vacuum Polarization – by studying the elastic scattering of muons on the electrons in targets with low atomic number. It is expected to operate at the muon beam of CERN SPS accelerator (see section 3.2) in years 2025-2030 and improve the precision of the Standard Model prediction at least twice. Furthermore, the design of the detector and very clean experimental environment make it particularly sensitive to the decay signatures of light exotic particles with non-zero lifetimes (see sections 2.3.2 and 2.3.3).

The primary measurement is beyond the scope of this thesis, hence only a brief introduction to the concept of anomalous magnetic moment and the role of MUonE experiment is given in section 7.2, in order to provide motivation for the experimental setup – which is described in section 7.3. Section 7.4 discusses most likely candidates for long-lived particles that could be searched for with MUonE detector and preliminary sensitivity studies.

7.2 MUonE experiment

The MUonE experiment is designed primarily to reduce the Standard Model uncertainty of muon's anomalous magnetic moment (a_μ). The novel approach relies on extracting its Hadronic Vacuum Polarization component from the measurement of the effective electromagnetic constant α. It avoids the challenges of previously established methods based on experimental data (i.e. hadron production cross-sections [163]) and lattice calculations [164], and is expected to improve the precision of determining a_μ at least twofold. Additionally, MUonE is planned to conduct a long-term search for exotic long-lived particles with signatures compatible with the detector design.

A brief overview of the concept of anomalous magnetic moment is given in section 7.2.1. The data-driven approach to Hadronic Vacuum Polarization using hadronic cross-sections is described in section 7.2.2, while section 7.2.3 discusses the method proposed for MUonE experiment.

7.2.1 Muon anomalous magnetic moment

The magnetic moment $\vec{\mu}$ of a lepton, originating due to its spin $\vec{S}$, is expressed as:

$$\vec{\mu} = g \frac{e}{2m} \vec{S}, \tag{7.1}$$

where e is the fundamental charge, m the mass of a particle and the strength of the coupling is determined by the dimensionless gyromagnetic factor g. For elementary point-like fermions, the value of g is given by the Dirac equation as exactly $g = 2$ [165]. The equation, however, does not account for higher order corrections due to effects like self-interaction and shielding by virtual pairs from quantum vacuum oscillations. Therefore, in reality the value is slightly larger and its relative distance from Dirac's result is denoted as the anomalous magnetic moment a:

$$a = \frac{g-2}{2}. \tag{7.2}$$

The magnitude of a depends greatly on the mass of a particle. For example, for an electron it is relatively small and dominated by QED corrections, which makes it useful as a Standard Model benchmark. The muon – on the other hand – while being significantly heavier, is also much more sensitive to contributions from hadronic loops and can effectively probe Beyond the Standard Model phenomena.

The most recent measurement [162], conducted by Fermilab's E989/Muon g-2 experiment, places the average value of a_μ at

$$a_\mu^{\text{exp}} = 116592059(22) \cdot 10^{-11}. \tag{7.3}$$

It is compatible with the previous measurement by the same experiment [166] and early results of the E821 experiment at Brookhaven National Laboratory [167]. They are shown in fig. 7.1. Since the main source of uncertainty is statistical, the precision is expected to increase about twofold as more data is collected and analysed. In addition, an independent study with competitive precision is foreseen from the muon g-2/EDM experiment at J-PARC and will be an important contribution, because of a different approach to the measurement [168].

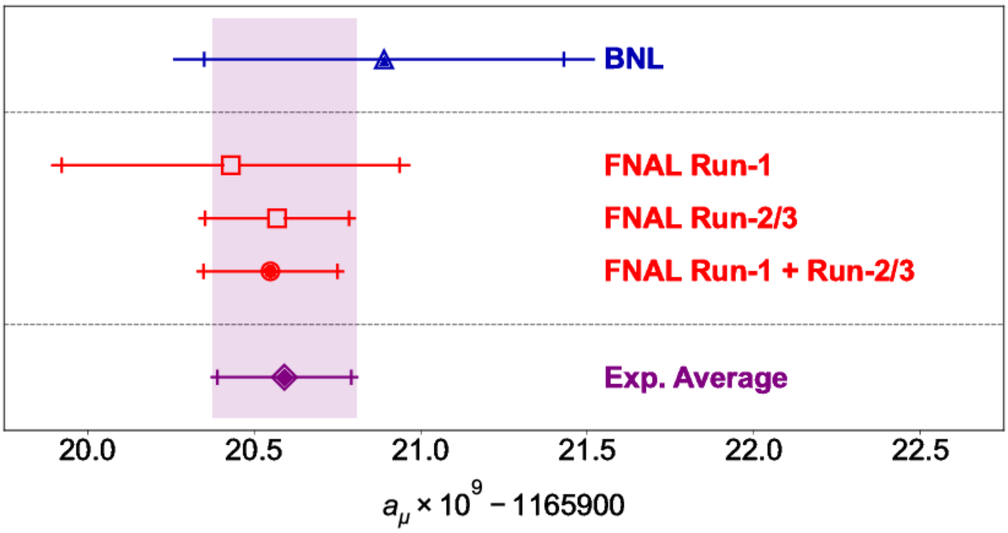

FIGURE 7.1: Values of α_μ measured experimentally by the E821 (BNL) experiment at Broohaven National Laboratory and Muon g-2 (FNAL) experiment at Fermilab. Vertical marks indicate statistical part of the total uncertainty. Figure taken from [162].

The value of a_μ, evaluated within the SM framework using a data-driven approach [169], is:

$$a_\mu^{\mathrm{SM}} = 116591810(43) \cdot 10^{-11}, \tag{7.4}$$

which yields a difference exceeding five standard deviations. On the other hand, calculations performed with lattice QCD [164] seem to be more compatible with the measured value, although a direct comparison is difficult due to their dependence on the computational model used. The difference between predictions obtained using both methods is illustrated in fig. 7.2, where the experimental result is taken from a previous Fermilab study [170] (preceding one shown in fig. 7.1).

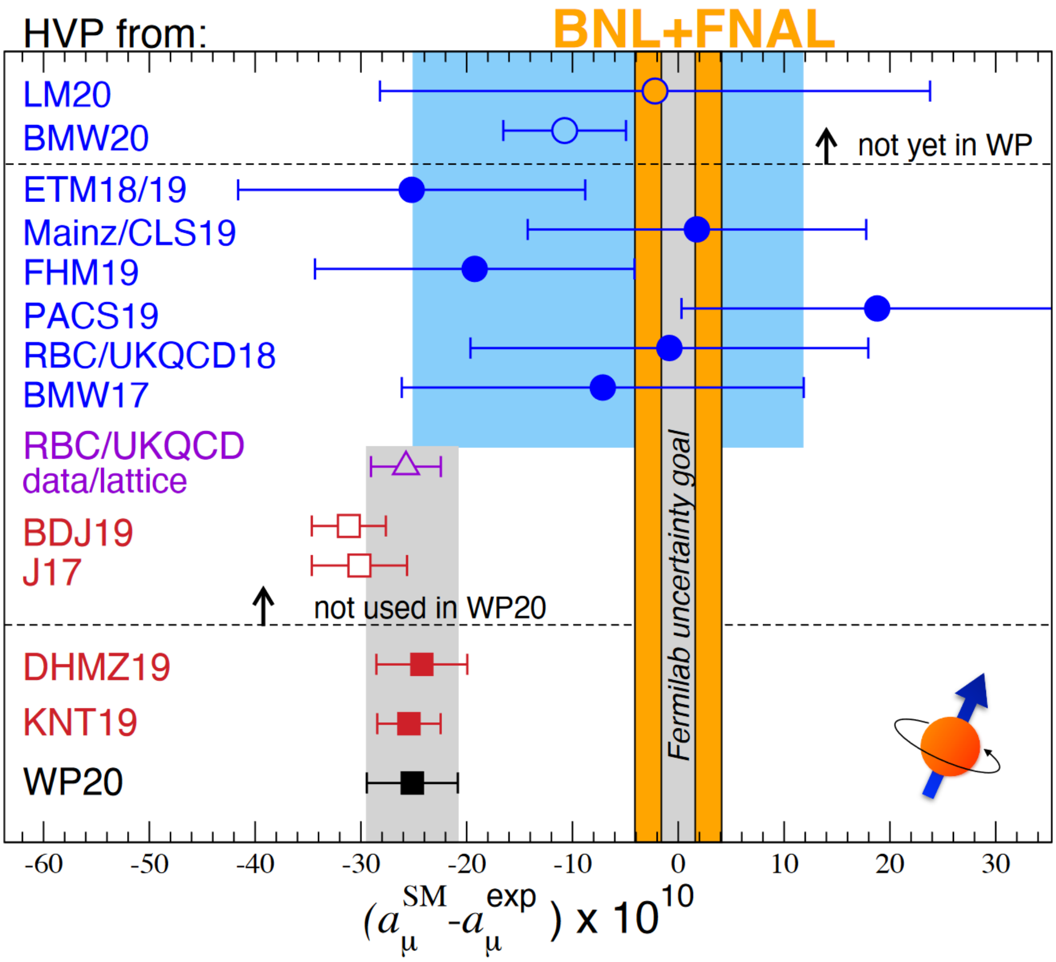

FIGURE 7.2: The experimental average of α_μ, including measurements up to the 2021 result of Muon g-2 experiment at Fermilab (shown as orange band), and Standard Model predictions evaluated using different methods. Results shown as circles are based on lattice QCD calculations and squares on data-driven approach. The triangle shows a hybrid evaluation combining both. Figure taken from [170].

The structure of a_μ^{SM}

Contributions giving rise to a non-zero value of a_μ^{SM} correspond to the three fundamental interactions – electromagnetic, weak and strong. The first two can be calculated with desired precision in the framework of quantum electrodynamics, while the strong term dominates the uncertainty. In particular, its two main components – Hadronic Vacuum Polarization and Hadronic Light-by-Light – are non-calculable from first principles. The Leading Order Feynman diagrams are illustrated in fig. 7.3.

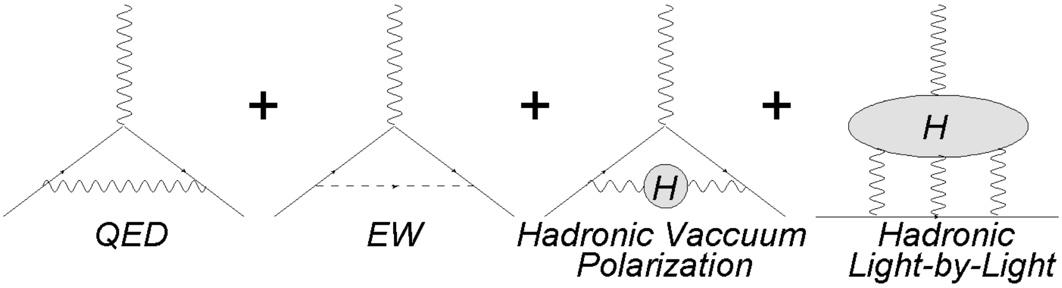

FIGURE 7.3: Leading Order processes contributing to a_μ^{SM}. From left to right – the electromagnetic, electroweak and two main strong interactions.

The electromagnetic term (a_μ^{QED}) is the largest in value and originates in the emission and absorption of virtual photons, combined with the subsequent pair creation and annihilation. It can be expressed as a sum of terms dependent on the mass ratios of electrons, muons and tau leptons (m_e, m_μ and m_τ respectively) [169]:

$$a_\mu^{QED} = A_1 + A_2\left(\frac{m_\mu}{m_e}\right) + A_2\left(\frac{m_\mu}{m_\tau}\right) + A_3\left(\frac{m_\mu}{m_e}, \frac{m_\mu}{m_\tau}\right), \tag{7.5}$$

where each A_i can be calculated by a perturbative expansion in α/π:

$$A_i = \left(\frac{\alpha}{\pi}\right) A_i^{(2)} + \left(\frac{\alpha}{\pi}\right)^2 A_i^{(4)} + \left(\frac{\alpha}{\pi}\right)^3 A_i^{(6)} + \cdots \tag{7.6}$$

and α is the fine structure constant. The most precise calculation so far has been performed up to the tenth order, resulting in a value of:

$$a_\mu^{QED(10)} = 116584718.931(104) \cdot 10^{-11}. \tag{7.7}$$

The electroweak term (a_μ^{EW}) includes all loop contributions involving the exchange of $\mathrm{W}^\pm$, Z^0, Higgs bosons and neutrinos. It has been calculated up to the leading three-loop term, which has been found to be effectively negligible at the level of required precision. Consequently [169]:

$$a_\mu^{EW(2)} = 153.6(1.0) \cdot 10^{-11}. \tag{7.8}$$

Strong contribution (a_μ^{QCD}) can be divided into two independent interactions – Hadronic Vacuum Polarization and Hadronic Light-by-Light (denoted by a_μ^{HVP} and a_μ^{HLbL}, respectively). The former originates in quantum fluctuations of strongly interacting particles, usually quark-antiquark pairs. The latter is a consequence of photon interaction producing another photon. In case of a muon's anomalous magnetic moment, an external on-shell photon interacts with three off-shell ones through a hadronic loop and those three couple to the muon. Both are fundamentally non-perturbative. The most precise values evaluated using data-driven methods are currently [169]:

$$a_\mu^{HLbL} = 92(19) \cdot 10^{-11} \tag{7.9}$$
$$a_\mu^{HVP} = 6845(40) \cdot 10^{-11}. \tag{7.10}$$

Their combined uncertainty constitutes approximately 99.8% of the total uncertainty of a_μ^{SM}. In fact, it is dominated by the leading order a_μ^{HVP} term:

$$a_\mu^{HVP,LO} = 6931(40) \cdot 10^{-11} \tag{7.11}$$

$$a_\mu^{HVP,NLO} = -98.3(7) \cdot 10^{-11} \tag{7.12}$$

$$a_\mu^{HVP,NNLO} = 12.4(1) \cdot 10^{-11}. \tag{7.13}$$

Owing to the presence of hadronic loops, both are also the most sensitive to BSM phenomena. A more precise evaluation of $a_\mu^{HVP,LO}$ is thus crucial and provides the main motivation for MUonE experiment.

7.2.2 Dispersive approach to a_μ^{HVP} measurement

At present, the most precise way of evaluating a_μ^{HVP} is based on dispersion relations, which lead to the expression involving an integral over hadronic cross-sections [163]. In particular, the leading order term of Hadronic Vacuum Polarization can be written as:

$$a_\mu^{HVP,LO} = \frac{\alpha^2}{3\pi^2} \int\limits_{4m_\pi^2}^{\infty} ds \, \frac{K(s)}{s} R(s), \tag{7.14}$$

where m_π is the rest mass of a pion, $K(s)$ is the kernel function and $R(s)$ is the hadronic ratio. It is expressed as:

$$R(s) = \frac{\sigma^0 \left(e^+e^- \to \text{hadrons}\,(+\gamma)\right)}{\sigma_{pt}}, \tag{7.15}$$

where

$$\sigma_{pt} = \frac{4\pi\alpha^2}{3s}. \tag{7.16}$$

The σ^0 is a cross-section of electron-positron pairs annihilating into hadrons and includes primarily processes where pions and photons are produced. Because it is measured experimentally, it has an inherent uncertainty and is subject to various detector related effects. Furthermore, the spectrum contains many sharp resonances, which necessitate collection of large amounts of data to achieve required precision of integration. An example distribution contributing to σ^0 is illustrated in fig. 7.4.

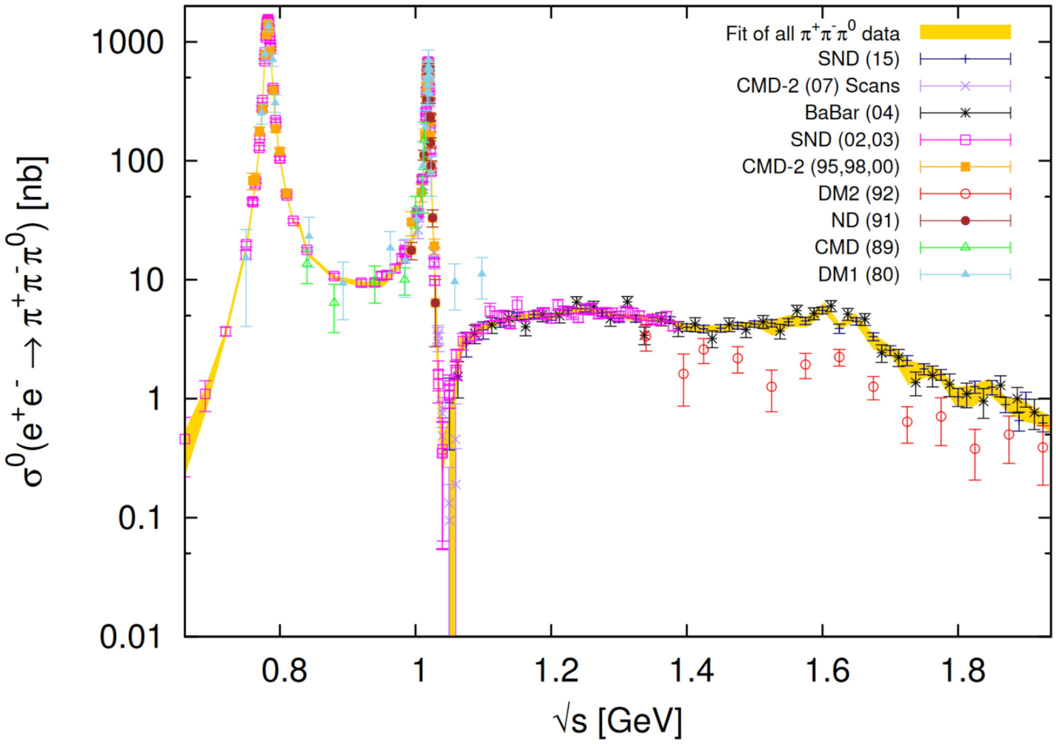

FIGURE 7.4: An example of a hadronic production cross-section used in data-driven evaluation of the non-perturbative part of a_μ. The ticks show measurements from various experiments as a function of the centre-of-mass energy. A combined fit is shown with the orange band. Figure taken from [163].

7.2.3 New approach using $\mu e^- \to \mu e^-$ elastic scattering

As an alternative to the existing data-driven approach, the MUonE experiment [9] has been proposed to precisely measure the running of electromagnetic coupling constant ($\alpha(t)$) in the space-like region. The Leading Order term of a_μ^{HVP} can then be expressed as an integral of its hadronic part ($\Delta\alpha_{had}$):

$$a_\mu^{HVP,LO} = \frac{\alpha}{\pi} \int_0^1 dx\ (1-x)\, \Delta\alpha_{had}\left[t(x)\right], \tag{7.17}$$

which is evaluated at the squared momentum transfer t:

$$t(x) = \frac{x^2 m_\mu^2}{x-1}. \tag{7.18}$$

The integrand is now a smooth function (as illustrated in fig. 7.5) and can be evaluated with much higher precision than the hadronic cross-sections, resulting in a significant reduction of a_μ^{SM} uncertainty. Furthermore, the running of α can be written as:

$$\alpha(t) = \frac{\alpha_0}{1 - \left(\Delta\alpha_{lep}(t) + \Delta\alpha_{had}(t)\right)}, \tag{7.19}$$

where the leptonic part, $\Delta\alpha_{lep}$, can be calculated using perturbative expansion. The effective coupling $\alpha(t)$ will be determined experimentally by measuring the differential cross-section shape of highly energetic muons scattered on atomic electrons in a target with low atomic number. Both are related by the effective Born cross-section σ_0 with:

$$\frac{d\sigma}{dt} = \frac{d\sigma_0}{dt}\left|\frac{\alpha(t)}{\alpha_0}\right|^2, \tag{7.20}$$

where t becomes $2m_e^2 - 2m_e E_e$.

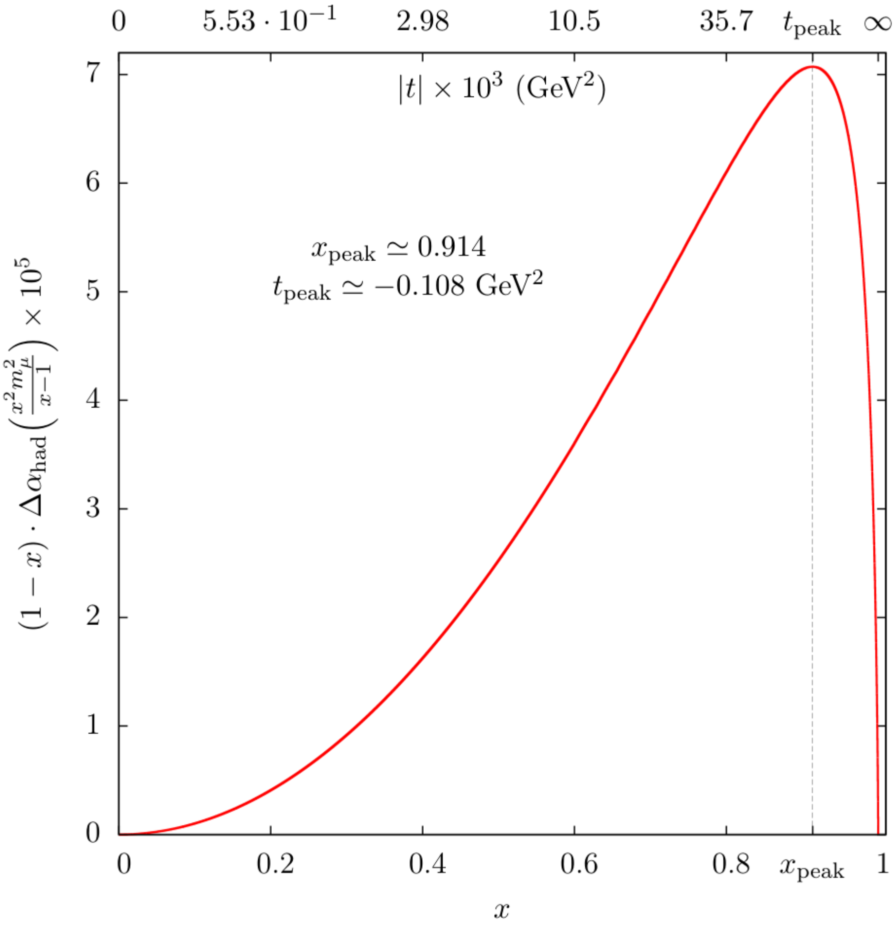

FIGURE 7.5: An integrand appearing in eq. (7.17), from which the value of $a_\mu^{HVP,LO}$ is calculated. Figure taken from [9].

Importantly, the kinematics of this system are predictable – the scattering angle of the electron (θ_e) and its energy (E_e) are strictly correlated with those of the muon (θ_μ, E_μ) and determined by the beam energy (E_{beam}):

$$E_e = m_e \frac{1 + r^2 \cos^2\theta_e}{1 - r^2\cos^2\theta_e} \tag{7.21}$$

$$\theta_e = \arccos\left(\frac{1}{r}\sqrt{\frac{E_e - m_e}{E_e + m_e}}\right), \tag{7.22}$$

where

$$r = \frac{\sqrt{(E_{beam})^2 - m_\mu^2}}{E_{beam} + m_e} \tag{7.23}$$

The theoretical correlation of electron and muon scattering angles is illustrated in fig. 7.6, where the different values of x variable can be related to fig. 7.5. Moreover, the correlation between scattering angles and differential cross-section allows to divide the reconstructed events into an elastic signal (close to the peaks in figs. 7.5 and 7.6) and normalisation region dominated by multiple scattering (far from the peaks). In turn, the common systematic uncertainties can be greatly suppressed by measuring the ratio of the corresponding cross-sections.

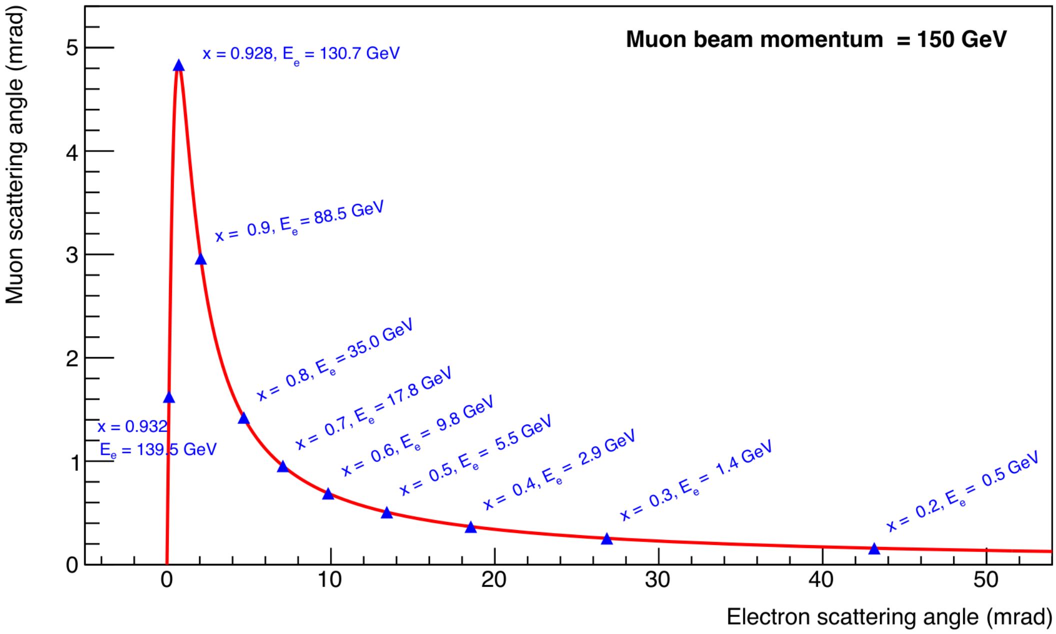

FIGURE 7.6: Correlation between scattering angles of muon and electron for beam momentum of 150 GeV. Ticks indicate points on the curve corresponding to different values of the scattered electron energy and the x variable, as defined in eq. (7.17) and shown in fig. 7.5. Figure taken from [9].

7.3 MUonE detector

The primary challenge faced by the MUonE experiment is achieving precise control over systematic effects – especially related to the software detector alignment, particle identification and event reconstruction efficiencies. The available material budget is also greatly limited, in order to minimise the impact of electron multiple scattering. For this reason, a modular design has been adopted. The detector consists of a series of independent stations – each being approximately a metre long and comprising a beryllium target with a series of tracking layers. This approach provides redundancy and scalability, while allowing to achieve a sufficiently high data collection rate with relatively thin targets. In the long-term, MUonE aims at operating 40 stations with an electromagnetic calorimeter and muon filter downstream of the detector (as illustrated in fig. 7.7). It will be mounted in the CERN North Area and use the M2 muon beam of CERN SPS (see section 3.2). It can provide muons with a variety of momenta and intensities, but the typical operating conditions are expected to be approximately 170 GeV and $10^7 \mu/\mathrm{s}$, respectively. The readout electronics will operate at 40 MHz frequency, resulting in 1.25 muons, on average, during SPS spill duration.

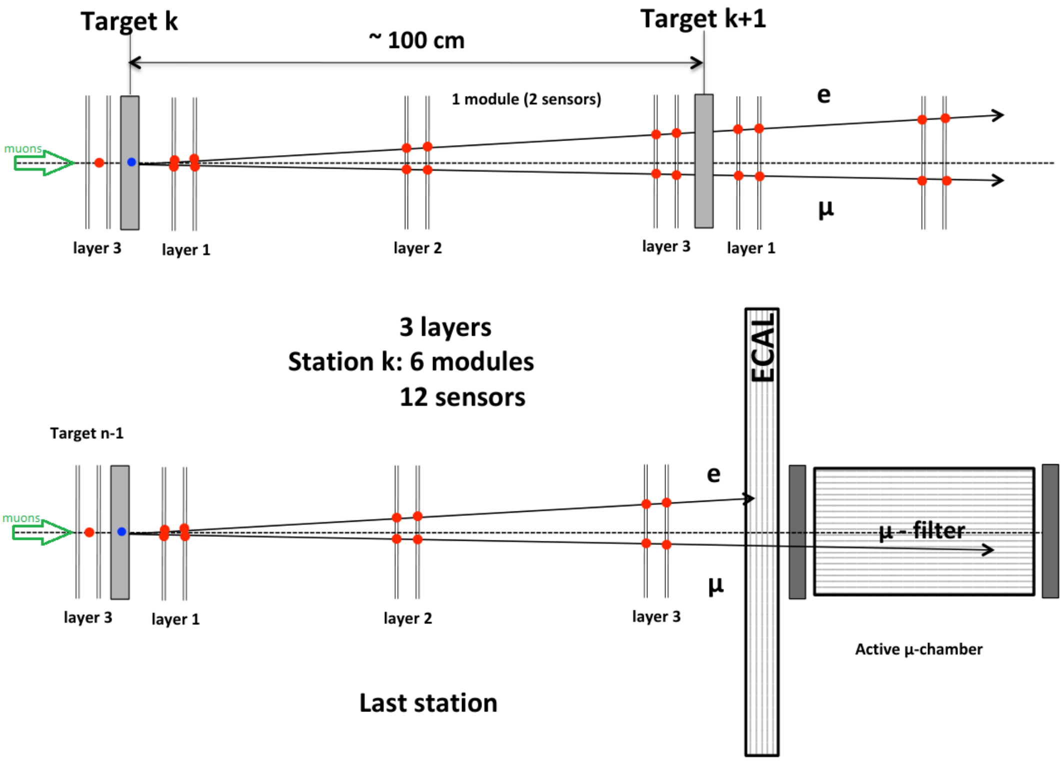

FIGURE 7.7: Schematic view of the MUonE detector. The top part shows one of the consecutive tracking stations, comprising a target and six silicon strip modules. The bottom illustrates the very last station, followed by an electromagnetic calorimeter and muon detection system. Figure taken from [9].

Each tracking station (fig. 7.8) starts with an approximately 15 millimetre thick beryllium target (assuming 40 stations, this sums up to an overall thickness of 60 centimetres). Track reconstruction is performed independently in each station, using hits from six silicon-strip modules. Four of them are installed pairwise at the beginning and end of the station, with each pair providing an independent measurement of the x and y coordinate. They are also tilted by 13.35 degrees towards the beam axis, to further increase the position resolution. The remaining two are rotated by a ±45 degree angle to form an additional (u, v) stereo plane in the middle of the station. The outermost modules are used to form a collection of 2D lines in the two orthogonal planes (ZX and ZY, where Z is the beam axis), which are later combined into 3D tracks, using information from the stereo plane to remove ambiguity. The detector components and data acquisition system are briefly discussed in the subsections below.

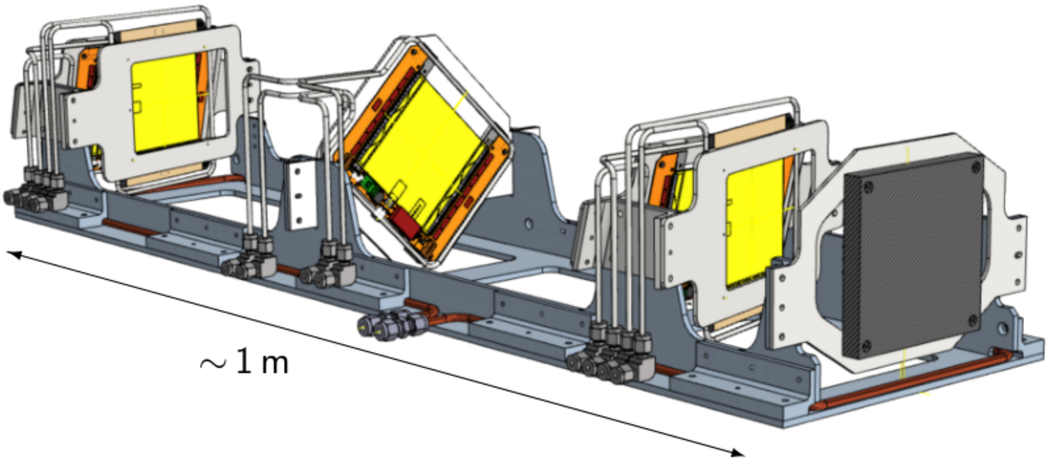

FIGURE 7.8: Model of a single MUonE tracking station. Figure taken from [171].

7.3.1 Tracking modules

The silicon strip sensors used in MUonE detector are designed for high-luminosity upgrade of the CMS Outer Tracker [172] (the schematic is depicted in fig. 7.9). Their active area of 10-by-10 centimetres fully covers the necessary range of scattering angles (up to 30 mrad). Likewise, the strip pitch of 90 micrometres (1016 strips in total) guarantees the required intrinsic angular resolution of 0.02 milliradians. By design, the sensors are paired into 2S modules with a spacing of 1.8 millimetres between their geometrical centres. The strips are divided into symmetric halves and each side of the module is read out by a series of 8 CBCs (CMS Binary Chips) with 254 channels each (corresponding to $2 \cdot 1016$ strips). Information from both sensors is combined by the readout system into hit-like objects (described in section 7.3.3).

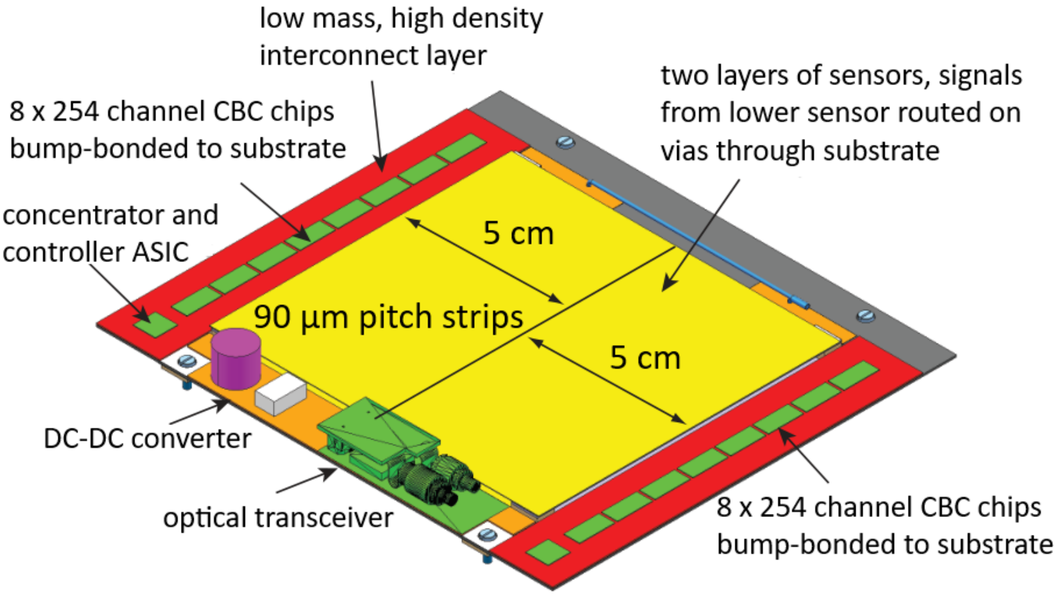

FIGURE 7.9: Schematic view of a 2S silicon strip tracking module used in MUonE tracking stations. Figure taken from [172].

7.3.2 Electromagnetic calorimeter and muon filter

The identification of muon and electron tracks will be based on a combination of an electromagnetic calorimeter and a muon filter, installed downstream of the detector. The former will comprise a grid of 23 centimetres long $PbWO_4$ crystals, each with a 2.5-by-2.5 centimetre surface, similar to ones used in the CMS electromagnetic calorimeter [173]. The overall size is chosen to provide an angular acceptance for electrons with energy above 10 GeV and a full containment of electromagnetic showers for energies above 30 GeV. Both systems are also important for the study of systematic effects, allowing for energy measurement and event selection.

7.3.3 Data acquisition and trigger system

Being designed for the CMS experiment, the data acquisition logic of MUonE detector works on a fixed 40 MHz clock of the LHC and is not synchronised with the M2 beam line (50 MHz). The mismatch introduces an expected pile-up of 1.25 muons per event. In addition, the data rate has to be reduced down to approximately 400 kHz, in order to make event recording possible.

A two-stage software trigger is planned. The initial reduction is achieved in a readout system, which processes signals from both sensors of each tracking module. One of the sensors is used to provide an initial set of hits, which are combined with those in the second one into non-overlapping pairs (so-called stubs). The ambiguity of matching is resolved primarily by restricting the maximum allowed distance between consecutive hits (in the module plane), in a way that is optimised for the detector design and kinematics of elastic scattering events. As a result, the collection of hits registered in all sensors is reduced to a collection of stubs associated with tracking modules. Each stub is characterised by two quantities – hit position in the base sensor and bend, which is defined as the distance between hits in both sensors (in the module plane). The first stage of the trigger will rely on a partial event reconstruction, performed in real time by a Field Programmable Gate Arrays (FPGA) circuit. The information will be used to reject events which do not match the elastic scattering signature (e.g. there are not enough hits registered to reconstruct the required number of particle tracks).

Accepted events will be subsequently passed to a second stage, where a full event reconstruction and selection will be performed online. In this way, the bottleneck of tape or disk storage can be mitigated, allowing for extracting high purity samples of processes under study from higher luminosity beams. In order to achieve offline reconstruction quality with the combinatorial complexity of each event (i.e. multiplicity of reconstructed tracks), a development of new computing techniques based on Graphics Processing Units (GPUs) is necessary.

7.4 Sensitivity of MUonE detector to exotic particles

The design of MUonE detector and clean experimental environment allow for an effective search for exotic long-lived particles decaying outside the target volume [174]. With the default detector configuration (as described in section 7.3), the available lifetime spectrum is restricted by the distance between the edge of the target and the first tracking sensor. The range of decay signatures is also limited by the configuration of the data acquisition system and trigger, which rejects events not compatible with the elastic scattering signal.

During dedicated runs, scheduled after the main measurement goal is achieved, the sensitivity can be significantly enhanced by adjusting the detector configuration. With data collected during normal operation, the focus will be placed on signatures with relatively low number of electrons and muons in the final state. The ideal candidates are thus processes where an additional light mediator (e.g. a dark photon or axion, see sections 2.3.2 and 2.3.3) is produced in the scattering and decays leptonically after travelling some distance from the target. Although, with trigger characteristics appropriately optimised, MUonE experiment may also look for decays of massive long-lived particles decaying into heavy quarks, since the tracking resolution allows for a good separation of close tracks in the resulting particle jets. What's more, their abundance would allow for a very precise reconstruction of the displaced vertex position, which is crucial to determine if it originated outside the target volume. Good candidates would be, for example, decays of Hidden Valley particles (see section 2.3.2).

A preliminary study has been conducted, focusing specifically on dark photons decaying into an electron-positron pair. It concludes that main backgrounds, expected to originate mainly in kaon and Λ hyperon decays, can be effectively vetoed using information from the calorimeter and particle identification. MUonE experiment is thus expected to provide sensitivity in the region of $m_{A'}$-ϵ parameter space (see section 2.3.2) not available with other detectors. Figure 7.10 shows the predicted coverage for two different search strategies, where the decay lengths are restricted by the distance from the target to the beginning of tracking system ($10 - 100$ mm) and considered masses are in range of $10 - 100$ MeV.

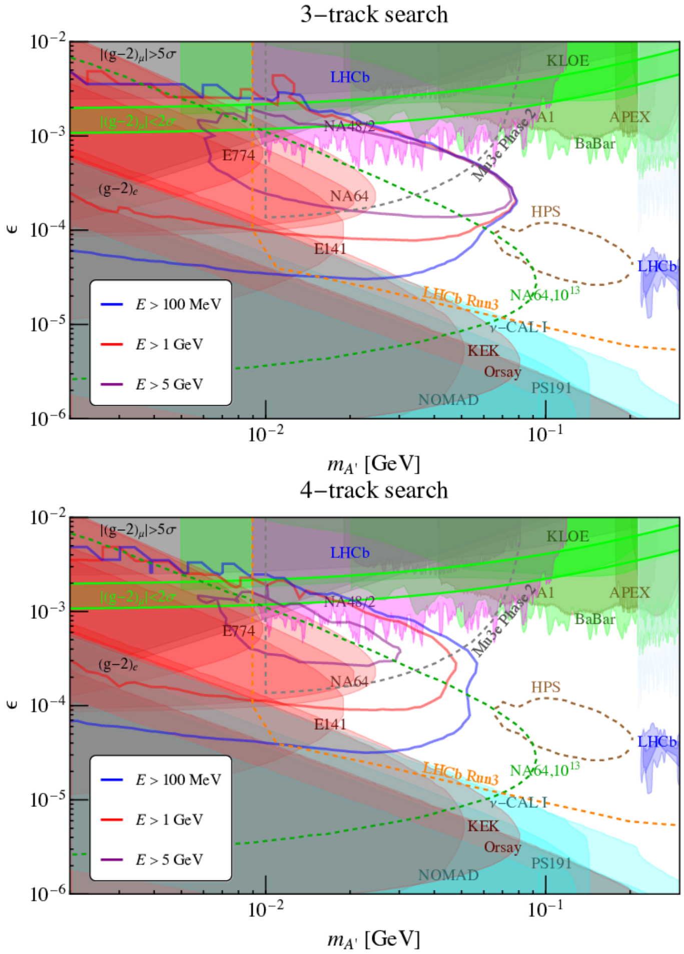

FIGURE 7.10: Dark photon phase space covered by different experiments. The top plot shows predictions for a search with three tracks required in the final state, and the bottom one – four. Shaded regions have already been excluded, dashed lines show predictions for future detectors and upgrades of those currently operating. Thick lines indicate parts available to MUonE with different colors representing different requirements on minimum electron energy. A 95% confidence level is assumed. Figure taken from [174].

Chapter 8

Event reconstruction and central software for the MUonE experiment

8.1 Introduction

The author of this thesis is the main developer and maintainer of the official event reconstruction and simulation software for the MUonE experiment (FairMUonE [175]), and has played a leading role in analysing data collected during the detector test-run in 2018 (published in the Journal of Instrumentation [3]). The present chapter focuses primarily on the reconstruction algorithms developed by the author and, in particular, how they can be used to search for exotic long-lived particle signatures. The FairMUonE software is briefly introduced as the experimental framework, while the results from the analysis are complemented with studies based on Monte Carlo simulation and used to evaluate the detector as well as software performance.

An overview of the MUonE experiment is presented in the preceding chapter 7. Section 8.2 briefly summarises the concept of FairMUonE software and the organisation of its event processing loop, and section 8.3 – generation of given processes and simulation of the detector. The main focus is placed on section 8.4, which describes the aforementioned event reconstruction algorithms. Section 8.5 discusses the evaluation of their performance, using collected data and Monte Carlo simulation. Finally, section 8.6 gives a summary and discussion.

8.2 FairMUonE software

Operation of the detector, along with the execution of planned measurements, requires development of a wide range of algorithms. To achieve the desired precision, the main focus has to be placed on maximising the efficiency and accuracy of reconstructing elastic μe^- scattering vertices. It is also necessary to perform a high quality software alignment, in order to account for the deviations of the detector from its idealised layout. Furthermore, the study of systematic uncertainties and background contributions necessitate an accurate simulation of the relevant physics processes and the corresponding detector response. Finally, a set of data analysis tools is needed to control the detector performance and validate collected data in real time.

The algorithms are implemented as a FairMUonE [175] package, which is based on the FairRoot [176], ROOT [135] and Geant4 [139] frameworks. The software offers tools for all major stages of the data acquisition and analysis, organized within an event processing model typical for high-energy experiments. Each stage is an independent algorithm with pre-defined configuration, input and output. The general pipeline for simulated events comprises the following algorithms:

- generation of Monte Carlo particles
- simulation of their passage through the detector
- simulation of detector's response and readout electronics
- event reconstruction
- preliminary event selection

The execution is flexible, allowing it to start at any stage of the pipeline and cover only a selected subset of steps. In particular, because the event reconstruction algorithms are designed to be the same for simulated events and collected data, they share the two final processing stages. In addition, FairMUonE provides algorithms for detector alignment and preliminary data analysis.

The algorithms used to produce Monte Carlo samples (the three initial steps) are described in section 8.3. Section 8.4 discusses event reconstruction and detector alignment. The data selection and analysis tools are not discussed in detail. The former is used primarily to reduce the size of output saved to disk by rejecting events, which did not pass the reconstruction or vertex quality requirements. The latter generates a set of control distributions, used to validate collected data. All major algorithms of the FairMUonE software, with an exception of detector readout simulation (discussed in section 8.3.2) and external packages (e.g. Monte Carlo event generators), were developed by the author of the present thesis.

8.3 Monte Carlo simulation

The precision of elastic scattering cross-section measurement is restricted primarily by the systematic effects. The main sources are related to the event reconstruction and selection efficiencies, background contributions, detector alignment and particle identification. In order to evaluate their impact, the physics processes have to be simulated and the detector has to be modelled with sufficient accuracy. In particular, the description of the elastic μe^- scattering process is required to include at least Next-to-Next-to-Leading-Order corrections. The same level of stringency is not necessary for the background processes, however, a relatively wide range of candidates has to be considered.

Generation of Monte Carlo particles and interactions is done in a twofold manner. If high accuracy is necessary or unusual calculations are considered (e.g. of exotic decays), FairMUonE interfaces a dedicated Monte Carlo event generator. Otherwise, the physical description implemented in Geant4 [139] package is used (section 8.3.1) – in particular, to simulate the propagation of particles through the detector matter and resulting secondary interactions (section 8.3.2). The simulation of tracking system readout electronics has been adapted from the CMS experiment, while the appropriate algorithms for the calorimeter are under active development (section 8.3.2).

8.3.1 Monte Carlo event generation

The most important processes for MUonE experiment physics program are the elastic μe^- scattering signal and the production of lepton pairs, which is the main background source for the primary measurement. The calculations of both are distributed as the Muon Electron Scattering with Multiple Electromagnetic Radiation (MESMER) [177–180] event generator, which is interfaced to FairMUonE as an external package. It provides accuracy of the elastic scattering description up to Next-to-Leading Order, with Next-to-Next-to-Leading Order corrections being developed. In addition, it is capable of simulating lepton pair production from the scattering of muons on nuclei ($\mu^\pm N \to \mu^\pm N l^+ l^-$) and electrons ($\mu^\pm e \to \mu^\pm e l^+ l^-$).

The remaining background sources (e.g. from nuclear interactions) are of less importance and are simulated using minimum bias events, where Geant4 package is used to produce interactions in the target volume during propagation of the generated beam muon. Furthermore, additional event generators are planned to be interfaced in the future, to provide simulation of exotic decays within different theoretical models.

8.3.2 Simulation of detector response

FairMUonE implements a flexible solution to define a detector with any number of tracking stations (with or without a target) and modules. The properties of each element can be defined globally, but also on a per-module and per-target basis. In particular, the geometry of modules may be modified freely, including switching between a one and two sensor configuration, changing the angle of tilt and the relative rotation of a stereo plane. Similarly, the targets may vary in thickness and material type. Simulation may also include a calorimeter comprising a crystal grid of any size.

The detector layout is automatically converted into a Geant4 compatible prescription. Furthermore, the settings provided by the package (e.g. accuracy of simulating electromagnetic showers in the calorimeter or number of steps considered while tracking the particle through a detector volume) are interfaced to FairMUonE.

The simulation of active detector elements results in a collection of energy deposits, which are associated with physical volumes and Monte Carlo particles. To make comparisons with collected data possible, they have to be converted into information consistent with the response of readout electronics of a real detector. It is done by two independent algorithms – one for the tracking system and one for the calorimeter. The former is adapted directly from the CMS experiment and only modified for compatibility with FairMUonE software.

Simulation of the response of tracking detectors

The initial stage of simulation translates the energy deposits, registered in tracking sensors, into binary responses from silicon strips. In order to increase the algorithm efficiency and decouple it from the (usually high) number of steps that Geant4 considers when tracking the particle through a volume, only the total deposit in each sensor is used. Instead, the path between entrance and exit point of a particle is split into 10 μm segments. The energy is distributed uniformly among their midpoints and rescaled to represent the number of induced electrons.

A drift of resulting charge clouds towards the collection points at the surface is then simulated by imposing a Gaussian smearing on the projected position, with magnitude determined by the distance travelled and diffusion coefficient. The resulting charge distribution at the surface is mapped to the grid of strips, but each deposit is allowed to contribute only to those within three standard deviations from the middle of the corresponding segment. If more than one strip is covered by the cloud, the contribution is distributed proportionally to the amount of overlap. Once all deposits are processed, the charge associated with each strip is modified with a Gaussian readout noise and if it is above a given readout threshold, the strip is considered activated. Consecutive active strips are combined into clusters, whose positions correspond to the midpoints of their centre strips (or points between the two centre strips if their number is even). The total energy contributed to the cluster by each Monte Carlo particle is associated with its identifier and saved for the purpose of linking to reconstructed tracks.

Finally, the clusters in both sensors of every module are paired to form stubs (matching the procedure used in the trigger, see section 7.3.3). One of them, depending on the detector configuration, is selected to be the seeding sensor. For each one of its clusters, a search for a matching one in the other (correlation) sensor is performed. Their maximum allowed distance is chosen to span the range of typical angles at which the particles may travel through the detector and the small separation between centres of both clusters (bend) is prioritised. The collection of stubs is saved and used as an input for the event reconstruction algorithm.

Simulation of the response of a calorimeter

At present, the simulation of the calorimeter readout is under active development. The temporary implementation calculates the total energy deposit in each crystal and applies a smearing effect using a Gaussian distribution with mean equal to the baseline electronic noise and standard deviation proportional to the number of expected photoelectrons. This approach is sufficient to provide a semi-realistic prediction of the total deposited energy, which may be used for a preliminary study of various background veto scenarios and systematic uncertainties. More detailed analyses, such as matching energy deposits with reconstructed tracks, require further investigation.

8.4 Event reconstruction

A successful realisation of the MUonE physics program (precise measurement of hadronic contribution to α_μ and search for exotic long-lived particle signatures) relies primarily on reconstruction of three classes of interactions – the elastic scattering of beam muon on an electron in one of the targets (the signal process), production of e^+e^- pairs incited by the collisions (main background source) and, finally, a wide array of Beyond the Standard Model scenarios with an additional decay vertex outside the target volume. The remaining background sources do not require dedicated treatment and will be rejected based on the characteristics of reconstructed interaction vertices.

Elastic scattering candidates are searched for by matching pairs of tracks reconstructed in a given station with a single track in the preceding one (outgoing and incoming tracks, respectively). Since the experiment is characterised by relatively low hit occupancy, all possible combinations can be considered within a reasonable CPU time limit. Furthermore, each candidate undergoes a kinematic fit procedure, where the tracks are fitted simultaneously to the collection of associated hits while also being required to pass through a common point inside the target volume. This serves two roles – it decreases the impact of multiple scattering on the reconstructed electron by anchoring it to, generally less affected, muon tracks and introduces a compact measure of how well the candidate fulfils the elastic signal hypothesis (in a form of a fit quality metric). Random combinations of tracks, which did not originate from the same interaction point, produce vertices with average fit quality lower than correct matching.

The dominant background contribution comes from the production of e^+e^- pairs. With three outgoing tracks in the interaction, they can form three vertex candidates with signal-like topology ($\mu \to \mu e^+$, $\mu \to \mu e^-$, $\mu \to e^+e^-$). While most of them can be rejected on the basis of their kinematic properties, an additional veto condition for the event may be provided by the presence of a high quality vertex candidate with three outgoing tracks. Such vertices are thus also searched for, with the reconstruction procedure appropriately adapted.

The detection of Beyond the Standard Model decays requires a more generic approach, as no initial assumptions on the event topology can be made. Their only distinguishing characteristic is the presence of two interaction vertices – one located within the target volume and the other displaced proportionally to the exotic particle's lifetime. Accordingly, the measurement focuses on two aspects – assigning the reconstructed tracks to appropriate vertices and determining vertex position along the beam axis with sufficient precision. The search for secondary vertices from relatively light long-lived particles is performed by testing all possible combinations of outgoing tracks. The vertices then undergo a kinematic fit and position estimation, allowing them to be tested for correct track assignment (fit quality) and position being compatible with the target volume. High multiplicity vertices are looked for with a two stage adaptive fitter (see section 8.4.3), which initially collects tracks using a distance-based seeding algorithm and then estimates the position of the resulting candidate, rejecting non-matching tracks in the process.

Event reconstruction starts with dividing the detector into logical sectors between consecutive targets (rather than considering physical tracking stations), which allows the algorithm to use all available hits if some of them are missing. Particle tracks are reconstructed independently in each sector and are subsequently used to form the vertices. Section 8.4.1 describes how the initial collection of stubs is converted into hits used in the reconstruction. Section 8.4.2 discusses the track reconstruction algorithm, section 8.4.3 the reconstruction of interaction vertex candidates and, finally, section 8.4.4 – the procedure of software detector alignment.

8.4.1 Hit construction

Before particle tracks are reconstructed, the information from the tracker readout system has to be transformed into a collection of points in the coordinate space. Because the detector is equipped with silicon strip sensors, each tracking module provides a position measurement only in one specific direction (perpendicular to the strips). Consequently, the hits are represented internally by (z, u, α) coordinates, where z is the position along the beam axis, u the perpendicular distance from this axis and α – the angle between the measurement direction of a given module and the positive direction of the X axis (an example is illustrated in fig. 8.1).

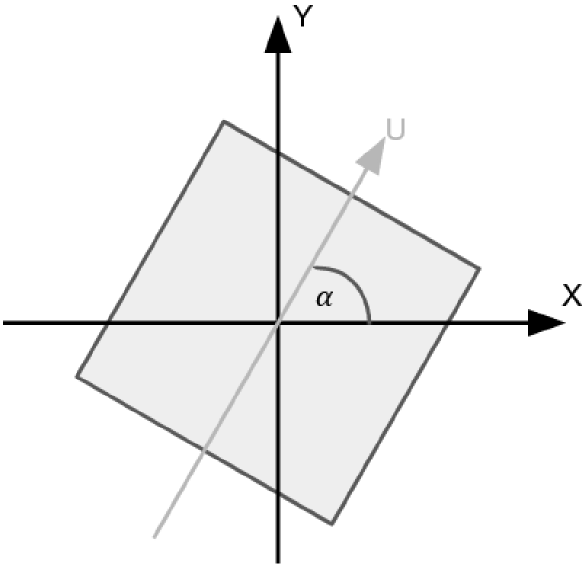

FIGURE 8.1: A global XY coordinate system of MUonE and local U coordinate axis of a tracking module rotated by the angle $\alpha = 30$ degrees.

For every event, a collection of stubs (discussed in sections 7.3.3 and 8.3.2) is loaded from either collected data or previous step of the simulation. They are converted into a unified hit format and assigned to their corresponding tracking modules. A stub is characterised by two numbers – the identifier of a centre strip of a cluster in the seeding sensor and the distance between cluster centres' in both sensors (bend). A tracking module is defined by the position of its geometrical centre along the beam axis z_{mod}, the rotation angle α and tilt angle θ. The conversion is done in two steps – first, the position u' in the module plane is averaged between both sensors and shifted to align the module midpoint with the origin of global coordinate system:

$$u' = \left(\text{cluster centre} + 0.5 \cdot \text{bend} + 0.5 - 0.5 \cdot \mathrm{N}_{\text{strips}}\right) \cdot \frac{\text{sensor length [cm]}}{\mathrm{N}_{\text{strips}}}, \tag{8.1}$$

where $\mathrm{N}_{\text{strips}}$ is the total number of strips in a sensor and the additional 0.5 factor moves the position from the edge to the centre of the strip. The u' is then assigned to the geometrical middle of the module z_{mod} (fig. 8.2, left). In the second step, the module tilt is accounted for by calculating the positions in a plane perpendicular to the beam axis, resulting in hit coordinates (fig. 8.2, right):

$$(z, u, \alpha) = (z_{\mathrm{mod}} - u' \cdot \sin\theta, u' \cdot \cos\theta, \alpha). \tag{8.2}$$

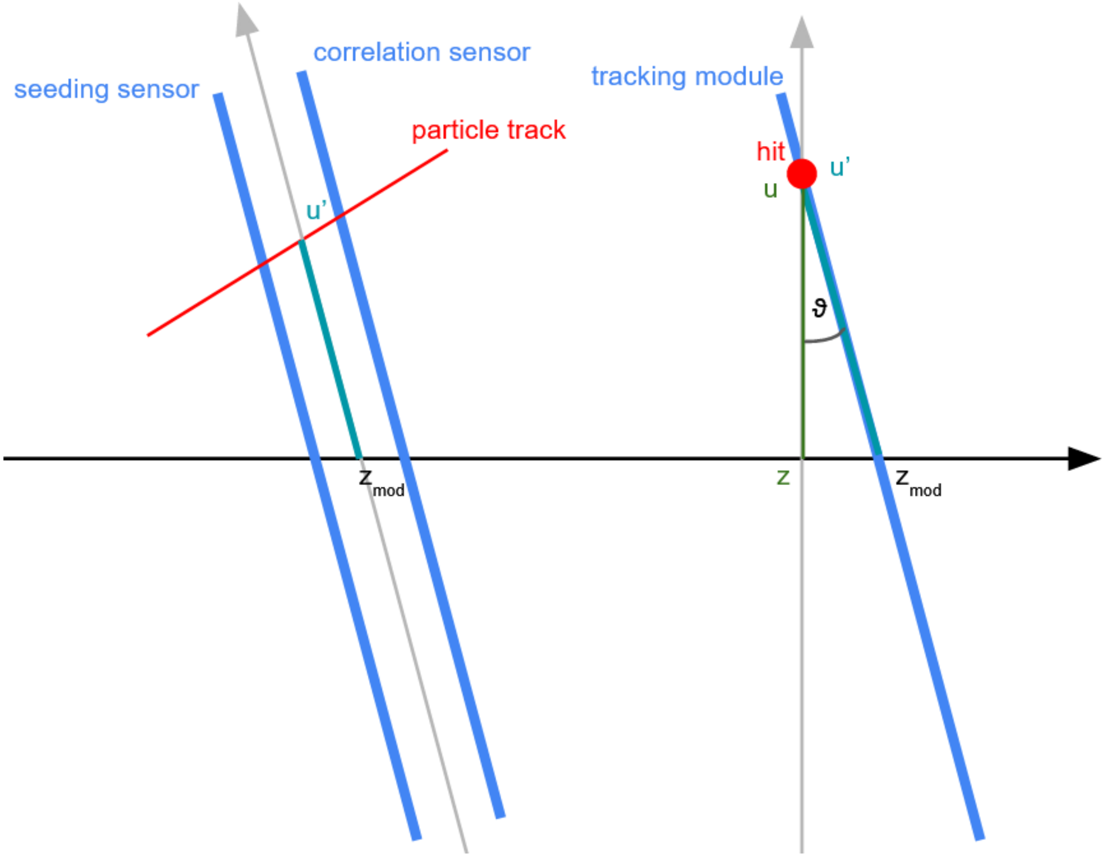

FIGURE 8.2: A hit position averaged between both sensors of a tracking module (left) and the conversion of a hit position in a tilted module (right).

8.4.2 Track reconstruction

With strip detectors being used, the reconstruction of track candidates has to be done in two stages. Initially, the hits registered in modules aligned with the X and Y coordinate axes are used to form 2D candidates (in the ZX and ZY plane, independently). Due to lack of magnetic field, they are considered to be straight lines with slope and intercept determined with a fit to the associated collection of hits. To maximise reconstruction efficiency, all hit collections which are even approximately compatible with lying on the same line are explored. However, with the default detector configuration (as shown in section 7.3, i.e. with 2 modules per projection), this step is equivalent to forming all unique pairs of hits at the beginning and end of the station.

The 2D candidates from both projections are then paired to form 3D track candidates (similarly, all possible combinations are tried and evaluated). Each track in the MUonE detector is defined by two line equations:

$$x(z) = a_x \cdot z + b_x \tag{8.3}$$

$$y(z) = a_y \cdot z + b_y, \tag{8.4}$$

each corresponding to one of the chosen 2D candidates. In order to reduce the ambiguity of matching, the candidates are tested for compatibility with hits from the stereo modules and rejected if none are found. Otherwise, the matching stereo hits are added to their respective collections and the tracks are refitted.

The set of remaining candidates still contains random hit combinations, which do not correspond to actual particles. A clone removal procedure is thus applied in order to select highest quality tracks with limited overlap of their hit collections. Although, a degree of hit sharing has to be allowed to preserve high reconstruction efficiency of close tracks. Finally, in simulated events, the reconstructed tracks are linked to generated Monte Carlo particles. The following subsections provide details of each step in the order they are executed in.

Reconstruction of 2D track candidates

The 2D track candidates are reconstructed independently in both ZX and ZY projections, using the same algorithm. Initially, the track seeds are formed from all unique pairs of hits registered in different modules. For each seed, a straight line is led through both hits and it undergoes an iterative hit assignment procedure. In each step, the line is tested for compatibility with hits in modules that haven't been used so far. If they match the criteria, they are included in the collection and the track parameters are fitted using a χ^2 minimisation algorithm. The procedure is repeated until no such hits are found. If the resulting collection is distinct from already existing ones, the candidate is added to the stack.

A perpendicular hit-line distance measure is used:

$$\mathrm{d}(\text{hit, 2D track}) = |u - (a \cdot z + b)|\,, \tag{8.5}$$

where u and z are the hit coordinates defined in eq. (8.2), and a and b are the slope and intercept of the line. During assignment, the closest hit is selected from each module, provided it is within a set distance window (taken by default to be ten standard deviations of the module's intrinsic resolution σ). The expression for χ^2, minimised in the fit, is defined as the sum:

$$\chi^2_{2D} = \sum_{\text{hits}} \left[\frac{\mathrm{d}\,(\text{hit, 2D track})}{\sigma_{\text{hit}}} \right]^2 , \tag{8.6}$$

performed over all hits associated with the candidate.

Reconstruction of 3D track candidates

Reconstruction of 3D track candidates starts with a collection of seeds, formed by all unique pairings of 2D ones from the previous step. For each candidate, the closest hit in each stereo module is added, if it is within the assignment window. While the condition is analogous to one used for 2D candidates, the assignment of stereo hits is done only once for each track to avoid potential bias introduced by refitting. The candidates which do not match with any stereo hit are rejected, as they are considered to be a combinatorial background. The remaining subset is fitted to their new hit collections.

To account for the relative rotation of x/y and stereo modules, the distance metric is generalised. It is calculated by projecting a point on the track at hit's z position onto a measurement direction α of the module it was registered in. Given a track described by eqs. (8.3) and (8.4) and hit with coordinates defined in eq. (8.2), the distance is:

$$\mathrm{d}(\text{hit, 3D track}) = |u - (x\,(z) \cdot \cos\alpha + y\,(z) \cdot \sin\alpha)|\,. \tag{8.7}$$

With an ideal detector model (i.e. no misalignment), the distance calculation for x and y modules (with α being 0 and 90 degrees, respectively) reduces back to eq. (8.5). This approach yields an additional benefit of making the stereo modules independent of x and y, rather than requiring a transformation of hits from UV into XY plane. Consequently, a higher reconstruction efficiency can be achieved as only one stereo hit is required to be matched with a candidate if the other is lost, for example, due to the module hit reconstruction inefficiency. The additional combinatorial background, introduced by allowing candidates with only one stereo hit associated, is counteracted by the clone removal procedure, where candidates with more hits are preferred.

The expression for χ^2, minimised during fit, is of the same form as for 2D candidates:

$$\chi^2_{3D} = \sum_{\text{hits}} \left[\frac{\mathrm{d}\,(\text{hit, 3D track})}{\sigma_{\text{hit}}} \right]^2 . \tag{8.8}$$

However, there are two major differences. The fit is now performed iteratively and in each step the outlier hits, whose contribution to the sum is greater than a certain threshold, are removed. The exact value of this threshold has to be optimised for a particular analysis based on simulated Monte Carlo events. The candidates, which become ill-defined in the process (have less than two hits in the ZX or ZY plane assigned or lack at least a single stereo hit) are rejected. The second difference is the inclusion of uncertainty originating in multiple scattering of particles passing through the tracking modules. Since no momentum determination or particle identification is available at this point of reconstruction, it is done under the assumption that all track candidates are muons with energy equal to the average beam energy and travelling downstream the detector. This correction is always underestimated by definition, hence the fit quality and resulting χ^2 value estimation are universally improved. Furthermore, accounting for multiple scattering increases the precision of detector alignment performed using beam muon tracks (see section 8.4.4).

The contribution to hit position uncertainty from a single element of detector geometry is calculated using the Gaussian dispersion approximation for thin targets:

$$\sigma_{MS} = 13.6 \cdot \Delta z \cdot \sqrt{x_0} \cdot \frac{1 + 0.038 \log x_0}{p}, \tag{8.9}$$

where Δz is the distance between the hit and detector volume, x_0 the ratio of thickness to material's radiation length and p – the momentum of a particle, which in this case is taken to be the average value of beam momentum.

Clone removal

To reject clone tracks (which are reconstructed using overlapping collections of hits), the 3D candidates are sorted based on their quality. The metrics are (in order):

- the overall number of assigned hits,
- the number of assigned stereo hits,
- and the χ^2 of a fit,

hence tracks compatible with more registered hits are preferred. The list is then traversed from worst to best candidate and those which do not pass the requirements are removed. In particular, they are not allowed to share more than a predefined number of hits with a better candidate. No assumptions, however, are made on how many shared hits should be allowed and in which modules, as both have to be optimised for a given detector configuration and analysis.

Monte Carlo particle matching

In case of simulated events, the reconstructed tracks are also matched to corresponding Monte Carlo particles. Since a single sensor strip can be activated by a combination of charge deposits, a one-to-one association of hits and particles is not possible. Instead, the procedure uses information about individual deposits and particles associated with them, registered during the simulation of tracking readout system (section 8.3.2). For each particle identifier appearing among the hits in track's collection, a weighted sum is calculated:

$$w_{\text{id}} = \sum_{\text{hits}} w_{\text{hit}} = \sum_{\text{hits}} \frac{1}{(1 + p_{\text{hit/id}})}, \tag{8.10}$$

where, for each hit, $p_{\text{hit/id}}$ is the position of the identifier in the list of deposits sorted by their size – thus the particle that contributed the most charge to the hit is assigned weight 1, the second one $1/2$ and so on. If the identifier does not appear for a given hit, the weight from that hit is zero.

The Monte Carlo particle with the highest value of the above sum is considered to be linked with the reconstructed track. The quality of this assignment is determined by the ratio of the number of hits associated with the linked particle and the total number of hits used to reconstruct the track.

8.4.3 Reconstruction of elastic μe^- scattering and exotic decay vertices

The elastic μe^- scattering vertices have a fixed topology, with one particle track entering the target volume and two tracks exiting. For each target in the detector configuration, the candidates are thus formed by all such unique triples. Because the reconstructed track multiplicity is relatively low on average, all of them can be fully processed and saved for further analysis. For each vertex, its position is estimated by finding a point in coordinate space which minimises the distance of closest approach to all three tracks. Next, they undergo a kinematic fit procedure where the tracks are refitted to their respective hit collections, while being forced to go through a common point in the target volume. The coordinates of this point can be taken from the preceding position determination or fitted alongside the track parameters.

Moreover, considering the reconstructed vertex as an elastic scattering candidate allows for labelling the outgoing tracks as corresponding to a muon and electron. Under this hypothesis, the momenta can be determined from their theoretical dependence on the scattering angles and a full treatment of multiple scattering uncertainty is possible. At present, due to lack of dedicated particle identification system, the electron is always assumed to be the track with larger scattering angle. While this assumption may be wrong for angles below approximately 5 mrad (fig. 7.6), the multiple scattering correction is then suppressed by high particle momenta and does not impact the fit quality significantly.

Similar algorithms were also developed for vertices with higher number of outgoing tracks and can be used to detect background events with lepton pair production or decays of light exotic particles. However, they applicability is greatly limited by the exponential increase in the number of potential candidates as higher multiplicities are considered. In order to provide sensitivity also to decay signatures of long-lived particles with more complex final states (e.g. containing particle jets), an adaptive secondary vertex reconstruction algorithm has been implemented. It focuses primarily on detecting tracks which are likely to originate from the same interaction and determining the position of a resulting vertex. In this case, a precise reconstruction is not required, as such interactions are expected to be incredibly rare and candidates can be studied in detail individually. The details on each algorithm are given in the subsections below.

Determination of vertex position

The design of MUonE detector is not particularly sensitive to the position of interaction along the beam axis. Because particles travel at very low polar angles, even small deviations in the slopes of reconstructed tracks result in significant shift of the projected z position. Nevertheless, a degree of precision required to effectively test the hypothesis of vertex originating within the target volume is achievable. A qualitative example is provided in the following sections (see fig. 8.22).

In order to find the vertex position, the three spatial coordinates are varied to minimise its distance to all tracks simultaneously. The expression for χ^2 is defined as:

$$\chi^2 = \sum_{\text{tracks}} \left[\mathrm{d}\left(\text{vertex, track}\right)\right]^2, \tag{8.11}$$

where the sum is performed over all tracks assigned to the vertex. The distance d is calculated as the shortest point-line distance:

$$\mathrm{d}\left(\text{vertex, track}\right) = \left|\left(\mathbf{v} - \mathbf{p}_0\right) - \left(\left(\mathbf{v} - \mathbf{p}_0\right) \cdot \mathbf{n}\right)\mathbf{n}\right|, \tag{8.12}$$

where $\mathbf{v}$ is the position of the vertex, $\mathbf{p}_0$ a point on the track and $\mathbf{n}$ a normalised tangent vector. The tracks used as input to the algorithm are taken before the kinematic fit to avoid bias. In case of elastic μe^- scattering candidates, they are first refitted with accurate multiple scattering correction included in the uncertainty. Otherwise, only the baseline (assuming a muon with average beam energy) correction is used.

Kinematic vertex fit

The main source of systematic uncertainty is the multiple scattering of the electron as it travels through consecutive tracking modules. Its consequence is an increased spread of registered hits, which hinders the precision of scattering angle measurement. The muons, on the other hand, are impacted much less (behaving as minimum ionising particles) and can be used to anchor the electron track to a common interaction point. Because the hit spread increases the further the particle travels, it prevents the contributions from modules in the end of the station from shifting the track origin away from the vertex during fit. The achieved improvement in scattering angle resolution is significant, especially in the normalisation region of the phase space (a qualitative result is discussed further, see fig. 8.7).

The kinematic fit is performed by minimising the value of a sum of χ^2 of tracks associated with the vertex:

$$\chi^2_{\text{vertex}} = \chi^2_{\text{incoming muon}} + \chi^2_{\text{outgoing muon}} + \chi^2_{\text{electron}}, \tag{8.13}$$

where each term is defined as in eq. (8.8). The common interaction point is introduced by setting the intercepts of all tracks to the same value. The intercepts of constituent 2D tracks then correspond to the vertex position in the XY plane, which is fitted alongside the track slopes. To preserve fit stability, the z coordinate has to be excluded and is thus fixed in the middle of the target. The benefit of this assumption is the additional veto condition for vertices originating in a silicon of the tracking modules, where it increases the resulting value of χ^2_{vertex} dramatically.

Optionally, the kinematic fit can be performed with the vertex position (either in all three spatial coordinates or only along the beam axis) fixed to one determined in the preceding position fit. While it is needed for the hypothetical decays outside the target, the exact benefit of choosing one over the other for elastic scattering vertices is still to be studied. It is expected to depend on the experimental setup, particularly the thickness of the target.

Vertices from exotic particle decays

The MUonE detector is sensitive to a wide range of exotic long-lived particles, whose decay vertices may differ significantly in track multiplicity. Consequently, two alternative detection methods have to be considered. The candidates with relatively low number of outgoing tracks can be searched for by considering all unique combinations matching the decay topology. They can also be reconstructed with high quality, using the same algorithms as for the elastic scattering vertices, with sums in eqs. (8.11) and (8.13) extended to include the additional tracks. This method, however, is unfeasible if the multiplicity is high or not constant (e.g. for signatures with particle jets). An alternative solution is thus implemented, which distributes tracks into vertices based on the likelihood of originating from the same interaction.

Initially, the pair with the smallest distance of closest approach is found and taken to be the seed if it is smaller than an optimised threshold. Additional tracks are then assigned based on distance to the point of closest approach of the initial pair. After the seed is formed, the constituting tracks are excluded and the procedure is repeated. In the second stage, the position of each seed is determined with an iterative fit. The initial guess is made to coincide with the common point of closest approach of all tracks. Each track gets assigned a χ^2 metric, based on the fit quality and impact parameter with respect to assumed seed position. The tracks with χ^2 above an optimised maximum (χ^2_{max}) are removed from the seed. For the remaining ones, weights are calculated as:

$$w = \chi^2 \cdot \left(1 - \frac{\chi^2}{\chi^2_{max}}\right)^2 \tag{8.14}$$

and a weighted fit of the new seed position is performed. The purpose of the above expression is to decrease sensitivity to outlier tracks. After the fit, the values of χ^2 are recalculated for the new position and the procedure is repeated until the shift along the beam axis is below a set threshold. As a result, a collection of secondary vertices with position estimate is obtained.

8.4.4 Detector alignment

The misalignment of the actual apparatus from the idealized geometry, assumed during event reconstruction, is one of the primary sources of systematic uncertainty. In order to minimise its impact and achieve required measurement precision, a high quality software alignment of the detector is necessary. While it is under active development, a simplified approach has been implemented to allow for treatment of data collected in test runs, where the ultimate precision is not needed yet.

For each of the tracking modules, the corrections in five degrees of freedom are considered – the three spatial translations x_0, y_0 and z_0, and two rotations – α_0 (measurement direction) and θ_0 (tilt angle). The rotation around an axis perpendicular to sensor strips is found to have a negligible impact and is not taken into account. The corrections are introduced into the reconstruction algorithm by modifying the hit positions (calculated in eq. (8.2)):

$$
\begin{aligned}
z &= (z_{\text{mod}} + z_0) - u' \cdot \sin(\theta + \theta_0) && (8.15)\\
u &= u' \cdot \cos(\theta + \theta_0) + (x_0 \cdot \cos(\alpha + \alpha_0) + y_0 \cdot \sin(\alpha + \alpha_0)) && (8.16)\\
\alpha &= (\alpha + \alpha_0)\,, && (8.17)
\end{aligned}
$$

where the second term in eq. (8.16) transforms spacial shifts into a local coordinate.

The alignment is performed in two stages (described in the subsections below), using data events with only beam muon and no interactions. They are selected primarily by requiring only one stub per module being registered. The modules are first aligned with respect to each other, in each tracking station independently, which allows for a reliable track reconstruction. The tracks are then used to align each station with respect to the preceding one. Both stages are alternated until a convergence of corrections is achieved.

Internal alignment of a single tracking station

The internal station alignment starts with reconstructing tracks corresponding to the beam muon, with no alignment corrections applied. In addition, the reconstruction thresholds are loosened to increase the efficiency (e.g. the rejection of outlier hits during track fitting is disabled). For each module independently, the alignment parameters are then found by minimising its contribution to the combined fit χ^2 of all tracks. The minimised expression is thus a sum of residuals:

$$\chi^2 = \sum_{\text{hits}} [\mathrm{d}\,(\text{hit},\ \text{3D track})]^2\,, \tag{8.18}$$

where the distance function is defined as in eq. (8.7) and the sum is performed over hits registered in a given module and the reconstructed tracks they belong to.

The procedure is repeated until a convergence of parameters is achieved, with tightened reconstruction settings and starting from the corrections determined in a preceding iteration.

Relative alignment between stations

The stations are aligned with respect to the preceding one in order (moving downstream through the detector). To avoid considering many degrees of freedom at once, they are treated as rigid bodies and the corrections are transformed into local module corrections afterwards. The algorithm starts with rotational degrees of freedom to make tracks reconstructed in both stations (corresponding to the same beam muon) parallel. It is achieved by minimising the differences in their slopes (with tracks defined as in eqs. (8.3) and (8.4)):

$$\chi^2 = \sum_{\text{events}} \left(a_{x,1} - a_{x,2}\right)^2 + \left(a_{y,1} - a_{y,2}\right)^2\,. \tag{8.19}$$

Next, the spatial misalignment is accounted for by minimising the differences in the intercepts:

$$\chi^2 = \sum_{\text{events}} \left(b_{x,1} - b_{x,2}\right)^2 + \left(b_{y,1} - b_{y,2}\right)^2 . \tag{8.20}$$

8.5 Data analysis and algorithm performance studies

The current section gives an overview of two studies, where the FairMUonE software and algorithms were used. The first is a full analysis of the data collected in 2018, when the initial proof-of-concept detector was installed on the M2 beam line. The study was made possible by the introduction of the FairMUonE software and was performed with a leading contribution from the author of this thesis. The results were published in the Journal of Instrumentation [3]. The second one concerns the recent 2023 test beam, which was the first one with two fully equipped tracking stations, using hardware planned for the ultimate apparatus. Since the physics analysis of 2023 data is still ongoing and the final results are not published yet, only selected performance studies based on Monte Carlo simulation are discussed.

8.5.1 Analysis of 2018 test beam data

The 2018 test beam focused on validating the concept of MUonE experiment. The detector comprised two tracking stations, 8 millimetre thick graphite target and an electromagnetic calorimeter. The modules were also of significantly lower quality and resolution than ones envisioned for the ultimate apparatus. The detector was installed downstream of COMPASS spectrometer on the M2 beam line of CERN SPS (see section 3.2). The test was successful and proved the ability to extract a clean sample of elastic scattering events from the collected data.

Detector configuration

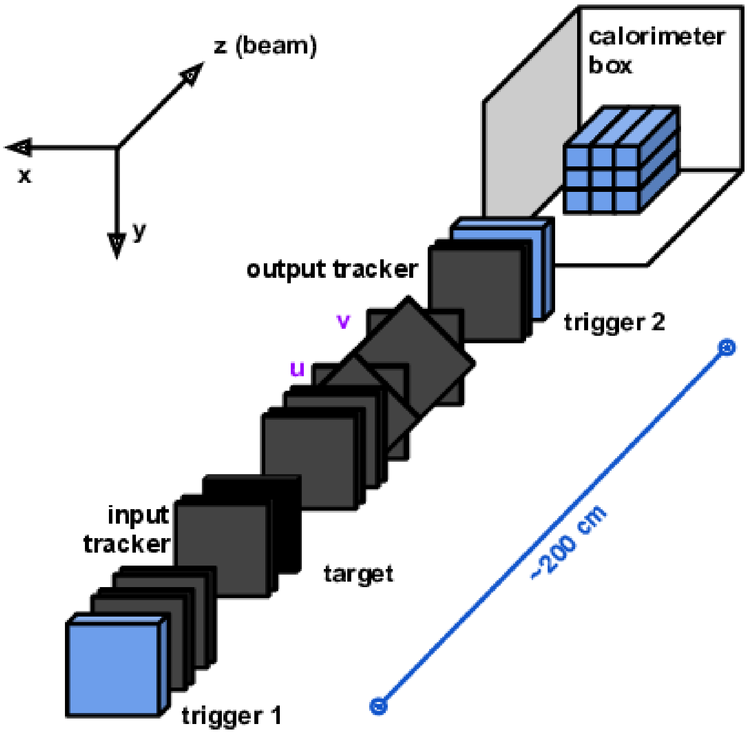

FIGURE 8.3: A schematic representation of the detector setup used during the 2018 test beam. The scintillating pads are shown in blue, the tracking modules in grey and graphite targets in black. Figure taken from [3].

The detector (illustrated in fig. 8.3) was equipped with silicon strip tracking modules manufactured for the AGILE experiment [181]. Each contains a single sensor with a 121 micrometre pitch (242 micrometre readout pitch), providing approximately 35 micrometres of the intrinsic spatial resolution. The sensors measure 9.293-by-9.293 centimetres, which is slightly short of the 10-by-10 centimetre target. A very robust detector layout was used, in order to account for the lower resolution. It consisted of 16 tracking modules (6 before and 10 after the target), although the stereo planes were included only in the second station. In addition, a pair of scintillating layers was installed on both ends and used as a trigger for beam muons.

An electromagnetic calorimeter, located downstream of the apparatus, was a makeshift construction, obtained by recycling the spare crystal blocks of the L3 endcap calorimeter [182]. It comprised a 3-by-3 grid of BGO crystals covered with a shielding paint – each being 23 centimetres thick and having a surface of 2.1-by-2.1 centimetres at the front and 2.8-by-2.8 centimetres downstream (fig. 8.4). Its measured energy resolution was $\sigma(E)/E = [(a/\sqrt{E})^2 + c^2]^{1/2}$, where $a = (3.73 \pm 0.36)\%\sqrt{\text{GeV}}$ and $c = (2.43 \pm 0.09)\%$ (fig. 8.5). The maximum energy was restricted to approximately 20 GeV to avoid saturation.

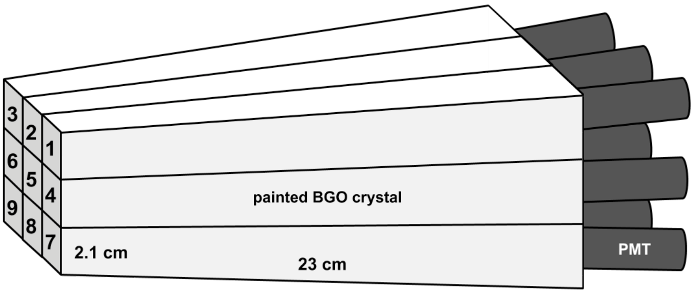

FIGURE 8.4: A schematic representation of the BGO calorimeter. Figure taken from [3].

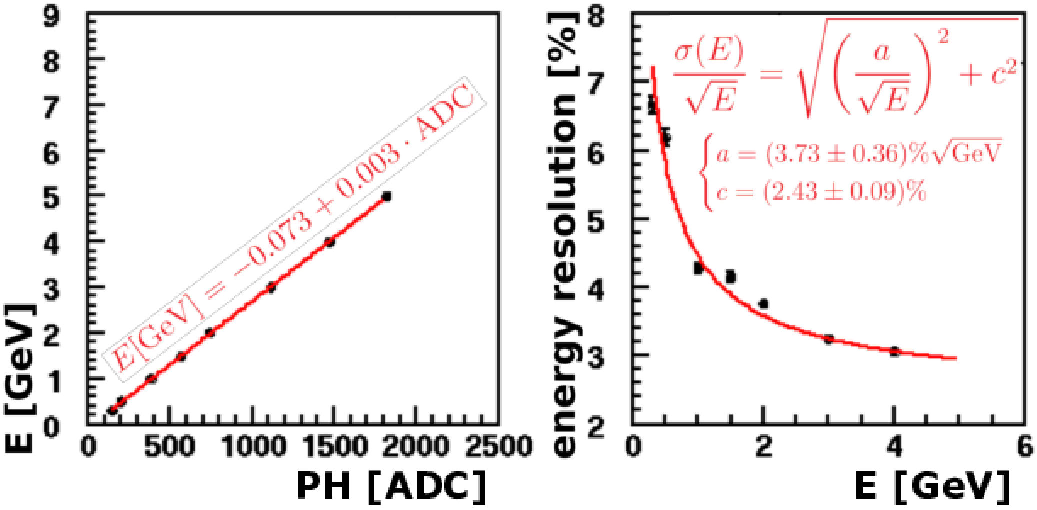

FIGURE 8.5: The measured resolution of the electromagnetic calorimeter as a function of the pulse height (left) and energy (right). Figure taken from [3].

Muon beam characteristics

The data was collected parasitically, with muons originating from the interactions of pions with the COMPASS apparatus and the beryllium hadron absorber. The resulting profile of the muon beam reaching MUonE detector is shown in fig. 8.6. The average intensity was approximately $0.6 \cdot 10^6$ particles per spill, with the momentum peak at 186 GeV and horizontal (vertical) divergence of 0.6 mrad (0.5 mrad).

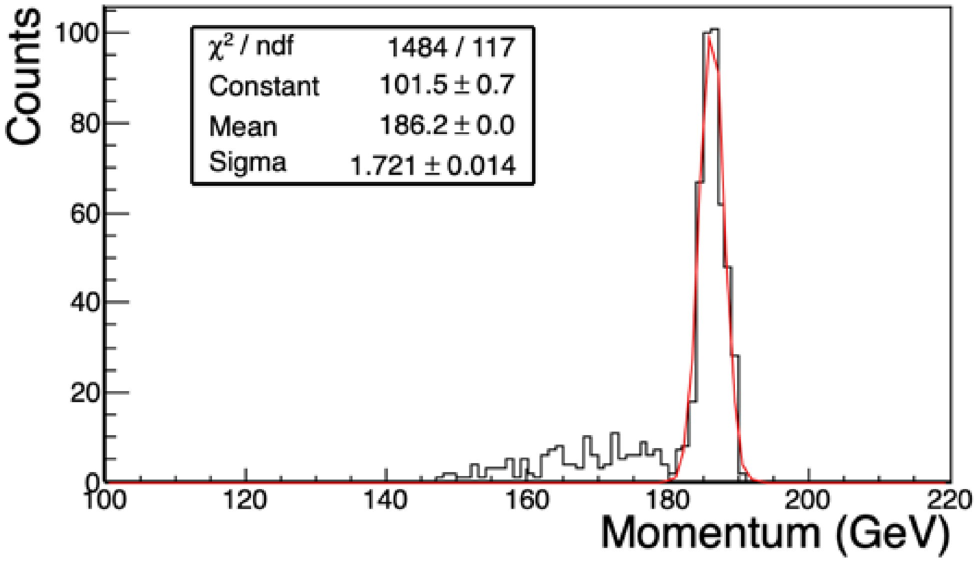

FIGURE 8.6: The profile of muon beam reaching MUonE apparatus. Figure taken from [3].

Dataset and simulated sample

The recorded dataset consisted of events, where activity was detected in the scintillating pads on both ends of the apparatus. Initially, they were required to have at least one hit registered in every module upstream of the target. This reduced the size of the dataset down to approximately 2M events, which were used to perform detector alignment. The signal candidates were then preselected by requiring enough hits in the second station to reconstruct two outgoing tracks. The remaining 94k events were used in the analysis.

In addition, a sample of 150k elastic μe^- scattering events was simulated at Leading Order accuracy, within the FairMUonE framework. The simulation used two simplifications with respect to the real detector. The electromagnetic calorimeter was included as a single block of material rather than a grid of distinct crystals. This has no impact on the study, as the calorimeter was used only to provide an approximate estimate of the total energy recorded in an event. Furthermore, because the simulation of the tracking system readout was not yet developed at the time, the uncertainty of position measurement was approximated by applying a Gaussian smearing with standard deviation evaluated in collected data. Similarly, because simulation of the main background source (production of lepton pairs) was not ready, the study focuses on comparing the data with elastic scattering signal exclusively.

Detector alignment and event reconstruction

The detector was aligned with a procedure similar to the first stage described in section 8.4.4. The main difference was that the beam muons were reconstructed using all available modules (across both stations) and the one being aligned was excluded from the track fit. The achieved resolutions varied between 15 and 37 micrometres, which is below the intrinsic resolution of the sensors used. Similarly, the tracks and interaction vertices were reconstructed with an early version of the algorithm described in section 8.4. The main differences are the inclusion of an outlier hit removal already at the stage of fitting 2D track candidates, less accurate treatment of the multiple scattering uncertainty and much stricter requirements imposed on the reconstructed tracks and vertex candidates at the level of reconstruction.

Analysis and results

The analysis focuses primarily on two aspects – evaluating the performance of event reconstruction algorithms and the ability to extract a clean sample of elastic scattering events, using relatively simple selection criteria (i.e. without a dedicated multivariate analysis). In particular, the impact of a kinematic fit on the resolution of scattering angles was studied in the simulated signal sample. Figure 8.7 shows the results for both outgoing tracks in bins of the generated scattering angle. The resolutions were determined as the standard deviation of a Gaussian distribution fitted to the difference between the reconstructed and generated angle. While this study is not quantitative for the ultimate detector configuration, two important trends are visible. Specifically, the resolution improves significantly for the electron, especially in the kinematic region where multiple scattering is prevalent, and remains stable throughout the entire range for the outgoing muon.

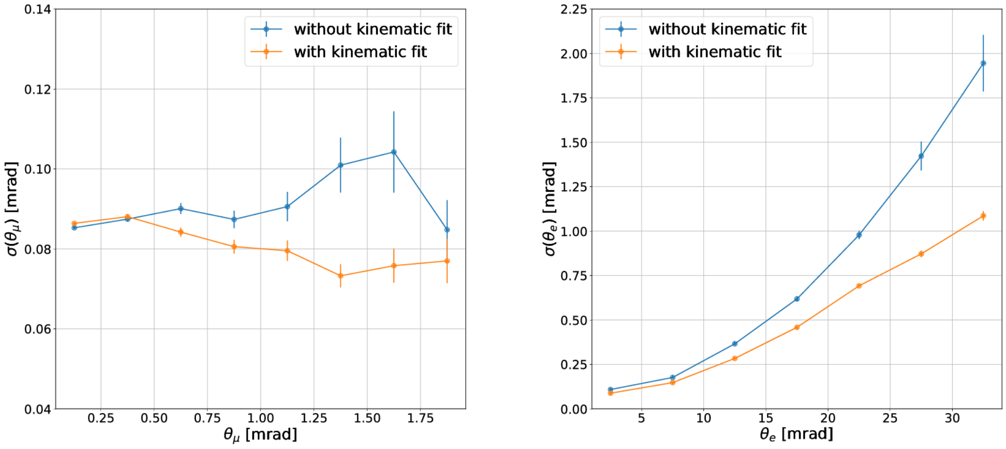

FIGURE 8.7: Resolution of reconstructed scattering angle before (blue) and after (yellow) the kinematic vertex fit procedure is applied. The left plot shows the results for the outgoing muon and right of the electron. Figure taken from [3].

The reconstructed data events were then used to explore different signal selection criteria. The events were required to have only one incoming track reconstructed (thus removing pileup contributions) and a non-zero energy deposit in the calorimeter, yielding 8556 candidates.

Three metrics were considered – the χ^2 of kinematic vertex fit normalised to the number of its degrees of freedom (χ^2_{vtx}), acoplanarity A and elasticity D_θ. The χ^2_{vtx} (defined in eq. (8.13)) quantifies the compatibility of tracks with a common interaction point. On average, it is significantly larger for random track combinations than for correctly matched vertices. The acoplanarity is defined as the angle between the incoming track and the plane spanned by the outgoing ones. It is zero for an ideal elastic scattering vertex, as all three lie in the same plane. Finally, the elasticity measures the shortest distance (in the $\theta_e\theta_\mu$ plane) of a given vertex and the theoretical elastic scattering curve (fig. 7.6), calculated assuming an average beam energy.

Figure 8.8 shows the distribution of χ^2_{vtx} for the reconstructed signal candidates and simulated elastic scattering vertices. The long tail visible in the data is caused by the presence of background events, which are not accounted for in the study. A requirement of $\chi^2_{\text{vtx}} < 10$ is thus imposed on the vertices to remove the kinematic region where the agreement is poor. In addition, θ_e is restricted to 30 mrad to match the generator level requirement in the simulated sample. Figure 8.9 illustrates the correlation between reconstructed scattering angles in the data and simulated signal after the selection, while fig. 8.10 shows the corresponding distributions of acoplanarity and elasticity. Due to lack of dedicated particle identification, the vertex track with larger scattering angle was always assumed to be the electron. This introduces a region (visible for low scattering angles in fig. 8.9), where the distribution is inverted with respect to the theoretical prediction.

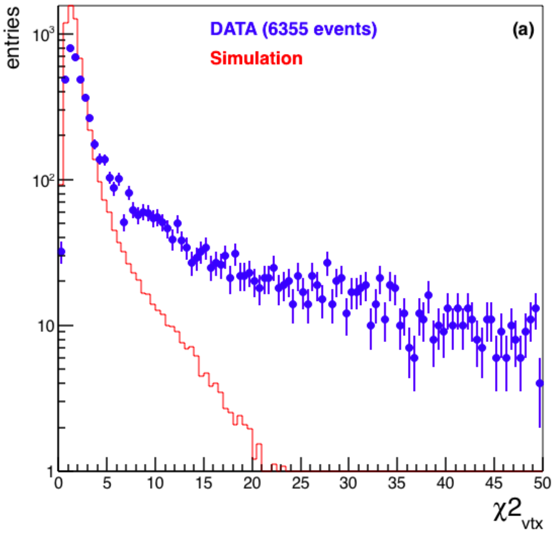

FIGURE 8.8: Distribution of kinematic vertex fit χ^2 per degree of freedom of reconstructed candidates (blue) and for the simulated signal events (red). Figure taken from [3].

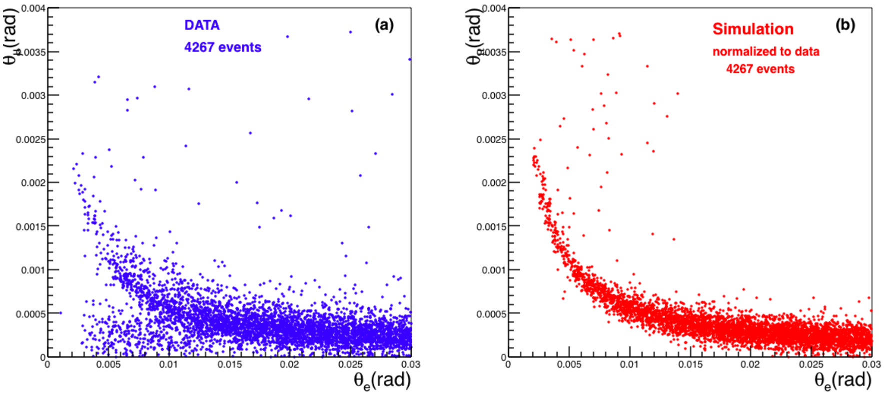

FIGURE 8.9: The correlation between reconstructed scattering angles in the data (left) and LO Monte Carlo (right). In both cases, a requirement of $\chi^2_{\text{vtx}} < 10$ and $\theta_e < 30$ mrad is imposed. Figure taken from [3].

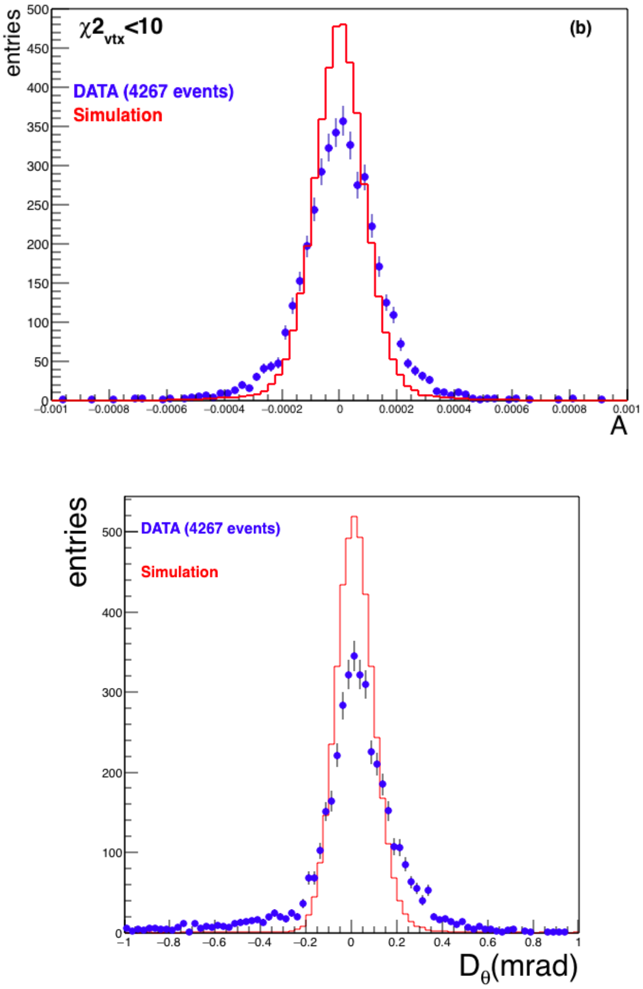

FIGURE 8.10: Distributions of acoplanarity (top) and elasticity (bottom) for the reconstructed candidates (blue) and in the LO Monte Carlo (red). In both cases, a requirement of $\chi^2_{\text{vtx}} < 10$ and $\theta_e < 30$ mrad is imposed. Figure taken from [3].

The distributions corresponding to data events in fig. 8.10 contain two-sided tails, which are populated primarily by non-elastic background. To achieve better agreement with simulated signal, two sets of additional requirements are considered (labelled in figures as sample 1 and sample 2, respectively):

- $|D_\theta| < 0.2$ mrad
- $|A| < 0.00035$ and $\chi^2_{\text{vtx}} < 5$.

The χ^2_{vtx} condition is introduced to approximately match the number of events remaining after the selection with both criteria. Figure 8.11 shows the correlation between reconstructed scattering angles, indicating that the elasticity requirement is more effective in removing the non-elastic background. Furthermore, fig. 8.12 shows that selected candidates match the Leading Order Monte Carlo relatively well in the electron scattering angle and acoplanarity.

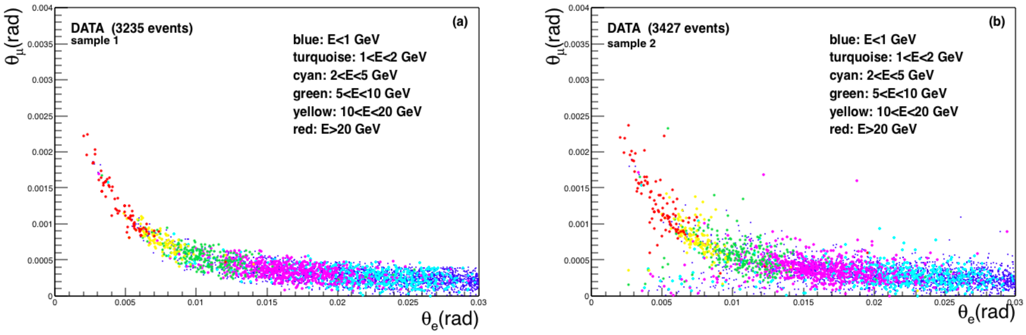

FIGURE 8.11: The correlation of scattering angles reconstructed in the data after requiring $\chi^2_{\text{vtx}} < 10$, $\theta_e < 30$ mrad and $|D_\theta| < 0.2$ (left), and $\chi^2_{\text{vtx}} < 5$, $\theta_e < 30$ mrad and $|A| < 0.00035$ (right). The colours represent different ranges of the total energy deposits registered in the calorimeter. Figure taken from [3].

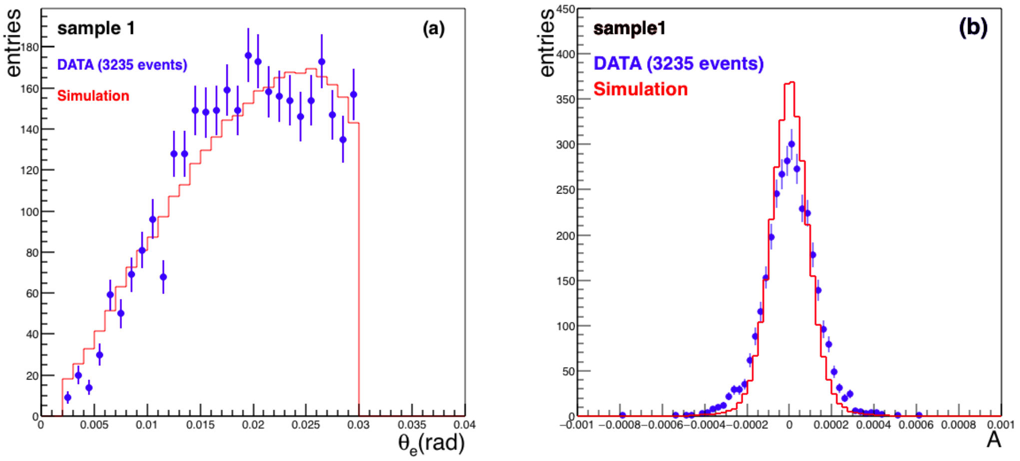

FIGURE 8.12: Distributions of electron scattering angle (left) and acoplanarity (right) in the data (blue) and LO Monte Carlo (red) with a requirement of $\chi^2_{\text{vtx}} < 10$, $\theta_e < 30$ mrad and $|D_\theta| < 0.2$ mrad. Figure taken from [3].

Conclusions

The presented study represents a significant milestone for the MUonE experiment. It provided important insight about the design of the final detector and validated the approach to event reconstruction, together with the FairMUonE software. It proved that the elastic scattering signal can be reliably extracted from the data, even using tracking sensors with significantly worse resolution and simple selection criteria. The study also emphasised the need for an electromagnetic calorimeter and muon detection system, to provide the means of particle identification and a way to understand the behaviour of background and systematic uncertainties.

8.5.2 Final detector model performance

The most recent test beam was conducted with a detector configuration planned for the ultimate operation (as detailed in section 7.3.1 and illustrated in fig. 7.8). Two tracking stations and an electromagnetic calorimeter (made of 23 centimetre thick $PbWO_4$ crystals) were installed at the M2 beam line and the data was collected with a dedicated muon beam. In addition, a variety of target materials and thicknesses were evaluated.

Because the analysis of collected data is currently in progress and the results are not public, only certain aspects can be discussed. The following study focuses on evaluating the performance of reconstructing elastic μe^- scattering vertices within the FairMUonE framework and using Monte Carlo simulation. A 9-by-9 centimetre, 2 centimetre thick graphite target is assumed.

Simulated sample and event reconstruction

A Monte Carlo sample of 200k elastic scattering vertices was simulated within the FairMUonE framework, at Next-to-Leading Order accuracy (using MESMER event generator, see section 8.3.1). Beam kinematics were drawn from an accurate description of the M2 line characteristics, with momentum peak at approximately 160 GeV (as shown in figs. 8.13 and 8.14). The tracks and vertices were reconstructed using algorithms described in section 8.4.

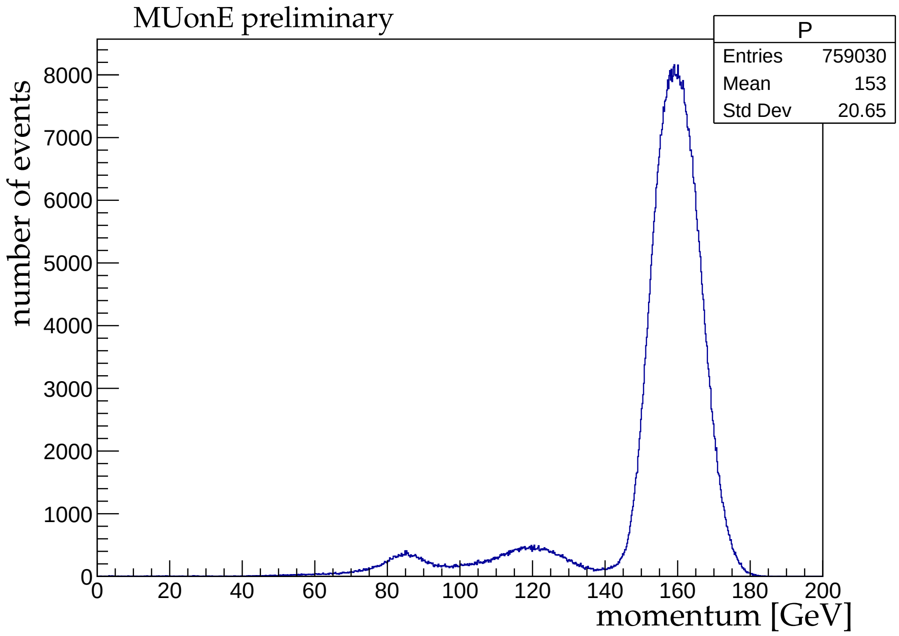

FIGURE 8.13: Beam momentum distribution. The number of entries is arbitrary.

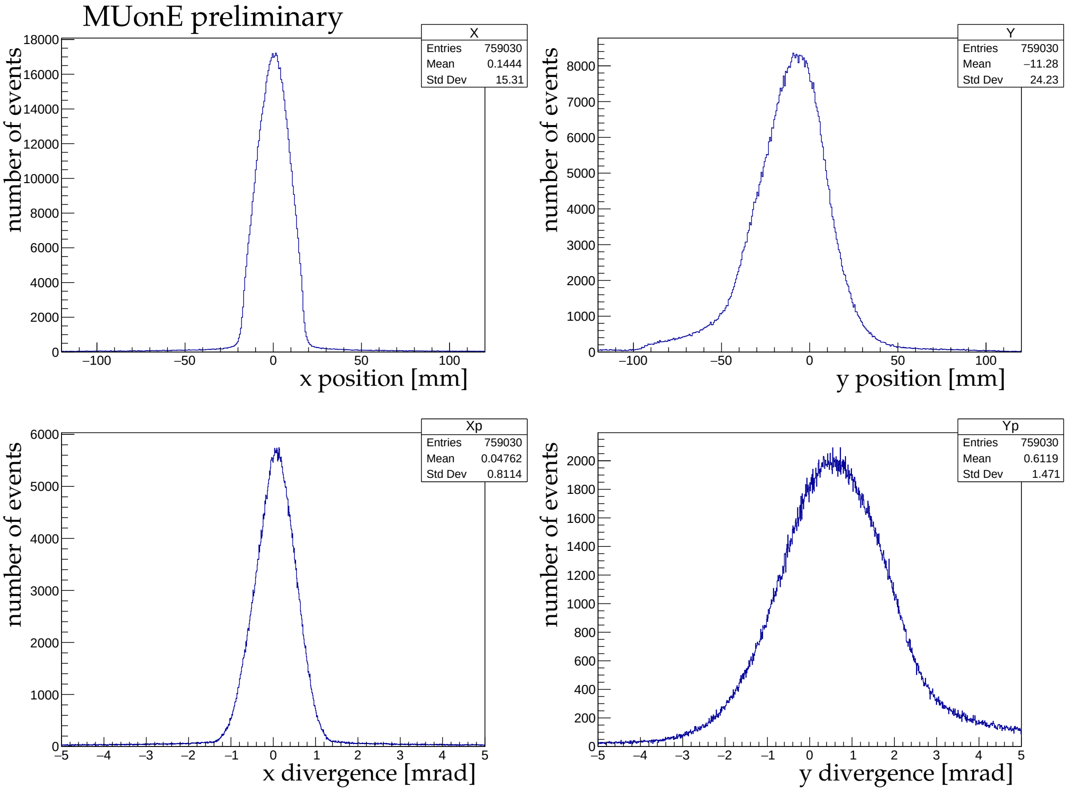

FIGURE 8.14: Distributions of the beam position in X (top left) and Y (top right) direction, and the corresponding divergences (bottom row). The parameters were calculated at approximately 8 metres upstream of the MUonE detector.

Signal reconstruction efficiency

The efficiency of reconstructing elastic μe^- scattering interactions was studied in the following way. First, events where the beam missed a target volume were removed, reducing the initial sample by approximately 1% – fig. 8.15 shows the spatial beam distribution extrapolated to the target position. The remaining events universally contain a signal vertex produced in the target. Furthermore, since the simulation uses accurate beam characteristics, the result indicates that chosen target dimensions are appropriate.

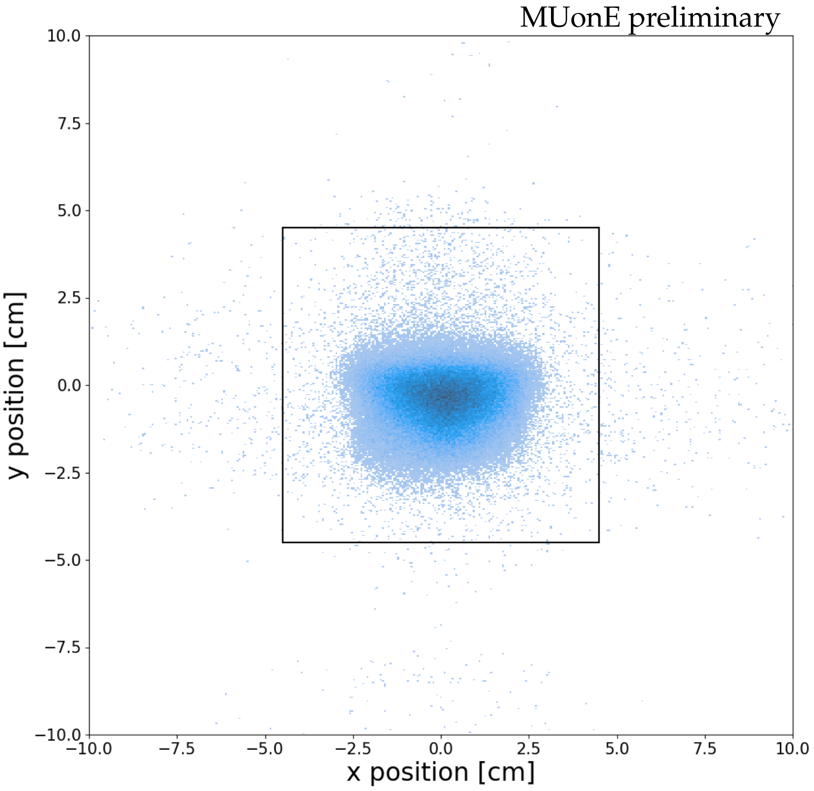

FIGURE 8.15: Beam position extrapolated to the middle of the target. The size of the target volume is overlaid with black box.

The losses of signal interactions due to detector acceptance were then investigated in the remaining events. A reconstructible track was defined as corresponding to a Monte Carlo particle, which has passed through enough tracking modules to allow for its reconstruction by the algorithm. Specifically, it was required to deposit a charge in both X and both Y modules of the station as well as in at least one stereo module. Table 8.1 summarises the fraction of generated tracks, which are also reconstructible. Figure 8.16 illustrates the difference in bins of generated electron momentum. The signal events which cannot be reconstructed with MUonE detector are primarily those with low momentum electron being produced at a large scattering angle and leaving the acceptance without passing through the tracking modules at the end of the station or being scattered outside the acceptance as it travels through the modules.

particle	reconstructible/generated tracks [%]
incoming muon	~ 100
outgoing muon	~ 100
outgoing electron	60

TABLE 8.1: Fraction of generated tracks, which are also reconstructible with MUonE detector.

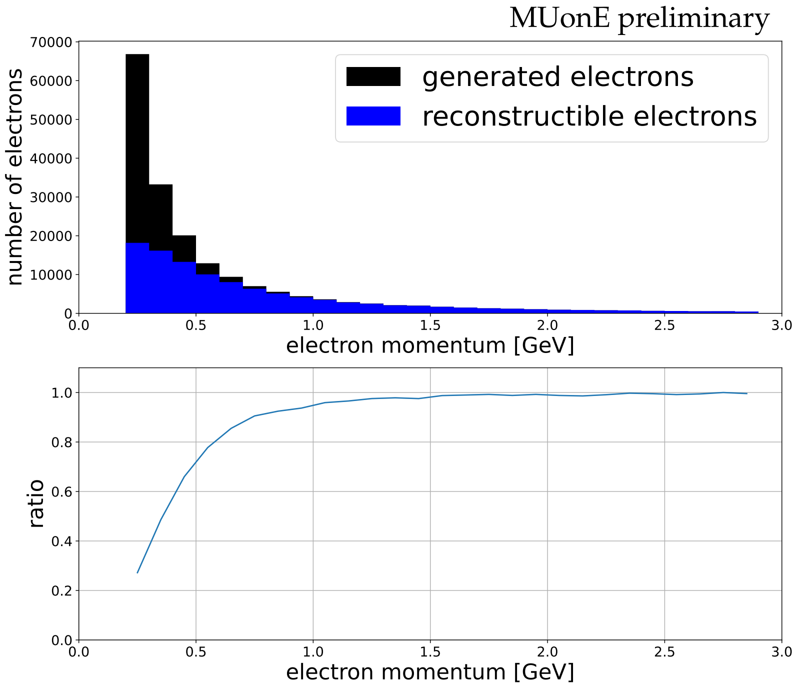

FIGURE 8.16: Number of generated and reconstructible electrons in bins of momentum (top) and the ratio of both (bottom).

Finally, the fraction of reconstructible tracks which get reconstructed by the algorithm is studied. To be considered correctly reconstructed, they are required to be linked to the corresponding Monte Carlo particle and have at least half of the assigned hits in common. The reconstruction efficiency is evaluated for zero, one and two hits allowed to be shared between tracks in the first two modules of each station. Table 8.2 summarises the efficiencies for each particle type, which is generally very high – in particular, both muon tracks are reconstructed almost universally. The impact of allowing overlapping hits is also visible, increasing the efficiency for electrons by approximately 6 pp. Such a situation may happen if the outgoing tracks are produced with a small opening angle or if the plane they span is approximately parallel to the strips of one of the modules, resulting in both tracks contributing deposited charge to the same hit. Furthermore, if hits in the first tracking modules of the station are close to each other, both reconstructed tracks may align better with only one of them due to hit spread in subsequent modules caused by multiple scattering. This effect is expected to concern primarily the very first module of a station, hence increasing the number of allowed shared hits from 1 to 2 provides a negligible gain. Figure 8.17 illustrates the reconstruction efficiency of electrons in bins of their generated momentum and fig. 8.18 – the efficiency of reconstructing elastic scattering vertices in bins of the generated electron scattering angle.

0 shared hits allowed	
particle	reconstructed/reconstructible tracks [%]
incoming muon	$\sim$100
outgoing muon	$\sim$100
outgoing electron	91
1 shared hit allowed	
particle	reconstructed/reconstructible tracks [%]
incoming muon	$\sim$100
outgoing muon	$\sim$100
outgoing electron	97
2 shared hits allowed	
particle	reconstructed/reconstructible tracks [%]
incoming muon	$\sim$100
outgoing muon	$\sim$100
outgoing electron	97

TABLE 8.2: Reconstruction efficiencies for different number of shared hits allowed in the first two tracking modules of each station.

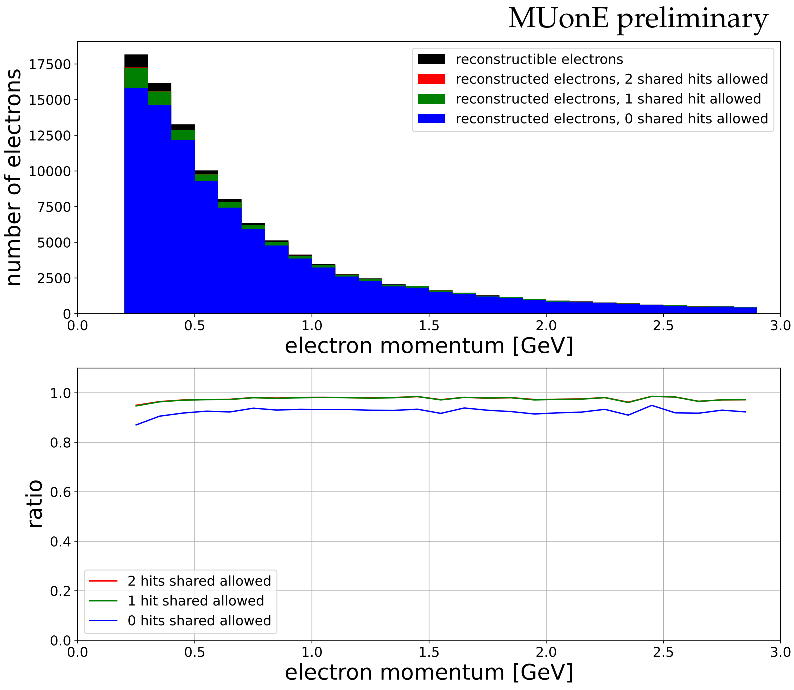

FIGURE 8.17: Number of reconstructed and reconstructible electrons in bins of momentum (top) and the ratio of both (bottom) for different number of hits allowed to be shared between the tracks.

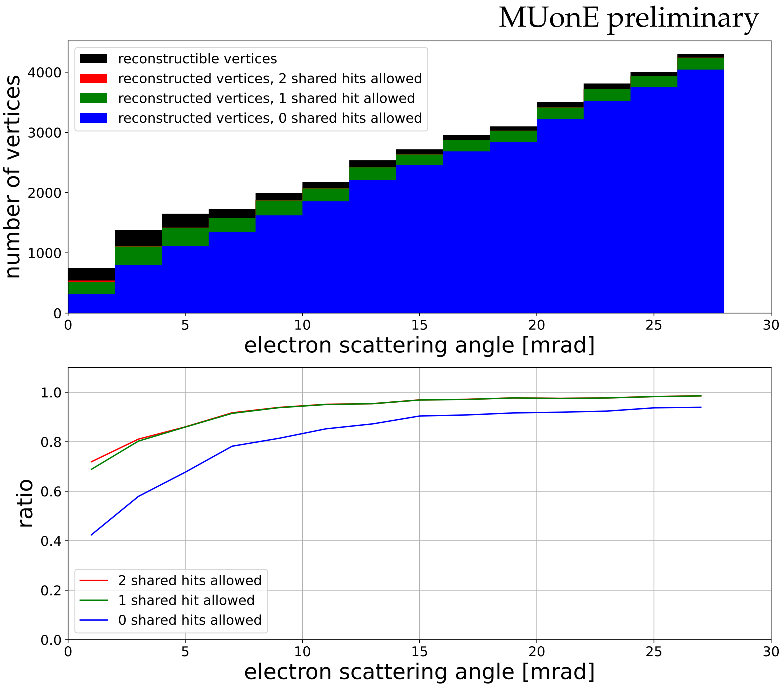

FIGURE 8.18: Number of reconstructed and reconstructible Next-to-Leading Order signal vertices in bins of electron scattering angle (top) and the ratio of both (bottom) for different number of hits allowed to be shared between the tracks.

Quality of reconstructed signal vertices

The quality of reconstructed elastic scattering vertices is studied using a set of metrics similar to those employed in the analysis of 2018 test beam data. To represent the widest range of signal vertices, the tracks are allowed to share at most two hits in the first two modules of each tracking station. For each reconstructed event, a candidate with lowest χ^2_{vtx} is selected as the signal vertex. Furthermore, because MUonE currently lacks particle identification system and algorithms, the track scattered at a smaller angle is always assumed to correspond to the muon. Similarly to the 2018 test beam, this assumption introduces a kinematic region (with both scattering angles below 5 mrad) where the reconstructed angles are inverted with respect to generated ones.

Figure 8.19 shows the distributions of χ^2_{vtx} of reconstructed vertices and the χ^2 per degree of freedom of their constituent tracks. The impact of a kinematic vertex fit on the electron track is visible as an overall decrease in χ^2. It is caused by the track being pulled towards the assigned hits in the first modules of the station, while the contributions from the ones further downstream are suppressed by multiple scattering correction. Figure 8.20 shows the distribution of acoplanarity (defined as in the analysis of 2018 data) and its modified version, which is the angle between the two planes spanned by the incoming track and each of the outgoing ones. The latter is characterised by significantly higher values, as the electron and muon tracks are misaligned with respect to each other by the kinematic vertex fit and the spread of hits caused by electron's scattering in the material.

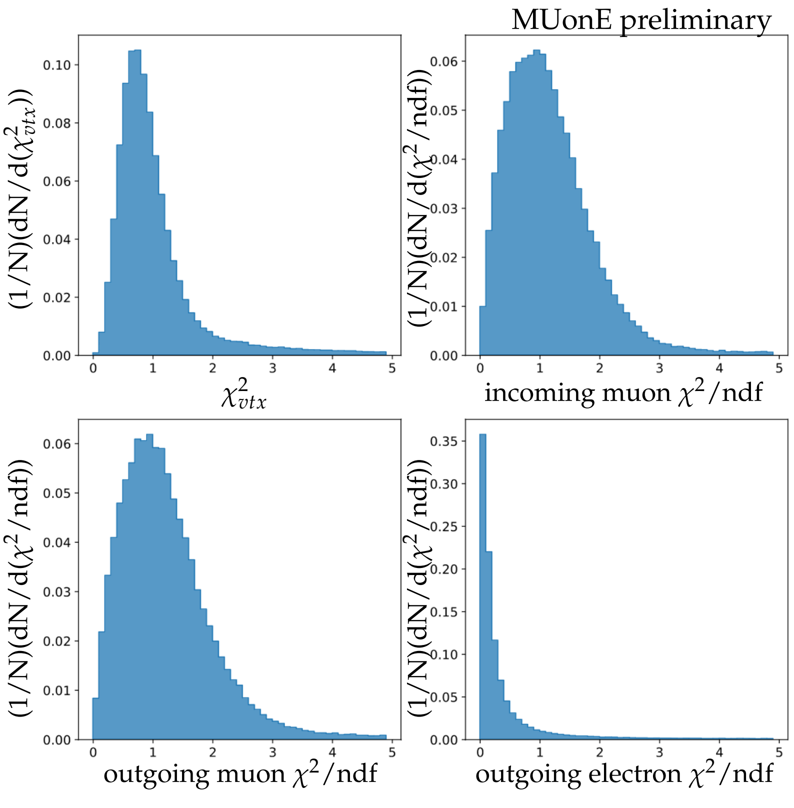

FIGURE 8.19: The χ^2 per degree of freedom of the reconstructed NLO signal vertices and of their constituent tracks.

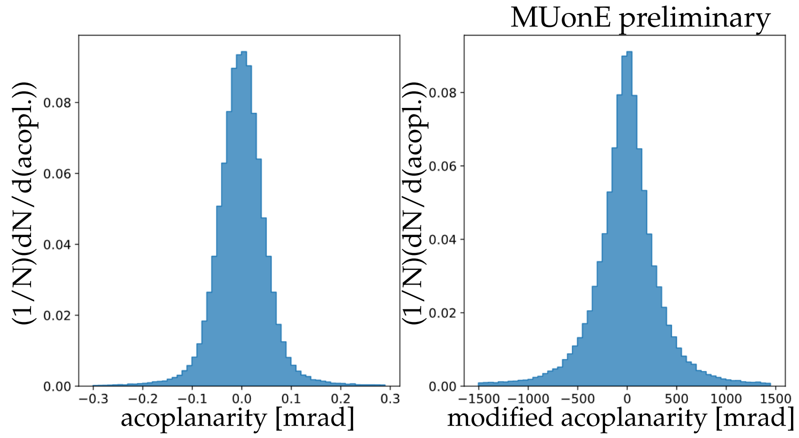

FIGURE 8.20: Distribution of acoplanarity and modified acoplanarity (as defined in the text) for the reconstructed NLO signal vertices.

Figure 8.21 shows the correlation of scattering angles for the reconstructed Next-to-Leading Order signal vertices. Compared to Leading Order simulation, the calculations include additional Feynman diagrams with a photon radiated during the interaction, which introduce the background visible in the lower part of the plots. Furthermore, fig. 8.22 shows the vertex position along the beam axis, determined using the position fit described in section 8.4.3. Multiple secondary peaks are visible downstream of the target and likely come from vertices containing hits from the photon and/or those originating in the silicon of the tracking layers. In both cases, the impact of imposing a requirement of $\chi^2_{vtx} < 2$ (which removes the tail of the distribution, fig. 8.19) is also illustrated. It is effective in removing most of the combinatorial background.

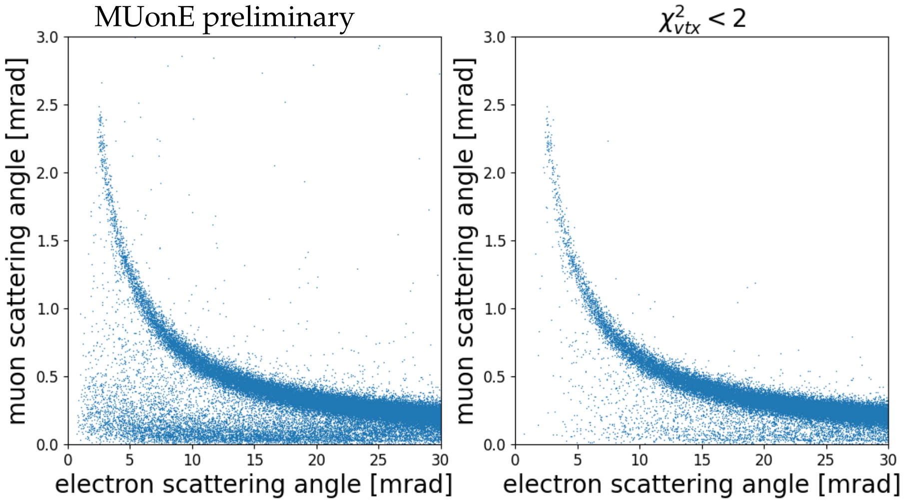

FIGURE 8.21: Correlation of scattering angles for the reconstructed Next-to-Leading Order signal vertices (left) and the same distribution with a $\chi^2_{vtx} < 2$ requirement (right).

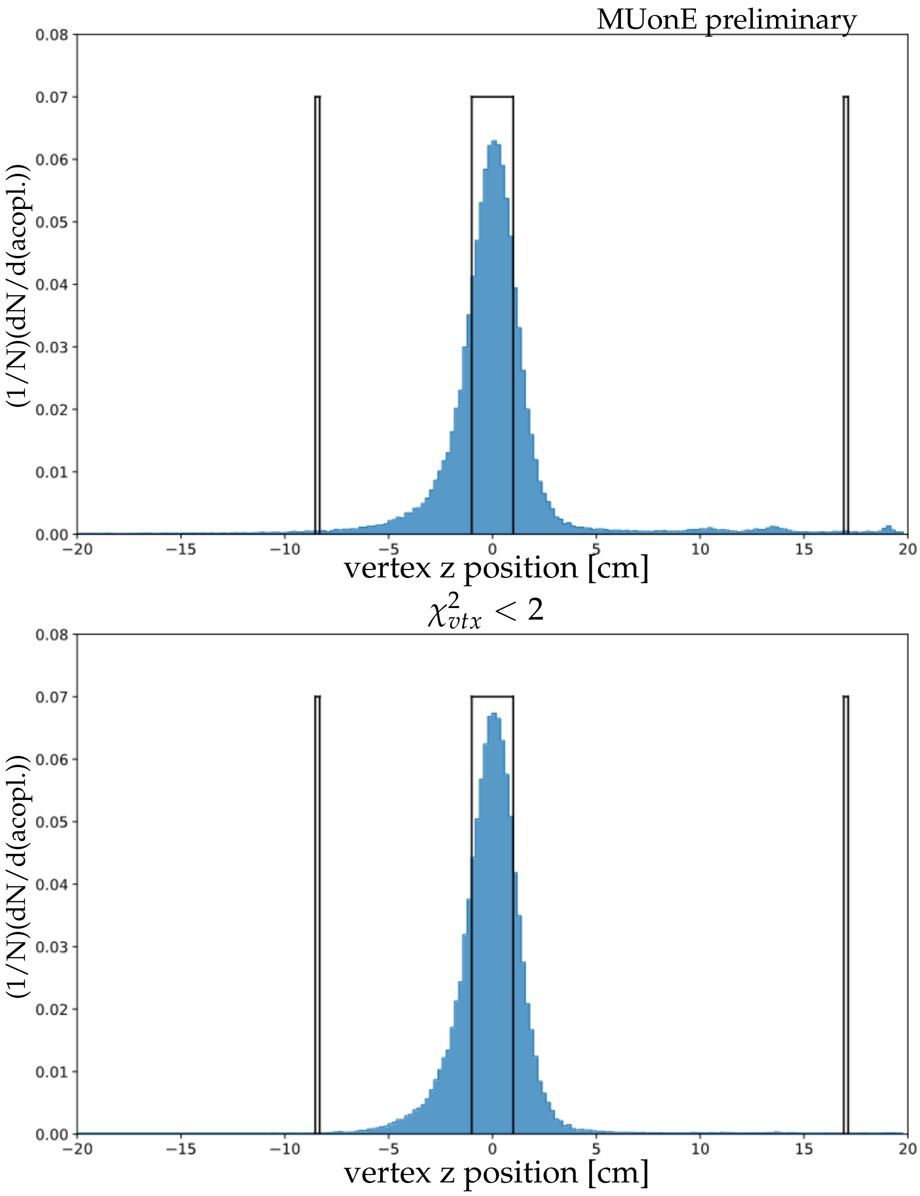

FIGURE 8.22: Vertex position along the beam axis (top) and the same distribution with a $\chi^2_{vtx} < 2$ requirement (bottom). The outline of the target and the two closest tracking modules is shown as black boxes.

Conclusions

The FairMUonE framework and included algorithms allow for a very efficient reconstruction of high quality elastic scattering vertices. The achievable reconstruction efficiency, with respect to events reconstructible with MUonE detector, is very high and the resulting signal vertices recreate the theoretical correlation of scattering angles very well. Similarly, their position along the beam axis is determined with a resolution high enough to exclude vertices originating in the silicon of tracking layers. The collected data is being studied and the results will be published soon.

8.6 Summary and conclusions

The MUonE experiment has been designed primarily to measure the Leading Order Hadronic Vacuum Polarisation component of the muon's anomalous magnetic moment. The novel approach, based on determining the elastic μe^- scattering cross-section, is expected to reduce the uncertainty of the Standard Model prediction at least twofold. Furthermore, the experimental setup provides a unique and clean environment to search for exotic long-lived particles decaying outside the target volumes, with the detector being sensitive to a wide range of signatures ranging from leptonic decays to jet-like final states. In particular, a preliminary study indicates that it is capable of expanding the coverage of dark photon phase space to a region, which is not available to other experiments.

The planned measurements necessitate the development of various software algorithms to process the collected data and simulate the detector's response to Monte Carlo particles. These algorithms were developed by the author of this thesis as part of a dedicated software package, FairMUonE, which has since become the official offline software for the MUonE experiment. Among other things, the package provides tools to perform the software detector alignment, reconstruction of particle tracks and interaction vertex candidates as well as to perform full simulation of the detector and its readout system. Alongside, the means to detect displaced vertices from Beyond the Standard Model decays are also implemented. They can be used to effectively search for exotic long-lived particles with signatures varying in outgoing track multiplicity.

The software has been successfully used and tested in several studies. In particular, the analysis of data collected during 2018 test beam, which was performed with a leading role of the author of the thesis and published in the Journal of Instrumentation. The goal of this test beam was to evaluate the ability to extract a clean sample of elastic scattering events. The test was successful, even though the apparatus used had a significantly lower resolution than the one planned for the final experiment. Currently, the analysis of data from the 2023 test beam – collected for the first time with a detector configuration that matches that of the final apparatus – is ongoing. The author is actively involved in this analysis, and the results are very promising and are planned to be published in the near future.

Chapter 9

Summary

The thesis comprises three topics, concerning various aspects of BSM searches. It focuses, in particular, on data analysis of experimental signatures with particle jets originating from heavy quarks and exotic dark matter candidates decaying in displaced vertices. The first study measures the $Z^0 b\bar{b}$ production cross-section, using the proton-proton collisions registered by the LHCb, at the centre-of-mass energy of 13 TeV. The considered process is naturally sensitive to BSM phenomena, due to the presence of two heavy quarks in the final state and thus receiving significant contributions from the massive quantum loops. Since it extends similar results of ATLAS and CMS experiments to the forward kinematic region, it increases the sensitivity to potential enhancement in the production cross-section, induced by decays of heavily boosted exotic states (e.g. Z' and b'). Furthermore, within the SM, it constitutes an irreducible background in the studies of the Higgs boson properties and is a benchmark for different approaches to the calculations involving beauty quarks (4FS and 5FS). The measurement is performed in the muon channel ($Z^0 \rightarrow \mu^+\mu^-$) and the cross-section is evaluated preliminarily as $\sigma_{Z^0(\rightarrow\mu^-\mu^+)b\bar{b}} = 70.70 \pm 26.56\,(\text{syst.}) \pm 0.74\,(\text{stat.})$ pb. The main source of the large systematic uncertainty is the temporary modelling of the $Z^0 q\bar{q}\,(q \neq b)$ background with simulated inclusive $q\bar{q}$ production. While the result is compatible with the NLO SM prediction, no further conclusions can be drawn at the moment. The final stage of the analysis is going to be repeated, once the appropriate Monte Carlo sample becomes available.

The second study evaluates the sensitivity of the CLIC detector model to exotic decays with displaced vertex signature. Such signatures are characteristic to dark matter candidates, which typically acquire significant lifetimes due to the strong suppression of their interactions with the SM particle sector. The study focuses on the first of the planned stages of CLIC operation, which would be conducted with a centre-of-mass energy of electron-positron collisions of 350 GeV. It extends the already existing result for the last stage (3 TeV), while adopting similar methods. In particular, in order to reach conclusions representative of a relatively wide class of massive, composite long-lived particles, a Hidden Valley scenario is assumed. The hidden sector is taken to have a QCD-like structure, and the communicator to be the Standard Model Higgs boson. The Higgs boson is then assumed to decay into a pair of π_v^0, which subsequently decay exclusively into a pair of b quarks each. The $m_{\pi_v^0} \in (25, 35, 50)$ GeV and $\tau_{\pi_v^0} \in (1, 10, 100, 300)$ ps hypotheses are explored and the corresponding upper limits on $\sigma\,(H) \cdot BR\,(H \rightarrow \pi_v^0 \pi_v^0)$ are calculated at 95% confidence level. They are at the order of 10^{-4} pb (or 10^{-3} if normalized to the SM Higgs boson production cross-section) and are several orders of magnitude better than for currently operating detectors.

The third and final part is dedicated to the work of the author of this thesis in the MUonE experiment. The experiment has been proposed to reduce the uncertainty of the SM prediction of muon's anomalous magnetic moment (and thus strengthen the observed measurement discrepancy), by employing a novel approach to measure its main non-perturbative contribution. It relies on a precise determination of the hadronic running of fine structure constant in the scatterings of beam muons on electrons, hence the detector layout comprises a series of targets, made of light material, and accompanying tracking stations. Such a unique design enables also searching for exotic long-lived particle signatures in parts of the kinematic phase space, which are unreachable by other experiments. A FairMUonE software has been developed for the off-line data processing, including – among others – the algorithms to perform detector alignment, Monte Carlo simulation as well as to reconstruct particle tracks and interaction vertices. Although the main focus has been placed on the elastic scattering, which constitutes the primary measurement, several tools have also been prepared to aid in detecting displaced vertices of various complexity. Furthermore, the analysis of data collected during the 2018 test beam is successfully performed and validates both the MUonE experiment concept and the FairMUonE toolkit. The algorithm and detector performance are also evaluated for the ultimate apparatus, using Monte Carlo simulation.

Bibliography

1. Kucharczyk, M., Goncerz, M. J., Matteuzzi, C. & Rachwal, B. Measurement of the production cross-section of Z^0 boson associated with two b-jets. LHCb-ANA-2024-032 (2024).
2. Kucharczyk, M. & Goncerz, M. Search for exotic decays of the Higgs boson into long-lived particles with jet pairs in the final state at CLIC. *JHEP* **03,** 131. arXiv: `2212.04147 [hep-ex]` (2023).
3. Goncerz, M. *et al.* A study of muon-electron elastic scattering in a test beam. *JINST* **16,** P06005. arXiv: `2102.11111 [hep-ex]` (2021).
4. Goncerz, M. Exotic Searches at LHCb. *Acta Phys. Polon. B* **51,** 1357–1362 (2020).
5. Goncerz, M. & Kucharczyk, M. MUonE experiment. *EPJ Web Conf.* **291,** 02007 (2024).
6. Raffelt, G. G. *Dark matter: Motivation, candidates and searches* in *The 1997 European School of High-Energy Physics* (May 1997), 235–278. arXiv: `hep-ph/9712538`.
7. Ade, P. A. R. *et al.* Planck 2013 results. I. Overview of products and scientific results. *Astron. Astrophys.* **571,** A1. arXiv: `1303.5062 [astro-ph.CO]` (2014).
8. Physics and Detectors at CLIC: CLIC Conceptual Design Report. arXiv: `1202.5940 [physics.ins-det]` (Feb. 2012).
9. Abbiendi, G. *Letter of Intent: the MUonE project* tech. rep. (CERN, Geneva, 2019). `https://cds.cern.ch/record/2677471`.
10. Schwartz, M. *Quantum Field Theory and the Standard Model* ISBN: 9781107034730. `https://books.google.pl/books?id=HbdEAgAAQBAJ` (Cambridge University Press, 2014).
11. Burgess, C. P. & Moore, G. D. *The standard model: A primer* ISBN: 978-0-511-25485-7, 978-1-107-40426-7, 978-0-521-86036-9 (Cambridge University Press, Dec. 2006).
12. Navas, S. *et al.* Review of particle physics. *Phys. Rev. D* **110,** 030001 (2024).
13. Tomonaga, S. On a Relativistically Invariant Formulation of the Quantum Theory of Wave Fields*. *Progress of Theoretical Physics* **1,** 27–42. ISSN: 0033-068X. eprint: `https://academic.oup.com/ptp/article-pdf/1/2/27/24027031/1-2-27.pdf`. `https://doi.org/10.1143/PTP.1.27` (Aug. 1946).
14. Schwinger, J. Quantum Electrodynamics. I. A Covariant Formulation. *Phys. Rev.* **74,** 1439–1461. `https://link.aps.org/doi/10.1103/PhysRev.74.1439` (10 Nov. 1948).
15. Feynman, R. P. Space-Time Approach to Quantum Electrodynamics. *Phys. Rev.* **76,** 769–789. `https://link.aps.org/doi/10.1103/PhysRev.76.769` (6 Sept. 1949).
16. Dyson, F. J. The Radiation Theories of Tomonaga, Schwinger, and Feynman. *Phys. Rev.* **75,** 486–502. `https://link.aps.org/doi/10.1103/PhysRev.75.486` (3 Feb. 1949).

17. Glashow, S. L. Partial-symmetries of weak interactions. *Nuclear Physics* **22,** 579–588. ISSN: 0029-5582. `https://www.sciencedirect.com/science/article/pii/0029558261904692` (1961).
18. Salam, A. & Ward, J. Electromagnetic and weak interactions. *Physics Letters* **13,** 168–171. ISSN: 0031-9163. `https://www.sciencedirect.com/science/article/pii/0031916364907115` (1964).
19. Weinberg, S. A Model of Leptons. *Phys. Rev. Lett.* **19,** 1264–1266. `https://link.aps.org/doi/10.1103/PhysRevLett.19.1264` (21 Nov. 1967).
20. Gell-Mann, M. THE EIGHTFOLD WAY: A THEORY OF STRONG INTERACTION SYMMETRY. `https://www.osti.gov/biblio/4008239` (Mar. 1961).
21. Gell-Mann, M. A schematic model of baryons and mesons. *Physics Letters* **8,** 214–215. ISSN: 0031-9163. `https://www.sciencedirect.com/science/article/pii/S0031916364920013` (1964).
22. Fritzsch, H., Gell-Mann, M. & Leutwyler, H. Advantages of the color octet gluon picture. *Physics Letters B* **47,** 365–368. ISSN: 0370-2693. `https://www.sciencedirect.com/science/article/pii/0370269373906254` (1973).
23. LHCb Collaboration. Observation of $J/\psi p$ Resonances Consistent with Pentaquark States in $\Lambda_b^0 \to J/\psi K^- p$ Decays. *Phys. Rev. Lett.* **115,** 072001. arXiv: `1507.03414 [hep-ex]` (2015).
24. Andersson, B., Gustafson, G., Ingelman, G. & Sjöstrand, T. Parton fragmentation and string dynamics. *Physics Reports* **97,** 31–145. `https://api.semanticscholar.org/CorpusID:121092649` (1983).
25. Higgs, P. W. Broken Symmetries and the Masses of Gauge Bosons. *Phys. Rev. Lett.* **13,** 508–509. `https://link.aps.org/doi/10.1103/PhysRevLett.13.508` (16 Oct. 1964).
26. Englert, F. & Brout, R. Broken Symmetry and the Mass of Gauge Vector Mesons. *Phys. Rev. Lett.* **13,** 321–323. `https://link.aps.org/doi/10.1103/PhysRevLett.13.321` (9 Aug. 1964).
27. Guralnik, G. S., Hagen, C. R. & Kibble, T. W. B. Global Conservation Laws and Massless Particles. *Phys. Rev. Lett.* **13,** 585–587. `https://link.aps.org/doi/10.1103/PhysRevLett.13.585` (20 Nov. 1964).
28. ATLAS Collaboration. Observation of a new particle in the search for the Standard Model Higgs boson with the ATLAS detector at the LHC. *Phys. Lett. B* **716,** 1–29. arXiv: `1207.7214 [hep-ex]` (2012).
29. CMS Collaboration. Observation of a New Boson at a Mass of 125 GeV with the CMS Experiment at the LHC. *Phys. Lett. B* **716,** 30–61. arXiv: `1207.7235 [hep-ex]` (2012).
30. Workman, R. L. *et al.* Review of Particle Physics. *PTEP* **2022,** 083C01 (2022).
31. 't Hooft, G. & Veltman, M. J. G. *Diagrammar* `https://cds.cern.ch/record/186259` (CERN, Geneva, 1973).
32. Ellis, J., Gaillard, M. K. & Nanopoulos, D. V. A Historical Profile of the Higgs Boson. An Updated Historical Profile of the Higgs Boson, 255–274. arXiv: `1504.07217`. `https://cds.cern.ch/record/2012465` (2016).
33. Heavens, A. The cosmological model: An overview and an outlook. *J. Phys. Conf. Ser.* **120,** 022001 (2008).

34. Milgrom, M. MOND theory. *Can. J. Phys.* **93,** 107–118. arXiv: `1404.7661 [astro-ph.CO]` (2015).
35. Schwarz, J. H. Superstring theory. *Physics Reports* **89,** 223–322. ISSN: 0370-1573. `https://www.sciencedirect.com/science/article/pii/0370157382900874` (1982).
36. Ashtekar, A. & Bianchi, E. A short review of loop quantum gravity. *Rept. Prog. Phys.* **84,** 042001. arXiv: `2104.04394 [gr-qc]` (2021).
37. Babu, K. S. & Khan, S. Minimal nonsupersymmetric $SO(10)$ model: Gauge coupling unification, proton decay, and fermion masses. *Phys. Rev. D* **92,** 075018. arXiv: `1507.06712 [hep-ph]` (2015).
38. Martin, S. P. A Supersymmetry primer. *Adv. Ser. Direct. High Energy Phys.* **18,** 1–98. arXiv: `hep-ph/9709356` (1998).
39. Bertolini, D., Thaler, J. & Thomas, Z. *Super-Tricks for Superspace* in *Theoretical Advanced Study Institute in Elementary Particle Physics: Searching for New Physics at Small and Large Scales* (2013), 421–496. arXiv: `1302.6229 [hep-ph]`.
40. Canepa, A. Searches for supersymmetry at the Large Hadron Collider. *Reviews in Physics* **4,** 100033. ISSN: 2405-4283. `https://www.sciencedirect.com/science/article/pii/S2405428318300091` (2019).
41. Cerdeno, D. G. & Munoz, C. An introduction to supergravity. *PoS* **CORFU98,** 011 (1998).
42. Csaki, C. The Minimal supersymmetric standard model (MSSM). *Mod. Phys. Lett. A* **11,** 599. arXiv: `hep-ph/9606414` (1996).
43. Carpenter, L. M., Kaplan, D. E. & Rhee, E.-J. Reduced fine-tuning in supersymmetry with R-parity violation. *Phys. Rev. Lett.* **99,** 211801. arXiv: `hep-ph/0607204` (2007).
44. Hewett, J. L., Lillie, B., Masip, M. & Rizzo, T. G. Signatures of long-lived gluinos in split supersymmetry. *JHEP* **09,** 070. arXiv: `hep-ph/0408248` (2004).
45. Ambrosanio, S. & Mele, B. Neutralino decays in the minimal supersymmetric Standard Model. *Phys. Rev. D* **53,** 2541–2562. arXiv: `hep-ph/9508237` (1996).
46. Djouadi, A., Mambrini, Y. & Muhlleitner, M. Chargino and neutralino decays revisited. *Eur. Phys. J. C* **20,** 563–584. arXiv: `hep-ph/0104115` (2001).
47. Bharucha, A., Heinemeyer, S., von der Pahlen, F. & Schappacher, C. Neutralino Decays in the Complex MSSM at One-Loop: a Comparison of On-Shell Renormalization Schemes. *Phys. Rev. D* **86,** 075023. arXiv: `1208.4106 [hep-ph]` (2012).
48. Cvetic, M., Langacker, P. & Shiu, G. Phenomenology of a three family standard like string model. *Phys. Rev. D* **66,** 066004. arXiv: `hep-ph/0205252` (2002).
49. Arkani-Hamed, N., Dimopoulos, S. & Kachru, S. Predictive landscapes and new physics at a TeV. arXiv: `hep-th/0501082` (Jan. 2005).
50. Strassler, M. J. & Zurek, K. M. Echoes of a hidden valley at hadron colliders. *Phys. Lett. B* **651,** 374–379. arXiv: `hep-ph/0604261` (2007).
51. Langacker, P. The Physics of Heavy Z' Gauge Bosons. *Rev. Mod. Phys.* **81,** 1199–1228. arXiv: `0801.1345 [hep-ph]` (2009).
52. Deliyergiyev, M. A. Recent Progress in Search for Dark Sector Signatures. *Open Phys.* **14,** 281–303. arXiv: `1510.06927 [hep-ph]` (2016).

53. Strassler, M. J. & Zurek, K. M. Discovering the Higgs through highly-displaced vertices. *Phys. Lett. B* **661,** 263–267. arXiv: `hep-ph/0605193` (2008).
54. Fabbrichesi, M., Gabrielli, E. & Lanfranchi, G. The Dark Photon. arXiv: `2005.01515 [hep-ph]` (May 2020).
55. Lees, J. P. *et al.* Improved Limits on B^0 Decays to Invisible Final States and to $\nu\bar{\nu}\gamma$. *Phys. Rev. D* **86,** 051105. arXiv: `1206.2543 [hep-ex]` (2012).
56. Hsu, C. L. *et al.* Search for B^0 decays to invisible final states. *Phys. Rev. D* **86,** 032002. arXiv: `1206.5948 [hep-ex]` (2012).
57. Fabbrichesi, M., Gabrielli, E. & Mele, B. Hunting down massless dark photons in kaon physics. *Phys. Rev. Lett.* **119,** 031801. arXiv: `1705.03470 [hep-ph]` (2017).
58. Cortina Gil, E. *et al.* First search for $K^+ \to \pi^+\nu\bar{\nu}$ using the decay-in-flight technique. *Phys. Lett. B* **791,** 156–166. arXiv: `1811.08508 [hep-ex]` (2019).
59. Ahn, J. K. *et al.* Search for the $K_L \to \pi^0\nu\bar{\nu}$ and $K_L \to \pi^0 X^0$ decays at the J-PARC KOTO experiment. *Phys. Rev. Lett.* **122,** 021802. arXiv: `1810.09655 [hep-ex]` (2019).
60. Fabbrichesi, M. & Gabrielli, E. Dark-sector physics in the search for the rare decays $K^+ \to \pi^+\nu\bar{\nu}$ and $K_L \to \pi^0\nu\bar{\nu}$. *Eur. Phys. J. C* **80,** 532. arXiv: `1911.03755 [hep-ph]` (2020).
61. Gabrielli, E., Heikinheimo, M., Mele, B. & Raidal, M. Dark photons and resonant monophoton signatures in Higgs boson decays at the LHC. *Phys. Rev. D* **90,** 055032. arXiv: `1405.5196 [hep-ph]` (2014).
62. Biswas, S., Gabrielli, E., Heikinheimo, M. & Mele, B. Higgs-boson production in association with a dark photon in $\mathrm{e}^+\mathrm{e}^-$ collisions. *JHEP* **06,** 102. arXiv: `1503.05836 [hep-ph]` (2015).
63. Biswas, S., Gabrielli, E., Heikinheimo, M. & Mele, B. Dark-photon searches via ZH production at e^+e^- colliders. *Phys. Rev. D* **96,** 055012. arXiv: `1703.00402 [hep-ph]` (2017).
64. Fabbrichesi, M., Gabrielli, E. & Mele, B. Z Boson Decay into Light and Darkness. *Phys. Rev. Lett.* **120,** 171803. arXiv: `1712.05412 [hep-ph]` (2018).
65. Cobal, M. *et al.* Z-boson decays into an invisible dark photon at the LHC, HL-LHC and future lepton colliders. *Phys. Rev. D* **102,** 035027. arXiv: `2006.15945 [hep-ph]` (2020).
66. Yang, C. N. Selection Rules for the Dematerialization of a Particle into Two Photons. *Phys. Rev.* **77,** 242–245. `https://link.aps.org/doi/10.1103/PhysRev.77.242` (2 Jan. 1950).
67. Gori, S. *et al.* Dark Sector Physics at High-Intensity Experiments. arXiv: `2209.04671 [hep-ph]` (Sept. 2022).
68. O'Hare, C. A. J. Cosmology of axion dark matter. *PoS* **COSMICWISPers,** 040. arXiv: `2403.17697 [hep-ph]` (2024).
69. Baker, C. A. *et al.* An Improved experimental limit on the electric dipole moment of the neutron. *Phys. Rev. Lett.* **97,** 131801. arXiv: `hep-ex/0602020` (2006).
70. Peccei, R. D. The Strong CP problem and axions. *Lect. Notes Phys.* **741,** 3–17. arXiv: `hep-ph/0607268` (2008).

71. Graham, P. W., Irastorza, I. G., Lamoreaux, S. K., Lindner, A. & van Bibber, K. A. Experimental Searches for the Axion and Axion-Like Particles. *Ann. Rev. Nucl. Part. Sci.* **65,** 485–514. arXiv: `1602.00039 [hep-ex]` (2015).
72. Co, R. T., Kumar, S. & Liu, Z. Searches for heavy QCD axions via dimuon final states. *JHEP* **02,** 111. arXiv: `2210.02462 [hep-ph]` (2023).
73. Mosala, K., Sharma, P., Kumar, M. & Goyal, A. Axion-like particles at future $e^- p$ collider. *Eur. Phys. J. C* **84,** 44. arXiv: `2307.00394 [hep-ph]` (2024).
74. d'Enterria, D. *Collider constraints on axion-like particles* in *Workshop on Feebly Interacting Particles* (Feb. 2021). arXiv: `2102.08971 [hep-ex]`.
75. Primakoff, H. Photoproduction of neutral mesons in nuclear electric fields and the mean life of the neutral meson. *Phys. Rev.* **81,** 899 (1951).
76. Frampton, P. H., Hung, P. Q. & Sher, M. Quarks and leptons beyond the third generation. *Phys. Rept.* **330,** 263. arXiv: `hep-ph/9903387` (2000).
77. Perelstein, M. Little Higgs models and their phenomenology. *Prog. Part. Nucl. Phys.* **58,** 247–291. arXiv: `hep-ph/0512128` (2007).
78. Kartavtsev, A. V. Breaking of B-L in superstring inspired E(6) model. *J. Phys. G* **31,** 1191–1206. arXiv: `hep-ph/0412196` (2005).
79. CMS Collaboration. Search for a heavy vector resonance decaying to a Z boson and a Higgs boson in proton-proton collisions at $\sqrt{s} = 13$ TeV. arXiv: `2102.08198 [hep-ex]` (Feb. 2021).
80. Bulava, J., Jansen, K. & Nagy, A. Constraining a fourth generation of quarks: non-perturbative Higgs boson mass bounds. *Phys. Lett. B* **723,** 95–99. arXiv: `1301.3416 [hep-lat]` (2013).
81. Das, D., Kundu, A. & Saha, I. Higgs data does not rule out a sequential fourth generation with an extended scalar sector. *Phys. Rev. D* **97,** 011701. arXiv: `1707.03000 [hep-ph]` (2018).
82. Hill, C. & Paschos, E. A naturally heavy fourth generation neutrino. *Physics Letters B* **241,** 96–100. ISSN: 0370-2693. `https://www.sciencedirect.com/science/article/pii/037026939091493U` (1990).
83. ATLAS Collaboration. Search for down-type fourth generation quarks with the ATLAS detector in events with one lepton and hadronically decaying W bosons. *Phys. Rev. Lett.* **109,** 032001. arXiv: `1202.6540 [hep-ex]` (2012).
84. CMS Collaboration. Search for a Vector-like Quark with Charge 2/3 in $t + Z$ Events from pp Collisions at $\sqrt{s} = 7$ TeV. *Phys. Rev. Lett.* **107,** 271802. arXiv: `1109.4985 [hep-ex]` (2011).
85. Bonvini, M., Papanastasiou, A. S. & Tackmann, F. J. Resummation and matching of b-quark mass effects in $b\bar{b}H$ production. *JHEP* **11,** 196. arXiv: `1508.03288 [hep-ph]` (2015).
86. Forte, S., Napoletano, D. & Ubiali, M. Higgs production in bottom-quark fusion: matching beyond leading order. *Phys. Lett. B* **763,** 190–196. arXiv: `1607.00389 [hep-ph]` (2016).
87. Gao, J. & Berger, E. L. Modeling of t-channel single top-quark production at the LHC. *Phys. Lett. B* **811,** 135886. arXiv: `2005.12936 [hep-ph]` (2020).
88. Demartin, F., Maltoni, F., Mawatari, K. & Zaro, M. Higgs production in association with a single top quark at the LHC. *Eur. Phys. J. C* **75,** 267. arXiv: `1504.00611 [hep-ph]` (2015).

89. Maltoni, F. *Discussion: 4- vs 5-flavor scheme* Workshop on Heavy Flavor Production at Hadron Colliders. 2013. `https://indico.cern.ch/event/222696/contributions/1529824/attachments/364875/507829/maltoni.pdf`.

90. Andersen, J. R. *et al.* Handbook of LHC Higgs Cross Sections: 3. Higgs Properties. arXiv: `1307.1347 [hep-ph]` (July 2013).

91. ATLAS Collaboration. Measurement of the Standard Model Higgs boson produced in association with a vector boson and decaying to a pair of b-quarks in p-p collisions at 13 TeV using the ATLAS detector. *PoS* **LHCP2020,** 241 (2021).

92. D0 Collaboration. Search for resonant pair production of neutral long-Lived particles decaying to $b\bar{b}$ in $p\bar{p}$ collisions at $\sqrt{s}$ = 1.96 TeV. *Phys. Rev. Lett.* **103,** 071801. arXiv: `0906.1787 [hep-ex]` (2009).

93. CDF Collaboration. Search for heavy metastable particles decaying to jet pairs in $p\bar{p}$ at $\sqrt{s}$ = 1.96 TeV. *Phys. Rev.* **D85,** 012007. arXiv: `1109.3136 [hep-ex]` (2012).

94. ATLAS Collaboration. Search for a light Higgs boson decaying to long-lived weakly-interacting particles in proton-proton collisions at $\sqrt{s} = 7$ TeV with the ATLAS detector. *Phys. Rev. Lett.* **108,** 251801. arXiv: `1203.1303 [hep-ex]` (2012).

95. ATLAS Collaboration. Search for exotic decays of the Higgs boson into long-lived particles in pp collisions at $\sqrt{s}$ = 13 TeV using displaced vertices in the ATLAS inner detector. *JHEP* **11,** 229. arXiv: `2107.06092 [hep-ex]` (2021).

96. ATLAS Collaboration. Search for the Higgs boson produced in association with a vector boson and decaying into two spin-zero particles in the $H \to aa \to 4b$ channel in pp collisions at $\sqrt{s} = 13$ TeV with the ATLAS detector. *JHEP* **10,** 031. arXiv: `1806.07355 [hep-ex]` (2018).

97. ATLAS Collaboration. Search for Higgs boson decays into two new low-mass spin-0 particles in the $4b$ channel with the ATLAS detector using pp collisions at $\sqrt{s} = 13$ TeV. *Phys. Rev. D* **102,** 112006. arXiv: `2005.12236 [hep-ex]` (2020).

98. ATLAS Collaboration. Search for long-lived neutral particles in pp collisions at $\sqrt{s}$ = 13 TeV that decay into displaced hadronic jets in the ATLAS calorimeter. *Eur. Phys. J. C* **79,** 481. arXiv: `1902.03094 [hep-ex]` (2019).

99. CMS Collaboration. Search for long-lived neutral particles decaying to quark-antiquark pairs in proton-proton collisions at $\sqrt{s} = 8$ TeV. *Phys. Rev. D* **91,** 012007. `https://link.aps.org/doi/10.1103/PhysRevD.91.012007` (1 Jan. 2015).

100. CMS Collaboration. Search for long-lived particles produced in association with a Z boson in proton-proton collisions at $\sqrt{s}$ = 13 TeV. *JHEP* **03,** 160. arXiv: `2110.13218 [hep-ex]` (2022).

101. CMS Collaboration. Search for long-lived particles decaying to jets with displaced vertices in proton-proton collisions at $\sqrt{s} = 13$ TeV. *Phys. Rev. D* **104,** 052011. arXiv: `2104.13474 [hep-ex]` (2021).

102. LHCb Collaboration. Search for long-lived particles decaying to jet pairs. *Eur. Phys. J. C* **75,** 152. arXiv: `1412.3021 [hep-ex]` (2015).

103. LHCb Collaboration. Updated search for long-lived particles decaying to jet pairs. *Eur. Phys. J. C* **77,** 812. arXiv: `1705.07332 [hep-ex]` (2017).

104. LHCb Collaboration. Search for massive long-lived particles decaying semileptonically at $\sqrt{s}$ = 13 TeV. *Eur. Phys. J. C* **82,** 373. arXiv: `2110.07293 [hep-ex]` (2022).

105. CDF Collaboration. Measurement of Cross Sections for b Jet Production in Events with a Z Boson in p^- anti-p Collisions at $\sqrt{s}$ = 1.96-TeV. *Phys. Rev. D* **79,** 052008. arXiv: `0812.4458 [hep-ex]` (2009).

106. D0 Collaboration. Measurement of the ratio of differential cross sections $\sigma(p\bar{p} \to Z + bjet)/\sigma(p\bar{p} \to Z + jet)$ in $p\bar{p}$ collisions at $\sqrt{s} = 1.96$ TeV. *Phys. Rev. D* **87,** 092010. arXiv: `1301.2233 [hep-ex]` (2013).

107. CMS Collaboration. Measurement of the production cross sections for a Z boson and one or more b jets in pp collisions at sqrt(s) = 7 TeV. *JHEP* **06,** 120. arXiv: `1402.1521 [hep-ex]` (2014).

108. ATLAS Collaboration. Measurement of differential production cross-sections for a Z boson in association with b-jets in 7 TeV proton-proton collisions with the ATLAS detector. *JHEP* **10,** 141. arXiv: `1407.3643 [hep-ex]` (2014).

109. ATLAS Collaboration. Measurements of the production cross-section for a Z boson in association with b-jets in proton-proton collisions at $\sqrt{s} = 13$ TeV with the ATLAS detector. *JHEP* **07,** 044. arXiv: `2003.11960 [hep-ex]` (2020).

110. CMS Collaboration. Measurement of the production cross section for Z+b jets in proton-proton collisions at $\sqrt{s}$ = 13 TeV. *Phys. Rev. D* **105,** 092014. arXiv: `2112.09659 [hep-ex]` (2022).

111. Alwall, J. *et al.* The automated computation of tree-level and next-to-leading order differential cross sections, and their matching to parton shower simulations. *JHEP* **07,** 079. arXiv: `1405.0301 [hep-ph]` (2014).

112. Frederix, R. *et al.* The automation of next-to-leading order electroweak calculations. *JHEP* **07.** [Erratum: JHEP 11, 085 (2021)], 185. arXiv: `1804.10017 [hep-ph]` (2018).

113. Bothmann, E. *et al.* Event Generation with Sherpa 2.2. *SciPost Phys.* **7,** 034. arXiv: `1905.09127 [hep-ph]` (2019).

114. LHCb Collaboration. Measurement of the Z+b-jet cross-section in pp collisions at $\sqrt{s}$ = 7 TeV in the forward region. *JHEP* **01,** 064. arXiv: `1411.1264 [hep-ex]` (2015).

115. LHCb Collaboration. LHCb SMOG Upgrade.

116. ATLAS Collaboration. The ATLAS Experiment at the CERN Large Hadron Collider. *JINST* **3,** S08003 (2008).

117. CMS Collaboration. The CMS Experiment at the CERN LHC. *JINST* **3,** S08004 (2008).

118. LHCb Collaboration. The LHCb Detector at the LHC. *JINST* **3,** S08005 (2008).

119. Aamodt, K. *et al.* The ALICE experiment at the CERN LHC. *JINST* **3,** S08002 (2008).

120. Mobs, E. The CERN accelerator complex - August 2018. Complexe des accélérateurs du CERN - Août 2018. General Photo. `https://cds.cern.ch/record/2636343` (2018).

121. Elsasser, C. *$b\bar{b}$ production angle plots* `https://lhcb.web.cern.ch/lhcb/speakersbureau/html/bb_ProductionAngles.html` (2024).

122. LHCb Collaboration. *LHCb reoptimized detector design and performance: Technical Design Report* https://cds.cern.ch/record/630827 (CERN, Geneva, 2003).
123. Muratori, B. & Pieloni, T. *Luminosity levelling techniques for the LHC* in *ICFA Mini-Workshop on Beam-Beam Effects in Hadron Colliders* (2014), 177–181. arXiv: 1410.5646 [physics.acc-ph].
124. *LHCb integrated luminosity* https://ep-news.web.cern.ch/sites/default/files/inline-images/EP%20September%202024/thumbnail_LumiSept2024_longyearsonly_0.png.
125. *Structure of light and heavy jets* https://i2.wp.com/www.particlebites.com/wp-content/uploads/2016/08/B-tagging_diagram.png.
126. LHCb Collaboration. Performance of the LHCb Vertex Locator. *JINST* **9,** P09007. arXiv: 1405.7808 [physics.ins-det] (2014).
127. LHCb Collaboration. Measurement of the track reconstruction efficiency at LHCb. *JINST* **10,** P02007. arXiv: 1408.1251 [hep-ex] (2015).
128. LHCb Collaboration. Design and performance of the LHCb trigger and full real-time reconstruction in Run 2 of the LHC. *JINST* **14,** P04013. arXiv: 1812.10790 [hep-ex] (2019).
129. Picatoste Olloqui, E. LHCb preshower(PS) and scintillating pad detector (SPD): Commissioning, calibration, and monitoring. *J. Phys. Conf. Ser.* **160,** 012046 (2009).
130. LHCb Collaboration. *Upgrade Software and Computing* tech. rep. (CERN, Geneva, 2018). https://cds.cern.ch/record/2310827.
131. Barrand, G. *et al.* GAUDI - A software architecture and framework for building HEP data processing applications. *Comput. Phys. Commun.* **140,** 45–55 (2001).
132. LHCb Collaboration. *LHCb computing: Technical Design Report* Submitted on 11 May 2005. https://cds.cern.ch/record/835156 (CERN, Geneva, 2005).
133. *The Brunel Project* https://lhcbdoc.web.cern.ch/lhcbdoc/brunel/ (2024).
134. *The DaVinci Project repository* https://gitlab.cern.ch/lhcb/DaVinci (2024).
135. Brun, R. & Rademakers, F. ROOT — An object oriented data analysis framework. *Nuclear Instruments and Methods in Physics Research Section A: Accelerators, Spectrometers, Detectors and Associated Equipment* **389.** New Computing Techniques in Physics Research V, 81–86. ISSN: 0168-9002. https://www.sciencedirect.com/science/article/pii/S016890029700048X (1997).
136. Clemencic, M. *et al.* The LHCb simulation application, Gauss: Design, evolution and experience. *J. Phys. Conf. Ser.* **331,** 032023 (2011).
137. Sjöstrand, T. The PYTHIA Event Generator: Past, Present and Future. *Comput. Phys. Commun.* **246,** 106910. arXiv: 1907.09874 [hep-ph] (2020).
138. Ryd, A. *et al.* EvtGen: A Monte Carlo Generator for B-Physics (May 2005).
139. Allison, J. *et al.* Geant4 developments and applications. *IEEE Transactions on Nuclear Science* **53,** 270–278 (2006).
140. LHCb Collaboration. The LHCb Upgrade I. *JINST* **19,** P05065. arXiv: 2305.10515 [hep-ex] (2024).
141. LHCb Collaboration. Physics case for an LHCb Upgrade II - Opportunities in flavour physics, and beyond, in the HL-LHC era. arXiv: 1808.08865 [hep-ex] (Aug. 2018).

142. Balagura, V. Van der Meer scan luminosity measurement and beam–beam correction. *Eur. Phys. J. C* **81,** 26. arXiv: `2012.07752 [hep-ex]` (2021).

143. Cacciari, M., Salam, G. P. & Soyez, G. The anti-k_t jet clustering algorithm. *JHEP* **04,** 063. arXiv: `0802.1189 [hep-ph]` (2008).

144. Cacciari, M., Salam, G. P. & Soyez, G. FastJet User Manual. *Eur. Phys. J. C* **72,** 1896. arXiv: `1111.6097 [hep-ph]` (2012).

145. LHCb Collaboration. Identification of beauty and charm quark jets at LHCb. *JINST* **10,** P06013. arXiv: `1504.07670 [hep-ex]` (2015).

146. Voss, H., Hocker, A., Stelzer, J. & Tegenfeldt, F. TMVA, the Toolkit for Multivariate Data Analysis with ROOT. *PoS* **ACAT,** 040 (2007).

147. Abada, A. *et al.* FCC-ee: The Lepton Collider: Future Circular Collider Conceptual Design Report Volume 2. *Eur. Phys. J. ST* **228,** 261–623 (2019).

148. Benedikt, M. *et al.* Future Circular Hadron Collider FCC-hh: Overview and Status. arXiv: `2203.07804 [physics.acc-ph]` (Mar. 2022).

149. Abe, T. *et al.* The International Large Detector: Letter of Intent. arXiv: `1006.3396 [hep-ex]` (Feb. 2010).

150. SiD Letter of Intent. arXiv: `0911.0006 [physics.ins-det]` (Nov. 2009).

151. The Compact Linear Collider (CLIC) - Project Implementation Plan. **4/2018.** arXiv: `1903.08655 [physics.acc-ph]` (Dec. 2018).

152. Robson, A. & Roloff, P. Updated CLIC luminosity staging baseline and Higgs coupling prospects. CLICdp-Note-2018-002. arXiv: `1812.01644 [hep-ex]` (Dec. 2018).

153. Kucharczyk, M. & Wojton, T. Hidden Valley searches at CLIC. CLICdp-Note-2018-001. `https://cds.cern.ch/record/2625054` (2018).

154. Suehara, T. & Tanabe, T. LCFIPlus: A Framework for Jet Analysis in Linear Collider Studies. *Nucl. Instrum. Meth. A* **808,** 109–116. arXiv: `1506.08371 [physics.ins-det]` (2016).

155. Read, A. L. Presentation of search results: the CLs technique. *Journal of Physics G: Nuclear and Particle Physics* **28,** 2693. `https://dx.doi.org/10.1088/0954-3899/28/10/313` (Sept. 2002).

156. Kilian, W., Ohl, T. & Reuter, J. WHIZARD: Simulating Multi-Particle Processes at LHC and ILC. *Eur. Phys. J. C* **71,** 1742. arXiv: `0708.4233 [hep-ph]` (2011).

157. Sjostrand, T., Mrenna, S. & Skands, P. Z. PYTHIA 6.4 Physics and Manual. *JHEP* **05,** 026. arXiv: `hep-ph/0603175` (2006).

158. Mora de Freitas, P. & Videau, H. *Detector simulation with MOKKA / GEANT4: Present and future* in *International Workshop on Linear Colliders (LCWS 2002)* (Aug. 2002), 623–627.

159. Gaede, F. Marlin and LCCD—Software tools for the ILC. *Nuclear Instruments and Methods in Physics Research Section A: Accelerators, Spectrometers, Detectors and Associated Equipment* **559.** Proceedings of the X International Workshop on Advanced Computing and Analysis Techniques in Physics Research, 177–180. ISSN: 0168-9002. `https://www.sciencedirect.com/science/article/pii/S0168900205022643` (2006).

160. Marshall, J. S., Münnich, A. & Thomson, M. A. Performance of Particle Flow Calorimetry at CLIC. *Nucl. Instrum. Meth. A* **700,** 153–162. arXiv: `1209.4039 [physics.ins-det]` (2013).

161. Catani, S., Dokshitzer, Y., Seymour, M. & Webber, B. Longitudinally-invariant kt-clustering algorithms for hadron-hadron collisions. *Nuclear Physics B* **406,** 187–224. ISSN: 0550-3213. `https://www.sciencedirect.com/science/article/pii/055032139390166M` (1993).
162. Aguillard, D. P. *et al.* Measurement of the Positive Muon Anomalous Magnetic Moment to 0.20 ppm. *Phys. Rev. Lett.* **131,** 161802. arXiv: `2308.06230 [hep-ex]` (2023).
163. Keshavarzi, A., Nomura, D. & Teubner, T. Muon $g-2$ and $\alpha(M_Z^2)$: a new data-based analysis. *Phys. Rev. D* **97,** 114025. arXiv: `1802.02995 [hep-ph]` (2018).
164. Lehner, C. High-precision lattice QCD calculations of the muon anomalous magnetic moment. *Nature Rev. Phys.* **4,** 14–15 (2022).
165. Dirac, P. A. M. The quantum theory of the electron. *Proc. Roy. Soc. Lond. A* **117,** 610–624 (1928).
166. Abi, B. *et al.* Measurement of the Positive Muon Anomalous Magnetic Moment to 0.46 ppm. *Phys. Rev. Lett.* **126,** 141801. arXiv: `2104.03281 [hep-ex]` (2021).
167. Bennett, G. W. *et al.* Final Report of the Muon E821 Anomalous Magnetic Moment Measurement at BNL. *Phys. Rev. D* **73,** 072003. arXiv: `hep-ex/0602035` (2006).
168. Abe, M. *et al.* A New Approach for Measuring the Muon Anomalous Magnetic Moment and Electric Dipole Moment. *PTEP* **2019,** 053C02. arXiv: `1901.03047 [physics.ins-det]` (2019).
169. Aoyama, T. *et al.* The anomalous magnetic moment of the muon in the Standard Model. *Phys. Rept.* **887,** 1–166. arXiv: `2006.04822 [hep-ph]` (2020).
170. Colangelo, G. *et al.* Prospects for precise predictions of a_μ in the Standard Model. arXiv: `2203.15810 [hep-ph]` (Mar. 2022).
171. Abbiendi, G. Status of the MUonE experiment. *Phys. Scripta* **97,** 054007. arXiv: `2201.13177 [physics.ins-det]` (2022).
172. CMS Collaboration. The Phase-2 Upgrade of the CMS Tracker (June 2017).
173. Adzic, P. *et al.* Energy resolution of the barrel of the CMS electromagnetic calorimeter. *JINST* **2,** P04004 (2007).
174. Galon, I., Shih, D. & Wang, I. R. Dark photons and displaced vertices at the MUonE experiment. *Phys. Rev. D* **107,** 095003. arXiv: `2202.08843 [hep-ph]` (2023).
175. *FairMUonE repository* `https://gitlab.cern.ch/muesli/offline-sw/fairmuone`.
176. *FairRoot repository* `https://github.com/FairRootGroup/FairRoot`.
177. Alacevich, M. *et al.* Muon-electron scattering at NLO. *JHEP* **02.** [Erratum: JHEP 02, 201 (2022)], 155. arXiv: `1811.06743 [hep-ph]` (2019).
178. Carloni Calame, C. M. *et al.* Towards muon-electron scattering at NNLO. *JHEP* **11,** 028. arXiv: `2007.01586 [hep-ph]` (2020).
179. Budassi, E. *et al.* NNLO virtual and real leptonic corrections to muon-electron scattering. *JHEP* **11,** 098. arXiv: `2109.14606 [hep-ph]` (2021).
180. Budassi, E., Carloni Calame, C. M., Del Pio, C. L. & Piccinini, F. Single $\pi 0$ production in μe scattering at MUonE. *Phys. Lett. B* **829,** 137138. arXiv: `2203.01639 [hep-ph]` (2022).

181. Prest, M. *et al.* The AGILE silicon tracker: An innovative gamma-ray instrument for space. *Nucl. Instrum. Meth. A* **501,** 280–287 (2003).

182. Adeva, B. *et al.* The Construction of the L3 Experiment. *Nucl. Instrum. Meth. A* **289,** 35–102 (1990).